THE UNIVERSITY *of* EDINBURGH

This thesis has been submitted in fulfilment of the requirements for a postgraduate degree (e. g. PhD, MPhil, DClinPsychol) at the University of Edinburgh. Please note the following terms and conditions of use:

- This work is protected by copyright and other intellectual property rights, which are retained by the thesis author, unless otherwise stated.
- A copy can be downloaded for personal non-commercial research or study, without prior permission or charge.
- This thesis cannot be reproduced or quoted extensively from without first obtaining permission in writing from the author.
- The content must not be changed in any way or sold commercially in any format or medium without the formal permission of the author.
- When referring to this work, full bibliographic details including the author, title, awarding institution and date of the thesis must be given.

Postnatal development of the somatosensory cortex in a rat model of Fragile X Syndrome

Anna Sumera, BSc (Hons)

THE UNIVERSITY *of* EDINBURGH

A thesis submitted for the degree of Doctor of Philosophy

Biomedical Sciences

College of Medicine and Veterinary Medicine

The University of Edinburgh

August 2025

Declaration

The work contained within this thesis was carried out in the Centre for Discovery Brain Sciences at the University of Edinburgh. Unless otherwise stated, the experiments and analysis were performed by myself, with the following exceptions:

- A subset of morphological reconstructions and dendritic spine density measurements presented in Chapter 4 was performed by Mona Khodary during her undergraduate Honours project in 2021 under my supervision.
- A subset of Sst-14 interneuron counts presented in Chapter 4 was performed by Abbi Crichton during her undergraduate Honours project in 2023 under my supervision.
- FACS sorting and library preparation for snRNAseq presented in Chapter 6 was done by the Institute for Regeneration and Repair at the University of Edinburgh. snRNA sequencing was performed by Edinburgh Genomics.
- MiSeq sequencing of Patch-seq samples in Chapter 7 was performed by me with assistance from Dr Jamie Toombs.

I declare that the presented thesis was composed entirely by myself and generative AI was not used in the writing of this thesis. With the exceptions listed above, no part of the work herein contained has been submitted for any other degree or professional qualification.

31/08/2025

Acknowledgements

This work would not have been possible without all the wonderful people in my life who have supported me along the way. First and foremost, I would like to extend my gratitude to my supervisors: Dr Sam Booker, Dr Chris Sibley and Prof Peter Kind. Your support and guidance have been invaluable throughout this PhD. Thank you for sharing your knowledge and enthusiasm with me, and always challenging me to become a better researcher.

I would like to thank the IRR Flow cytometry team, Dr Meryam Beniazza and Edinburgh Genomics for performing the FACS sorting, library preparation and snRNA sequencing; Dr Owen Dando for guiding me through my first steps into the world of bioinformatics; Dr Max Wilson for sharing the drug dosing duties, even on the weekends; Dr Laura Simões de Oliveira for teaching me everything I know about immunohistochemistry. Thank you to members of the Sibley lab – Josh, Fiona, Maja, Daniel, Jamie and Manon – for making me feel welcome in their lab, their encouragement and advice. Thanks to Manon Tourbez for teaching me the basics of molecular biology techniques and Dr Jamie Toombs for assisting with the sequencing process. Thanks to the BVS team for taking such great care of my animals, especially Chris Wilson, who graciously accommodated all of my requests, even the very last minute ones. Thank you to James Griffiths and the tech team for their support. Special thanks to those who offered to provide feedback on this thesis – Dr Darren Walsh, Dr Calvin Chan and Dr Susana Ribeiro dos Louros.

Thanks to Darren Walsh for being a great friend and mentor, all the pep talks and Red Bulls; and to all of my friends in SIDB (and beyond) who have made my PhD a really special experience – Noah Moore, Sydni Weissgold, Patrícia Bispo, Mila Redžić, James Hogg, Calvin Chan, Lysandra Fryer-Petridis, Lucy Pritchard, Nathalie Ling Sum Hung, Britt van de Gevel, Emma Perkins, Han Tan, Marie Pronot, Chloe Henley, Sabina Couto and Irenie Shiangoli.

A very special thanks to my dearest friends Wiktoria Galara, Yuly Romero and Rikuo Miyamoto for believing in me even when I did not. Thank you to my siblings Krzysztof and Agnieszka, my father Tomasz and my extended family for encouraging me to embark on this journey.

To Nina Petrović and Nawon Kim – I never thought that doing a PhD would let me meet my best friends. Without you I truly would not have been able to get to where I am now. Thank you for making this PhD so enjoyable, it would have felt lonely without you both. I can't wait for the lifetime of friendship that still awaits us.

I am especially grateful to the most important person in my life – my mom, Jolanta Sumera, who has patiently supported me through the highs and lows, heard about every failed experiment and reminded me about all the successes – dziękuję. Jestem Ci niezmiernie wdzięczna za Twoje wsparcie. Kocham Cię najbardziej na świecie.

Finally, my gratitude goes out to the person who has inspired me to pursue neuroscience research – the late Professor Jerzy Vetulani. Your passion for studying the human brain is what led be to begin this journey in the first place. I will be forever grateful to have attended your lectures in my teenage years, where I discovered my love for neuroscience.

And to anyone else who has inspired and supported me throughout the years – thank you.

Abstract

Fragile X Syndrome (FXS) is a common single-gene cause of autism and intellectual disability. Prevalent symptoms such as seizures and sensory hypersensitivity arise from cortical dysfunction, which could be underpinned by cortical hyperexcitability. Despite extensive research, currently there are no effective therapies targeting the underlying mechanisms, which could be due to species differences and limited understanding of how cortical dysfunction arises during development. In this thesis, I examined the first 4 weeks of postnatal development of the somatosensory cortex (S1) in a rat model of FXS, by characterizing the electrophysiological properties and morphology of S1 neurons, combined with an investigation of interneuron density. Using whole-cell patch clamp recordings from layer 4 of S1, I found that *Fmr1*$^{-/y}$ stellate cells (SCs) are hyperexcitable during early development, in agreement with previous research. Thanks to the high temporal resolution of these recordings, I have identified multiple phases of development in *Fmr1*$^{-/y}$ SCs, with distinct periods of intrinsic hyperexcitability flanked by typical excitability, which were not previously described. The different phases could arise due to different mechanisms, as SCs have a reduced dendritic complexity during the second postnatal week that is normalized before hyperexcitability arises for the second time. Changes in excitability are accompanied by an increase in the density of somatostatin-expressing interneurons. Early pharmacological treatment with BPN14770 was able to normalize the action potential output and morphology of the SCs during the second postnatal week, but did not provide a long-term rescue of excitability. Additionally, I have identified cell type-specific transcriptomic differences in the developing somatosensory cortex of *Fmr1*$^{-/y}$ rats, which support the physiological changes. Together, these data suggest that the developmental trajectory taken by the *Fmr1*$^{-/y}$ cortex is significantly altered, but partially amenable to therapeutic intervention albeit without long-term effects.

Lay summary

Neurodevelopmental disorders are caused by differences in how the brain develops in early life. One such disorder is Fragile X Syndrome (FXS), which is one of the most common inherited single gene causes of autism and intellectual disability, with common symptoms including seizures and increased sensitivity to stimuli such as touch. While such symptoms are known to be caused by changes in brain function, it is unclear how these changes arise during development. Therefore, I have used a rat model of FXS to characterize their brain development in early life. I found that in the somatosensory cortex, a brain area that is responsible for processing touch sensation, specific brain cells are more active, due to changes in their electrical properties. These changes follow a dynamic trajectory with age, with two distinct periods of increased activity during the second and fourth week of life, and typical activity in between. Increased activity in the second week coincides with, and is likely caused by, changes in the shape of these brain cells. I identified changes in gene expression that differ between cell types, and could explain their different activity. I also found an increase in the number of a specific type of inhibitory cells, which could be responsible for rebalancing cortical function by decreasing overall activity. Finally, I found that a brief treatment with a previously clinically successful drug in early life is able to rescue the early increase in brain cell activity and their shape, but this rescue does not last long term. Overall, in this thesis I showed that in a rat model of FXS, the somatosensory cortex development follows a different trajectory, which can be partially rescued with drug therapy. These findings provide novel insight into the role of early life cortical development in FXS that can inform the development of more successful therapies in the future.

Table of Contents

Declaration **1**

Acknowledgements **2**

Abstract **4**

Lay summary **5**

List of abbreviations **11**

List of Figures **13**

List of Tables **16**

Chapter 1 ..... **18**

Introduction **18**

1.1 Neurodevelopmental disorders 18

1.2 Fragile X Syndrome 22

1.2.1 Molecular basis of FXS and FMRP functions 23

1.3 Models of Fragile X Syndrome 26

1.3.1 *Fmr1*$^{-/y}$ mouse phenotypes 26

1.3.2 Rat model of FXS 31

1.4 Proposed mechanisms 35

1.4.1 Therapeutic interventions in FXS 38

1.5 Barrel cortex as a model for sensory development 40

1.5.1 Structure of the barrel cortex 40

1.5.2 Postnatal development of the barrel cortex 42

1.5.3 S1 development in rodent models of FXS 43

1.6 Aims of this thesis 46

Chapter 2 ..... **48**

Materials & Methods **48**

2.1 Animals 48

2.2 Electrophysiology 49

2.2.1 Acute cortical slice preparation 49

2.2.2 Whole-cell patch clamp recordings 49

2.2.3 Intrinsic properties 50

2.2.4 Synaptic properties 52

2.3 BPN14770 treatment 53

2.3.1 Dosing protocol 53
2.4 Histology 54
2.4.1 Cell morphology labelling 54
2.4.2 Perfusion fixation 54
2.4.3 Immunolabelling 55
2.5 Confocal imaging & image analysis 56
2.5.1 Cell morphology 56
2.5.2 Dendritic spine density 57
2.5.3 Interneuron density 57
2.6 Transcriptomics 59
2.6.1 Single nuclei isolation 59
2.6.2 snRNAseq 59
2.7 Bioinformatics 61
2.7.1 snRNAseq analysis 61
2.8 Statistics 64
Chapter 3 65
Electrophysiological characterization of S1 development in a rat model of FXS 65
3.1 Introduction 65
3.2 Electrophysiological characterization of S1 L4 SCs during development in *Fmr1*$^{-/y}$ rats 67
3.2.1 L4 SCs are hyperexcitable in *Fmr1*$^{-/y}$ rats 68
3.2.2 Passive properties are altered in *Fmr1*$^{-/y}$ L4 SCs 71
3.2.3 *Fmr1*$^{-/y}$ have altered action potential kinetics 73
3.2.4 mAHP is not affected in *Fmr1*$^{-/y}$ L4 SCs 76
3.2.5 No change in sag in L4 SCs 77
3.2.6 Resonance 79
3.2.7 Excitatory synaptic properties 82
3.3 Discussion 84
3.3.1 AP firing, intrinsic and synaptic properties 85
3.3.2 Depolarization block 86
3.3.3 AP dynamics and mAHP 87
3.3.4 Sag and resonance 90
3.3.5 Summary 92
Chapter 4 93

Anatomical characterization of S1 development in *Fmr1*$^{-/y}$ rats 93
4.1 Introduction 93
4.2 L4 SC morphology during development of *Fmr1*$^{-/y}$ rats 95
4.2.1 *Fmr1*$^{-/y}$ L4 SCs have less complex dendritic arbours at P9-14 95
4.2.2 Dendritic spine density is unaffected in *Fmr1*$^{-/y}$ L4 SCs 98
4.3 Interneuron density 99
4.3.1 Parvalbumin^{+} cell density is not affected in *Fmr1*$^{-/y}$ rats 99
4.3.2 *Fmr1*$^{-/y}$ rats have typical reelin^{+} cell density 101
4.3.3 Somatostatin-14^{+} cell density is increased in *Fmr1*$^{-/y}$ rats 102
4.4 Discussion 104
4.4.1 Morphology 104
4.4.2 Spine density 107
4.4.3 Interneuron density 108
4.4.4 Summary 114
Chapter 5 116
Pharmacological rescue of *Fmr1*$^{-/y}$ L4 SC development through BPN14770 treatment 116
5.1 Introduction 116
5.2 BPN14770 treatment partially corrects *Fmr1*$^{-/y}$ development at P10-14 119
5.2.1 *Fmr1*$^{-/y}$ L4 SC depolarization block but not passive intrinsic properties are rescued by BPN14770 treatment 119
5.2.2 AP kinetics are not affected by BPN14770 treatment 123
5.2.3 BPN14770 rescues dendritic morphology of *Fmr1*$^{-/y}$ L4 SCs 125
5.3 Early BPN14770 treatment does not rescue *Fmr1*$^{-/y}$ L4 SC hyperexcitability at P25-28 127
5.3.1 Intrinsic physiology of L4 SCs is minimally affected by BPN14770 127
5.3.2 AP kinetics 129
5.3.3 Morphology 130
5.4 Discussion 132
5.4.1 BPN14770 treatment in early development 132
5.4.2 Limitations 135
5.4.3 Summary 139
Chapter 6 140
Transcriptomic characterization of S1 development in *Fmr1*$^{-/y}$ rats 140

6.1 Introduction....140
6.2 Transcriptomic characterization of developing S1 in *Fmr1*$^{-/y}$ rats....143
6.2.1 Clustering of single nuclei transcriptomes....143
6.2.2 Cell type composition of the S1 does not differ between WT and *Fmr1*$^{-/y}$....144
6.2.3 Cell type identification by cluster....145
6.2.4 Differential gene expression analysis identifies neurons as the most affected cell type in *Fmr1*$^{-/y}$ cortex....149
6.2.5 Excitatory neuron subclusters show cortical lamination....152
6.2.6 Excitatory neuron transcriptomes differ by subtype....155
6.2.7 Inhibitory neurons separate into subtype clusters....160
6.2.8 Inhibitory neurons show subtype-specific gene expression changes in *Fmr1*$^{-/y}$....163
6.3 Discussion....165
6.3.1 Excitatory neurons....165
6.3.2 Inhibitory neurons....168
6.3.3 General and non-neuronal changes....169
6.3.4 Summary....171
Chapter 7....172
Detailed Patch-seq protocol & optimization in S1 L4 SCs....172
7.1 Introduction....172
7.2 Recording and sample collection....174
7.3 Sample processing optimization....180
7.3.1 Sample lysis and storage buffer....180
7.3.2 First-strand cDNA synthesis....182
7.3.3 cDNA amplification by PCR....183
7.3.4 Bead purification....184
7.3.5 Selecting samples for library preparation....185
7.4 Library preparation....187
7.5 Sequencing....190
7.6 Discussion....191
Chapter 8....195
General discussion....195
8.1 Summary of findings....195

8.2 Role of homeostatic compensation in FXS 197
8.3 Species differences and future considerations 200
8.4 Therapeutic perspective in FXS 202
8.5 Limitations 203
8.6 Conclusion 204
Appendix 205
9.1 Detailed statistics 205
9.1.1 Chapter 3 – Electrophysiology 205
9.1.2 Chapter 4 – Anatomy 207
9.1.3 Chapter 5 – BPN14770 treatment 210
9.1.4 Chapter 7 – Patch-seq 214
9.2 Differentially expressed gene list 215
9.2.1 Excitatory neurons 215
9.2.2 Inhibitory neurons 220
9.3 *FMR1* gene re-expression in mouse hippocampus 223
References 225

List of abbreviations

AC – adenylate cyclase

ACSF – artificial cerebrospinal fluid

ADHD – attention deficit hyperactivity disorder

ANOVA – analysis of variance

ASD – autism spectrum disorder

BMP – bone morphogenic protein

CA1 – *Cornu Ammonis* 1

CA3 – *Cornu Ammonis* 3

cACSF – cutting artificial cerebrospinal fluid

CaM – calmodulin

cAMP – cyclic adenosine monophosphate

C_m – membrane capacitance

CNV – copy number variation

DAG – diacylglycerol

DEG – differentially expressed gene

DGE – differential gene expression

DSM-5 – Diagnostic and Statistical Manual of Mental Disorders, Fifth Edition

EEG – electroencephalography

ELISA – enzyme-linked immunosorbent assay

ERK – extracellular signal-regulated kinase

ERP – event-related potential

FFI – feed-forward inhibition

FMRP – Fragile X Messenger Ribonucleoprotein

FXS – Fragile X Syndrome

GLMM – generalized linear mixed model

GPCR – G-protein coupled receptor

GWAS – genome-wide association study

HC – hippocampus

ID – intellectual disability

IN – interneuron

IP3 – inositol-1,4,5-trisphosphate

iPSC – induced pluripotent stem cell

IQ – intelligence quotient

IR – input resistance

IR-DIC – infrared differential inference contrast

KO – knockout

LFS – low frequency stimulation

LTD – long-term depression

LTP – long-term potentiation

mAHP – medium afterhyperpolarization

MAPK – mitogen-activated protein kinase

MGE – medial ganglionic eminence

mGluR – metabotropic glutamate receptor

mPFC – medial prefrontal cortex

MRI – magnetic resonance imaging

MTC – membrane time constant

NDD – neurodevelopmental disorder

NGS – normal goat serum

OPC – oligodendrocyte precursor cell

PB – phosphate buffer

PBS – phosphate buffered saline

PC – pyramidal cell

PCR – polymerase chain reaction

PDE – phosphodiesterase

PI3K – phosphoinositide 3-kinase

PKC – protein kinase C

PLC – phospholipase C

PV – parvalbumin

R_a – access resistance

R_f – resonant frequency

RMP – resting membrane potential

S1 – primary somatosensory cortex

sAHP – slow afterhyperpolarization

SD – standard deviation

SEM – standard error of the mean

sEPSC – spontaneous excitatory postsynaptic current

SNP – single nucleotide polymorphism

snRNAseq – single nucleus RNA sequencing

Sst – somatostatin

UMAP – uniform manifold approximation and projection

UMI – unique molecular identifier

UPS – ubiquitin proteasome system

UTR – untranslated region

YFP – yellow fluorescent protein

V1 – primary visual cortex

VEGF – vascular endothelial growth factor

VGAT – vesicular GABA transporter

VGKC – voltage-gated potassium channel

VGSC – voltage-gated sodium channel

VIP – vasoactive intestinal peptide

VLMC – vascular leptomeningeal cell

V_m – membrane potential

V_{thresh} – voltage threshold

WT – wild-type

List of Figures

Figure 1.1. Diagram of the molecular basis of Fragile X Syndrome. 24

Figure 1.2. Simplified diagram of mGluR and cAMP signalling pathways. 37

Figure 1.3 Excitatory circuitry within the rodent barrel cortex. 41

Figure 2.1. Diagram of passive and active intrinsic properties measurements. 51

Figure 2.2. BPN14770 treatment results in lower body weight in WT and *Fmr1*$^{-/y}$ rats. 53

Figure 2.3. Timeline of BPN14770 treatment experiments. 54

Figure 2.4. Morphology analysis in L4 SCs. 57

Figure 2.5. Diagram of the optical disector method for unbiased stereological estimation of cell density within three dimensional structures. 58

Figure 3.1. *Fmr1*$^{-/y}$ L4 stellate cells (SCs) are hyperexcitable during development. 70

Figure 3.2. *Fmr1*$^{-/y}$ cells have altered passive membrane properties during development. 72

Figure 3.3. *Fmr1*$^{-/y}$ show altered AP kinetics in the rising phase. 75

Figure 3.4. mAHP is mostly intact in *Fmr1*$^{-/y}$ rats. 76

Figure 3.5. Hyperpolarization-induced sag and rebound are intact in *Fmr1*$^{-/y}$ rats. 78

Figure 3.6. *Fmr1*$^{-/y}$ L4 SCs have altered resonance properties. 80

Figure 3.7. *Fmr1*$^{-/y}$ resonant cells show higher impedance and lower resonant frequency at P21-28. 81

Figure 3.8. Spontaneous excitatory postsynaptic currents are unaffected in *Fmr1*$^{-/y}$. 83

Figure 4.1. *Fmr1*$^{-/y}$ L4 SCs show lower dendritic complexity at P9-14, but not P15-20 and P21-28. 97

Figure 4.2. L4 SC dendritic spine density is unaltered in *Fmr1*$^{-/y}$, but increases during development. 98

Figure 4.3. *Fmr1*$^{-/y}$ have typical PV^{+} cell density during development. 100

Figure 4.4. Reelin^{+} cell density is unaltered in *Fmr1*$^{-/y}$ during development. 101

Figure 4.5. *Fmr1*$^{-/y}$ have an increased Sst-14^{+} cell density during development. 103

Figure 4.6. Diagram of proposed mechanism of Sst signalling in FXS. 113

Figure 5.1. BPN14770 treatment rescues the AP firing but not the intrinsic properties of *Fmr1*$^{-/y}$ L4 SCs at P10-14. 122
Figure 5.2. AP kinetics are not significantly affected by BPN14770 treatment at P10-14. 124
Figure 5.3. BPN14770 treatment rescues reduced dendritic complexity in *Fmr1*$^{-/y}$ L4 SCs at P10-14. 126
Figure 5.4. BPN14770 treatment does not rescue the AP firing and intrinsic properties of L4 SCs at P25-28. 128
Figure 5.5. BPN14770 treatment does not affect AP kinetics at P25-28. 130
Figure 5.6. BPN14770 treatment does not affect L4 SC morphology at P25-28. 131
Figure 6.1. Unsupervised clustering divides S1 cells into 18 clusters. 143
Figure 6.2. *Fmr1*$^{-/y}$ S1 does not differ in cell type composition at P9. 145
Figure 6.3. Transcriptomic clusters represent distinct cell types in the S1. 146
Figure 6.4. Feature UMAP plots of selected gene marker expression. 147
Figure 6.5. Summary of gene marker expression by cell type cluster. 148
Figure 6.6. Differential gene expression analysis reveals cell-type specific patterns of altered gene expression in *Fmr1*$^{-/y}$ S1. 152
Figure 6.7. Excitatory neuron subclusters show evidence of cortical layers. 154
Figure 6.8. Excitatory neurons show subtype-specific differences in differentially expressed genes in *Fmr1*$^{-/y}$ S1. 156
Figure 6.9. Upper layer excitatory neurons 1 and 2 differentially express mitochondrial, ribosomal and cell morphology genes. 158
Figure 6.10. Deep layer excitatory neuron 3 and 4 subclusters differentially express synaptic and developmental genes. 159
Figure 6.11. Inhibitory neuron subclusters contain several distinct classes of interneurons. 162
Figure 6.12. *Fmr1*$^{-/y}$ inhibitory neurons show subtype-specific changes in gene expression. 164
Figure 7.1. Diagram of the Patch-seq workflow. 174
Figure 7.2. Patch-seq recording conditions significantly affect several intrinsic physiology parameters in L4 SCs. 177
Figure 7.3. Example Patch-seq cell extractions. 179

Figure 7.4. Storage buffer optimization. 181
Figure 7.5. PCR cycle number optimization. 184
Figure 7.6. Bead concentration optimization. 185
Figure 7.7 Quantification of cDNA quality. 186
Figure 7.8. Library amplification optimization. 189
Figure 7.9. Final library quantification. 189
Figure 7.10. Sankey plot of Patch-seq samples showing the number of cells at each step of the protocol. 191
Figure 8.1. Summary of key findings. 196
Figure 9.1. FMR1 re-expression in the CA1 does not rescue exaggerated LTD in *Fmr1*$^{-/y}$ mice. 233

List of Tables

Table 1.1. Behavioural, circuit and cellular phenotypes of *Fmr1*$^{-/y}$ mice. 28

Table 1.2. Behavioural, circuit and cellular phenotypes of *Fmr1*$^{-/y}$ rats. 33

Table 1.3. Developmental phenotypes in S1 of *Fmr1*$^{-/y}$ mice (<2 months of age). ... 44

Table 2.1. Composition of cutting and recording ACSF solutions used for electrophysiology recordings. 49

Table 2.2. Composition of 8 mM Cl^- potassium gluconate internal solution used for intrinsic physiology recordings..... 50

Table 2.3. List of primary antibodies used. 55

Table 2.4. List of secondary antibodies used. 56

Table 2.5. Summary of outliers removed and thresholds for the selected criteria. . 61

Table 2.6. Summary of doublets removed per sample. 62

Table 2.7. Summary of filtered cells per sample. 62

Table 2.8. Summary of gene markers used to identify cell types..... 63

Table 2.9. Summary of cortical layer markers used to identify excitatory neuron subtypes. 63

Table 3.1. Summary of WT and *Fmr1*$^{-/y}$ cells recorded per age group. 67

Table 3.2. Summary of Chapter 3 results. 84

Table 4.1. Summary of Chapter 4 results. 104

Table 5.1. Summary of Chapter 5 results. 132

Table 5.2. Comparison of selected intrinsic properties for P9-12 control (Chapter 3) and P10-14 vehicle and BPN1770-treated L4 SCs. 138

Table 6.1. Cell numbers by cell type and genotype. 144

Table 6.2. Number of excitatory neurons by subcluster and genotype. 153

Table 6.3. Number of inhibitory neurons by subcluster and genotype..... 161

Table 7.1. Composition of modified 8 mM Cl^- potassium gluconate internal solution used for Patch-seq recordings..... 175

Table 7.2. Summary of criteria for assessing Patch-seq extraction quality..... 179

Table 7.3. Sample preparation..... 180

Table 7.4. Composition of the lysis storage buffer. 181

Table 7.5. Composition of the RT master mix..... 182

Table 7.6. RT-PCR program setup. 182
Table 7.7. Composition of the PCR master mix. 183
Table 7.8. PCR program setup. 183
Table 7.9. Composition of the adjusted test PCR master mix. 185
Table 7.10. Composition of the PCR master mix for the final PCR. 186
Table 7.11. Composition of the Library Prep master mix. 187
Table 7.12. Library preparation program setup. 187
Table 7.13. Composition of the Library Amplification master mix 187
Table 7.14. Library amplification program setup. 188
Table 7.15. Summary of amplified cDNA concentration, average size and reads obtained from Patch-seq samples. 190
Table 9.1. Summary of GLMM results for L4 SC electrophysiological properties.. . 205
Table 9.2. Summary of 2-way ANOVA results for L4 SC morphology. 207
Table 9.3. Summary of GLMM results for L4 SC dendritic spine density. 207
Table 9.4. Summary of 2-way ANOVA results for PV^+ cell density. 208
Table 9.5. Summary of 2-way ANOVA results for $reelin^+$ cell density. 208
Table 9.6. Summary of 2-way ANOVA results for $Sst\text{-}14^+$ cell density. 209
Table 9.8. Summary of 2-way ANOVA results for L4 SC morphology at P10-14 after treatment with vehicle or BPN14770. 211
Table 9.9. Summary of GLMM results for intrinsic properties of L4 SCs at P25-28 after BPN14770 treatment. 212
Table 9.10. Summary of 2-way ANOVA results for L4 SC morphology at P25-28 after treatment with vehicle or BPN14770. 213
Table 9.11. Summary of GLMM results for intrinsic properties of P9-12 L4 SCs recorded under standard whole-cell patch clamp or Patch-seq conditions. 214
Table 9.12. Upregulated genes in excitatory neurons – Figure 6.6B. 215
Table 9.13. Downregulated genes in excitatory neurons – Figure 6.6B. 218
Table 9.14. Upregulated genes in inhibitory neurons – Figure 6.6D. 220
Table 9.15. Downregulated genes in inhibitory neurons – Figure 6.6D. 222

Chapter 1

Introduction

1.1 Neurodevelopmental disorders

Neurodevelopmental disorders (NDDs) comprise a wide range of disorders typically diagnosed in childhood, including autism, intellectual disability (ID), attention deficit hyperactivity disorder (ADHD) and specific learning disorders. Depending on the specific condition, the prevalence of NDDs typically ranges from 1-20% worldwide (Francés *et al.*, 2022, 2023; Q. Li *et al.*, 2023). Autism spectrum disorder and intellectual disability (ASD/ID) are among the most common NDDs, affecting 3-5% of the population (Srivastava and Schwartz, 2014).

According to Diagnostic and Statistical Manual of Mental Disorders (DSM-5) criteria, ASD diagnoses are made based on difficulties in social interaction and communication, restricted or repetitive behaviours and interests, which are present during childhood and impair function (American Psychiatric Association, 2022). Intellectual disability is defined by an intelligence quotient (IQ) of 70 or less, accompanied by deficits in adaptive function (American Psychiatric Association, 2022). These conditions show a large degree of comorbidity, with 40-70% of all autistic individuals receiving a diagnosis of ID (Baird *et al.*, 2006; Micai *et al.*, 2023) and at least 10-20% of individuals with ID also having ASD, although the degree of comorbidity depends on the specific condition in this case (Srivastava and Schwartz, 2014). The degree of intellectual impairment in ASD/ID exists on a wide spectrum of severity, ranging from mild, with impaired function but capable of independent living, to severe and even profound, in which case the individual requires constant care and support. The severity of ID is greater in individuals who also received an ASD diagnosis than ID alone (Schieve *et al.*, 2015). Furthermore, ASD/ID frequently co-occur with a range of other conditions, with over half of individuals with autism having 4 or more

comorbid conditions in addition to ID (Lundström *et al.*, 2015). These include conditions such as ADHD, disruptive impulse control disorder, language disorder, sleep problems, as well as mental health issues such as depression and anxiety (Micai *et al.*, 2023). Sensory abnormalities, such as hypo- and hypersensitivity, span multiple sensory domains and contribute to behavioural problems such as inattention and aggression (Leekam *et al.*, 2007). Epilepsy is another condition comorbid with ASD/ID, affecting 16-44% of individuals with ASD (Lee, Smith and Paciorkowski, 2015), with a co-diagnosis of ID being a major risk factor for epilepsy, making epilepsy three times as common in ASD/ID than in autism alone (Amiet *et al.*, 2008). The onset of epilepsy in ASD/ID typically falls before the age of 5 years and is associated with a developmental regression and impaired language ability (Tuchman and Cuccaro, 2011; Zarakoviti *et al.*, 2023). Notably, the aforementioned comorbidities are more common in severely affected individuals, suggesting the possibility of a common etiology between ASD/ID and its co-occurring conditions such as epilepsy (Khachadourian *et al.*, 2023).

The underlying causes of ASD/ID are highly heterogenous, including genetic and environmental factors, or idiopathic. Environmental influences have been estimated to account for up to 40-50% of ASD cases (Hallmayer, 2011; Deng *et al.*, 2015) and can include perinatal factors such as preterm birth, low birth weight and hypoxia (Schieve *et al.*, 2015; Karimi *et al.*, 2017). Parental age and obesity, gestational diabetes, maternal autoimmune disease as well as maternal infections during pregnancy have likewise been associated with increased ASD risk (reviewed in Modabbernia, Velthorst and Reichenberg, 2017).

Twin studies have revealed that the etiology of ASD has a strong genetic component, estimating the heritability at up to 80-90% with concordance rates of 40-80% in monozygotic twins (Bailey *et al.*, 1995; Hallmayer, 2011; Lundström *et al.*, 2012, 2015; Sandin *et al.*, 2014; Deng *et al.*, 2015). However, early genome-wide association studies (GWAS) largely failed to reliably and consistently identify common inherited single-nucleotide polymorphisms (SNPs) associated with ASD risk, and suggested that the individual contribution of common variants to the ASD risk is likely minor (Wang *et al.*, 2009; Weiss *et al.*, 2009; Anney *et al.*, 2010, 2012). Subsequent

large-scale GWAS revealed that common ASD risk variants may be shared with other psychiatric conditions such as schizophrenia and depression (Anney *et al.,* 2017; Grove *et al.*, 2019).

Instead, microarray, whole-exome and whole-genome sequencing have proven instrumental in identifying the genetic causes of ASD, such as inherited and *de novo* copy number variations (CNVs) contributing to 10% of ASD cases (Devlin and Scherer, 2012; C Yuen *et al.*, 2017; Stessman *et al.*, 2017). *De novo* genetic mutations account for 13-60% of ASD diagnoses, which are typically comorbid with ID (Wilfert *et al.*, 2017). These include CNVs such as 15q11-13 duplication and 16p11.2 microdeletion, single nucleotide variants, small insertions/deletions (indels) and likely gene-disruptive mutations, e.g. *CHD8*, *SYNGAP1, SCN2A* or *ARID1B*. The SFARI Gene database, which collates genes associated with ASD (Arpi and Simpson, 2022), currently contains 1161 genes, including 218 syndromic genes. Syndromic ASD/ID is associated with a broader genetically encoded – often monogenic – condition, such as Fragile X Syndrome (FXS), which accounts for 2-5% of all ASD/ID cases (Schaefer and Mendelsohn, 2008; Sztainberg and Zoghbi, 2016).

Despite the diverse etiology, several mechanisms have been proposed to underlie ASD. Rubenstein and Merzenich (2003) suggested that ASD could be underlain by an imbalance between the levels of excitation and inhibition in the brain. Such an imbalance may arise as a result of cortical hyperexcitability and/or impaired inhibition failing to effectively regulate network-level activity, which have been found in multiple animal models of ASD and may also underlie conditions frequently co-occurring with ASD such as epilepsy and sleep disturbances (Zahra *et al.*, 2022; Bridi and Peixoto, 2025). Alternatively, it has been suggested that changes to the excitation/inhibition (E/I) balance are themselves homeostatic, in order to stabilize cortical activity on a circuit level (Antoine *et al.*, 2019). ASD could also be a result of impaired synaptic function, as synaptic signalling and plasticity are known to be disrupted in several models of ASD, including Fragile X Syndrome (Huber *et al.*, 2002; Wang *et al.*, 2011; Barnes *et al.*, 2015; Ellingford *et al.*, 2021; Simões de Oliveira *et al.*, 2024). Many genes associated with ASD risk themselves code for synaptic proteins, or are involved in synaptic structure and function e.g., *SYNGAP1, NLGN3, NRXN1,*

ILRAPL1, CNTNAP2 (Devlin and Scherer, 2012; Wang *et al.*, 2016; C Yuen *et al.*, 2017; Stessman *et al.*, 2017). Finally, anatomical differences or changes in connectivity could underlie the ASD phenotype, such as decreased inter-regional functional connectivity and local hyperconnectivity in the brains of ASD individuals (Haberl *et al.*, 2015; Moseley *et al.*, 2015; Xu *et al.*, 2018).

1.2 Fragile X Syndrome

FXS is an NDD and a leading inherited single-gene cause of ASD/ID, which affects 1:4000 males and 1:8000 females globally (Turner *et al.*, 1996; Crawford, Acuña and Sherman, 2001; O'Donnell and Warren, 2002). As FXS is caused by mutations on the X chromosome, it is more common in males, and typically less severe in females (Turner *et al.*, 1996; Bartholomay *et al.*, 2019). 20-50% of FXS individuals receive an autism diagnosis, thus accounting for 1-6% of all autism cases (Kaufmann *et al.*, 2004, 2017; Muhle, Trentacoste and Rapin, 2004; Clifford *et al.*, 2007; Harris *et al.*, 2008; Hernandez *et al.*, 2009). Cognitive impairment or intellectual disability represents a hallmark of FXS, with IQ scores ranging from mild (50-70) to profound intellectual disability (Wright-Talamante *et al.*, 1996; Hessl *et al.*, 2009). Behavioural issues are common in FXS, and include general inattentiveness, cognitive inflexibility, anxiety, social withdrawal or avoidance as well as impaired impulse control occasionally leading to aggression (Cordeiro *et al.*, 2011; Cregenzán-Royo, Brun-Gasca and Fornieles-Deu, 2022). Perseveration, repetitive behaviours and self-injury are characteristic of FXS individuals and associated with anxiety and autism (Oakes *et al.*, 2016). Up to 20% of FXS individuals experience seizures, which typically begin in childhood (Berry-Kravis, 2002). Seizures are more common in severely affected FXS individuals and thus may be correlated with the degree of intellectual disability (Berry-Kravis, Filipink, *et al.*, 2021). Additionally, FXS individuals frequently experience sensory processing issues across multiple modalities (Rais *et al.*, 2018). Sensory hypersensitivity often manifests as tactile defensiveness starting from early development, and is more common in FXS individuals who also have autism (Rogers, Hepburn and Wehner, 2003; Baranek *et al.*, 2008). Altered auditory processing and auditory hypersensitivity are also common, alongside impaired performance in tasks assessing visuomotor function and spatial cognition (Cornish, Munir and Cross, 1999; Kogan, 2003). Atypical sensory profiles in FXS individuals show an association with their social and communication deficits (Rogers, Hepburn and Wehner, 2003). Sleep disturbances are a prevalent feature in FXS, affecting up to 45% of FXS individuals and correlating with other symptoms such as aggression and inattention (Budimirovic *et al.*, 2022). Furthermore, FXS is associated with physical features such as prominent

ears, a long and narrow face, macroorchidism in males, flat feet, high palate, hypotonia, as well as looser connective tissue giving rise to abnormally flexible joints and more stretchable skin (Chudley and Hagerman, 1987; Crawford *et al.*, 2020).

Core symptoms in FXS are associated with changes in cortical function. FXS individuals exhibit deficits in oscillatory brain activity, with elevated gamma power and impaired synchronization of auditory-evoked potentials, which are associated with cortical hyperexcitability and hypersensitivity to sensory stimuli (Ethridge *et al.*, 2016, 2017). Structural magnetic resonance imaging (MRI) studies and *post mortem* examinations have identified neuroanatomical differences in the brains of FXS individuals, including vermis and superior temporal gyrus hypoplasia, atypical hippocampal morphology or increased hippocampal and ventricular volume as well as decreased functional connectivity in the insular cortex; changes that are believed to contribute to some of the behavioural phenotypes in FXS (Reyniers *et al.*, 1999; Sabaratnam, 2000; Hessl, Rivera and Reiss, 2004; Lee *et al.*, 2007; Hoeft *et al.*, 2010; Hall *et al.*, 2013). White matter microstructure is affected in development, with reductions in the density of several white matter tracts, such as the anterior limb of the internal capsule, inferior longitudinal fasciculus and superior cerebellar peduncles in infants with FXS from as early as 6 months of age, which are associated with cognitive deficits and persist into adulthood (Barnea-Goraly *et al.*, 2003; Hall, Dougherty and Reiss, 2016; Swanson *et al.*, 2018). Changes in dendritic spine morphology (increased abundance of long and thin filopodia-like spines, few short mushroom-like spines) as well as an increase in their density have been described in the cortex of FXS individuals, implying deficits in processes such as synaptogenesis or pruning (Rudelli *et al.*, 1985; Hinton *et al.*, 1991; Irwin *et al.*, 2001; Greco *et al.*, 2011).

1.2.1 Molecular basis of FXS and FMRP functions

Fragile X Syndrome is most frequently caused by the expansion of the CGG repeat in the 5' untranslated region (UTR) of the *FMR1* gene (Figure 1.1), located at the Xq27.3 locus on the X chromosome (Verkerk *et al.*, 1991). While the 5' UTR typically contains under 55 CGG repeats, an expansion of >200 is considered a full mutation giving rise to FXS (Kaufmann and Reiss, 1999). A full mutation leads to the

hypermethylation of the *FMR1* gene within the CGG repeat region, rendering the *FMR1* promoter inaccessible to RNA polymerase, leading to transcriptional inactivation, preventing the expression of the *FMR1* gene (Bell *et al.*, 1991; Sutcliffe *et al.*, 1992). As a result, in FXS the *FMR1* mRNA and the subsequent protein product, Fragile X Ribonucleoprotein (FMRP) are lost (Pieretti *et al.*, 1991).

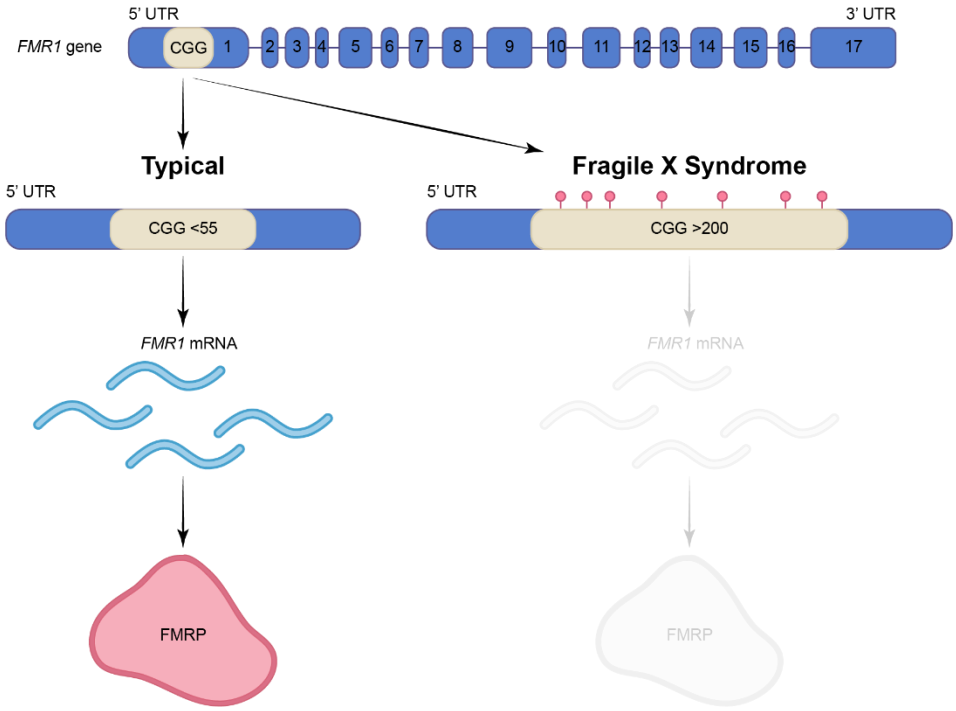

Figure 1.1. Diagram of the molecular basis of Fragile X Syndrome. Typically, the 5'UTR in exon 1 of the *FMR1* gene contains <55 CGG repeats, allowing for the transcription into the *FMR1* mRNA and synthesis of its protein product FMRP. In Fragile X Syndrome, the CGG repeat expansion of >200 repeats leads to the hypermethylation of the *FMR1* gene, its transcriptional silencing and the subsequent loss of the FMRP protein product.

FMRP canonically functions as a translational repressor, negatively regulating the expression of 100s of genes (Zalfa *et al.*, 2003; Darnell *et al.*, 2011). FMRP contains at least 3 mRNA binding domains (Schaeffer, 2001; Athar and Joseph, 2020; Richter and Zhao, 2021), allowing it to directly bind to and regulate mRNA translation as well as metabolism. 85-90% of FMRP in the brain is associated with polyribosomes, binding to actively translating mRNAs, stalling the translation complex (Stefani *et al.*, 2004; Darnell *et al.*, 2011). As such, protein synthesis rates are elevated in the absence of FMRP, both at rest and in activity-dependent *de novo* protein translation (Osterweil *et al.*, 2010; Bowling *et al.*, 2019). FMRP is particularly enriched in dendritic spines and its expression is regulated by neuronal activity (Weiler and Greenough, 1999; Gabel *et al.*, 2004; Till *et al.*, 2012). FMRP preferentially binds to long mRNA

transcripts with targets including several pre- and postsynaptic proteins that are involved in synaptic transmission, structure and function (Brown *et al.*, 2001; Darnell *et al.*, 2011). Consequently, FMRP plays a key role in regulating synaptic plasticity (reviewed in Sidorov, Auerbach and Bear, 2013), as well as synaptogenesis, dendritic spine formation, stability and maturation (Khayachi *et al.*, 2018; Wang *et al.*, 2018). Furthermore, FMRP plays a significant role in early brain development by regulating Wnt, mTOR and MAPK signalling; and may be required for axon guidance as well as the activity-dependent refinement of neuronal circuits (Antar *et al.*, 2006; Doll and Broadie, 2015; Casingal *et al.*, 2020; Marfull-Oromí *et al.*, 2023). Additional mechanisms of FMRP action have been proposed, including directly binding to ion channels such as BK and SK channels, thus influencing the excitability and action potential kinetics of neurons (Deng *et al.*, 2013, 2019). FMRP has also been suggested to contribute to alternative splicing, RNA editing and regulating mRNA stability (Zalfa *et al.*, 2007; Filippini *et al.*, 2017; Zhou *et al.*, 2017; F. Zhang *et al.*, 2018).

In rare cases (<1% of FXS individuals), FXS can also be caused by rare point mutations, or deletions within the promoter or coding regions of the *FMR1* gene, giving rise to an altered or truncated protein or loss of FMRP expression (Hammond *et al.*, 1997; Coffee *et al.*, 2008; Handt *et al.*, 2014; Quartier *et al.*, 2017; D'Incal *et al.*, 2025). As FMRP may still be expressed – albeit at a reduced level – the degree of intellectual disability may be less severe in these cases, since *FMR1* mRNA expression correlates with IQ (Straub *et al.*, 2023; D'Incal *et al.*, 2025). While individuals with such mutations present with the typical FXS phenotype including seizures and intellectual disability, little is known about the consequences of these mutations on a cellular level. Animal models of missense mutations within the *Fmr1* mRNA-binding domains suggest that while some behavioural and cellular phenotypes (e.g. increased spine density) are replicated, the molecular mechanisms may not be shared with a complete loss of FMRP (Prieto *et al.*, 2021). Nevertheless, the loss of FMRP's RNA binding activity may be necessary and sufficient to cause FXS.

1.3 Models of Fragile X Syndrome

As FXS is a monogenic condition caused by the silencing of the *FMR1* gene, it has been modelled in the laboratory through *Fmr1* gene knockout, most commonly in mice (Kooy *et al.*, 1996; Kazdoba *et al.*, 2014). Whilst a full *Fmr1* knockout does not replicate the more complex molecular mechanisms underlying FXS in humans, it can be employed to elucidate the roles of FMRP in brain development and function. Many studies have used the *Fmr1*$^{-/y}$ mouse to investigate the behavioural, functional and structural changes in various brain regions including the primary somatosensory cortex (S1) and the hippocampus (reviewed in Dahlhaus, 2018). Other frequently used models are cell culture models, such as induced pluripotent stem cells (iPSCs), patient-derived or *FMR1*-KO (Bhattacharyya and Zhao, 2016; Giri *et al.*, 2019). Additionally, a drosophila model of FXS has been produced, where the drosophila homologue of the *FMR1* gene (*dFmr1*) was knocked out (Drozd, Bardoni and Capovilla, 2018). More recently, several rat models of FXS have been generated via *Fmr1* gene knock out, allowing for more complex behavioural testing, as well as a providing more genetically diverse, outbred background unlike inbred mice (Hamilton *et al.*, 2014; Till *et al.*, 2015).

1.3.1 *Fmr1*$^{-/y}$ mouse phenotypes

The *Fmr1*$^{-/y}$ mouse model has been extensively used for behavioural and physiological profiling, which has identified key phenotypes resulting from the loss of FMRP expression (Table 1.1). *Fmr1*$^{-/y}$ mice exhibit behavioural deficits, some of which bear likeness to the human condition, such as hyperactivity, anxiety, learning deficits and impaired social interactions (Spencer *et al.*, 2005; Mineur, Huynh and Crusio, 2006; Ding, Sethna and Wang, 2014). *Fmr1*$^{-/y}$ mice underperform in contextual fear conditioning, novel object recognition as well as visual and visuospatial discrimination tasks, which may be underlain by the reduced visually-evoked activity of parvalbumin (PV)-expressing interneurons in the primary visual cortex (V1; Krueger et al., 2011; Ding, Sethna and Wang, 2014; Goel et al., 2018). Excessive startle in response to air puff may be representative of hypersensitivity to innocuous somatosensory stimuli (Orefice *et al.*, 2016). Increased susceptibility to audiogenic

seizures has been reported in juvenile and adult *Fmr1*$^{-/y}$ mice (Chen and Toth, 2001; Ding, Sethna and Wang, 2014), which may be due to dysfunction of the auditory cortex (Goswami *et al.*, 2019). Like FXS individuals, adult *Fmr1*$^{-/y}$ mice show alterations in cortical oscillatory activity, including enhanced gamma power at rest and reduced phase-locking to auditory stimuli (Lovelace *et al.*, 2018; Jonak *et al.*, 2024). Similarly to the human condition, rearrangement of neocortical circuitry in *Fmr1*$^{-/y}$ mice leads to long-range hypoconnectivity and local hyperconnectivity, giving rise to functional decoupling of multiple cortical areas, including V1, S1, motor and auditory cortices (Haberl *et al.*, 2015). The S1 of adult *Fmr1*$^{-/y}$ mice shows interneuron subtype-specific changes in inhibitory cytoarchitecture (Kourdougli *et al.*, 2023). Loss of FMRP leads to increased ribogenesis and protein translation in *Fmr1*$^{-/y}$ mice, contributing to excessive metabotropic glutamate receptor (mGluR) dependent long-term depression (LTD) in the CA1 region (Huber *et al.*, 2002; Osterweil *et al.*, 2010; Seo *et al.*, 2022; Louros *et al.*, 2023). Depending on the brain area and cell type, *Fmr1*$^{-/y}$ mice show typical or increased dendritic spine density (Comery *et al.*, 1997; Hayashi *et al.*, 2007; Harlow *et al.*, 2010; Till *et al.*, 2012; Dolan *et al.*, 2013; Borreca *et al.*, 2023), similarly to FXS individuals (Irwin *et al.*, 2001; Hutsler and Zhang, 2010). However, increased dendritic spine density could be restricted to specific subcellular locations, as some studies have found a higher dendritic spine density on the apical, but not basal dendrites of *Fmr1*$^{-/y}$ mouse neurons in multiple cortical areas (Bland *et al.*, 2021). As such, *Fmr1*$^{-/y}$ mice exhibit a range of structural and functional deficits spanning multiple brain areas, which are established in development and underlie their behaviour.

Table 1.1. Behavioural, circuit and cellular phenotypes of *Fmr1*$^{-/y}$ mice. AC – auditory cortex, AG – amygdala, Ctx – cortex, DG – dentate gyrus, EC – entorhinal cortex, FC – frontal cortex, HC – hippocampus, lCC – lateral corpus callosum, mCC – medial corpus callosum, PFC – prefrontal cortex, S1 – primary somatosensory cortex, TC – temporal cortex, V1 – primary visual cortex.

Cat.	Area	Age	Phenotype	Reference
Behaviour	N/A	2-5 months	↑ hyperactivity	(Hayashi *et al.*, 2007; Dolan *et al.*, 2013; Kramvis *et al.*, 2013; Ding, Sethna and Wang, 2014)
		2-4 months	= activity	(Eadie *et al.*, 2009; Baker *et al.*, 2010)
		3-5 months	= sustained attention	(Kramvis *et al.*, 2013)
		3-5 months	= impulsive behaviour	(Kramvis *et al.*, 2013)
		3-5 months	↑ repetitive behaviour	(Kramvis *et al.*, 2013)
		3-4 months	↑ anxiety	(Spencer *et al.*, 2005)
		2-4 months	↓ anxiety	(Hayashi *et al.*, 2007; Eadie *et al.*, 2009; Baker *et al.*, 2010)
		3-4 months	↓ social dominance	(Spencer *et al.*, 2005)
		1-2 months	↓ novel object recognition	(Orefice *et al.*, 2016; Borreca *et al.*, 2023)
		2-4 months	↓ visual & visuospatial discrimination	(Krueger *et al.*, 2011; Goel *et al.*, 2018)
		3-4 months	↓ spatial memory	(D'Hooge *et al.*, 1997; Baker *et al.*, 2010)
		2-4 months	= spatial memory	(Eadie *et al.*, 2009)
		3-4 months	↓ social interaction	(Spencer *et al.*, 2005; Mineur, Huynh and Crusio, 2006)

		2-3 months	↑ social interaction	(Baker *et al.*, 2010)
		3-4 months	= social recognition	(Spencer *et al.*, 2005)
		2-3 months	↓ contextual fear memory	(Hayashi *et al.*, 2007; Ding, Sethna and Wang, 2014)
		2-3 months	↓ passive avoidance memory	(Ding, Sethna and Wang, 2014)
		1.5-3 months	= acoustic startle	(Ding, Sethna and Wang, 2014; Orefice *et al.*, 2016)
		2-4 months	↓ acoustic startle	(Chen and Toth, 2001; Baker *et al.*, 2010)
		1.5-4 months	↑ prepulse inhibition	(Chen and Toth, 2001; Baker *et al.*, 2010; Ding, Sethna and Wang, 2014; Orefice *et al.*, 2016)
		1.5-2 months	↑ air puff startle	(Orefice *et al.*, 2016)
		18-24 days, 2.5-8 months	↑ audiogenic seizures	(Chen and Toth, 2001; Osterweil *et al.*, 2010; Dolan *et al.*, 2013; Ding, Sethna and Wang, 2014)
		3-4 months	= chemically induced seizures	(Chen and Toth, 2001)
Circuit	Brain-wide	2-3 months	↑ local connectivity	(Haberl *et al.*, 2015)
	Brain-wide	2-3 months	↓ long-range connectivity	(Haberl *et al.*, 2015)
	AC, FC	19-23 days, 1-3 months	↑ gamma power	(Lovelace *et al.*, 2018; Goswami *et al.*, 2019; Wen *et al.*, 2019; Jonak *et al.*, 2024)

	AC	21 days	= gamma power	(Wen *et al.*, 2019)
	AC	1.5-3 months	↓ synchronization to stimuli	(Lovelace *et al.*, 2018)
	CA1	21-30 days, 1-2 months	↑ mGluR-LTD	(Huber *et al.*, 2002; Zhang *et al.*, 2009; Osterweil *et al.*, 2010; Seo *et al.*, 2022)
	CA1	21-30 days	= NMDAR-LTD	(Huber *et al.*, 2002)
	TC	2-3 months	↓ LTP	(Hayashi *et al.*, 2007)
	CA1	4-6 months	= LTP	(Zhang *et al.*, 2009)
	AG	20-30 days	↓ inhibitory transmission	(Olmos-Serrano *et al.*, 2010)
Anatomy	S1	2 months, 9-10 months	↓ PV IN density	(Lee *et al.*, 2019; Kourdougli *et al.*, 2023)
	S1	4-5 months	↑ Sst IN density	(Kourdougli *et al.*, 2023)
	M1, S1	2 months	= neuron density	(Lee *et al.*, 2019)
	Ctx	2 months	↑ oligodendrocyte density	(Lee *et al.*, 2019)
	mCC	2 months	↑ myelination	(Lee *et al.*, 2019)
	lCC	2 months	= myelination	(Lee *et al.*, 2019)
	Ctx	2 months	↑ microglia density	(Lee *et al.*, 2019)
	Ctx	2 months	↑ reactive astrocyte density	(Lee *et al.*, 2019)
Cellular	CA1, DG, EC	2-3 months	↑ dendritic spines (apical & basal)	(Borreca *et al.*, 2023)

	AC, S1, TC, V1	2-4 months	↑ apical dendritic spines	(Comery *et al.*, 1997; Hayashi *et al.*, 2007; Dolan *et al.*, 2013; Bland *et al.*, 2021)
	S1	>4 months	↑ dendritic spine turnover	(Pan *et al.*, 2010)
	AG	20-30 days	↓ inhibitory synapses	(Olmos-Serrano *et al.*, 2010)
	AG	20-30 days	↓ excitatory synapses	(Olmos-Serrano *et al.*, 2010)
	AG, EC, CA1, CA3	20-35 days	↑ intrinsic excitability	(Olmos-Serrano *et al.*, 2010; Deng and Klyachko, 2016; Deng *et al.*, 2019; Booker *et al.*, 2020)
	HC	25-32 days	↑ ribogenesis	(Seo *et al.*, 2022)
	CA1	25-32 days	↑ protein translation	(Osterweil *et al.*, 2010; Seo *et al.*, 2022)
	HC	25-32 days	↑ protein degradation	(Louros *et al.*, 2023)

1.3.2 Rat model of FXS

The rat model of FXS replicates some, but not all phenotypes present in the *Fmr1*$^{-/y}$ mice (Table 1.2), allowing the identification of common phenotypes likely arising due to conserved functions of FMRP. Adult *Fmr1*$^{-/y}$ rats show hyperactivity in novel environments and deficits in novel object recognition, social recognition, associative and spatial memory tasks (Tian *et al.*, 2017; Asiminas *et al.*, 2019; Kozono *et al.*, 2020; Ntoulas *et al.*, 2024), however this could be dependent on the task used (Till *et al.*, 2015). Contrary to mice, *Fmr1*$^{-/y}$ rats do not show increased anxiety (Tian *et al.*, 2017). Stereotyped and repetitive behaviours are expressed through an increase in wood chewing in *Fmr1*$^{-/y}$ rats (Hamilton *et al.*, 2014; Wong *et al.*, 2020). Additionally, *Fmr1*$^{-/y}$ rats show deficits in complex behaviours which are not studied in mice, such as social play (Hamilton *et al.*, 2014). In electroencephalography (EEG) recordings, *Fmr1*$^{-/y}$ rats have increased power in the gamma range, consistent with mouse and human findings (Kozono *et al.*, 2020; Wong *et al.*, 2020). Interestingly, in

early postnatal development gamma power is reduced in the V1 alongside an increase in visually-evoked responses at 3 weeks of age, indicating a shift in the developmental trajectory of the V1 (Berzhanskaya *et al.*, 2016). In agreement with mouse findings, alterations in synaptic plasticity have been found, with reduced LTP and exaggerated low-frequency stimulation-induced (LFS) LTD, as well as mGluR-LTD, in line with elevated protein synthesis in the CA1 region (Till *et al.*, 2015; Tian *et al.*, 2017). Similarly to mice, CA1 pyramidal cells of *Fmr1*$^{-/y}$ rats have an increased density of apical, but not basal dendritic spines (Till *et al.*, 2015). Additionally, *Fmr1*$^{-/y}$ rats show brain area-specific changes in the subunit composition of NMDA and AMPA receptors, as well as glutamatergic and GABAergic neurotransmission, alongside increased neuronal excitability in the hippocampus (Leontiadis *et al.*, 2023; Ntoulas *et al.*, 2024).

Table 1.2. Behavioural, circuit and cellular phenotypes of *Fmr1*$^{-/y}$ rats. AC – auditory cortex, dHC – dorsal hippocampus, HC – hippocampus, PFC – prefrontal cortex, V1 – primary visual cortex, vHC – ventral hippocampus.

Cat.	Area	Age	Phenotype	Reference
Behaviour	N/A	2 months	↑ hyperactivity	(Kozono *et al.*, 2020; Ntoulas *et al.*, 2024)
		2-3 months	= activity	(Tian *et al.*, 2017)
		2-3 months	= anxiety	(Tian *et al.*, 2017)
		3-6 months	↓ novel object recognition	(Till *et al.*, 2015; Ntoulas *et al.*, 2024)
		2-3 months	↓ spatial memory	(Tian *et al.*, 2017; Ntoulas *et al.*, 2024)
		3-6 months	= spatial memory	(Till *et al.*, 2015)
		2-3 months	↓ social recognition	(Tian *et al.*, 2017)
		25-40 days	↓ social play	(Hamilton *et al.*, 2014)
		1-6 months	↓ associative memory	(Till *et al.*, 2015; Asiminas *et al.*, 2019)
		1-3 months	↑ wood chewing	(Hamilton *et al.*, 2014; Wong *et al.*, 2020)
		36-90 days	↓ social dominance	(Wong *et al.*, 2020)
Circuit	Brain-wide	1-2 months	↑ EEG gamma power	(Kozono *et al.*, 2020; Wong *et al.*, 2020)
	V1	10 days	↓ EEG gamma power	(Berzhanskaya *et al.*, 2016)
	V1	10 days	↑ visually-evoked responses	(Berzhanskaya *et al.*, 2016)
	AC	Not reported	↓ auditory-evoked responses	(Engineer *et al.*, 2014)

	CA1	2-3 months	↓ LTP	(Tian *et al.*, 2017)
	CA1	21-32 days, 1-3 months	↑ mGluR-LTD & LFS-LTD	(Till *et al.*, 2015; Tian *et al.*, 2017; Asiminas *et al.*, 2019)
	CA1	2-3 months	= paired-pulse facilitation	(Tian *et al.*, 2017)
	dHC	3-4 months	↑ excitatory synaptic transmission	(Leontiadis *et al.*, 2023)
	CA1	2-3 months	↓ excitatory synaptic transmission	(Tian *et al.*, 2017)
	vHC	3-4 months	↑ phasic inhibition	(Leontiadis *et al.*, 2023)
Cellular	CA1	27-32 days	↑ apical dendritic spines	(Till *et al.*, 2015)
	CA1	2-3 months	= dendritic spines	(Asiminas *et al.*, 2022)
	HC	1 month	↑ protein synthesis	(Till *et al.*, 2015; Asiminas *et al.*, 2019)
	PFC, HC	2 months	↑ GluN2A/GluN2b ratio	(Ntoulas *et al.*, 2024)
	PFC	2 months	↓ glutamate levels	(Ntoulas *et al.*, 2024)
	HC	2 months	↑ glutamate & GABA levels	(Ntoulas *et al.*, 2024)
	HC, CA1	2-3 months	↑ intrinsic excitability	(Asiminas *et al.*, 2022; Ntoulas *et al.*, 2024)
	CA1	2-3 months	= AIS length	(Asiminas *et al.*, 2022)
	CA1	2-3 months	= dendritic complexity	(Asiminas *et al.*, 2022)

1.4 Proposed mechanisms

Due to the great diversity of FMRP's targets it is difficult to pinpoint a singular molecular mechanism underlying the widespread dysfunction in the FXS brain. Huber *et al.* found that mGluR-mediated signalling is disrupted in FXS, leading to increased protein synthesis and directly underlying exaggerated mGluR-dependent, but not NMDAR-dependent LTD, a key synaptic plasticity phenotype present in *Fmr1*$^{-/y}$ mice and rats (Huber *et al.*, 2002; Osterweil *et al.*, 2010; Till *et al.*, 2015). mGluR-dependent LTD occurs following the stimulation of mGluRs, leading to the internalization of synaptic AMPARs in a *de novo* translation-dependent manner (reviewed in Bear, Huber and Warren, 2004). Excitatory glutamatergic neurotransmission activates mGluRs (Figure 1.2; reviewed in Wang and Zhuo, 2012), such as Group I mGluR1 and mGluR5, which are G-protein coupled receptors (GPCRs) coupled to phospholipase C (PLC), increasing the production of the second messengers inositol-1,4,5-trisphosphate (IP3) and diacylglycerol (DAG). Additionally, mGluR1/5 activation facilitates Ca^{2+} influx via L-type voltage-gated calcium channels, while IP3 triggers the release of Ca^{2+} from intracellular stores. Ca^{2+} acts on calmodulin (CaM) to activate adenylate cyclase 1 (AC1) and upregulate cyclic adenosine monophosphate (cAMP) synthesis. DAG acts via protein kinase C (PKC) to stimulate the phosphoinositide 3-kinase (PI3K) and mitogen activated protein kinase/extracellular signal regulated kinase (MAPK/ERK) signalling pathways. Consequently, the downstream effectors of mGluR signalling affect gene expression by activating several transcription factors, including CREB, Elk-1 and AP-1. Typically, FMRP is synthesized and trafficked to dendrites in an activity-dependent manner following the stimulation of mGluR-mediated signalling (Todd, Malter and Mack, 2003; Antar *et al.*, 2004; Hou *et al.*, 2006). This allows FMRP to inhibit protein translation locally by interfering with the translation complex (Darnell *et al.*, 2011). In the absence of FMRP, mGluR signalling gives rise to excessive protein synthesis, and consequently – altered synaptic plasticity phenotypes (Huber *et al.*, 2002; Osterweil *et al.*, 2010). Thus, in the 'mGluR theory of FXS', elevated mGluR signalling has been proposed to underlie key phenotypes in FXS (Bear, Huber and Warren, 2004).

Beyond elevated mGluR1/5 signalling, a reduction in cAMP levels is a phenotype prevalent in FXS individuals, as well as multiple models of FXS (Berry-Kravis, Hicar and Ciurlionis, 1995; Kelley *et al.*, 2007, 2008). Likely arising due to increased cAMP degradation via phosphodiesterases (PDEs), which are direct targets of FMRP (Darnell *et al.*, 2011). Intrinsic cAMP signalling can affect gene transcription by activating protein kinase (PKA), which then phosphorylates the transcription factors CREB, CREM and ATF1 (Sassone-Corsi, 2012). Dysregulated cAMP signalling has also been shown to directly underlie intrinsic hyperexcitability of L4 and L5 neurons in the S1 of *Fmr1*$^{-/y}$ mice due to a cAMP-dependent reduction in I_h current (Zhang *et al.*, 2014; Booker *et al.*, 2019). Thus, dysregulation of cAMP-mediated intracellular signalling may have widespread effects on neuronal function in FXS (Bardoni, Gwizdek and Maurin, 2025).

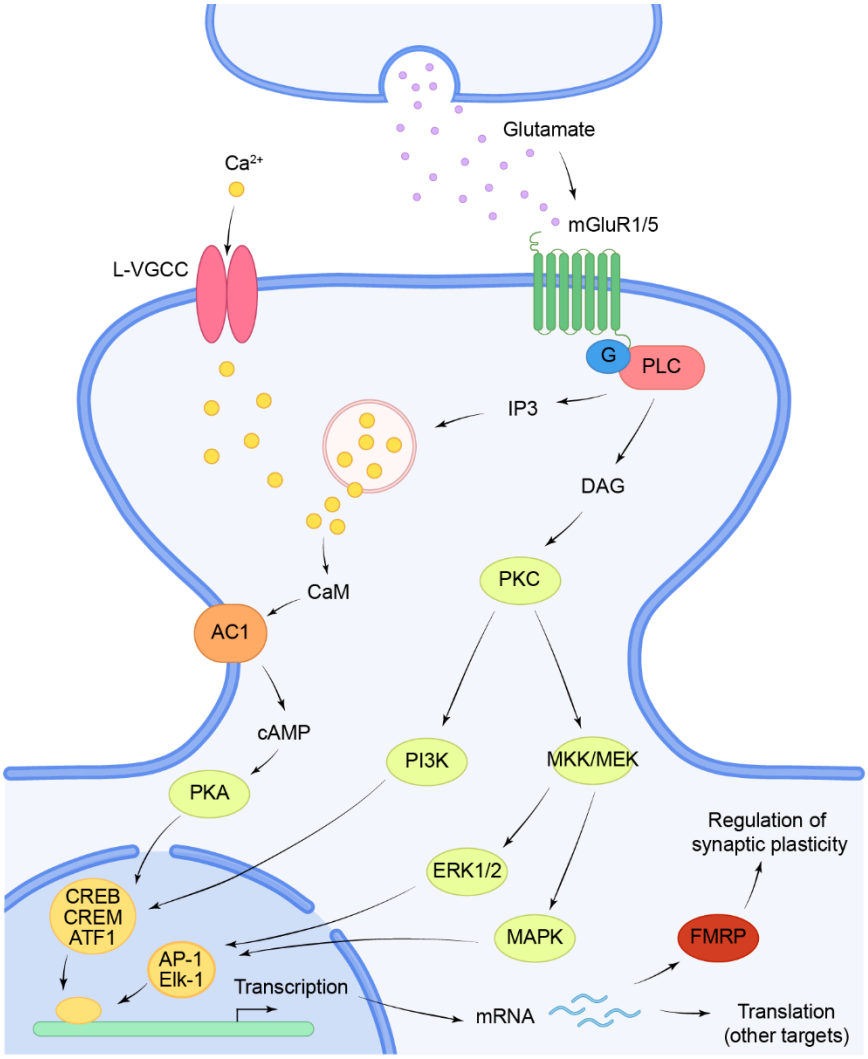

Figure 1.2. Simplified diagram of mGluR and cAMP signalling pathways. Presynaptic glutamate release stimulated mGluR1/5, which facilitates Ca^{2+} entry via L-type voltage-gated calcium channels (L-VGCC). G protein (G) coupled to mGluR1/5 activates phospholipase (PLC), stimulating the production of the second messengers IP3 and DAG. IP3 triggers the release of Ca^{2+} from intracellular stores, stimulating the production of cAMP by adenylate cyclase 1 (AC1) via calmodulin (CaM). cAMP activates PKA. DAG activates PI3K and MKK/MEK via protein kinase C (PKC). MKK/MEK activates the ERK1/2 and MAPK signalling pathways. PKA, PI3K, ERK1/2 and MAPK regulate gene expression via multiple transcription factors, including CREB, CREM, ATF1, AP-1, Elk-1, leading to the expression of FMRP, which regulates synaptic plasticity, as well as other targets.

1.4.1 Therapeutic interventions in FXS

Currently there are no FDA-approved targeted treatments for FXS. Individuals with FXS typically receive medication aimed at relieving their individual symptoms, such as antiepileptic, anxiolytic, antidepressant and antipsychotic drugs (Lee *et al.*, 2018; Berry-Kravis, 2022). As such, there is an unmet need which sparks great interest in identifying viable therapeutic interventions that target the underlying mechanisms in FXS.

In line with the mGluR theory of FXS, targeting signalling via mGluR5 has been proposed as a potential treatment. Acute treatment with mGluR5 negative allosteric modulators such as MPEP and CTEP prevents audiogenic seizures in *Fmr1*$^{-/y}$ mice by rescuing the elevated protein synthesis (Yan *et al.*, 2005; Michalon *et al.*, 2012). However, these effects dissipate with chronic treatment in as few as 3 doses due to treatment resistance (Stoppel *et al.*, 2021). Drugs targeting mGluR signalling such as fenobam, mavoglurant and basimglurant showed little to no improvement in clinical trials (Berry-Kravis, 2022). Downstream of mGluRs, the ERK1/2 signalling pathway inhibitor lovastatin has been shown to prevent audiogenic seizures in *Fmr1*$^{-/y}$ mice (Muscas, Louros and Osterweil, 2019), and reverse associative memory deficits, excessive protein synthesis and LTP deficits in *Fmr1*$^{-/y}$ rats, with persistent effects even 3 months after the end of the treatment (Asiminas *et al.*, 2019). Subsequently, lovastatin has initially met the primary outcome measures, e.g. verbal and social impairment, in a double-blind placebo controlled clinical trial (Thurman *et al.*, 2020), but failed to produce significant improvement in EEG and behavioural measures in a further phase 2 clinical trial in FXS individuals (McKinney *et al.*, 2025).

PDE inhibition could address the reduction in cAMP levels seen in FXS individuals and animal models, thus targeting the proposed mechanism underlying cortical hyperexcitability (Choi *et al.*, 2015). Several drugs targeting the reduction in cAMP levels (lithium, LY341495, rolipram) have been shown to rescue the long term memory deficits and intracellular signalling in the drosophila model of FXS (Choi *et al.*, 2015, 2016). Clinically, lithium showed significant improvements on behaviour, however its toxicity precludes long-term use (Berry-Kravis, 2022). Inhibiting PDE2A activity with BAY607550 rescues the exaggerated mGluR-LTD (Maurin *et al.*, 2019),

while the PDE10A inhibitor TAK-063 has been shown to reverse EEG deficits in *Fmr1*$^{-/y}$ mice (Jonak *et al.*, 2021). Finally, the PDE4D negative allosteric modulator BPN14770 was able to rescue a wide range of behavioural deficits and protein synthesis rates in *Fmr1*$^{-/y}$ mice, with long-term effects lasting beyond the original treatment window (Gurney *et al.*, 2017; Rosenheck *et al.*, 2021). BPN14770 has been successful in a phase 2 clinical trial in FXS individuals, showing improvement in cognitive and language performance, daily functioning, as well as EEG results, which were still detectable 12 weeks after cessation of treatment (Berry-Kravis, Harnett, *et al.*, 2021; Norris *et al.*, 2024). Several drugs targeting the same or alternative pathways (e.g. GABA signalling) have been tested in clinical trials for FXS to show no or mixed results, highlighting the discrepancy between animal studies and the real condition of FXS (Berry-Kravis, 2022).

1.5 Barrel cortex as a model for sensory development

1.5.1 Structure of the barrel cortex

Considering that tactile hypersensitivity is a common and disruptive symptom in FXS individuals, understanding the mechanisms through which it arises is an important question that can inform future therapeutic approaches. In rodents, the myofascial vibrissae, or whiskers provide a key tactile sensory modality through which they explore the external environment even in the absence of light, a crucial adaptation for their nocturnal lifestyle. The whisker system is highly sensitive and specialized, allowing the animals to locate objects, discriminate textures, and develop spatial representations of their surroundings. As such, the whisker system is a relevant model for studying somatosensation in rodents, with a well-characterized structure and function (Petersen, 2007; Feldmeyer, 2012).

Barrel cortex, forming a major part of the rodent S1, is responsible for processing somatosensory inputs from the whiskers. Neurons within L4 of the S1 form distinct structures known as barrels. The barrel organization of the S1 provides a somatotopic map of the whisker pad, whereby each barrel receives direct input from a single whisker. While the barrel layout within S1 is the same in mice and rats, some species differences exist in their structure and cytoarchitecture (reviewed in Petersen, 2007). In mouse barrel cortex L4 stellate cells (SCs), are positioned around the barrel edges, with asymmetrical dendritic arbours which project into the barrel hollows, while in rat S1 L4 SCs are present throughout the barrel (Welker and Woolsey, 1974; Staiger, 2004). Rat barrel cortex also contains functionally and structurally distinct inter-barrel regions known as septa, as well as barrel subdivisions, neither of which are present in the mouse (Kim and Ebner, 1999; Pierret, Lavallée and Deschênes, 2000; Land and Erickson, 2005). Excitatory circuitry in the barrel cortex exhibits canonical cortical column organization, with barrels forming the basis of each column (Figure 1.3; reviewed in Feldmeyer, 2012). Sensory information from the whiskers is relayed via the infraorbital branch of the trigeminal nerve to the ventroposterior medial nucleus of the thalamus, from where it projects directly into

L4, with a portion of the same afferents also innervating L6. SCs, the primary excitatory cell type within L4, are thus responsible for the initial integration and processing of sensory information. L4 SCs show a high degree of interconnectivity within the barrel, allowing them to efficiently integrate thalamocortical inputs before projecting onto L2/3, L5 and L6. Pyramidal neurons in L2/3 innervate L5, which is the main output layer of the cortex, relaying the processed information to other cortical areas such as the secondary somatosensory cortex, contralateral S1 and primary motor cortex.

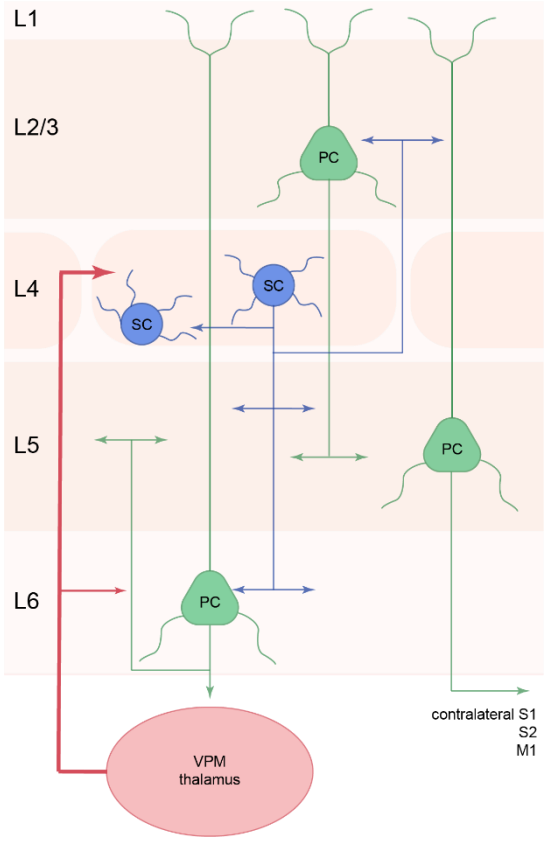

Figure 1.3. Excitatory circuitry within the rodent barrel cortex. Thalamocortical inputs from the ventroposterior medial nucleus of the thalamus (VPM) directly innervate L4 and L6. Stellate cells (SC) residing within barrels in L4 send projections to L2/3, L5 and L6, in addition to reciprocal connections with other SCs. Pyramidal cells (PC) in L2/3 project onto L5, while L6 PCs project to L5 and thalamus. L5 provides the output of the barrel cortex, sending projections into other cortical areas such as the contralateral primary somatosensory cortex (S1) via the corpus callosum, secondary somatosensory cortex (S2) and primary motor cortex (M1).

In addition to the excitatory circuitry, inhibitory interneurons provide targeted negative control of cortical activity, comprising up to 20-30% of all cortical neurons (Hendry *et al.*, 1987; Tamamaki *et al.*, 2003). Cortical interneurons are highly varied in their function, typically characterized based on a combination of their action

potential firing pattern, gene marker expression and morphology (Rudy *et al.*, 2011). Fast-spiking, PV-expressing interneurons such as basket cells and chandelier cells comprise nearly half of all interneurons and function to provide rapid and strong feed-forward inhibition (FFI) targeted to the soma and axon initial segments of excitatory neurons. In the barrel cortex, PV interneurons in L4-6 receive direct thalamocortical inputs, and form reciprocal connections with L4 SCs and Sst-expressing interneurons (Yu *et al.*, 2019). Sst interneurons, such as Martinotti cells, target the dendrites of pyramidal neurons, thus influencing dendritic integration (Yu *et al.*, 2019). Some Sst interneurons, especially in L4, synapse onto other (typically PV) interneurons, in feedback inhibitory manner (Xu *et al.*, 2013). Vasoactive intestinal peptide (VIP) interneurons are prominent in L2/3 of the S1, where they form a disinhibitory circuit with Sst interneurons (Feldmeyer *et al.*, 2018). Neurogliaform cells are small interneurons expressing reelin which provide slow inhibition onto the dendrites of pyramidal neurons while electrically coupling to other interneurons (Simon *et al.*, 2005; Rudy *et al.*, 2011; Pohlkamp *et al.*, 2014). Inhibitory interneuron subtypes and their varied functions are discussed further in Chapter 4.

1.5.2 Postnatal development of the barrel cortex

While the early patterning of the S1 is primarily driven by genetically-encoded programming, the postnatal development of the barrel cortex involves the activity-dependent refinement of circuits (Van der Loos and Woolsey, 1973; Killackey and Belford, 1979; Feldman *et al.*, 1998; Fukuchi-Shimogori and Grove, 2001; O'Leary and Sahara, 2008). Critical periods define the points in development at which factors such as experience and activity levels can permanently and irreversibly change the development of cortical circuitry (Crair and Malenka, 1995). Critical periods were originally discovered in the visual system, where monocular deprivation in early life leads to a permanent shift of neuronal responses in the visual cortex in favour of the non-deprived eye (Hubel and Wiesel, 1963, 1970). Likewise, lesioning of the whiskers during the first four postnatal days leads to an anatomical reorganization of the whisker map, preventing the formation of the corresponding barrels (Van der Loos

and Woolsey, 1973; Killackey and Belford, 1979). At this age, the barrel segregation becomes apparent (Rice, 1985). Excitatory synaptic transmission plays a critical role in the developing rodent barrel cortex, as blocking glutamate signalling disrupts critical period plasticity (Schlaggar, Fox and O'Leary, 1993). Experience-dependent plasticity allows for the selective strengthening and weakening of thalamocortical inputs based on their activity during the first postnatal week, until the onset of active whisking in the second postnatal week (Crair and Malenka, 1995; Feldman *et al.*, 1998). As such, altered activity states during early development can permanently impair cortical function in later life.

1.5.3 S1 development in rodent models of FXS

The development of the rodent barrel cortex is disrupted in the absence of FMRP expression. Juvenile *Fmr1*$^{-/y}$ mice show exaggerated behavioural responses to whisker stimulation indicative of tactile defensiveness, and reduced network adaptation of whisker-evoked activity (He *et al.*, 2017). L2/3 of the S1 exhibits network hypersynchrony, with a higher proportion of recruited neurons and a developmental delay in desynchronization of neuronal ensemble activity in *Fmr1*$^{-/y}$ mice (Gonçalves *et al.*, 2013). An increase in the duration of UP states is an expression of network hyperexcitability in the developing S1 (Gibson *et al.*, 2008). Loss of FMRP does not impair the broad organization of the S1, but gives rise to a delay in developmental barrel segregation (Till *et al.*, 2012). Furthermore, Harlow *et al.* (2010) found a shift in the timing of the critical period for thalamocortical synapse plasticity, but not map plasticity in the S1 of *Fmr1*$^{-/y}$ mice. Such a delay could contribute to changes in connectivity within S1, with *Fmr1*$^{-/y}$ mice showing a delay in the development of L4 to L2/3 connectivity (Bureau, Shepherd and Svoboda, 2008).

Early postnatal development of the S1 is also altered on a cellular level in the absence of FMRP. During S1 development, L4 neurons in *Fmr1*$^{-/y}$ mice show normal dendritic complexity, but a reduction in dendritic asymmetry and more spatially diffuse axons (Bureau, Shepherd and Svoboda, 2008; Till *et al.*, 2012). Reduced I_h current contributes to intrinsic hyperexcitability of L4 and L5 neurons in *Fmr1*$^{-/y}$ mice at 2 and 4-6 weeks of age (Zhang *et al.*, 2014; Booker *et al.*, 2019). The same neurons

also show excessive dendritic summation, and an increase in silent and multi-innervated synapses (Harlow *et al.*, 2010; Booker *et al.*, 2019). Dendritic spine turnover is increased in L5 neurons, indicating instability (Pan *et al.*, 2010). In line with the altered E/I balance (Gibson *et al.*, 2008), inhibitory function is significantly impaired in the developing S1 of *Fmr1*$^{-/y}$ mice. Changes in inhibitory cytoarchitecture in the developing S1 involve specific interneuron subtypes, such as PV and Sst-expressing interneurons, which persists into adulthood (Kourdougli *et al.*, 2023). Furthermore, PV interneurons are functionally impaired, providing ineffective and mistimed FFI to L4 in *Fmr1*$^{-/y}$ mice (Domanski *et al.*, 2019), as well as homeostatic dysregulation of activity into later life (Antoine *et al.*, 2019).

Table 1.3. Developmental phenotypes in S1 of *Fmr1*$^{-/y}$ mice (<2 months of age).

Cat.	Layer	Age	Phenotype	Reference
Behaviour	N/A	14-16 days	↑ tactile defensiveness	(He *et al.*, 2017)
Circuit	L2/3	14-16 days	↓ whisker-evoked network adaptation	(He *et al.*, 2017)
	L2/3	9-40 days	↑ network synchronization	(Gonçalves *et al.*, 2013)
	L4	2-4 weeks	↑ UP states	(Gibson *et al.*, 2008)
	S1	4-6 weeks	↑ evoked activity spread	(Zhang *et al.*, 2014)
	L2/3, L4	2 weeks	↓ L4 to L2/3 connectivity	(Bureau, Shepherd and Svoboda, 2008)
	L4	10-11 days	↓ FFI	(Domanski *et al.*, 2019)
Anatomy	L4	7-14 days	↓ barrel segregation	(Till *et al.*, 2012)
	L1-L6	15 days	↓ PV IN density	(Kourdougli *et al.*, 2023)
	L1-L6	15 days	↑ Sst IN density	(Kourdougli *et al.*, 2023)
Cellular	L4	14 days	↓ dendritic asymmetry	(Till *et al.*, 2012)
	L4	7-60 days	= dendritic spine density	(Harlow *et al.*, 2010; Till *et al.*, 2012)
	L5	20-30 days	↑ dendritic spine turnover	(Pan *et al.*, 2010)
	L4	7 days	↑ silent synapses	(Harlow *et al.*, 2010)

	L4	10-15 days	↑ multi-innervated synapses	(Booker *et al.*, 2019)
	L4, L5	10-15 days, 4-6 weeks	↑ intrinsic excitability	(Gibson *et al.*, 2008; Zhang *et al.*, 2014; Booker *et al.*, 2019; Domanski *et al.*, 2019)
	L5	10-18 days	= intrinsic excitability	(Desai *et al.*, 2006)
	L5	10-18 days	= intrinsic excitability LTP	(Desai *et al.*, 2006)
	L4, L5	10-15 days, 4-6 weeks	↑ dendritic summation	(Zhang *et al.*, 2014; Booker *et al.*, 2019)
	L4, L5	10-15 days, 4-6 weeks	↓ I_h	(Zhang *et al.*, 2014; Booker *et al.*, 2019)
	L4	10-15 days	↑ NMDA/AMPA ratio	(Booker *et al.*, 2019)
	L5	10-18 days	= NMDA/AMPA ratio	(Desai *et al.*, 2006)

1.6 Aims of this thesis

Many studies have provided a snapshot view into the differences caused by the loss of FMRP at various developmental timepoints and most often – adulthood. However, little is known about the dynamics of how and when these changes arise, and how long they persist immediately following the S1 critical period. Additionally, while the *Fmr1*$^{-/y}$ rat model reveals some species-specific differences in behaviour and function in the absence of FMRP, its early development is largely uncharacterized, as previous work primarily focused on hippocampal function in adult and adolescent rats, starting from the third postnatal week. To the best of my knowledge, no currently published studies examine the S1 in the rat model of FXS at any age, including during development. ***I hypothesize that the loss of FMRP gives rise to an alternative developmental trajectory in the S1 of Fmr1*$^{-/y}$ *rats, and that such altered trajectory may be corrected by targeted therapy during early life.*** As such, in this thesis I set out to provide a detailed electrophysiological, anatomical and transcriptomic characterization of the early life development in the primary somatosensory cortex of the *Fmr1*$^{-/y}$ rat. Additionally, I tested whether a brief pharmacological intervention using the PDE4D inhibitor BPN14770 during the S1 critical period could restore the developmental trajectory of the S1 with long-lasting effects.

Chapter 3: In this chapter I demonstrate that S1 L4 SCs of *Fmr1*$^{-/y}$ rats show dynamic alterations in their developmental trajectory, giving rise to multiple periods of intrinsic hyperexcitability separated by a period of typical excitability. These changes are directly underlain by differences in the passive and active properties of L4 SCs, with no alterations in their excitatory synaptic function.

Chapter 4: In this chapter I identify a developmental delay in the dendritic complexity of S1 L4 SCs in *Fmr1*$^{-/y}$ rats, which could directly underlie their hyperexcitability in early development. I find no differences in the dendritic spine density during development. Finally I show that the inhibitory cytoarchitecture is altered during S1 development in *Fmr1*$^{-/y}$ rats, with a subtype-specific increase in interneuron density.

Chapter 5: In this chapter I examine the potential for morphological and physiological rescue of *Fmr1*$^{-/y}$ L4 SC development by a brief treatment with BNP14770 during the critical period for plasticity in S1. However, I find no long-term benefit on intrinsic hyperexcitability in L4 SCs.

Chapter 6: Here, I identify the cell-type-specific differences in gene expression which contribute to the altered developmental trajectory of *Fmr1*$^{-/y}$ rat S1. I find that upper cortical layer excitatory neurons show similar dysregulation of genes involved in mitochondrial and ribosomal function as well as morphological development.

Chapter 7: In this chapter I discuss the technical considerations for implementing a Patch-seq protocol for combined electrophysiological and transcriptomic analysis in L4 SCs to directly identify transcriptomic correlates of neuronal function in *Fmr1*$^{-/y}$ rats, as well as the limitations of such an approach.

Chapter 2

Materials & Methods

2.1 Animals

All experiments were performed using an outbred strain of Long Evans Hooded rats at ages P6-38. Due to the X-linked nature of the model, only male *Fmr1*$^{+/y}$ and *Fmr1*$^{-/y}$ littermates were used for experiments. For cell count and identification purposes, the line used also expresses yellow fluorescent protein (YFP) under the vesicular GABA transporter (VGAT) promoter, rendering GABAergic cells fluorescent in approximately 75% of the offspring. Compound *Fmr1* & *Vgat-Venus1* heterozygote females were generated by crossing *Fmr1*$^{-/+}$ females (Asiminas *et al.*, 2022) with *Vgat-Venus1*$^{+/+}$ males (Uematsu *et al.*, 2008). *Fmr1*$^{-/+}$; *Vgat-Venus1*$^{-/+}$ females were crossed with *Fmr1*$^{+/y}$; *Vgat-Venus1*$^{+/+}$ males to produce offspring with wild-type (WT) or *Fmr1*$^{-/y}$ genotypes in a 1:1 Mendelian ratio in males. Animals were housed on a 12h light/dark cycle with *ad libitum* access to food and water. Pups were housed with their parents until weaning at P21. All experiments were performed blind to genotype. Post-hoc genotyping was performed on tail biopsy samples by Transnetyx (US), through real-time polymerase chain reaction (RT-PCR) for *Fmr1* (forward primer: CTCCCGGCGCGAGGAA; reverse primer: CCATTGGAGCCCCGCAC) and *Venus1* genes (forward primer: GCTGGACGGCGACGTAA; reverse primer: CCCTCGCCGGACACG). All procedures were performed in line with the Animals (Scientific Procedures) Act 1986 under project license PP2262369 and personal license I52730868.

2.2 Electrophysiology

2.2.1 Acute cortical slice preparation

Animals were briefly anaesthetized with isoflurane until paw-pinch reflex was no longer present, then decapitated and their brains placed in ice-cold cutting artificial cerebrospinal fluid (cACSF; Table 2.1) that was saturated with carbogen (95% O_2 / 5% CO_2). 400 µm thick coronal slices containing the barrel cortex were cut using a Leica VT1200 vibratome at a speed of 0.1 mm/s. Immediately following slicing, the slices were incubated at 35°C for 30 mins then stored at room temperature until use.

Table 2.1. Composition of cutting and recording ACSF solutions used for electrophysiology recordings.

	Cutting ACSF	**Recording ACSF**
	Concentration (mM)	
NaCl	87.0	125.0
KCl	2.5	2.5
$NaHCO_3$	25.0	25.0
NaH_2PO_4	1.25	1.25
Glucose	25.0	25.0
Sucrose	75.0	-
$CaCl_2$	0.5	2
$MgCl_2$	7	1

2.2.2 Whole-cell patch clamp recordings

Whole-cell patch clamp recordings were performed with the slices placed in a submerged recording chamber and held down with a slice weight. Carbogenated rACSF was heated to 30°C with an inline heater (LinLab, Scientifica) and perfused through the chamber at a rate of 8 ml/min. The slices were visualized through IR-DIC. S1 L4 barrels were identified using x4 objective, before switching to a x40 immersion objective. L4 SCs were identified based on their position inside a barrel, small and round somata, and lack of fluorescence where possible (as opposed to GABAergic

neurons). Recording pipettes of 3-6 MΩ resistance were made using borosilicate glass capillaries (30-0060, Harvard Apparatus), pulled with a horizontal electrode puller (P-1000, Sutter Instruments) and filled with 8 mM Cl^- potassium gluconate internal solution (Table 2.2). Recordings were obtained using a MultiClamp 700B amplifier and digitized at 20 kHz with an Axon Digidata 1550 digitizer (Molecular Devices). A Bessel filter was applied at 10 kHz, with the exception of sEPSC recordings, which were filtered at 2 kHz. pCLAMP 10 software was used for data acquisition. Cells were excluded if the resting membrane potential (RMP) was more depolarized than -50 mV in current clamp, if access resistance (R_a) was >30 mΩ or changed more than 20% over the course of the recording.

Table 2.2. Composition of 8 mM Cl^- potassium gluconate internal solution used for intrinsic physiology recordings.

	Concentration (mM)
K-Gluconate	142
KCl	4
EGTA	0.5
HEPES	10
$MgCl_2$	2
Na_2ATP	2
Na_2GTP	0.3
Na_2Phosphocreatine	10
Biocytin	5.4

2.2.3 Intrinsic properties

In order to measure the intrinsic properties of neurons at P9-28, 3 protocols were performed in current clamp mode. First, a -10 pA step was applied from the cell's RMP, allowing to measure the passive intrinsic properties (Figure 2.1A). Intrinsic properties of neurons were analysed manually using the Stimfit software while blind to genotype and treatment (where applicable). Input resistance (IR) was calculated based on Ohm's law, using ΔV_m:

$$R = \frac{V}{I}$$

$$IR = \frac{\Delta V_m}{10}$$

Membrane time constant (τ_m) was calculated as time to reach 63% of ΔV_m, based on a monoexponential curve fitted to the voltage response. Membrane capacitance (C_m) was calculated from the τ_m and IR:

$$C_m = \frac{\tau_m}{IR} \times 1000$$

In order to investigate the firing and the action potential properties, the cell was held at-70 mV while current steps were applied from -125 pA to +400 pA in 25 pA increments. Action potential properties were measured from the first action potential fired in the rheobase step for each cell (Figure 2.1B), while sag was measured from the hyperpolarizing current steps as ΔV_m from the peak response until steady state.

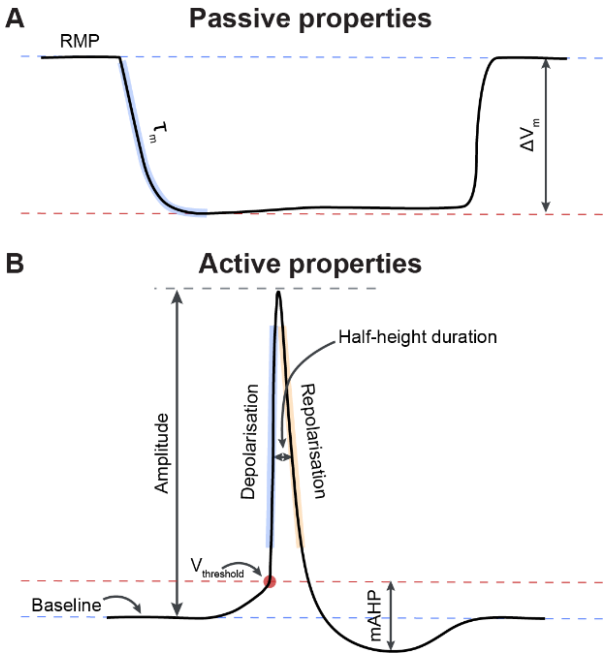

Figure 2.1. Diagram of passive and active intrinsic properties measurements. A. Passive properties were measured from a -10 pA current step. **B.** Active properties were measured from the first action potential fired at rheobase.

Finally, a 50 pA chirp stimulus was applied while holding the cell at -70 mV to investigate the cell's response to an analogue input. The resonance properties (impedance, Q-factor, resonant frequency) were analysed using a custom Matlab script written by members of the Kind Lab.

2.2.4 Synaptic properties

In order to measure the synaptic properties at P9-28, spontaneous activity was recorded for 1 minute in voltage clamp while holding the cell at -70 mV for sEPSCs. The recordings were analysed manually in Stimfit software blind to genotype. A triexponential non-linear regression template was generated based on a subset of events in the recording and template scaling (Clements and Bekkers, 1997) was used to detect events. Any events with an amplitude smaller than 3x the baseline SD were excluded to minimize Type I errors caused by electrical noise.

2.3 BPN14770 treatment

2.3.1 Dosing protocol

To determine whether the early developmental trajectory of S1 L4 SCs is amenable to therapeutic intervention, WT and *Fmr1*$^{-/y}$ rats were administered vehicle or 1 mg/kg of BPN14770 (PDE4D inhibitor). Vehicle consisted of 5% DMSO, 5% Solutol and 90% water. Animals were dosed via modified oral gavage every 24h for 5 days starting from P5. Only male pups were used, and all males within a litter were dosed with the same formulation. To ensure the lack of adverse effects, the pups were monitored for 30 minutes after dosing and weighed daily until use. BPN14770 treatment led to a decrease in body weight by the fourth postnatal week in both genotypes (Figure 2.2).

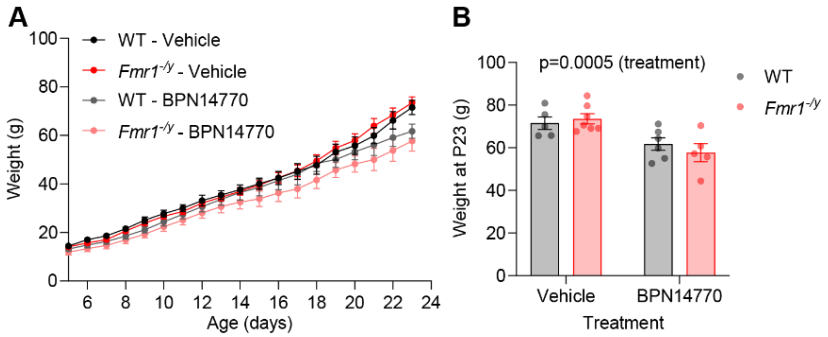

Figure 2.2. BPN14770 treatment results in lower body weight in WT and *Fmr1*$^{-/y}$ rats. A. All animals increased in body weight from P5 until P23. **B.** BPN14770 treatment leads to a reduction in body weight at P23 regardless of genotype (2-way ANOVA; treatment: F=17.21, p=0.0005; genotype: F=0.10, p=0.75; treatment × genotype: F=0.95, p=0.34).

Dosing and all subsequent experiments were performed blind to formulation (BPN14770 or vehicle – prepared by another researcher and labelled A or B) and genotype (see Section 2.1). Animals were taken for Patch-seq experiments at P10-14 (see Chapter 7 for methods) or whole-cell patch clamp at P25-28 (Figure 2.3). For all animals a sample of trunk blood was snap frozen on dry ice immediately after decapitation to allow the future determination of the final concentration of BPN14770 in the body through mass spectrometry.

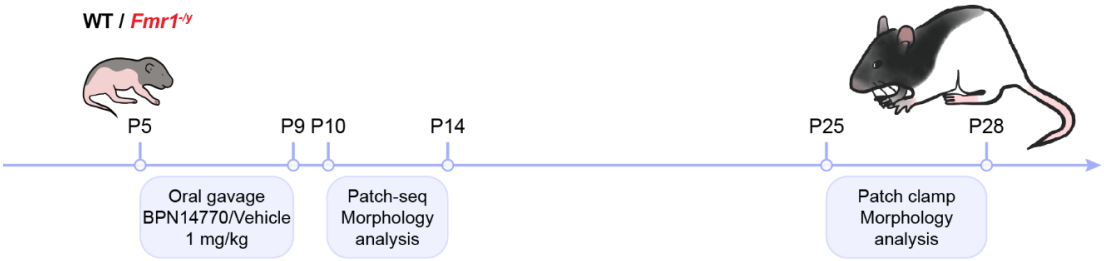

Figure 2.3. Timeline of BPN14770 treatment experiments. WT and *Fmr1*$^{-/y}$ littermates were given 1 mg/kg BPN14770 or vehicle via oral gavage daily from P5 until P9. Patch-seq recordings and morphology analysis were performed at P10-14. To test for long-term effects whole-cell patch clamp recordings and morphology analysis were performed at P25-28.

2.4 Histology

2.4.1 Cell morphology labelling

To allow the visualization of morphology of recorded cells, following whole-cell patch clamp or Patch-seq recordings the slices were immediately fixed in 4% PFA overnight, and subsequently stored in PBS at 4°C. The slices were incubated at 4°C overnight in PBS containing 0.5% Triton X-100 and AlexaFluor633-conjugated streptavidin (1:500 dilution, S21375, Invitrogen), then washed in 0.1M PB for 1h and mounted onto glass slides using Vectashield HardSet mounting medium (H-1400-10, Vector Labs).

2.4.2 Perfusion fixation

Animals were sedated with isoflurane then deeply anaesthetised via intraperitoneal injection of sodium pentobarbital (100mg/kg). The animal was then pinned down and the ribcage removed. The animal was then transcardially perfused with filtered PBS until all blood was removed. Filtered 4% PFA was perfused the same way, following which the animal was decapitated, their brain carefully removed and placed in 4% PFA for 3h. Fixed brains were stored in PBS at 4°C until they were used for immunohistochemistry.

2.4.3 Immunolabelling

For the immunolabelling of interneuron density perfusion-fixed brains were sectioned coronally into 60 µm sections using a Leica VT1000S (Leica Biosystems) vibratome and stored in PBS at 4°C.

Prior to labelling the sections were washed in PBS twice for 15 mins and placed in 10% NGS, 0.3% Triton X-100 and 0.05% NaN_3 in PBS for 1h at room temperature to block non-specific labelling. The sections were incubated with primary antibodies for 72h at 4°C (primary antibodies – see Table 2.3; 5% NGS, 0.3% Triton X-100, 0.05% NaN_3 in PBS). The sections were then washed twice in PBS for 15 mins and transferred into secondary antibody (Table 2.4) solution containing 3% NGS, 0.1% Triton X-100 and 0.05% NaN_3 in PBS for 24h at 4°C. Following labelling, the sections were washed twice in PBS for 15 mins then transferred into 0.1M PB for at least 1h and mounted onto glass slides with Vectashield HardSet (H-1400-10, Vector Labs) or Fluoromount G (00-4958-02, Invitrogen) mounting media.

Table 2.3. List of primary antibodies used.

Target	Host species	Dilution	Manufacturer	ID
NeuN	Mouse	1:1000	Sigma Aldrich	MAB377
NeuN	Rabbit	1:1000	Sigma Aldrich	ABN78
PV	Mouse	1:1000	Swant	PV-235PUR
Reelin	Mouse	1:500	Sigma Aldrich	MAB5364
SST-14	Rabbit	1:1000	BMA	T-4103

Table 2.4. List of secondary antibodies used. All secondary antibodies were IgG H+L with a stock concentration of 2 mg/ml.

Target	Host species	Conjugated with	Dilution	Manufacturer	ID
Mouse	Goat	AlexaFluor488	1:500	Invitrogen	A11001
Mouse	Goat	AlexaFluor568	1:500	Invitrogen	A11004
Mouse	Goat	AlexaFluor633	1:500	Invitrogen	A21050
Rabbit	Goat	AlexaFluor488	1:500	Invitrogen	A11008
Rabbit	Goat	AlexaFluor568	1:500	Invitrogen	A11011
Rabbit	Goat	AlexaFluor633	1:500	Invitrogen	A21070

2.5 Confocal imaging & image analysis

2.5.1 Cell morphology

For visualising the morphology of recorded neurons, 1024x1024 tiled Z-stack images were taken using a Leica SP8 confocal microscope at 20x magnification with a 0.5 µm step size. The dendritic tree was reconstructed manually using the SNT plugin for FIJI ImageJ (Figure 2.4A; Schindelin et al., 2012). Axons were not reconstructed as they were frequently incompletely filled or cut during the slicing process. To quantify the dendritic complexity of L4 SCs at P9-28, Sholl analysis was performed using a 10 µm step size (Figure 2.4B; Sholl, 1953).

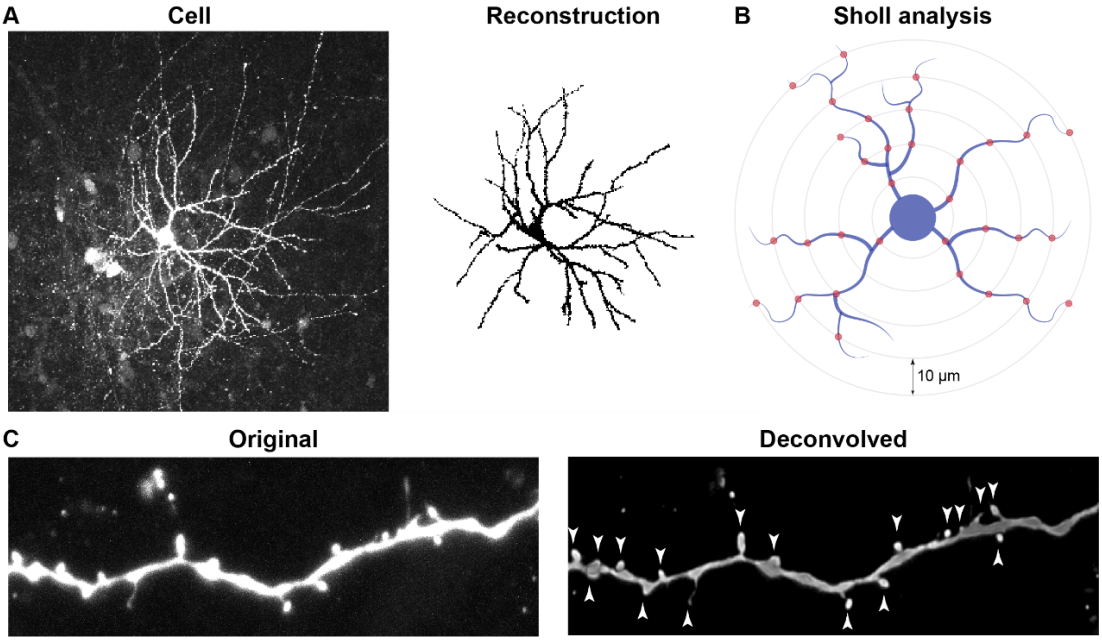

Figure 2.4. Morphology analysis in L4 SCs. A. Confocal images of L4 SCs (left) were used to produce 3D reconstructions of L4 SC dendritic arbours (right). **B.** Schematic of Sholl analysis in L4 SCs. Concentric circles are drawn from a set centre point (soma – blue circle) at set intervals (10 µm). Throughout the reconstructed dendritic arbour every dendrite intersection (red dots) with each Sholl circle is counted, giving a measure of dendritic complexity across the span of the dendritic arbour. **C.** Example image of a dendritic section before (left) and after deconvolution (right) used for dendritic spine density analysis. Arrows indicate dendritic spines.

2.5.2 Dendritic spine density

For spine density measurements 2-3 terminal dendrite sections per cell were imaged as Z-stacks at 63x magnification on a Leica SP8 confocal microscope at P9-38. Images were taken at 2048x2048 resolution, with 2.4x zoom and 0.13 µm step size to achieve Nyquist sampling. All images were deconvolved using Huygens Professional software (Scientific Volume Imaging) adjusting for the refractive index of the embedding medium (1.46). Dendritic spine density analysis was performed manually in FIJI ImageJ (Schindelin *et al.*, 2012) using the Cell counter plugin based on Z-projected images (Figure 2.4C).

2.5.3 Interneuron density

In order to estimate the density of interneuron subpopulations based on the marker labelling (PV, Sst-14, reelin) at P6-38, tiled Z-stack images of the S1 cortical column were taken on a Leica SP8 confocal microscope. Images were taken at 1024x1024 resolution with 1 µm step size at 20x magnification.

Cortical layers (L1, L2/3, L4, L5) were identified based on the Z-projected NeuN labelling. Interneuron density was measured manually for each cortical layer in FIJI ImageJ (Schindelin *et al.*, 2012) using the Cell counter plugin, following the optical disector method (Figure 2.5; Gundersen et al., 1988; Brown, 2017).

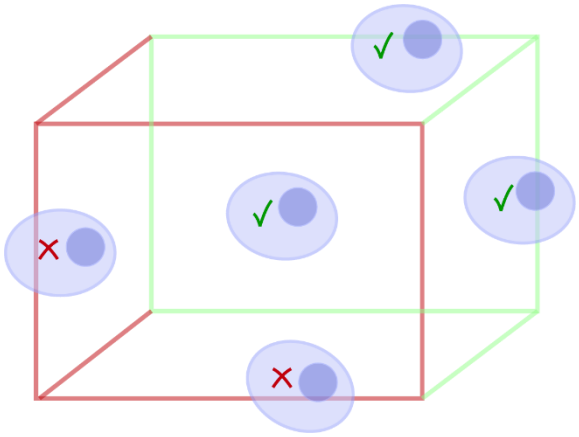

Figure 2.5. Diagram of the optical disector method for unbiased stereological estimation of cell density within three dimensional structures. 3 out of the 6 faces of the structure (here approximated to a cube) are excluded (e.g. front, left and bottom – red) such that cells intersecting these faces are not counted while cells inside the structure and cells intersecting the remaining faces are included in the count (green).

2.6 Transcriptomics

2.6.1 Single nuclei isolation

For 10X snRNAseq, S1 cortical nuclei were isolated from 3 WT and 3 *Fmr1*$^{-/y}$ rats at P9. Genotypes were confirmed prior to tissue processing by tail biopsy genotyping like previously (Section 2.1). Acute 1 mm thick coronal slices containing the S1 were prepared as described in Section 2.2.1. S1 was dissected out and immediately snap frozen on dry ice. The samples were stored at -80°C until use. Single nuclei isolation was performed using a nuclei isolation kit (NUC201, Sigma), according to previous methods (O'Keeffe *et al.*, 2025).

The tissue was thawed on ice, then suspended in 200 µl of lysis buffer (1700 µl PURE lysis buffer, 17 µl 0.1M DTT, 17 µl 10% Triton X-100, 8 µl SUPERaseIn RNase inhibitor (AM2696, Invitrogen) diluted 1:100 in nuclease-free water) per sample and homogenized using insulin needles (324826, BD). 360 µl of sucrose cushion (5 ml PURE 2M sucrose solution, 550 µl sucrose cushion buffer 55µl 0.1M DTT, 8 µl 1:100 RNase inhibitor) was added to each sample, which was then filtered through a sterile 30 µm CellTrics filter (04-004-2326, Sysmex). The filtrate was gently overlaid on top of 200 µl of sucrose cushion, ensuring separation between the two layers. The samples were centrifuged for 45 mins at 16,100g and 4°C. The supernatant was removed and the remaining pellet was resuspended in 100 µl elution solution (7 ml PURE storage buffer, 70 µl 1:100 RNase inhibitor) and transferred to a fresh microcentrifuge tube and another 100 µl of the elution solution was added. The samples were then centrifuged for 5 mins at 1,000g, after which the supernatant was discarded and the pellet resuspended in 1% w/v BSA (A9418, Sigma-Aldrich) diluted in Dulbecco's PBS (14190144, Gibco). The samples were kept on ice and immediately taken for FACS sorting.

2.6.2 snRNAseq

FACS sorting was performed by the Institute for Regeneration and Repair (University of Edinburgh). Nuclei were sorted on BD Fusion Q and BD Aria II flow cytometers, using DAPI for detection. Gating criteria were set based on forward/side

scatter to capture singlet nuclei and filter out debris. Quality control was performed using the Luna FX7 automated cell counter to confirm a sufficient number of nuclei was present in each sample. Library preparation was carried out by the Institute for Regeneration and Repair (University of Edinburgh) using the 10X Genomics scRNA-seq 3' v4 workflow, with an input of 30,000 nuclei per sample. Libraries were purified with SPRIselect Beads (Beckman Coulter) and quality controlled using TapeStation and DNA ScreenTape D1000 (Agilent). Sequencing was performed by Edinburgh Genomics on a NovaSeq 6000 system using the S2 flow cell (Illumina).

2.7 Bioinformatics

2.7.1 snRNAseq analysis

Reads from snRNAseq were mapped to a custom-built rat reference genome (Ensembl mRatBN7.2.113) and per cell per gene counts were produced with CellRanger (10X Genomics). R package SoupX (Young and Behjati, 2020) was used to filter out ambient RNA from each sample individually. Count data were merged, clustered using the Louvain algorithm and quality controlled using the R package Seurat (Hao *et al.*, 2024). Outliers were identified using the isOutlier function from the scater R package (McCarthy *et al.*, 2017) and removed based on high mitochondrial gene expression percentage, low/high feature and count numbers as well as high feature/count ratios (Table 2.5). Doublets were removed on a per sample basis (Table 2.6) with scDblFinder R package (Germain *et al.*, 2022). Total number of filtered cells per sample is provided in Table 2.7.

Table 2.5. Summary of outliers removed and thresholds for the selected criteria.

	Cells removed	**Threshold**
Mitochondrial genes	17750	0.18%
Features – low	3992	945.10
Features – high	245	6808.91
Counts – low	1342	856.70
Counts – high	2695	29434.30
Feature/count ratio - high	4064	0.74
Total	24033	

Table 2.6. Summary of doublets removed per sample.

Sample	Doublets	% Doublets
1	3407	12.32
2	2844	10.95
3	3321	11.65
4	823	6.41
5	2302	9.87
6	3439	12.50
Total	16136	

Table 2.7. Summary of filtered cells per sample.

Sample	Before filtering	After filtering
1	33690	24245
2	30531	23136
3	31819	25181
4	17044	12021
5	25217	21019
6	31537	24067
Total	169838	129669

For PCA, the number of dimensions (14) was selected based on the elbow plot, variable feature heatmaps as well as UMAP and feature plots to ensure correct separation of cell types into clusters. Clustering resolution (0.04) was selected based on a clustering tree diagram from the clustree R package (Zappia and Oshlack, 2018). Cell types were identified automatically based on a custom list of gene markers using the SCINA R package (Table 2.8; Zhang et al., 2019). Cluster identity was assigned based on the most abundant cell type within the cluster. Counts were aggregated on sample level using the aggregateBioVar R package (Thurman *et al.*, 2021) and pseudobulk differential expression analysis was performed by cell type with the R package DESeq2 (Love, Huber and Anders, 2014). Volcano plots were produced using

the R package ggplot2 (Wickham *et al.*, 2016); genes were considered to be significantly differentially expressed if p-adj<0.05. Gene ontology (GO) analysis was performed using enrichGO from the R package ClusterProfiler (Yu *et al.*, 2012) separately for upregulated and downregulated genes. A list of all the genes detected in the dataset was used as a custom background. Redundant GO terms were removed or replaced using the simplify function in ClusterProfiler.

Table 2.8. Summary of gene markers used to identify cell types.

Cell type	Gene marker	Reference
Excitatory neuron	*Slc17a7 Satb2*	(Lake *et al.*, 2016)
Inhibitory neuron	*Gad1 Gad2*	
Astrocyte	*Aqp4 Gfap Aldh1l1*	(Jurga *et al.*, 2021)
OPC	*Pdgfra Sox10*	(Kuhn *et al.*, 2019)
Oligodendrocyte	*Mog Mbp Plp1*	
Microglia	*Csf1r P2ry12 Aif1*	(Butovsky and Weiner, 2018)
Endothelial cell	*Vwf Flt1*	(Bryant *et al.*, 2023)
Pericyte	*Pla1a Cox4i2*	(Kang *et al.*, 2025)
VLMC	*Dcn Lum Ptgds*	(Zeisel *et al.*, 2018)

Excitatory neurons were extracted and re-clustered with 5 dimensions and a clustering resolution of 0.05, selected as above. Excitatory neuron subtypes were identified based on the expression of cortical layer markers (Kwan *et al.*, 2008; Oishi, Aramaki and Nakajima, 2016; Rosenberg *et al.*, 2018; Qian *et al.*, 2024).

Table 2.9. Summary of cortical layer markers used to identify excitatory neuron subtypes.

Cortical layer	Gene marker
L2/3	*Cux2 (Rorb$^-$)*
L4	*Cux2 Rorb*
L5	*Sox5 Foxp2 Tle4 Etv1*
L6	*Sox5 Foxp2 Tle4 Syt6*

Likewise, clustering of the extracted inhibitory neurons was performed using 9 dimensions and a clustering resolution of 0.05. Interneuron subtypes were identified based on the expression of commonly used interneuron markers (Rudy *et al.*, 2011; Shi *et al.*, 2021). Sample level aggregation and pseudobulk differential gene expression analysis were performed on each subset like previously.

2.8 Statistics

All data were analysed in R. Unless otherwise indicated, data were analysed using GLMM based on cell averages with animal ID as a random factor to account for pseudoreplication (Eleftheriou *et al.*, 2025). If the assumptions of normality or equal variance were not met, the data were transformed using log or square root link functions. Wherever applicable, transformations are indicated in figure caption, while the data are presented on the original scale. Significance was assumed at $p<0.05$, while $p<0.1$ was considered a trend.

Chapter 3

Electrophysiological characterization of S1 development in a rat model of FXS

3.1 Introduction

Sensory hypersensitivity is a common feature in FXS, frequently manifesting in FXS individuals as tactile defensiveness (Rogers, Hepburn and Wehner, 2003; Baranek *et al.*, 2008). Changes in sensory processing phenotypes could arise as a result of cortical hyperexcitability, which has been found in multiple sensory cortical areas of FXS individuals, including somatosensory and auditory cortex using EEG and transcranial magnetic stimulation (Ferri *et al.*, 1994; Van der Molen *et al.*, 2012; Morin-Parent *et al.*, 2019). Similarly, the loss of FMRP causes circuit and cellular-level hyperexcitability in *Fmr1*$^{-/y}$ mice. Sensory-evoked cortical activity spreads faster in the somatosensory cortex of *Fmr1*$^{-/y}$ mice (Zhang *et al.*, 2014). S1 neurons, including L4 SCs, have previously been found to be hyperexcitable due to altered intrinsic properties in the *Fmr1*$^{-/y}$ mouse model (Gibson *et al.*, 2008; Zhang *et al.*, 2014; Booker *et al.*, 2019; Domanski *et al.*, 2019). Dendritic function is impaired in *Fmr1*$^{-/y}$ mice, with changes in dendritic spine structure and function contributing to excessive summation in L4 SCs (Booker *et al.*, 2019). Many of these deficits have been linked to changes in ion channel function, such as HCN, SK and BK channels (Deng *et al.*, 2013; Zhang *et al.*, 2014; Deng and Klyachko, 2016; Booker *et al.*, 2019). This can occur through indirect mechanisms, like in the case of HCN channels, where a reduction in cAMP signalling caused by the loss of FMRP leads to a reduction in I_h or altered I_h current activation kinetics (Zhang *et al.*, 2014; Booker *et al.*, 2019). Additionally, FMRP has been proposed to directly influence ion channel function through protein-protein interactions with SK and BK channels (Deng *et al.*, 2013, 2019). This is in addition to the canonical function of FMRP as a translational repressor with 100s of

targets, many of which include proteins that are crucial for synaptic function and plasticity (Darnell *et al.*, 2011).

Previous studies have provided a snapshot of the differences that arise between WT and *Fmr1*$^{-/y}$ animals at specific developmental timepoints (see Section 1.3). However, cortical development in early life is a highly dynamic process that is tightly regulated by activity-dependent and homeostatic mechanisms in order to establish a circuit that is capable of receiving and processing information (Van der Loos and Woolsey, 1973; Killackey and Belford, 1979; Schlaggar, Fox and O'Leary, 1993; Feldman *et al.*, 1998; Fukuchi-Shimogori and Grove, 2001; O'Leary and Sahara, 2008). This delicate process could be skewed into an alternative developmental trajectory as a result of the loss of FMRP. While similar findings of hyperexcitability have been replicated separately at individual timepoints during development, to my knowledge, no study has focused on the developmental trajectory of electrophysiological properties of cortical neurons in *Fmr1*$^{-/y}$ animals. Therefore, in this chapter I will address the hypothesis that the loss of FMRP gives rise to an altered developmental trajectory, which leads to intrinsic hyperexcitability in rat S1 L4 SCs. As L4 is the primary recipient of thalamocortical inputs, L4 SCs, the primary excitatory cell type in L4, play a crucial role in the initial processing of sensory information arriving from the whiskers. Therefore, changes in the maturation of electrical properties of L4 SCs could have severe consequences for downstream sensory processing. A detailed characterization of L4 SC development in the rat model of FXS could provide novel insight into when and how points of divergence between WT and *Fmr1*$^{-/y}$ arise. This could help to better understand their potential consequences for cortical function in later life as well as identify critical periods during which the *Fmr1*$^{-/y}$ brain might be most amenable to therapeutic intervention with long-term effects.

3.2 Electrophysiological characterization of S1 L4 SCs during development in *Fmr1*$^{-/y}$ rats

Although the electrical properties of S1 L4 neurons have been found to be altered in juvenile *Fmr1*$^{-/y}$ mice from P10 (Booker *et al.*, 2019; Domanski *et al.*, 2019), little is known about the complete trajectory of these changes. Since cortical development is highly dynamic in early life, I set out to deeply characterize the entire developmental trajectory of electrophysiological properties of excitatory L4 neurons in WT and *Fmr1*$^{-/y}$ rats during the first 4 weeks of life after the closure of the critical period of experience-dependent thalamocortical plasticity (Crair and Malenka, 1995; Feldman *et al.*, 1998) i.e., P9-28 (Table 3.1). Whole-cell patch clamp recordings allow for a detailed and relatively high-throughput investigation of intrinsic and synaptic properties of individual neurons, while sampling the high inter- and intra-animal variability (Pastoll *et al.*, 2020). Thus, I performed *ex vivo* whole-cell patch clamp recordings in S1 L4 stellate cells (Figure 3.1A) in order to investigate their action potential firing, intrinsic and synaptic properties.

Table 3.1. Summary of WT and *Fmr1*$^{-/y}$ cells recorded per age group.

	WT			*Fmr1*$^{-/y}$		
Age group	**Cells**	**Animals**	**Mean age**	**Cells**	**Animals**	**Mean age**
P9-12	22	6	11.2±0.5	25	10	10.0±0.3
P13-16	36	13	14.1±0.3	28	7	14.7±0.4
P17-20	21	5	17.6±0.2	41	11	18.6±0.4
P21-24	30	9	22.8±0.3	34	7	21.9±0.5
P25-28	26	8	25.9±0.5	22	8	25.8±0.5

3.2.1 L4 SCs are hyperexcitable in *Fmr1*$^{-/y}$ rats

All neurons in each age group fired action potentials (APs) when injected with current steps from 0 to +400 pA in current clamp (Figure 3.1B). At P9-12 WT L4 SCs achieved peak firing at 325 pA, where they fired 17.91 ± 1.75 APs, after which the number of APs reached a plateau. In later development, the AP firing of these cells gradually decreased, with WT neurons achieving peak firing of 13.69 ± 1.07 APs without a plateau at P25-28 (Figure 3.1C). In contrast, at P9-12 *Fmr1*$^{-/y}$ L4 SCs fired more action potentials with increasing current steps, achieving a similar maximum firing rate of 17.72 ± 1.54 with current injections of only 275 pA. However, it is important to consider that the average age of *Fmr1*$^{-/y}$ rats in the P9-12 group was younger than WT (WT: 11.2 ± 0.5 days; *Fmr1*$^{-/y}$: 10.0 ± 0.3 days), which may contribute to the difference in AP firing since AP output typically decreases with age in early postnatal development (Valiullina *et al.*, 2016). Additionally, there was a notable trend in some cells (WT: 36%, 8 cells out of 22; *Fmr1*$^{-/y}$: 80%, 20 cells out of 25; Chi-square test; X^2=22.07, p<0.0001) to reduce their firing with increasing current injection in a phenomenon known as depolarization block, caused by the prolonged inactivation of voltage-gated sodium channels (Bianchi *et al.*, 2012; Lee *et al.*, 2024). Interestingly, *Fmr1*$^{-/y}$ neurons exhibited no difference in firing compared to WT in the P13-16, P17-20 and P21-24 groups. While WT neurons continued to decrease their AP discharge until P25-28, the AP output of the *Fmr1*$^{-/y}$ L4 SCs remained comparable between P21-24 and P25-28. Consequently, at P25-28 the *Fmr1*$^{-/y}$ cells displayed higher AP firing compared to WT, indicating the absence of a typical developmental decline in excitability giving rise to hyperexcitability in the 4th postnatal week. To quantify these changes, the rate of change in firing was calculated as the slope of the linear phase of the current-frequency plot from rheobase to peak firing (Figure 3.1D). A significant effect of age was found, confirming that the firing pattern changes as the cells mature. TheF-I slope was increased in *Fmr1*$^{-/y}$ rats overall compared to WT, without an interaction between age and genotype, suggesting that this effect is not strongly developmentally regulated. However, pairwise comparisons suggest that the increased F-I slope in *Fmr1*$^{-/y}$ cells relative to WT is driven solely by the P9-12 group. Furthermore, P9-12 was the only age where WT and *Fmr1*$^{-/y}$ had non-overlapping

confidence intervals (WT 95% CI: 0.056–0.076; *Fmr1*$^{-/y}$ 95% CI: 0.078–0.097). While this provides some evidence that the genotype effect could be particularly pronounced in the P9-12 age group, the lack of a significant interaction warrants cautious interpretation. Overall, this suggests that *Fmr1*$^{-/y}$ SCs may be especially hyperexcitable at P9-12, with more comparable F-I slopes in later development.

Rheobase, also known as current threshold, is the minimum amount of current required for a cell to fire an action potential (Figure 3.1E). In the recorded cells rheobase increased over development as the cells reduced their excitability, but a lower rheobase was found in the *Fmr1*$^{-/y}$ compared to WT, without an interaction of age and genotype. Pairwise comparisons revealed a significant decrease in rheobase in *Fmr1*$^{-/y}$ compared to WT only at P25-28. Therefore, *Fmr1*$^{-/y}$ cells required less current to fire an action potential in the 4th postnatal week. Finally, peak firing was quantified as the maximum number of APs fired by each cell (Figure 3.1F). On average, WT neurons fired a maximum of 20.88 ± 1.29 APs at P9-12 and only 13.69 ± 1.07 APs at P25-28. Similarly, *Fmr1*$^{-/y}$ fired 22.71 ± 0.96 APs at P9-12 and 16.52 ± 1.10 at P25-28. Indeed, a significant effect of age indicates that peak firing decreases during development in both genotypes. Peak firing was significantly higher in the *Fmr1*$^{-/y}$ compared to WT, suggesting that *Fmr1*$^{-/y}$ cells fire more action potentials than WT, regardless of age. In conclusion, the loss of FMRP leads to hyperexcitability in L4 SCs during the first 4 weeks of development.

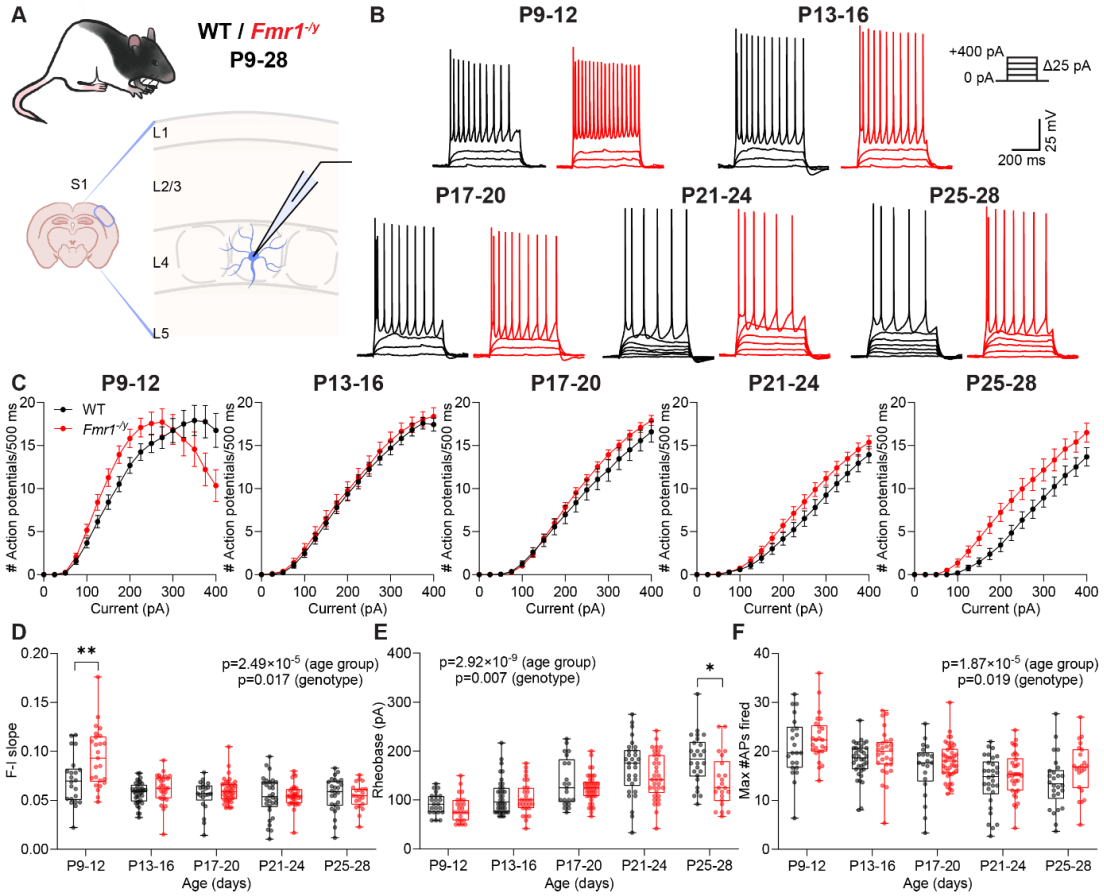

Figure 3.1. *Fmr1*$^{-/y}$ L4 stellate cells (SCs) are hyperexcitable during development. **A.** Schematic of recording setup. Whole cell patch clamp recordings were performed in L4 SCs in the S1 of WT and *Fmr1*$^{-/y}$ rats at P9-28. **B.** Representative traces from WT (black) and *Fmr1*$^{-/y}$ (red) cells in each age group. Current steps were applied from -125 pA to +400 pA in 25 pA increments to elicit action potential firing. **C.** Current-frequency plots suggest increased firing in *Fmr1*$^{-/y}$ cells at P9-12 and P25-28. **D.** *Fmr1*$^{-/y}$ showed an increase in F-I slope compared to WT at P9-12. F-I slope decreased with age in both genotypes (GLMM; age: F=7.98, p=2.49×10^{-5}; genotype: F=6.02, p=0.017; age × genotype: F=1.45, p=0.23). **E.** Rheobase increased with age and was reduced in the *Fmr1*$^{-/y}$ at P25-28 (GLMM; age: F=20.78, p=2.92×10^{-9}; genotype: F=8.25, p=0.007; age × genotype: F=0.87, p=0.49). **F.** The maximum number of APs fired decreased with age and was higher in the *Fmr1*$^{-/y}$ cells overall (GLMM; age: F=8.51, p=1.87×10^{-5}; genotype: F=5.86, p=0.019; age × genotype: F=0.078, p=0.99). WT: n=135 cells from N=41 animals; *Fmr1*$^{-/y}$: n=150 cells from N=43 animals.

3.2.2 Passive properties are altered in *Fmr1*$^{-/y}$ L4 SCs

A neuron's ability to fire action potentials is underlain by its passive membrane properties, which are known to be affected in the *Fmr1*$^{-/y}$ mice during the second postnatal week and contribute to their intrinsic hyperexcitability (Domanski *et al.*, 2019). Age-dependent changes in passive membrane properties could directly underlie the altered developmental trajectory of L4 SC excitability described in Section 3.2.1. Therefore, I next investigated the input resistance, membrane time constant and membrane capacitance of L4 SCs at P9-28 by injecting a -10 pA hyperpolarizing current step, measured from the RMP (Figure 3.2A).

At P9-12, WT cells had an RMP of -61.90 ± 1.24 mV, while *Fmr1*$^{-/y}$ had a similar RMP of -60.34 ± 1.08 mV. At P25-28, the RMP was more hyperpolarized, but comparable between genotypes (WT: -68.36 ± 1.42 mV; *Fmr1*$^{-/y}$: -67.68 ± 1.56 mV; Figure 3.2B). Thus, I found no genotype differences in the resting membrane potential between WT and *Fmr1*$^{-/y}$ neurons at any age, although the cells became more hyperpolarized with age in both genotypes. Similarly, input resistance generally decreased with age (Figure 3.2C). The main effects of age and genotype showed a significant interaction, while pairwise comparisons revealed an increase in input resistance of *Fmr1*$^{-/y}$ cells compared to WT at P9-12 ($p=0.0068$), P21-24 ($p=0.024$), and P25-28 ($p=0.005$), with no genotype differences at P13-16 ($p=0.79$) and P17-20 ($p=0.68$). Therefore, input resistance is selectively increased at P9-12 and P21-28, showing dynamic regulation during development. The membrane time constant (τ_m) provides a measure of how quickly the neuron's membrane responds to a change in current (Figure 3.2D). τ_m decreased with age and was significantly longer in *Fmr1*$^{-/y}$ than WT throughout development. Membrane capacitance (C_m) is a measure related to the size of the cell, and is directly dependent on the input resistance and the time constant (Figure 3.2E). As the neurons mature and grow in size, their C_m increased with age. As no genotype effect was observed and there was no interaction between age and genotype, the C_m was comparable between WT and *Fmr1*$^{-/y}$ at all ages tested.

Taken together, these data show that *Fmr1*$^{-/y}$ L4 neurons exhibit altered passive intrinsic properties during early development, in a manner consistent with

hyperexcitability. An increase in input resistance could be indicative of higher intrinsic excitability in L4 SCs, thus contributing to their increased firing rates.

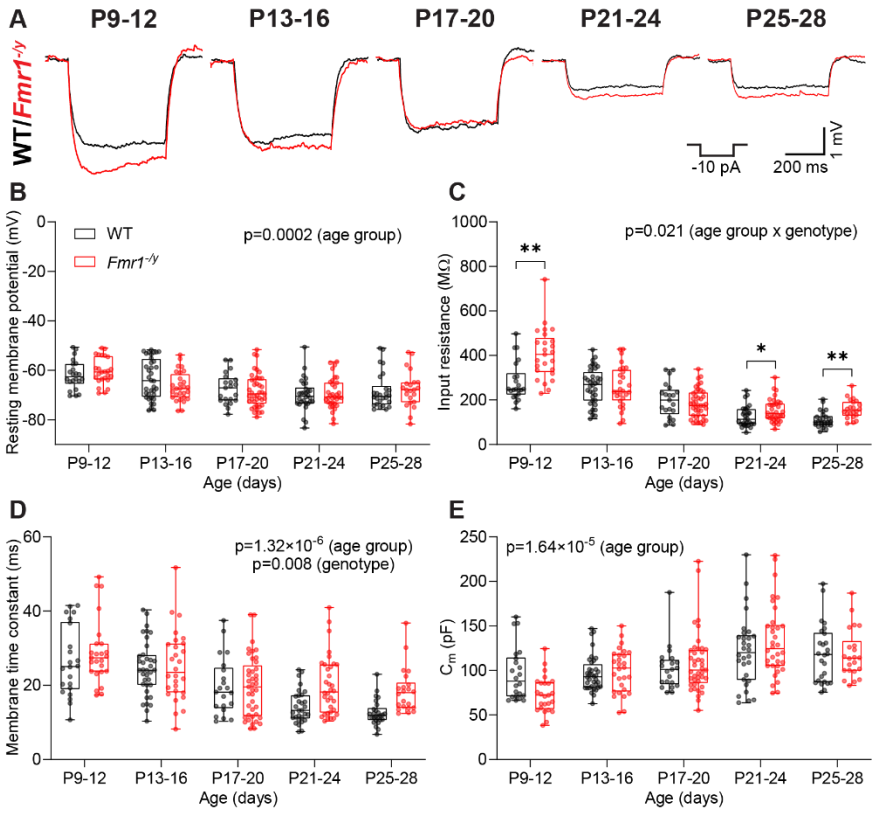

Figure 3.2. ***Fmr1*$^{-/y}$ cells have altered passive membrane properties during development. A.** Representative traces from WT (black) and *Fmr1*$^{-/y}$ (red) L4 SCs at P9-28. A single -10 pA step was applied to measure the passive membrane properties. **B.** Resting membrane potential is developmentally regulated in L4 SCs (GLMM; age: F=6.36, p=0.0002; genotype: F=0.0024, p=0.96; age × genotype: F=0.35, p=0.84). **C.** *Fmr1*$^{-/y}$ show an increase in input resistance at P9-12 (p=0.003), P21-24 (p=0.026) and P25-28 (p=0.006) (GLMM; age: F=38.61, p=9.15×10^{-16}; genotype: F=12.03, p=0.001; age × genotype: F=3.14, p=0.021; log-transformed). **D.** Membrane time constant decreased with age and was longer in *Fmr1*$^{-/y}$ (GLMM; age: F=10.63, p=1.32×10^{-6}; genotype: F=7.50, p=0.0081; age × genotype: F=1.29, p=0.29). **E.** Membrane capacitance increased with age (GLMM; age: F=8.78, p=1.64×10^{-5}; genotype: F=0.00, p=0.99; age × genotype: F=1.32, p=0.27). WT: n=135 cells from N=41 animals; *Fmr1*$^{-/y}$: n=150 cells from N=43 animals.

3.2.3 *Fmr1*$^{-/y}$ have altered action potential kinetics

The kinetics of action potential firing, or the active membrane properties, are underlain by the expression, phosphorylation and function of multiple ion channels, such as voltage-gated sodium channels (Hodgkin and Huxley, 1952; West *et al.*, 1991; Deng *et al.*, 2013; Routh, Johnston and Brager, 2013). AP kinetics can affect neuronal function, such as spike rate and plasticity (Kole, Letzkus and Stuart, 2007; Kimm, Khaliq and Bean, 2015). Changes in AP kinetics have been found in the *Fmr1*$^{-/y}$ mouse (Deng *et al.*, 2013, 2019; Routh *et al.*, 2017; Domanski *et al.*, 2019), are linked to neurotransmitter release properties (Deng *et al.*, 2013), and are associated with conditions such as epilepsy (Brown *et al.*, 2024). Therefore, I measured the first AP fired at rheobase in WT and *Fmr1*$^{-/y}$ L4 SCs at P9-28 in order to investigate their active properties (Figure 3.3A).

Action potential phase-plots show the rate of change in membrane voltage (dV/dt) as a function of voltage, thus allowing to better examine the rapidly changing kinetics of the AP (Bean, 2007). The AP phase plots suggest deficits in AP kinetics of *Fmr1*$^{-/y}$ L4 SCs at P9-12 and P21-28, and imply slower rate of depolarization during the rising phase (Figure 3.3B). Voltage threshold is the membrane potential at which an action potential is initiated (Figure 3.3C). The mean V_{thresh} at P9-12 was -33.70 ± 0.62 mV in WT at -32.69 ± 0.87 mV in *Fmr1*$^{-/y}$. Similarly, at P25-28, WT had a V_{thresh} of -33.75 ± 0.64 mV and *Fmr1*$^{-/y}$ had a V_{thresh} of -35.37 ± 0.82 mV at the same age. I found no differences in voltage threshold between WT and *Fmr1*$^{-/y}$ cells, or age groups. Therefore, the V_{thresh} is unaltered in *Fmr1*$^{-/y}$ rats, with no developmental regulation in either genotype. The action potential amplitude, measured from RMP, increased during development (Figure 3.3D) and showed an interaction between age and genotype, due to a decrease in *Fmr1*$^{-/y}$ relative to WT at P25-28 ($p=0.011$). Therefore, the AP amplitude is developmentally regulated and reduced in *Fmr1*$^{-/y}$ compared to WT at P25-28. Half-height duration is the width of the action potential at 50% of its amplitude (Figure 3.3E). As the APs became narrower during development, half-height duration decreased with age. *Fmr1*$^{-/y}$ showed an increase in half-height duration compared to WT, but there was no interaction between age and genotype. Rise time is the time it takes for the membrane potential to change from 20% to 80%

of the AP's amplitude (Figure 3.3F). The rise time was increased in the *Fmr1*$^{-/y}$ L4SCs compared to WT and decreased with age in both genotypes. The maximum rise rate was lower in the *Fmr1*$^{-/y}$ than WT throughout development, and increased with age without an interaction (Figure 3.3G). In contrast, the maximum decay rate did not differ between genotypes, although it also increased with age (Figure 3.3H) without an interaction of age and genotype.

To conclude, the L4 SCs of *Fmr1*$^{-/y}$ rats display altered action potential kinetic properties during the rising phase at P9-12 and P25-28, with no changes in V_{thresh} or decay. A slower rise is also reflected in the broadening of APs in the *Fmr1*$^{-/y}$. As the AP rising phase is driven primarily by voltage-gated sodium channels (VGSCs), these changes could be reflective of a shift in VGSC expression or activation kinetics in the *Fmr1*$^{-/y}$. Altered AP kinetics could reflect changes in Na^+/K^+ channel gating, testable with pharmacological isolation.

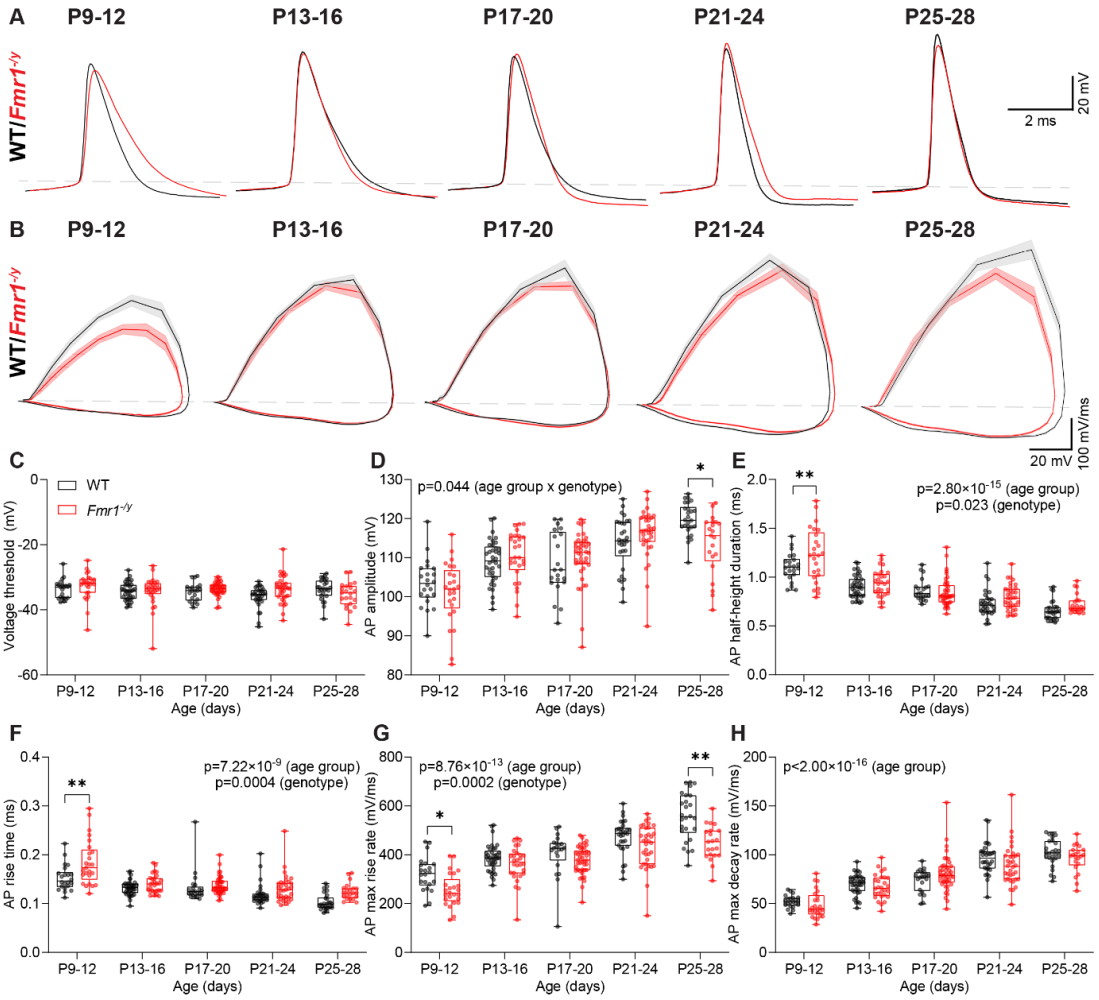

Figure 3.3. *Fmr1*$^{-/y}$ show altered AP kinetics in the rising phase at P9-12 and P25-28. A. Representative AP traces from WT (black) and *Fmr1*$^{-/y}$ (red) L4 SCs at P9-28. AP kinetic properties were measured from the first AP fired at rheobase. Grey dashed line shows voltage threshold. **B.** AP phase plots from WT (black) and *Fmr1*$^{-/y}$ L4 SCs at P9-28. Thick line represents the mean, shaded area shows SEM. Grey dashed line indicates baseline. **C.** Voltage threshold does not differ between ages and genotypes (GLMM; age: F=0.88, p=0.49; genotype: F=0.14, p=0.71; age × genotype: F=1.27, 0.30). **D.** AP amplitude shows a tendency towards a decrease at P9-12 (p=0.095) and is decreased at P25-28 (p=0.011) (GLMM; age: F=13.49, p=6.13×10^{-8}; genotype: F=1.13, p=0.29; age × genotype: F=2.60, p=0.044). **E.** Half-height duration decreases with age and is higher in the *Fmr1*$^{-/y}$ (GLMM; age: F=40.30, p=2.80×10^{-15}; genotype: F=5.51, p=0.023; age × genotype: F=1.63, p=0.18). **F.** AP rise time is higher in the *Fmr1*$^{-/y}$ at P9-12 and decreases with age (GLMM; age: F=16.42, p=7.22×10^{-9}; genotype: F=14.44, p=0.0004; age × genotype: F=1.07, p=0.38; log-transformed). **G.** The maximum rise rate is reduced in the *Fmr1*$^{-/y}$ at P9-12 and P25-28 and decreases during development regardless of genotype (GLMM; age: F=28.50, p=8.76×10^{-13}; genotype: F=15.83, p=0.0002; age × genotype: F=1.13, p=0.35). **H.** The maximum decay rate increases with age (GLMM; age: F=45.44, p<2.00×10^{-16}; genotype: F=0.74, p=0.39; age × genotype: F=1.32, p=0.27). WT: n=135 cells from N=41 animals; *Fmr1*$^{-/y}$: n=150 cells from N=43 animals.

3.2.4 mAHP is not affected in *Fmr1*$^{-/y}$ L4 SCs

Medium afterhyperpolarization (mAHP) contributes to the relative refractory period after the firing of an AP, where the membrane potential undershoots below the baseline due to the rapid opening and slower closing of voltage-gated potassium channels (Hodgkin and Huxley, 1952), effectively setting the maximum AP firing rate. In order to determine whether mAHP is developmentally affected in the *Fmr1*$^{-/y}$ rats, I measured the magnitude of the mAHP from the first action potential fired at rheobase (Figure 3.4A). WT cells had a mAHP of -18.00 ± 0.71 mV at P9-12 and -19.53 ± 0.56 mV at P25-28 (Figure 3.4B). Meanwhile, *Fmr1*$^{-/y}$ cells had a mAHP of -16.03 ± 0.87 mV at P9-12 and -18.26 ± 0.84 mV at P25-28. Hence, *Fmr1*$^{-/y}$ showed a tendency towards a reduction in mAHP overall relative to WT, without an effect of age and no interaction. Therefore, mAHP is minimally, if at all, altered in *Fmr1*$^{-/y}$ L4 SCs at P9-28.

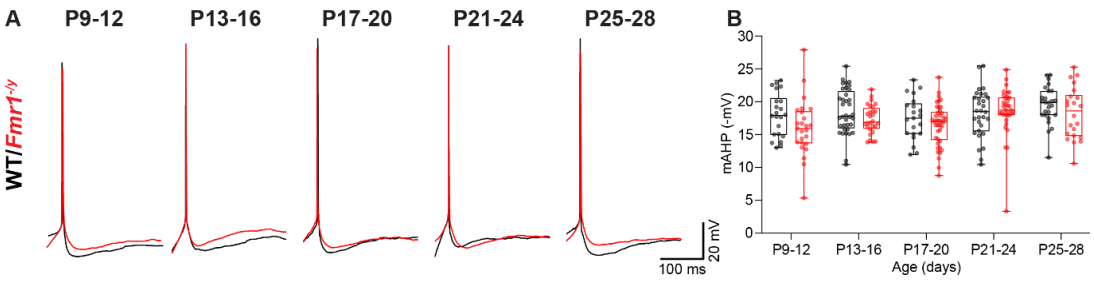

Figure 3.4. mAHP is mostly intact in *Fmr1*$^{-/y}$ rats. A. Representative mAHP traces from WT (black) and *Fmr1*$^{-/y}$ (red) L4 SCs at P9-28. mAHP was measured from the first AP fired at rheobase relative to the voltage threshold. **B.** *Fmr1*$^{-/y}$ cells show a tendency towards reduced mAHP (GLMM; age: F=1.52, p=0.22; genotype: F=3.64, p=0.065; age × genotype: F=0.55, p=0.70). WT: n=135 cells from N=41 animals; *Fmr1*$^{-/y}$: n=150 cells from N=43 animals.

3.2.5 No change in sag in L4 SCs

I_h current is a hyperpolarization-activated depolarizing current mediated by HCN channels (Momin *et al.*, 2008). Alterations in I_h activation, which are reflected in reduced membrane sag, have been found to contribute to hyperexcitability in the *Fmr1*$^{-/y}$ mouse L4 SCs and L5 PCs (Zhang *et al.*, 2014; Booker *et al.*, 2019). As such, I measured the hyperpolarization-induced sag and rebound in WT and *Fmr1*$^{-/y}$ L4 SCs at P9-28 by injecting hyperpolarizing steps of current from -125 pA to 0 pA in 25 pA increments (Figure 3.5A). The hyperpolarization-induced sag decreased with age, but did not differ between genotypes (Figure 3.5B). As the absolute sag amplitude is dependent on the cell's input resistance (which is increased in the *Fmr1*$^{-/y}$), I normalized it to the peak voltage deflection during the hyperpolarizing current injection relative to baseline (Figure 3.5C). The relative sag produced by the -125 pA current step also did not differ between WT and *Fmr1*$^{-/y}$, but decreased with age. I also measured the rebound potential generated when the cell returns to resting membrane potential (Figure 3.5D-E). The rebound potential and the rebound slope both showed an effect of age. The rebound potential showed a tendency towards an increase in *Fmr1*$^{-/y}$ relative to WT, but there was no difference between the genotypes in the rebound slope. Therefore, sag and rebound potentials are developmentally regulated and highest at P9-12, but there is no significant difference between WT and *Fmr1*$^{-/y}$ regardless of developmental stage.

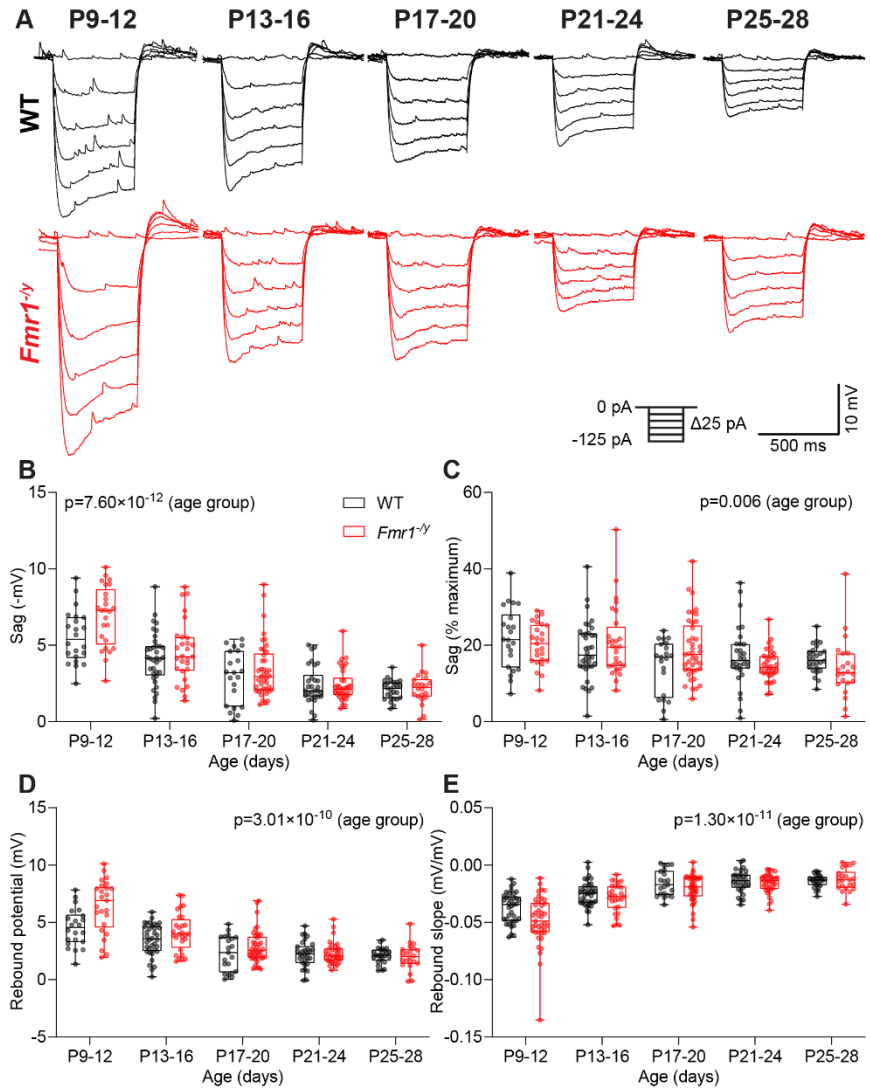

Figure 3.5. Hyperpolarization-induced sag and rebound are intact in *Fmr1*$^{-/y}$ rats. A. Representative sag traces from WT (black) and *Fmr1*$^{-/y}$ (red) L4 SCs at P9-28. Hyperpolarizing current steps were injected in 25 pA increments from -125 pA to 0 pA. Sag was measured from the -125 pA step. **B.** Sag decreases with age (GLMM; age: F=30.03, p=7.60×10^{-12}; genotype: F=2.79, p=0.10; age × genotype: F=0.41, p=0.80; square root-transformed). **C.** Relative sag decreases with age (GLMM; age: F=4.08, p=0.006; genotype: F=0.02, p=0.88; age × genotype: F=1.79, p=0.14; square root-transformed). **D.** Rebound potential decreases with age and tends to be higher in *Fmr1*$^{-/y}$ (GLMM; age: F=20.81, p=3.01×10^{-10}; genotype: 3.47, p=0.068; age × genotype: F=1.20, p=0.32). **E.** Rebound slope increases with age (GLMM; age: F=25.74, p=1.30×10^{-11}; genotype: F=2.50, p=0.12; age × genotype: F=0.90, p=0.47). WT: n=135 cells from N=41 animals; *Fmr1*$^{-/y}$: n=150 cells from N=43 animals.

3.2.6 Resonance

Network-level activity in a functioning brain is coordinated into rhythmic patterns known as oscillations (Hutcheon and Yarom, 2000). One way in which such rhythms can be generated is through resonance at the level of individual neurons. Resonance refers to a phenomenon where neurons are more responsive to oscillatory inputs at particular frequencies, making it crucial for controlling the timing and synchrony of spiking as well as synaptic integration (Hutcheon and Yarom, 2000). In order to investigate the resonant properties of WT and *Fmr1*$^{-/y}$ L4 SCs, a subthreshold 50 pA chirp stimulus i.e., a sinusoidal current wave of variable frequency (0.5-20 Hz), was injected into the cell allowing the measurement of the membrane's response to a dynamic analogue input (Figure 3.6A).

In line with developmental regulation of excitability, L4 SCs exhibited a gradual decrease in impedance with age (Figure 3.6B). At P9-12, *Fmr1*$^{-/y}$ cells showed a higher impedance in response to the entire frequency range. From P13-16 until P21-24, the impedances of WT and *Fmr1*$^{-/y}$ SCs converged, showing no difference in their response. However, at P25-28, the *Fmr1*$^{-/y}$ displayed an increased impedance in the low frequency range, but overlapping with WT at high frequencies. Resonant frequency (R_f) is the frequency which evoked the maximal response (Figure 3.6C). R_f was increased in the *Fmr1*$^{-/y}$ at P9-12 ($p=0.034$) and decreased at P25-28 compared to WT ($p=0.021$), with no differences at P13-16 ($p=0.37$), P17-20 ($p=0.64$) and P21-24 ($p=0.12$). Peak impedance represents the maximum response that is elicited, typically at the resonant frequency (Figure 3.6D). The peak impedance tended to be higher in the *Fmr1*$^{-/y}$ than WT and decreased with age, regardless of genotype. Q-factor, also known as the dampening factor, describes how sharply the neuron is tuned to its resonant frequency (Figure 3.6E). A high Q-factor means the resonance only occurs within a narrow range of frequencies (Hutcheon and Yarom, 2000). L4 SCs showed no genotype, or age differences in the Q-factor, and no interaction of age and genotype.

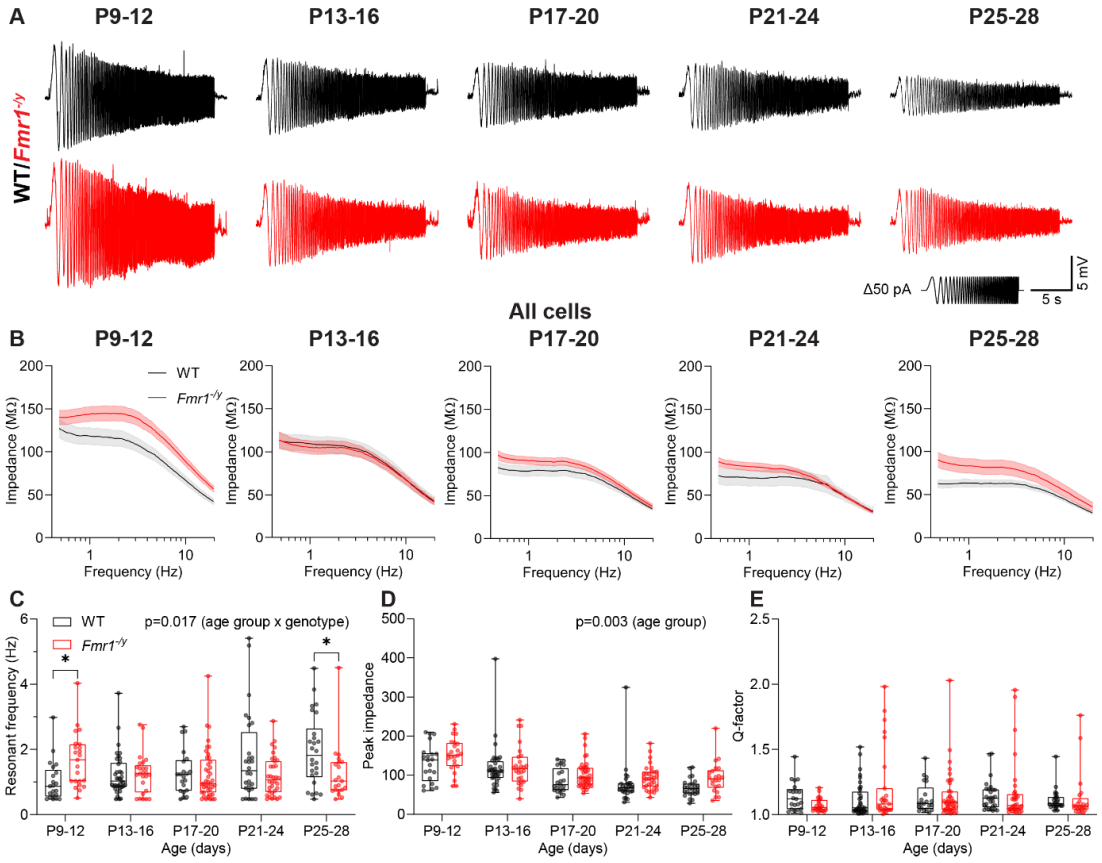

Figure 3.6. ***Fmr1*$^{-/y}$ L4 SCs have altered resonance properties. A.** Representative traces from WT (black) and *Fmr1*$^{-/y}$ (red) L4 SCs at P9-28. A 50 pA chirp stimulus was injected to measure resonance. **B.** Impedance-frequency plots of recorded cells. Thick line represents the mean, shaded area shows SEM. **C.** Resonant frequency is increased in *Fmr1*$^{-/y}$ at P9-12 (p=0.034) and reduced at P25-28 (p=0.021) (GLMM; age: F=0.50, p=0.74; genotype: F=0.33, p=0.57; age × genotype: F=3.52, p=0.017; log-transformed). **D.** Peak impedance decreases with age and tends to be higher in *Fmr1*$^{-/y}$ (GLMM; age: F=4.58, p=0.003; genotype: F=3.25, p=0.072; age × genotype: F=0.71, p=0.59; log-transformed). **E.** Q-factor shows no difference between genotypes and ages (GLMM; age: F=0.53, p=0.71; genotype: F=0.82, p=0.37; age × genotype: F=1.43, p=0.24; log-transformed). WT: n=133 from N=41 animals; *Fmr1*$^{-/y}$: 144 cells from N=43 animals.

Since resonance is not present in all neurons (Hutcheon and Yarom, 2000), I selected only those cells which showed a resonant peak in impedance at a specific frequency based on a qualitative examination of their individual impedance plots – hereinafter termed resonating cells. Similarly, the current-impedance plots of actively resonating cells revealed an increased impedance in *Fmr1*$^{-/y}$ cells compared to WT at P9-12 across the frequency range and at P25-28 at lower frequencies, with no changes in impedance at the intermediate ages (Figure 3.7A). The *Fmr1*$^{-/y}$ resonating cells showed a significant reduction in their resonant frequency at P21-24 and P25-28 relative to WT, but not at the younger ages (Figure 3.7B). Peak impedance on the other hand, showed no change between WT and *Fmr1*$^{-/y}$, but decreased with age (Figure 3.7C). Q-factor was consistent across genotypes and age groups without an interaction (Figure 3.7D).

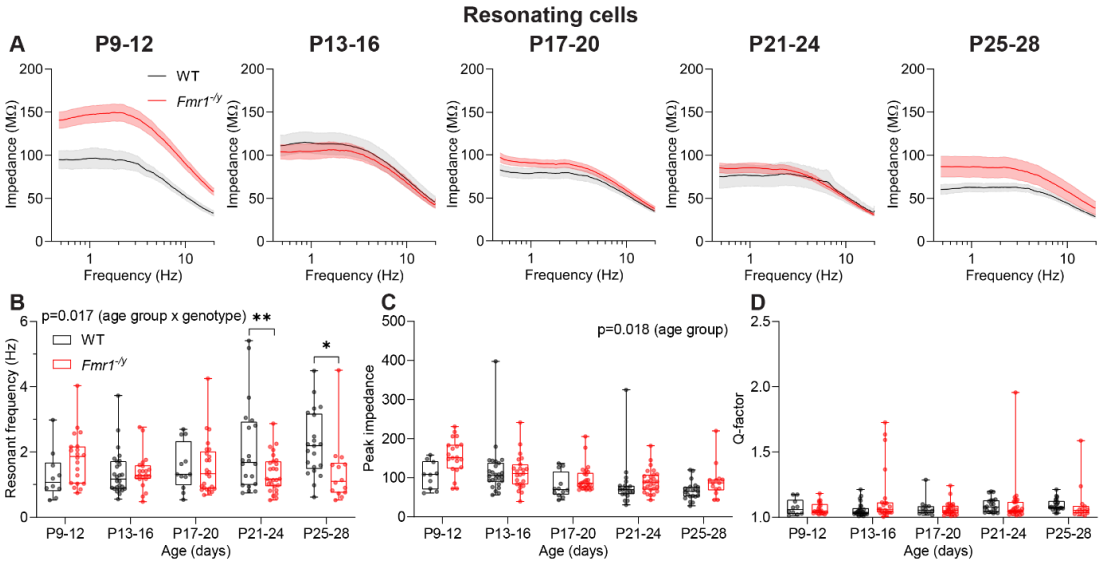

Figure 3.7. *Fmr1*$^{-/y}$ resonant cells show higher impedance and lower resonant frequency at P21-28. A. Impedance-frequency plots for resonating cells at P9-28. **B.** Resonant frequency is lower in *Fmr1*$^{-/y}$ in resonating cells at P21-24 and P25-28. (GLMM; age: F=1.35, p=0.27; genotype: F=2.70, p=0.11; age × genotype: F=3.35, p=0.016). **C.** Peak impedance decreases with age in resonating cells (GLMM; age: F=3.27, p=0.018; genotype: F=2.73, p=0.10; age × genotype: F=0.96, p=0.44; log-transformed). **D.** Resonating cells show no difference in Q-factor between age groups and genotypes (GLMM; age: F=0.58, p=0.68; genotype: F=0.71, p=0.40; age × genotype: F=1.47, p=0.22). WT: n=89 cells from N=38 animals; *Fmr1*$^{-/y}$: n=109 cells from N=39 animals.

In summary, *Fmr1*$^{-/y}$ L4 SCs show changes in their resonance properties during development, with a reduction in resonant frequency at P21-28 suggesting the neurons are more responsive to lower frequency inputs at this age.

3.2.7 Excitatory synaptic properties

While L4 SCs have altered intrinsic properties giving rise to intrinsic hyperexcitability in *Fmr1*$^{-/y}$ rats, whether their AP output could be affected is also dependent on the synaptic inputs they receive. L4 SCs are the primary recipients of direct thalamocortical inputs, making them responsible for integrating sensory stimuli from the whiskers before relaying them onto L2/3 (Feldmeyer, 2012). A neuron's spontaneous synaptic properties can give a measure of the synaptic inputs they receive, both stochastic and AP-driven, thus also reflecting circuit-level activity. In order to measure the synaptic properties of L4 SCs, I recorded the spontaneous excitatory postsynaptic currents (sEPSCs) in voltage clamp in WT and *Fmr1*$^{-/y}$ at P9-28 (Figure 3.8A).

The frequency of sEPSCs increased with age in both genotypes with WT cells showing an sEPSC frequency of 6.62 ± 0.45 Hz at P9-12 and 8.48 ± 0.67 Hz at P25-28 (Figure 3.8B). Likewise, *Fmr1*$^{-/y}$ had an sEPSC frequency of 5.86 ± 0.80 Hz at P9-12 and 8.80 ± 0.66 Hz at P25-28. Thus, *Fmr1*$^{-/y}$ showed no difference in sEPSC frequency compared to WT and there was no interaction of age and genotype. Similarly, sEPSC amplitude decreased with age, with WT cells having an sESPSC amplitude of 16.69 ± 0.83 pA at P9-12 and 12.75 ± 0.95 pA at P25-28 (Figure 3.8C). Since *Fmr1*$^{-/y}$ had an sEPSC amplitude of 17.64 ± 1.35 pA at P9-12 and 12.15 ± 1.09 pA at P25-28, there was no difference between WT and *Fmr1*$^{-/y}$ (Figure 3.8C). However, the cumulative frequency plots suggest that *Fmr1*$^{-/y}$ could have a higher proportion of high amplitude events compared to WT, at P21-24 (Figure 3.8D). Therefore, *Fmr1*$^{-/y}$ L4 SCs show no differences in sEPSCs throughout development, although there may be a shift in the proportion of larger events at P21-24. Overall, the excitatory synaptic inputs are unlikely to contribute to the altered developmental trajectory of L4 SCs in the *Fmr1*$^{-/y}$ rats.

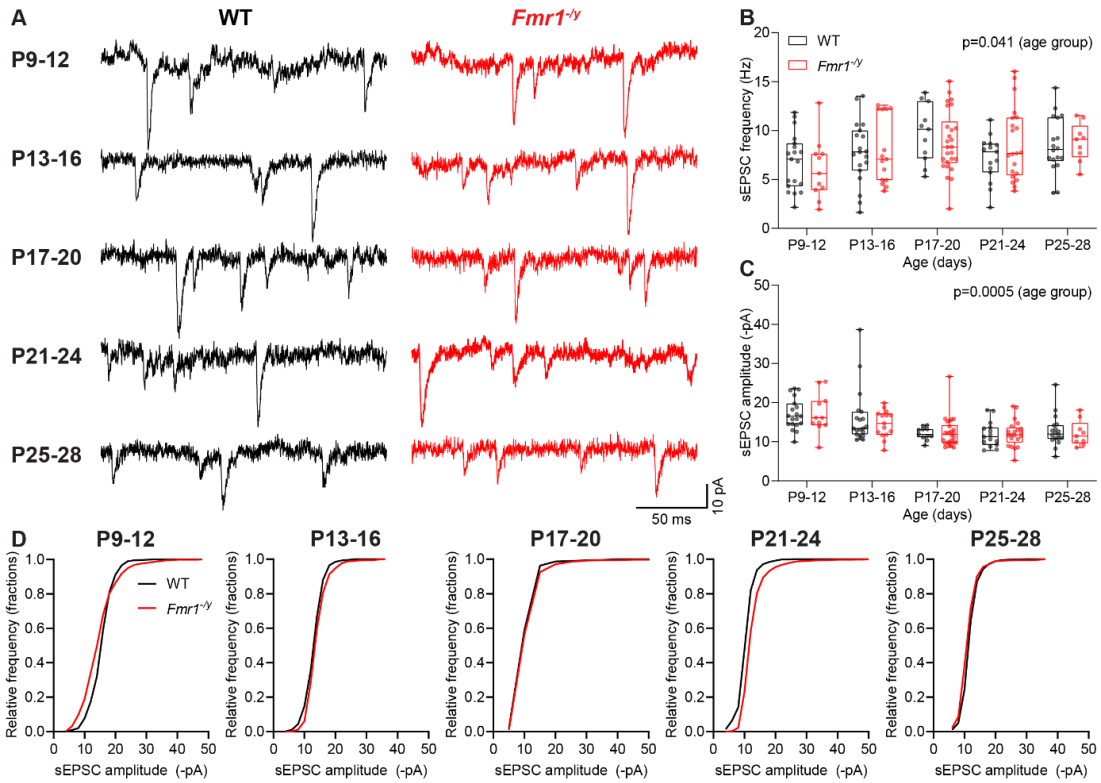

Figure 3.8. Spontaneous excitatory postsynaptic currents are unaffected in *Fmr1*$^{-/y}$. A. Representative sEPSC traces from WT (black) and *Fmr1*$^{-/y}$ (red) L4 SCs at P9-28. Spontaneous activity was recorded in voltage clamp while holding the cell at -70 mV. **B.** sEPSC frequency increases with age (GLMM; age: F=2.67, p=0.041; genotype: F=0.03, p=0.86; age × genotype: F=0.46, p=0.76). **C.** sEPSC amplitude increases with age (GLMM; age: F=5.93, p=0.0005; genotype: F=0.10, p=0.76; age × genotype: F=0.27, p=0.89). **D.** Cumulative frequency plots of sEPSC amplitudes at P9-28. WT: n=82 cells from N=41 animals; *Fmr1*$^{-/y}$: n=82 cells from N=41 animals.

3.3 Discussion

In this chapter, I have addressed the hypothesis that the loss of FMRP gives rise to an alternative developmental trajectory of rat L4 SCs leading to their intrinsic hyperexcitability. As such, I have systematically characterized a wide range of electrophysiological properties of L4 SCs in WT and *Fmr1*$^{-/y}$ rats during the first four weeks of postnatal development. I found that in WT rats L4 SCs decrease their intrinsic excitability during early development, as they fine-tune their active intrinsic, resonant and synaptic properties, in line with previously published data in L2/3, L4 and L5 neurons in S1 and V1 (Maravall, Stern and Svoboda, 2004; Valiullina *et al.*, 2016; Ciganok-Hückels *et al.*, 2023). Loss of FMRP however leads to changes in the intrinsic properties of *Fmr1*$^{-/y}$ during development, giving rise to increased AP firing, similarly to previous findings in *Fmr1*$^{-/y}$ mice (Booker *et al.*, 2019; Domanski *et al.*, 2019). Unlike the previous studies in *Fmr1*$^{-/y}$ mice, the hyperexcitability I observed is only apparent during the second postnatal week, after which it subsides and re-emerges in the fourth postnatal week, suggesting dynamic shifts in the developmental trajectory of L4 SCs in the absence of FMRP. Key findings of this chapter are summarized in Table 3.2.

Table 3.2. Summary of Chapter 3 results.

Age	**P9-12**	**P13-16**	**P17-20**	**P21-24**	**P25-28**
Excitability	↑	=	=	=	↑
AP rise kinetics	↓	=	=	=	↓
AP decay kinetics	=	=	=	=	=
Sag	=	=	=	=	=
Resonant frequency	=	=	=	↓	↓
sEPSCs	=	=	=	=	=

3.3.1 AP firing, intrinsic and synaptic properties

Increased AP firing in the second and fourth postnatal weeks falls in line with previous findings in juvenile and adolescent *Fmr1*$^{-/y}$ mice (Booker *et al.*, 2019; Domanski *et al.*, 2019). Unexpectedly, F-I plots of WT and *Fmr1*$^{-/y}$ rats converged in the third postnatal week, suggesting no change in firing properties at those ages. Increased AP firing can be explained by changes in input resistance, which is selectively increased at P9-12 and P21-28. Indeed, previous studies have found that increased input resistance directly underlies the intrinsic hyperexcitability of L4 SCs in *Fmr1*$^{-/y}$ mice (Booker *et al.*, 2019; Domanski *et al.*, 2019). Similarly to *Fmr1*$^{-/y}$ mice, this intrinsic hyperexcitability is associated with a reduction in rheobase and longer membrane time constants (Domanski *et al.*, 2019). The lower rheobase of the *Fmr1*$^{-/y}$ SCs is likely a reflection of a higher input resistance, as the amount of current necessary to produce an action potential is dependent on the cell's passive properties and the voltage threshold, which was not affected.

I found no genotype differences in sEPSC frequency nor amplitude, which suggests that spontaneous excitatory synaptic transmission onto L4 SCs is intact in the *Fmr1*$^{-/y}$ rats during development. This is in agreement with the normal dendritic spine density of S1 L4 SCs of *Fmr1*$^{-/y}$ mice (Harlow *et al.*, 2010; Till *et al.*, 2012), and indicates that the synaptic inputs received by L4 SCs are not altered during development and do not contribute to their altered excitability. While the excitatory synaptic inputs onto L4 SCs are unchanged, a longer membrane time constant could affect the temporal summation of thalamocortical inputs, making neurons more responsive to repeated stimulation over time. Indeed, an increase in spatial and temporal dendritic summation has been found in the L4 SCs of *Fmr1*$^{-/y}$ mice in addition to elevated postsynaptic summation in response to high frequency thalamocortical inputs (Booker *et al.*, 2019; Domanski *et al.*, 2019). Additionally, Domanski *et al.* found that similar changes in intrinsic physiology of L4 SCs led to significant deficits in information processing at circuit level, suggesting differences in spike timing that could impair experience-dependent processes in S1 of the *Fmr1*$^{-/y}$ mice. Excessive summation of dendritic inputs could lead to exaggerated responses to even minor sensory stimuli, reduced specificity in encoding of such inputs, loss of

pattern coding, as well as impaired ability to adapt to changing stimuli (Domanski *et al.*, 2019). Additionally, L4 SCs in *Fmr1*$^{-/y}$ mice have larger, more diffuse axonal arbours in L2/3 (Bureau, Shepherd and Svoboda, 2008), which could further compound with their increased output to produce broad activation of their downstream synaptic targets while contextual information (e.g. whisker specificity) could be lost at this level. Indeed, a reduced response selectivity to whisker stimulation and expansion of whisker receptive fields have been found in L2/3, but not L4 in *Fmr1*$^{-/y}$ mice (Juczewski *et al.*, 2016; He *et al.*, 2019). As such, a longer membrane time constant in *Fmr1*$^{-/y}$ rats could likewise contribute to exaggerated and non-specific responses to thalamocortical inputs leading to sensory hypersensitivity and tactile defensiveness. Further exploration of dendritic summation and circuit-level function in response to electrically stimulating thalamic axons in a thalamocortical slice preparation in *Fmr1*$^{-/y}$ rats could therefore provide useful insight into the functional ramifications of these changes.

3.3.2 Depolarization block

A particularly interesting feature of *Fmr1*$^{-/y}$ L4 SCs at P9-12 was their increased propensity for exhibiting depolarization block. This rarely studied property appears to be present in immature neurons, as it was not seen beyond the second week of life in either genotype, possibly due to the developmental decrease in input resistance. Depolarization block is caused by the prolonged inactivation of VGSCs (Bianchi *et al.*, 2012; Lee *et al.*, 2024), thus pointing to a deficit in VGSC inactivation kinetics of *Fmr1*$^{-/y}$ L4 SCs. However, the opposite is true in the prefrontal cortex of *Fmr1*$^{-/y}$ mice, as the inactivation of VGSCs is slower in *Fmr1*$^{-/y}$ L2/3 neurons, also contributing to their increased firing (Routh *et al.*, 2017).

Bianchi *et al.* (2012) argue that depolarization block is a property of all neurons, which plays an important role by allowing neurons to rapidly shut down their activity in response to large network activation, such as gamma range oscillations. However, in most cases the threshold for depolarization block is considered to be beyond the physiological range and is thus not typically observed in whole-cell patch clamp recordings. As such, in addition to the potential changes in

VGSC inactivation, this increased propensity for depolarization block could arise as a result of an increase in the input resistance of L4 SCs, which leads to increased AP firing to the point of achieving depolarization block even with smaller current injections. Additionally, the equilibrium value of the membrane potential at the depolarization block is not dependent on input resistance, but rather can be shifted by VGKC-mediated currents involved in the mAHP e.g., via SK channels (Bianchi *et al.*, 2012). Here, a tendency towards a reduced mAHP amplitude was observed, suggesting that VGKC-mediated currents could be mildly affected in the *Fmr1*$^{-/y}$ rats. As such, it would be interesting to investigate whether this voltage equilibrium is likewise altered, as well as whether the individual cell's mAHP correlates with its depolarization block kinetics. Finally, the current threshold to achieve depolarization block is directly related to dendrite diameter, with smaller dendrites exhibiting a lower threshold for depolarization block (Bianchi *et al.*, 2012). As such, considering that input resistance is also inversely correlated with dendritic membrane size (Golowasch *et al.*, 2009), it is likely that the observed increase in the input resistance and depolarization block could both be reflective of a morphological deficit in L4 SCs of *Fmr1*$^{-/y}$ rats, at least at P9-12. The dendritic complexity of L4 SCs during development is discussed in Chapter 4.

3.3.3 AP dynamics and mAHP

The shape of an action potential waveform is determined by the expression of multiple ion channels as well as their activation/inactivation kinetics (Hodgkin and Huxley, 1952). Changes to the kinetic properties of an action potential could shape downstream information transfer within the circuit by influencing presynaptic neurotransmitter release through AP-evoked Ca^{+} current (Yang and Wang, 2006; Scarnati *et al.*, 2020).

Unlike previous findings in *Fmr1*$^{-/y}$ mice (Booker *et al.*, 2019), I found a decrease in the maximum AP rise rate, suggesting slower AP rise dynamics in L4 SCs of *Fmr1*$^{-/y}$ rats which could underlie the AP broadening and lower AP amplitudes observed. As voltage gated sodium channels are the primary drivers of the rising phase of the action potential (Hodgkin and Huxley, 1952), these changes, as well as

the increased prominence of the depolarization block, implicate VGSCs in shaping the AP waveform deficits in *Fmr1*$^{-/y}$ L4 SCs. Routh *et al*. (2017) found that transient sodium conductance is increased in L2/3 PC in the mPFC of *Fmr1*$^{-/y}$ mice, giving rise to taller and narrower APs, the exact opposite of data presented in this chapter. As such, it is possible that dysregulation of transient sodium conductance also underlies the AP kinetic deficits in *Fmr1*$^{-/y}$ rat S1 L4 SCs, although the dysregulation occurs in opposite directions. If true, this would imply that FMRP can have contradictory effects on sodium conductance depending on the cell type, brain area, species or all of the above.

The loss of FMRP has previously been shown to lead to slower AP kinetics in CA3 PCs and L4 SCs of *Fmr1*$^{-/y}$ mice, resulting in wider APs of a lower amplitude (Deng *et al.*, 2013; Domanski *et al.*, 2019). This broadening of APs has significant ramifications for neuronal output, contributing to a substantial increase in Ca^{2+} current activation and thus an increase in intracellular Ca^{2+} levels (Scarnati *et al.*, 2020). This in turn gives rise to elevated neurotransmitter release, synaptic transmission and in consequence – synaptic plasticity. Indeed, broadening of the AP was found to result in increased neurotransmitter release and exaggerated short term plasticity in CA3 pyramidal neurons of juvenile *Fmr1*$^{-/y}$ mice, although this was attributed to FMRP's direct modulation of BK channels (Deng *et al.*, 2013). This effect of slower AP kinetics becomes more apparent during repetitive firing of APs, which contributes to the loss of information transmission at their outputs (Deng *et al.*, 2013; Domanski *et al.*, 2019). While the data presented in this chapter indicate slower AP kinetics similar to the findings from *Fmr1*$^{-/y}$ mice, all measurements of active properties presented in this thesis were taken from the first AP fired at rheobase and not repetitive firing, and thus are independent of BK channel function (Shao *et al.*, 1999). Instead, considering that I found no change in the voltage threshold, the altered AP kinetics observed could arise due to differences in the phosphorylation states of VGSCs, which may impact their gating properties (West *et al.*, 1991). As such, the mechanisms underlying the AP broadening could differ between *Fmr1*$^{-/y}$ mice and rats, although it is unclear whether repetitive AP firing is likewise affected in the *Fmr1*$^{-/y}$ rats. If true, the altered AP kinetics could further contribute to L4 SCs of

Fmr1$^{-/y}$ rats producing excessive, but non-specific synaptic outputs onto L2/3, leading to impaired sensory processing and hypersensitivity to innocuous stimuli, similarly to *Fmr1*$^{-/y}$ mice (Juczewski *et al.*, 2016). Hence, a detailed investigation of AP kinetics during repetitive stimulation and excitatory neurotransmission onto L2/3 is necessary to confirm whether these changes in AP shape indeed impair the quality of information relayed downstream of L4 SCs in the *Fmr1*$^{-/y}$ rats.

The broadening of the action potential waveform and its slower kinetics have previously been attributed to FMRP's direct modulation of BK channels leading to reduced BK currents in *Fmr1*$^{-/y}$ mice (Deng *et al.*, 2013). In addition to wider APs I found a tendency towards a reduction in mAHP amplitude in *Fmr1*$^{-/y}$ L4 SCs, which could be reflective of changes in VGKC-mediated currents, primarily via SK channels (Villalobos *et al.*, 2004). Indeed, a reduction in mAHP amplitude has been found in the CA3 PCs of *Fmr1*$^{-/y}$ mice, underlain by a direct interaction of FMRP with SK channels, similar to BK channels (Deng *et al.*, 2019). While BK or SK channel-mediated conductance was not assessed explicitly in this thesis, the fact that both AP broadening and tendency towards lower mAHP amplitudes are present throughout the assayed developmental period (as opposed to only coinciding with intrinsic hyperexcitability) supports the idea that these deficits could arise directly due to the loss of FMRP and its modulation of potassium channel-mediated conductance (Deng *et al.*, 2013, 2019).

Taken together, it is currently unclear whether the altered AP kinetics in *Fmr1*$^{-/y}$ rats arise due to changes in VGSC or VGKC-mediated currents. A direct investigation of pharmacologically isolated sodium and potassium channel-mediated currents would help to elucidate how the loss of FMRP affects voltage-gated ion channel function in developing rat cortex and the downstream ramifications of such altered AP kinetics.

3.3.4 Sag and resonance

I_h is an inward depolarizing current mediated through HCN channels that is activated by the hyperpolarization of the neuronal membrane. This allows it to modulate neuronal firing frequency, effectively acting as a pacemaker for neuronal activity (Momin *et al.*, 2008). Consequently, I_h is a critical component of membrane sag and resonance properties. Neuronal resonance is a preferential responsiveness of neurons to rhythmic stimuli within a particular frequency range (Hutcheon and Yarom, 2000). Activation of the I_h current directly underlies the resonant frequency, dictating the types of stimuli neurons are preferentially tuned into (Ulrich, 2002). This allows neurons to dynamically respond to changes in voltage while filtering out less relevant or mistimed stimuli.

Changes in I_h current are believed to be a major contributor to S1 hyperexcitability in *Fmr1*$^{-/y}$ mice (Zhang *et al.*, 2014; Booker *et al.*, 2019), with a reduction in HCN1 expression giving rise to higher impedance and lower resonant frequency as well as altered intrinsic properties of L5 pyramidal neurons leading to their intrinsic hyperexcitability (Zhang *et al.*, 2014). Additionally, reduced I_h current underlies the excessive dendritic summation in L4 SCs and L5 PCs of *Fmr1*$^{-/y}$ mice (Zhang *et al.*, 2014; Booker *et al.*, 2019), which contributes to their impaired sensory processing and sensory hypersensitivity (Juczewski *et al.*, 2016; He *et al.*, 2019). Unexpectedly, I found no change in sag in the *Fmr1*$^{-/y}$ rats which suggests that the magnitude of I_h current is likely unaffected. However, as sag is recorded in current clamp mode, it is an indirect measure of I_h current. Therefore, it is not possible to definitively conclude that I_h is intact in L4 SCs of *Fmr1*$^{-/y}$ rats *per se*. Actively resonant *Fmr1*$^{-/y}$ cells show a reduction in resonant frequency at P21-28, which suggests I_h could be reduced in the rat at this age. Alternatively, it is possible that rather than due to changes in the size of I_h current, the reduction in resonant frequency could arise as a result of a shift in the activation or kinetics of I_h, which could also contribute to hyperexcitability in L4 SCs during the fourth postnatal week despite the lack of changes in the total I_h. Indeed, Booker *et al.* (2019) found that rather than a decrease in total I_h, a cAMP-dependent shift in I_h activation properties underlies the changes in sag and resonance in *Fmr1*$^{-/y}$ mouse L4 SCs. Nevertheless, the sag and resonance

findings appear to be at odds with each other and should be investigated further. Ultimately, using an HCN1 channel blocker such as ZD7288 while recording I_h conductance in voltage clamp in the presence of ion channel and receptor blockers could help to directly confirm whether changes in I_h are present in the *Fmr1*$^{-/y}$ rats. Whether or not due to cAMP-dependent alterations in I_h, changes in the resonant properties of neurons could have significant consequences for circuit-level function during oscillatory activity, by making them more responsive to even minor, low frequency stimuli.

3.3.5 Summary

In summary, the data presented in this chapter support the hypothesis that the loss of FMRP leads to an altered developmental trajectory causing hyperexcitability in the primary somatosensory cortex. This hyperexcitability shows previously unknown dynamic changes during development, with distinct periods of increased AP firing rather than a persistent upregulation of activity. Although both periods of developmental hyperexcitability appear to be driven by an increase in input resistance, it is possible that they arise due to different underlying mechanisms, such as changes in morphology or I_h current. As such, morphological changes of developing *Fmr1*$^{-/y}$ L4 SCs are discussed in Chapter 4. Further work is necessary to characterize the role of I_h current in developing *Fmr1*$^{-/y}$ L4 SCs.

A detailed investigation of S1 L4 SC development in *Fmr1*$^{-/y}$ rats revealed that changes in intrinsic properties and excitability are already present from as early as P9, suggesting that if an optimal window for therapeutic intervention exists, it could be during the first postnatal week, before these changes occur. Additionally, such alterations in the developmental trajectory of S1 could have major functional consequences, giving rise to impaired information transfer within S1 contributing to sensory hypersensitivity in *Fmr1*$^{-/y}$ rats. However, it is currently unclear whether sensory processing and sensory-related behaviours (e.g., hypersensitivity) are affected in *Fmr1*$^{-/y}$ rats, as these have only been studied in mice thus far (Section 1.5.3). Therefore, an open question remains - how do these deficits affect sensory processing and by extension – experience-dependent processes that occur during development? Conversely, could these changes be in part driven by sensory experience? Future work should address these questions to identify the downstream implications of developmental hyperexcitability in models of FXS.

Chapter 4

Anatomical characterization of S1 development in *Fmr1*$^{-/y}$ rats

4.1 Introduction

The anatomy of the somatosensory cortex is established during early development (Rice, 1985). Processes such as dendritic arborisation, dendritic spine formation as well as interneuron elimination, are coordinated through activity- and experience-dependent mechanisms to build a balanced circuit that can efficiently process synaptic inputs and generate synchronized activity (Valverde, 1967; Van der Loos and Woolsey, 1973; Greenough and Chang, 1988; Petersen, 2007; Ashby and Isaac, 2011; Southwell *et al.*, 2012). The dendritic morphology of neurons can play a critical role in their ability to integrate synaptic inputs as well as dictate what inputs they receive (Greenough and Chang, 1988; Jaffe and Carnevale, 1999). The loss of FMRP expression has been shown to have effects not only on the function of S1 (Chapter 3), but also its structure. One of the most common anatomical changes associated with FXS is increased dendritic spine density and impaired spine morphology, which have been found in FXS individuals (Wisniewski *et al.*, 1991; Irwin *et al.*, 2001) and *Fmr1*$^{-/y}$ mice, including in S1 (Comery *et al.*, 1997; Galvez and Greenough, 2005; Till *et al.*, 2012; Dolan *et al.*, 2013; Bland *et al.*, 2021). Additionally, the loss of FMRP can lead to impaired refinement of the dendritic arbour. While *Fmr1*$^{-/y}$ L4 SCs have typical dendritic complexity, they show a reduction in dendritic asymmetry in juvenile mice, likely due to a delay in dendritic arbour reorganization that occurs during development (Till *et al.*, 2012). In mouse S1, loss of FMRP gives rise to a delay in barrel segregation and an increase in the number of dendrites in the barrel septa of adult *Fmr1*$^{-/y}$ mice (Galvez, Gopal and Greenough, 2003; Till *et al.*, 2012). This contributes to somatosensory map expansion, which produces imprecise

topographical mapping of the whiskers and neurons that are responsive to stimulation from multiple whiskers (Juczewski *et al.*, 2016).

Cortical dysfunction in FXS has been proposed to arise due to an altered E/I balance (Gibson *et al.*, 2008). *Fmr1*$^{-/y}$ mice exhibit changes in their inhibitory function which are consistent with ineffective and mistimed inhibitory control over the cortical circuit (Domanski *et al.*, 2019; Cea-Del Rio *et al.*, 2020). A contributing factor to such inhibitory dysfunction could lie in the size and diversity of interneuron populations in the cortex. Indeed, PV-expressing interneurons have been shown to have a reduced density in the cortex of developing and adult *Fmr1*$^{-/y}$ mice (Selby, Zhang and Sun, 2007; Lee *et al.*, 2019; Kourdougli *et al.*, 2023). This arises as a result of their hypoactivity in early development, leading to excessive activity-dependent apoptosis, which can be corrected by chemogenetically activating PV interneuron precursors. Additionally, the density of Sst-expressing interneurons is elevated in the *Fmr1*$^{-/y}$ mice, possibly as a compensatory mechanism for cortical hyperexcitability and PV interneuron dysfunction (Kourdougli *et al.*, 2023). Therefore, whether directly caused by the loss of FMRP, or indirectly (e.g., as a consequence of cortical hyperexcitability), an *Fmr1*$^{-/y}$ cortex could show significant anatomical reorganization which could contribute to or further exacerbate its dysfunction on a cellular and circuit level. However, it is currently unclear whether the loss of FMRP affects the neuronal morphology and inhibitory cytoarchitecture in the developing rat S1. Thus, in this chapter I will investigate the hypothesis that the loss of FMRP leads to an altered developmental trajectory of the rat S1, by giving rise to structural changes in the S1 during development. I will address this question through morphological reconstructions of L4 SCs to investigate whether their dendritic complexity is affected in the *Fmr1*$^{-/y}$ rats during the first 4 weeks of postnatal development. Moreover, I will examine the dendritic spine density in the *Fmr1*$^{-/y}$ rats, as an estimate of the excitatory inputs onto L4 SCs. Finally, I will investigate the inhibitory cytoarchitecture of the S1 during development, through immunohistochemical labelling of selected interneuron subtypes – PV, reelin and Sst-14-expressing cells. This could help to further identify species differences in the cortical development of *Fmr1*$^{-/y}$ mice and rats as well as potential biomarkers to assess the efficacy of therapeutic interventions.

4.2 L4 SC morphology during development of *Fmr1*$^{-/y}$ rats

4.2.1 *Fmr1*$^{-/y}$ L4 SCs have less complex dendritic arbours at P9-14

In order to determine whether the loss of FMRP affects L4 SC morphology during development, I reconstructed biocytin-filled neurons obtained from whole-cell patch clamp recordings in WT and *Fmr1*$^{-/y}$ rats at P9-28. As morphological development of neurons typically occurs on slower timescales than the rapid maturation of their intrinsic properties (Ciganok-Hückels *et al.*, 2023) and to ensure even powering between the groups, the cells were divided into 3 age groups, corresponding to the 2nd, 3rd and 4th postnatal weeks. L4 SCs had small, round somata found within the barrel and exhibited a star-like, or 'stellate' morphology, with some cells showing an asymmetrical distribution of dendrites (Figure 4.1A). I performed Sholl analysis to investigate the dendritic complexity of L4 SCs in WT and *Fmr1*$^{-/y}$ rats. Sholl analysis measures the number of dendritic intersections at set intervals away from the soma (every 10µm in this case), giving a measure of the extent of the dendritic arbour, as well as its complexity across the measured distances from the soma (Sholl, 1953). Sholl analysis revealed a reduction in the number of intersections across the entire range of distances from the soma in the *Fmr1*$^{-/y}$ L4 SCs compared to WT at P9-14 (Figure 4.1B). Such a change in the Sholl distribution suggests a reduction in the dendritic complexity of L4 SCs during the second postnatal week. At P15-20 however, there was no difference in the Sholl distributions of WT and *Fmr1*$^{-/y}$ neurons, suggesting no change in morphology (Figure 4.1C). Similarly, at P21-28 L4 SCs showed no genotype difference in the distribution of Sholl intersections across all distances from the soma (Figure 4.1D). Therefore, *Fmr1*$^{-/y}$ L4 SCs show a dendritic morphology deficit at P9-14, with no changes in later development.

The total number of Sholl intersections (Figure 4.1E) and Sholl peak (Figure 4.1F) both increased with age, suggesting a developmental increase in dendritic

complexity. As there was no significant genotype effect or interaction, the total number of Sholl intersections and Sholl peak were not affected in the *Fmr1*$^{-/y}$ at any age tested. Sholl span indicates the furthest extent of the cell's dendrites when measured from the soma (Figure 4.1G). There was no difference in the Sholl span of L4 SCs across genotypes and age groups, suggesting that the furthest dendritic distance from the soma does not change during development and is unaltered in the *Fmr1*$^{-/y}$. Similarly, the total number of dendrites did not show a genotype or age effect (Figure 4.1H), indicating that the number of dendritic branches is not significantly affected by the loss of FMRP and is not developmentally regulated. Finally, the total dendritic length increased with age, but did not differ between WT and *Fmr1*$^{-/y}$ L4 SCs at any age (Figure 4.1I). Therefore, *Fmr1*$^{-/y}$ L4 SCs show a mild deficit in their Sholl distribution at P9-14, but no differences in later development and no changes in any other morphological measures regardless of age.

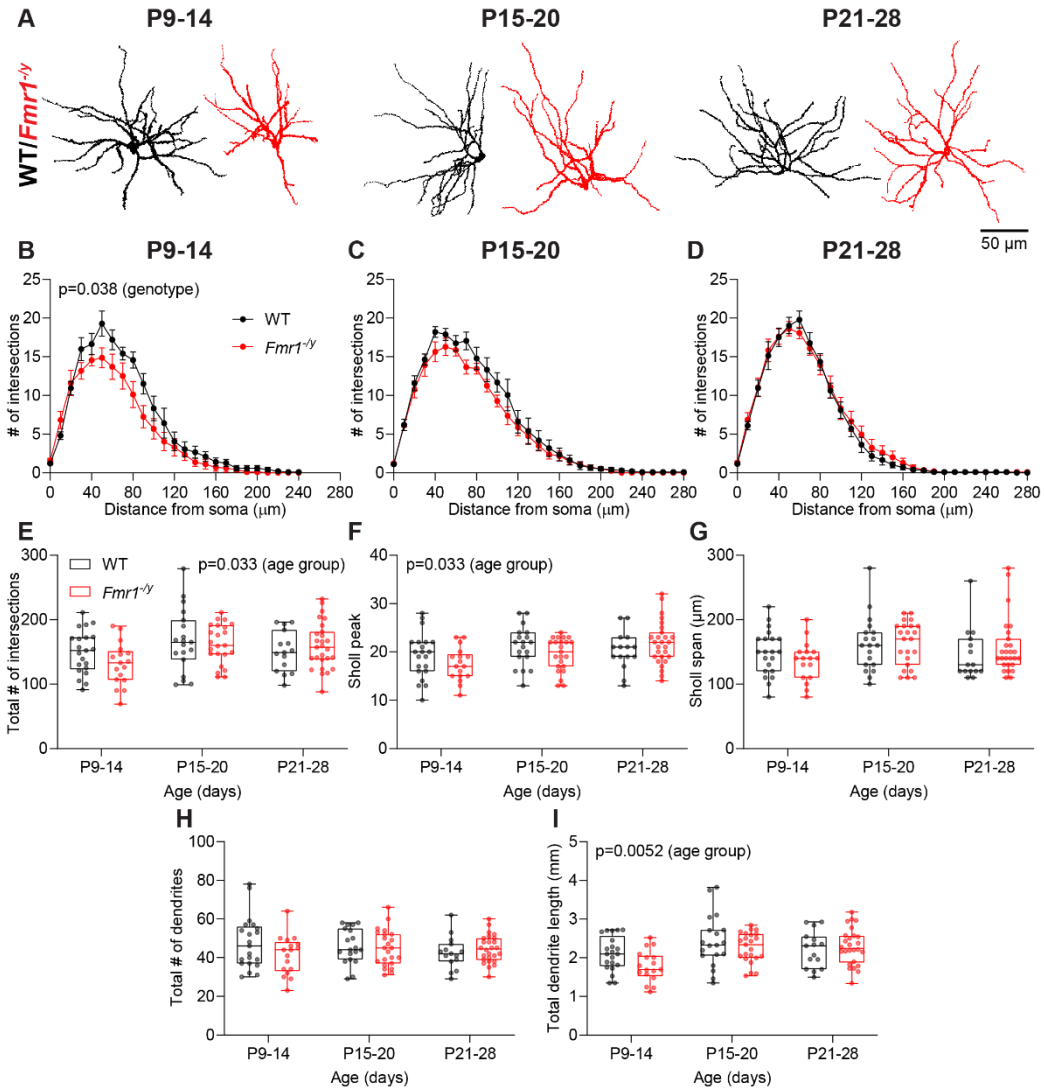

Figure 4.1. ***Fmr1*$^{-/y}$ L4 SCs show lower dendritic complexity at P9-14, but not P15-20 and P21-28. A.** Representative dendritic arbour reconstructions from WT (black) and *Fmr1*$^{-/y}$ (red) L4 SCs at P9-14, P15-20 and P21-28. **B.** *Fmr1*$^{-/y}$ L4 SCs have a lower number of Sholl intersections compared to WT at P9-14 (2-way repeated measures ANOVA on animal average values; Sholl: F=90.51, p<0.0001; genotype: F=5.018, P=0.038; Sholl × genotype: F=1.77, p=0.16). **C.** *Fmr1*$^{-/y}$ show no change in Sholl analysis at P15-20 (2-way ANOVA on animal average values; Sholl: F=140.90, p<0.0001; genotype: F=1.49, p=0.24; Sholl × genotype: F=0.85, p=0.46). **D.** There is no genotype difference in the Sholl distributions of WT and *Fmr1*$^{-/y}$ L4 SCs at P21-28 (2-way ANOVA on animal average values; Sholl: F=162.60, p<0.0001; genotype: F=0.26, p=0.62; Sholl × genotype: F=0.32, p=0.75). **E.** Total number of Sholl intersections increases with age (GLMM; age: F=3.74, p=0.033; genotype: F=1.25, p=0.27; age × genotype: F=1.15, p=0.33). **F.** Sholl peak increases with age (GLMM; age: F=3.64, p=0.033; genotype: F=1.34, p=0.25; age × genotype: F=1.62, p=0.21). **G.** Sholl span does not differ between genotypes and tends to increase with age (GLMM; age: F=2.55, p=0.088; genotype: F=0.22, p=0.64; age × genotype: F=0.81, p=0.45). **H.** Total number of dendrites is consistent between age groups and genotypes (GLMM; age: F=0.26, p=0.77; genotype: F=1.25, p=0.27; age × genotype: F=1.53, p=0.23). **I.** Total dendritic length increases with age, but does not differ between genotypes (GLMM; age: F=6.40, p=0.0052; genotype: F=2.60, p=0.12; age × genotype: F=1.60, p=0.22). WT: n=55 cells from N=30 animals; *Fmr1*$^{-/y}$: n=66 cells from N=28 animals. A subset of neuron reconstructions presented in this figure were performed by Mona Khodary as part of her undergraduate Honours project under my supervision.

4.2.2 Dendritic spine density is unaffected in *Fmr1*$^{-/y}$ L4 SCs

Excitatory synapses are formed onto specialized protrusions on the dendritic membrane known as dendritic spines (Nimchinsky, Sabatini and Svoboda, 2002). Thus, a neuron's dendritic spine density can give an estimate of its excitatory synaptic inputs. Increased dendritic spine density was found in L5 pyramidal neurons in the temporal and visual cortex of individuals with FXS as well as L2 pyramidal neurons in the parietal, temporal and frontal cortex of individuals with ASD (Irwin *et al.*, 2001; Hutsler and Zhang, 2010). In *Fmr1*$^{-/y}$ mice however, L4 SCs show no change in spine density during development (Harlow *et al.*, 2010; Till *et al.*, 2012; Booker *et al.*, 2019). Therefore, I measured the dendritic spine density from terminal dendrites of biocytin-filled WT and *Fmr1*$^{-/y}$ L4 SCs at P9-38 (Figure 4.2A) to determine whether spine density is affected by the loss of FMRP in rats. The dendritic spine density – measured as the number of spines per 10 µm of dendrite – increased with age (Figure 4.2B). There was no difference in spine density between WT and *Fmr1*$^{-/y}$ neurons and no interaction of age and genotype. Hence, while the density of dendritic spines on L4 SCs is developmentally regulated, it is not altered in the *Fmr1*$^{-/y}$ rats.

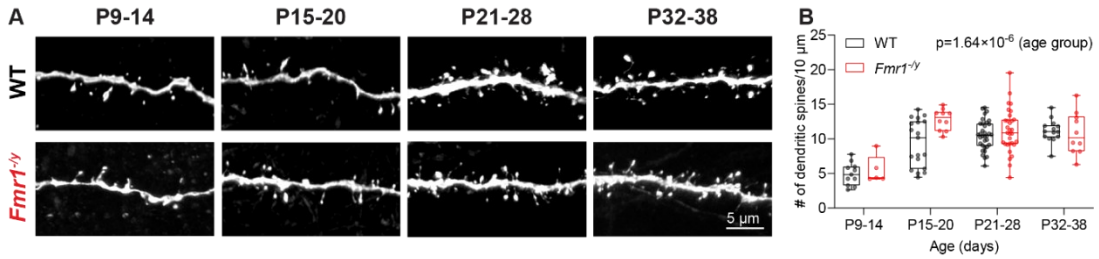

Figure 4.2.L4 SC dendritic spine density is unaltered in *Fmr1*$^{-/y}$, but increases during development. A. Representative images of dendrite sections from WT (top) and *Fmr1*$^{-/y}$ (bottom) L4 SCs at P9-38. **B.** Dendritic spine density increases with age, but does not differ between genotypes (GLMM; age: F=14.086, p=1.64×10^{-6}; genotype: F=2.44, p=0.13; age × genotype: F=0.91, p=0.45). WT: n=78 cells from N=34 animals; *Fmr1*$^{-/y}$: n=56 cells from N=24 animals. A subset of spine density measurements was performed by Mona Khodary under my supervision.

4.3 Interneuron density

Hyperexcitability in the developing S1 could arise in part due to an altered E/I ratio, with changes in inhibition affecting circuit-level activity in the cortex (Gibson *et al.*, 2008). Indeed, ineffective inhibition in the developing S1 contributes to cortical hyperexcitability in *Fmr1*$^{-/y}$ mice (Domanski *et al.*, 2019). In addition to altered interneuron function, deficits in cortical inhibition can arise due to changes in the abundance of inhibitory interneurons, which have been found in the S1 of *Fmr1*$^{-/y}$ mice and in FXS individuals (Selby, Zhang and Sun, 2007; Lee *et al.*, 2019; Kourdougli *et al.*, 2023).

In order to investigate whether the development of selected interneuron populations is affected by the loss of FMRP, I immunolabelled S1 sections from WT and *Fmr1*$^{-/y}$ rats for interneuron markers representing three of the most abundant interneuron subtypes i.e., PV, reelin and Sst-14, which altogether account for nearly 80% of all cortical interneurons (Rudy *et al.*, 2011). I measured the density of cells positive for each marker in upper cortical layers L1-L4.

4.3.1 Parvalbumin^{+} cell density is not affected in *Fmr1*$^{-/y}$ rats

Parvalbumin-expressing interneurons are the most abundant class of interneurons in the cortex, comprising nearly half of all interneurons. As PV interneurons tend to be fast spiking and include basket and chandelier cells, they are ideally placed to provide strong FFI onto the perisomatic compartment and the axon initial segment (Rudy *et al.*, 2011). The density of PV interneurons and their precursors has previously been found to be reduced in *Fmr1*$^{-/y}$ mice and FXS individuals (Selby, Zhang and Sun, 2007; Lee *et al.*, 2019; Kourdougli *et al.*, 2023). Therefore, I investigated the density of PV^{+} cells in L1-4 of S1 from WT and *Fmr1*$^{-/y}$ rats (Figure 4.3A). As PV is not expressed in the rodent cortex until P14 (Lecea, del Ri´o and Soriano, 1995), I assessed this at P15-38.

In line with previous reports (Rudy *et al.*, 2011), PV^{+} cells were largely absent in L1 of the somatosensory cortex in both genotypes (Figure 4.3B). No age differences

were found, although *Fmr1*$^{-/y}$ showed a tendency towards a reduced PV^{+} cell density in L1. Therefore, L1 PV^{+} cell density is largely unaffected by the loss of FMRP and does not change during development. Unlike L1, L2/3 showed substantial PV immunoreactivity, but there was no difference in L2/3 PV^{+} cell density between WT and *Fmr1*$^{-/y}$ rats (Figure 4.3C). Age effect was not significant, suggesting their density is not strongly developmentally regulated within the P15-38 window. Finally, the PV^{+} cell density in L4 did not differ between WT and *Fmr1*$^{-/y}$ rats, but decreased with age in both genotypes (Figure 4.3D). Therefore, PV^{+} cell density is unaltered in the S1 of *Fmr1*$^{-/y}$ rats, but shows age-dependent downregulation in L4.

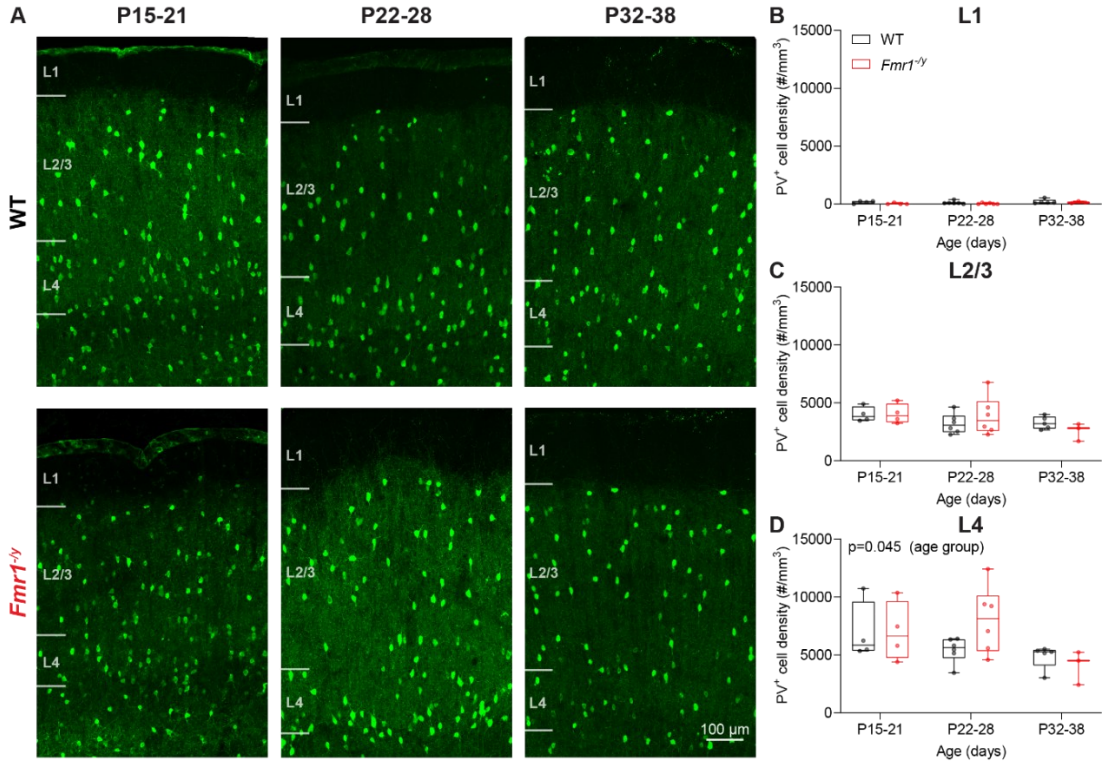

Figure 4.3. *Fmr1*$^{-/y}$ have typical PV^{+} cell density during development. A. Representative PV^{+} cell density images from WT and *Fmr1*$^{-/y}$ S1 at P15-38. **B.** PV^{+} cell density in L1 shows a tendency towards a reduction in *Fmr1*$^{-/y}$ (2-way ANOVA; age: F=1.54, p=0.24; genotype: F=3.42, p=0.078; age × genotype: F=0.21, p=0.81). **C.** *Fmr1*$^{-/y}$ rats show no change in L2/3 PV^{+} cell density (2-way ANOVA; age: F=2.25, p=0.13; genotype: F=1.84×10^{-5}, p=0.99; age × genotype: F=1.05, p=0.37). **D.** L4 PV^{+} cell density decreases with age, but does not differ between WT and *Fmr1*$^{-/y}$ (2-way ANOVA; age: F=3.58, p=0.045; genotype: F=0.58, p=0.45; age × genotype: F=1.81, p=0.19). WT: N=15 animals; *Fmr1*$^{-/y}$: N=13 animals.

4.3.2 *Fmr1*$^{-/y}$ rats have typical reelin^{+} cell density

Reelin-expressing interneurons, such as neurogliaform or bitufted cells are present throughout the cortical column and tend to have an adapting, late or fast-spiking firing pattern (Pohlkamp *et al.*, 2014). In order to investigate this population of interneurons during development, I measured the density of reelin^{+} cells in L1-4 of the S1 in WT and *Fmr1*$^{-/y}$ rats at P6-28 (Figure 4.4A). In agreement with published findings, reelin^{+} cells were found in all cortical layers, including L1. The density of reelin^{+} cells in L1 was consistent across age groups, and did not differ between WT and *Fmr1*$^{-/y}$ rats (Figure 4.4B). In L2/3 there was no age difference in reelin^{+} cell density, but *Fmr1*$^{-/y}$ showed a tendency towards an increase (Figure 4.4C). There was no age or genotype effect on the reelin^{+} cell density in L4 (Figure 4.4D). Therefore, the density of reelin^{+} cells is mostly intact in *Fmr1*$^{-/y}$ rats in all of the cortical layers tested. Additionally, I found no developmental changes in the density of these cells.

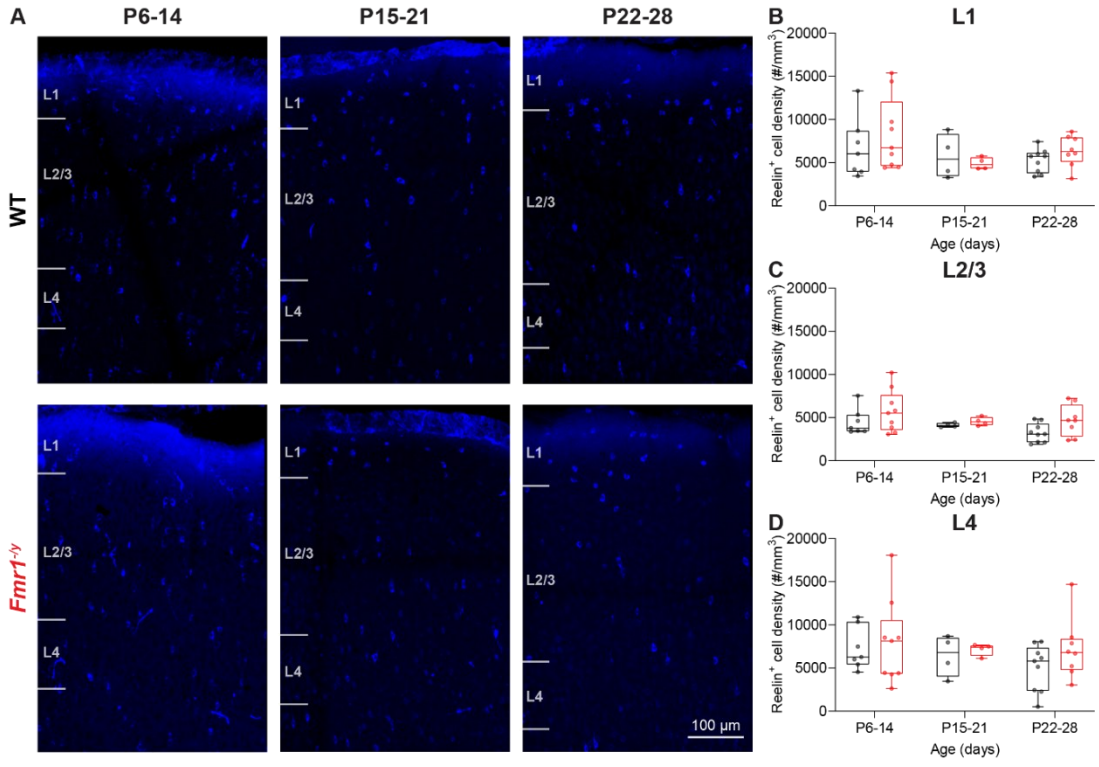

Figure 4.4. Reelin^{+} cell density is unaltered in *Fmr1*$^{-/y}$ during development. A. Representative reelin^{+} cell density images from WT and *Fmr1*$^{-/y}$ S1 at P6-28. **B.** L1 of *Fmr1*$^{-/y}$ rat S1 does not differ in reelin^{+} cell density (2-way ANOVA; age: F=2.27, p=0.12; genotype: F=0.48, p=0.49; age × genotype: F=0.52, p=0.60). **C.** *Fmr1*$^{-/y}$ rats show a trend towards an increase in L2/3 reelin^{+} cell density (2-way ANOVA; age: F=2.078, p=0.14; genotype: F=3.55, p=0.068; age × genotype: F=0.25, p=0.78). **D.** L4 reelin^{+} cell density does not differ between WT and *Fmr1*$^{-/y}$ (2-way ANOVA; age: F=0.84, p=0.44; genotype: F=1.16, p=0.29; age × genotype: F=0.25, p=0.78). WT: N=20 animals; *Fmr1*$^{-/y}$: N=21 animals.

4.3.3 Somatostatin-14^{+} cell density is increased in *Fmr1*$^{-/y}$ rats

Somatostatin-expressing interneurons are present throughout the cortical column except L1 (Xu, Roby and Callaway, 2010). The majority of somatostatin-expressing neurons are Martinotti cells, which primarily convey inhibition onto the distal dendrites of pyramidal and stellate neurons, thus having a role in the integration of synaptic inputs in the dendrites (Wang *et al.*, 2004). In somatostatin-expressing cells, the somatostatin gene *Sst* gives rise to preprosomatostatin, which then undergoes several post-translational modifications to produce Sst-28 and Sst-14, with Sst-14 being the CNS-dominant form, responsible for 90% of somatostatin-mediated signalling within the cerebral cortex (Warren and Shields, 1984; Epelbaum, 1986; Bonanno *et al.*, 1991). In order to determine whether the distribution of Sst-expressing interneurons is affected by the loss of FMRP, I investigated the Sst-14^{+} cell density in the S1 of WT and *Fmr1*$^{-/y}$ rats during development i.e., at postnatal days P6-28. Sst-14^{+} cells were largely absent from L1 in WT rats. In contrast, L1 Sst-14^{+} cell density was elevated in the *Fmr1*$^{-/y}$ (Figure 4.5B). There was no difference between age groups, suggesting the density is consistent during development. Likewise, in L2/3 the Sst-14^{+} cell density was increased in the *Fmr1*$^{-/y}$ compared to WT with no effect of age (Figure 4.5C). The Sst-14^{+} cell density was also significantly higher in L4 of *Fmr1*$^{-/y}$ rats relative to WT. However, I found no difference in the density of Sst-14^{+} cells in L4 between the age groups. In summary, I found that Sst-14-expressing cells are significantly more abundant in the S1 of *Fmr1*$^{-/y}$ rats during development, but do not show any developmental regulation in either genotype.

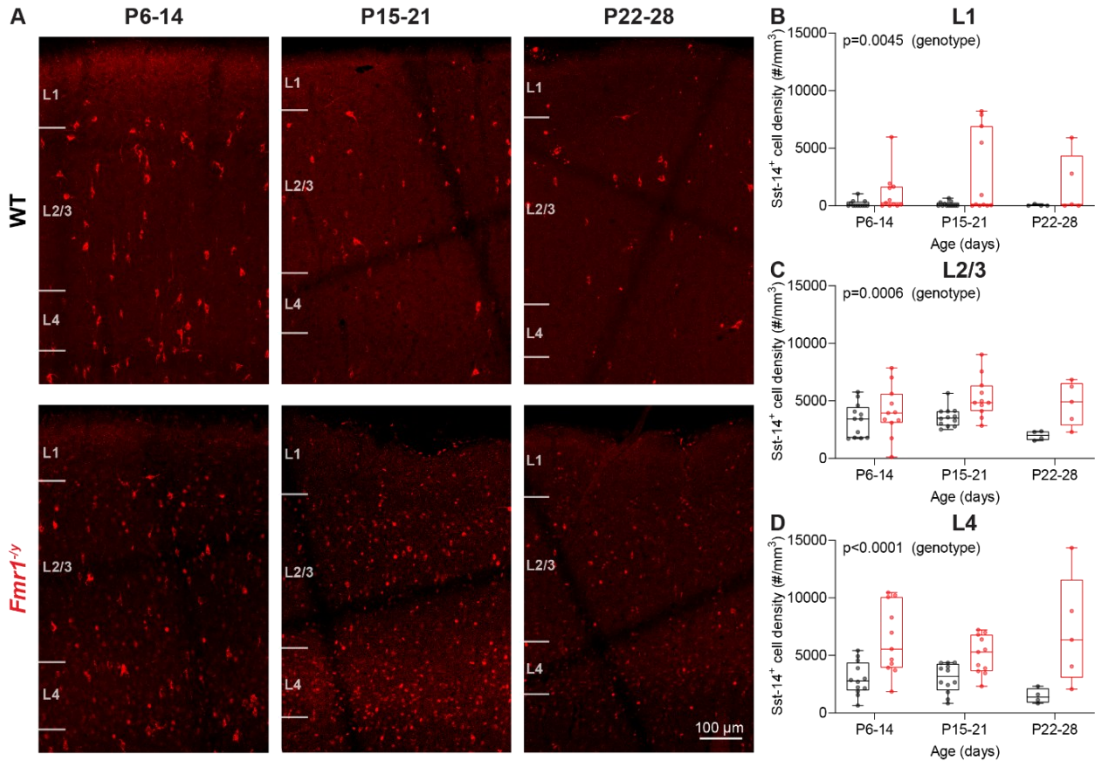

Figure 4.5. *Fmr1*$^{-/y}$ have an increased Sst-14^{+} cell density during development. A. Representative Sst-14^{+} cell density images from WT and *Fmr1*$^{-/y}$ S1 at P6-28. **B.** *Fmr1*$^{-/y}$ have an increased Sst-14^{+} cell density in L1 of S1 (2-way ANOVA; age: F=0.92, p=0.41; genotype: F=8.86, p=0.0045; age × genotype: F=1.01, p=0.37). **C.** L2/3 Sst-14^{+} cell density is increased in *Fmr1*$^{-/y}$ rats (2-way ANOVA; age: F=1.96, p=0.15; genotype: F=13.28, p=0.0006; age × genotype: F=1.34, p=0.27). **D.** L4 Sst-14^{+} cell density is increased in *Fmr1*$^{-/y}$ rats (2-way ANOVA; age: F=0.45, p=0.64; genotype: F=29.97, p<0.0001; age × genotype: F=2.07, p=0.14). WT: N=28 animals; *Fmr1*$^{-/y}$: N=27 animals. Presented data also include a subset of Sst-14+ cell counts performed by Abbi Crichton under my supervision during her undergraduate Honours project.

4.4 Discussion

In this chapter I investigated the anatomical characteristics of the developing S1 in WT and *Fmr1*$^{-/y}$ rats to test the hypothesis that the loss of FMRP disrupts the typical development of S1 in the rat model of FXS. As such, I reconstructed the dendritic arbours of L4 SCs of WT and *Fmr1*$^{-/y}$ rats at P9-28. Sholl analysis of the reconstructed neurons revealed an age-dependent reduction in dendritic complexity that was specific to the P9-14 group. I found no change in dendritic spine density during development.

In order to address the development of the inhibitory cytoarchitecture in the rat model of FXS I examined the densities and distribution of specific subclasses of interneurons in the upper layers (L1-4) of S1 in WT and *Fmr1*$^{-/y}$ rats during the first postnatal month. While the density of cells expressing PV and reelin was unchanged, I found that *Fmr1*$^{-/y}$ rats have a significantly higher density of cells expressing Sst-14. The main findings of this chapter are summarized in Table 4.1.

Table 4.1. Summary of Chapter 4 results.

Age	1-2 weeks	2-3 weeks	3-4 weeks	4-5 weeks
Dendritic complexity	↓	=	=	?
Spine density	=	=	=	=
PV$^+$ cell density	N/A	=	=	=
Reelin$^+$ cell density	=	=	=	?
Sst-14$^+$ cell density	↑	↑	↑	?

4.4.1 Morphology

Dendritic arbour reconstructions of L4 SCs revealed that dendrite length, Sholl peak and total intersections increase with age, reflective of a developmental increase in dendritic complexity. At the same time, Sholl span shows no effect of age, suggesting that while the extent of the dendritic arbour does not change with age, the dendrites themselves become longer and denser during development. While no statistically significant genotype effects were found in other measures of cellular morphology (e.g. dendrite number or length), a reduction in the Sholl distribution at

P9-14 could indicate subtle deficits in the dendritic morphology of *Fmr1*$^{-/y}$ L4 SCs. As this effect was only seen at P9-14, with no changes in Sholl distribution or other measures at the later stages of development, it is likely reflective of a developmental delay in the *Fmr1*$^{-/y}$ rats.

In the previous chapter I have characterized the electrophysiological properties of *Fmr1*$^{-/y}$ L4 SCs during development and found that they are hyperexcitable at specific developmental periods – P9-12 and P25-28. Here, I inquired whether such increased excitability could have a basis in the morphological characteristics of *Fmr1*$^{-/y}$ L4 SCs. Although not statistically significant, the mean C_m was 16% lower in the *Fmr1*$^{-/y}$ at P9-12 (Chapter 3). As membrane capacitance is correlated with neuronal size (Golowasch *et al.*, 2009), such a reduction could be indicative of a smaller, more electrically compact cell, in agreement with the reduced dendritic complexity described here. Indeed, as input resistance is inversely proportional to membrane capacitance, a reduction in dendritic complexity can be expected to result in a higher input resistance, and in consequence – hyperexcitability. Therefore, I propose that a delay in the morphological development of *Fmr1*$^{-/y}$ SCs could underlie their hyperexcitability during the second postnatal week. Whether delayed morphological development is causal to the intrinsic hyperexcitability of *Fmr1*$^{-/y}$ L4 SCs could be tested with whole-cell patch clamp recordings following chemogenetic stimulation of neuronal activity in early life, which can accelerate the development of dendritic complexity (Köhler *et al.*, 2025). As the morphology catches up to WT levels during the third postnatal week, so does the intrinsic excitability. However, after P25 the hyperexcitability of *Fmr1*$^{-/y}$ L4 SCs re-emerges, despite their typical morphology. Therefore, this second period of hyperexcitability likely occurs due to an unrelated process.

Previous investigations of L4 SC dendritic morphology have shown no difference in the *Fmr1*$^{-/y}$ mice (Harlow *et al.*, 2010; Till *et al.*, 2012), although an age-dependent deficit in the asymmetry of the dendritic arbour was found. In mouse S1, mature L4 SCs typically have asymmetrical dendrites projecting into the barrel hollows and somata positioned around the barrel septa. Crucially, in both mice and rats, thalamocortical inputs into the barrel cortex are anatomically segregated,

forming the basis of one-to-one topographical mapping between individual whiskers and their corresponding barrels (Greenough and Chang, 1988). A reduction in dendritic asymmetry could therefore affect the integration of dendritic inputs, as the dendrites of individual SCs cross over into the neighbouring barrel more frequently (Galvez, Gopal and Greenough, 2003), thus receiving more varied inputs from multiple whiskers. Indeed, somatosensory map expansion and a reduction in whisker selectivity has been found in the *Fmr1*$^{-/y}$ mice, leading to disrupted processing of sensory inputs in the S1 (Juczewski *et al.*, 2016). As dendritic asymmetry has not been assayed in this thesis, it is unclear whether it is similarly affected in the *Fmr1*$^{-/y}$ rats.

Notably, in the presented dataset, only dendritic arbours of L4 SCs were reconstructed. As the neurons were filled with biocytin during whole-cell patch clamp recordings in cortical slices, most of the reconstructed cells were positioned close to the surface of the slice, allowing better access for electrophysiological recordings. Consequently, while cells with incomplete dendritic arbours were excluded from this analysis, the axons of the remaining cells were mostly incomplete, or even fully severed. While the axonal arbours of L4 SCs have not been extensively studied in the *Fmr1*$^{-/y}$ mice, Bureau, Shepherd and Svoboda (2008) found that *Fmr1*$^{-/y}$ L4 SCs have more diffuse axonal projections in L2/3. The synaptic strength of these connections was not affected in the *Fmr1*$^{-/y}$, but the connection probability between L4 and L2/3 was reduced. Considering that FMRP plays a role in axon guidance and outgrowth (Antar *et al.*, 2006; Li, Bassell and Sasaki, 2009; Zhang *et al.*, 2015; Marfull-Oromí *et al.*, 2023), it would be interesting to investigate the axonal domain of L4 SCs in *Fmr1*$^{-/y}$ rats to verify whether it is similarly affected in the rats. As the main axonal projection of L4 SCs is in L2/3 (Egger, Nevian and Bruno, 2008), changes at this level could have consequences for the downstream processing of sensory inputs.

In summary, while *Fmr1*$^{-/y}$ L4 SCs show a reduction in their dendritic complexity at P9-14, this deficit is transient and not present in later development. At the same time, none of the other measures of neuronal morphology showed a genotype difference, suggesting that the changes in Sholl distribution might be too subtle to be reflected in broader measures such as total dendritic length.

4.4.2 Spine density

In agreement with the typical excitatory synaptic properties of *Fmr1*$^{-/y}$ L4 SCs (Chapter 3), I found no change in the density of dendritic spines in the *Fmr1*$^{-/y}$ rats during development. An increase in the dendritic spine density has been described in the cortex of FXS individuals (Irwin *et al.*, 2001). In the *Fmr1*$^{-/y}$ mice however, this appears to be dependent on the cell type and brain area studied. L2/3 temporal cortex pyramidal neurons and L5 pyramidal neurons in the visual cortex of *Fmr1*$^{-/y}$ mice were shown to have an increased spine density (Comery *et al.*, 1997; Dolan *et al.*, 2013). Hippocampal CA1 PCs of *Fmr1*$^{-/y}$ rats have an increased apical, but not basal dendritic spine density (Till *et al.*, 2015), similar to the S1 L5 PCs of *Fmr1*$^{-/y}$ mice. However, no changes have been found in the dendritic spine density of *Fmr1*$^{-/y}$ mouse S1 L4 SCs during the first and second postnatal weeks (Harlow *et al.*, 2010; Till *et al.*, 2012). It is worth noting however, that dendritic spines can vary in their size and shape, which has previously been suggested to be related to their function (Ultanir *et al.*, 2007; Oh, Hill and Zito, 2013). As such, several studies have found changes in spine morphology in post mortem brains of FXS individuals as well as *Fmr1*$^{-/y}$ mice. The proportion of thin, long dendritic spines is increased in the cortex of FXS individuals (Wisniewski *et al.*, 1991; Irwin *et al.*, 2001). Likewise, an increase in the proportion of 'immature' (filopodia) dendritic protrusions was found at the expense 'mature' (mushroom-like) spines in L4 SCs of juvenile *Fmr1*$^{-/y}$ mice (Till *et al.*, 2012). In contrast, (Galvez and Greenough, 2005) found that spine density and proportion of spines with 'immature' morphologies is only increased in L5 neurons of adult, but not juvenile *Fmr1*$^{-/y}$ mice. This could be in part due to higher dendritic spine turnover rates and a higher proportion of transient spines, which has been found in adult *Fmr1*$^{-/y}$ mouse L5 neurons, indicating instability (Pan *et al.*, 2010). Altered spine morphology could also be related to NMDAR function, as the spine head volume increases when the GluN1 subunit of the NMDAR is knocked out, effectively preventing all NMDAR expression (Ultanir *et al.*, 2007). In contrast, *Fmr1*$^{-/y}$ mice could present the opposite scenario, with smaller spines and a higher NMDA:AMPA ratio (Harlow *et al.*, 2010; Till *et al.*, 2012). Notably, both NMDAR subunits GluN2a and GluN2b are direct targets of FMRP and thus likely to be upregulated in the *Fmr1*$^{-/y}$

mice (Darnell *et al.*, 2011). However, it is worth noting that many studies examining dendritic spine morphologies use inappropriate imaging methods which are unable to sufficiently resolve such microscopic structures (B.-Z. Li *et al.*, 2023). Therefore, it is crucial that these findings are revisited with the use of super-resolution, expansion or electron microscopy before any conclusions can be made about the morphology of dendritic spines in an FMRP-deficient brain. For example, Booker *et al.* (2019) used electron microscopy to find no change in spine density or morphology, but instead an increased incidence of multi-innervated spines i.e., spines receiving more than one excitatory synaptic contact, in juvenile *Fmr1*$^{-/y}$ mice. As such, there are many conflicting reports, suggesting that changes in spine density and morphology in the *Fmr1*$^{-/y}$ mice could be cell type- and age-dependent, or not present at all. Moreover, spine turnover i.e., generation and elimination of dendritic spines, is not affected by sensory deprivation in the *Fmr1*$^{-/y}$ mice, indicating that their dendritic spines are less responsive to changes in sensory experience (Pan *et al.*, 2010). Such a deficit could thus impair the ability of cortical circuits to appropriately adapt to variable stimulation.

Overall, alterations to dendritic spine structure and function could affect the ability of neurons to integrate synaptic inputs, which is known to be altered in the *Fmr1*$^{-/y}$ mice, leading to excessive summation of inputs (Booker *et al.*, 2019; Domanski *et al.*, 2019). Therefore, while I found no evidence of broad changes in dendritic spine density during L4 SC development in *Fmr1*$^{-/y}$ rats, detailed measures such as spine morphology and turnover warrant further investigation.

4.4.3 Interneuron density

Inhibitory interneurons play a crucial role in controlling and synchronizing cortical activity (Cardin *et al.*, 2009). It has been proposed that the loss of FMRP disrupts cortical function by changing the E/I balance (Gibson *et al.*, 2008; Domanski *et al.*, 2019). In addition to the hyperactivity of excitatory neurons, ineffective or mistimed cortical inhibition has been found in the *Fmr1*$^{-/y}$ mice, thus contributing to circuit-level hyperexcitability (Gibson *et al.*, 2008; Domanski *et al.*, 2019; Cea-Del Rio *et al.*, 2020). Likewise, in the previous chapter I showed that L4 SCs of *Fmr1*$^{-/y}$ rats are

hyperexcitable during development. This could drive some interneurons to upregulate their activity in order to stabilize the cortical output. As the final determination of interneuron density in the cortex is driven by activity-dependent apoptosis in the second postnatal week (Southwell *et al.*, 2012; Priya *et al.*, 2018), I hypothesized that such hyperexcitability would disrupt the interneuron diversity in the rat S1, thus contributing to the atypical developmental trajectory of the rat S1 in the absence of FMRP. An investigation of interneuron populations in WT and *Fmr1*$^{-/y}$ rats revealed no change in the densities of PV^{+} and reelin^{+} cells, but a significant increase in Sst-14^{+} cells, suggesting that changes in interneuron diversity could be restricted to a specific class of interneurons. This increase was present in all cortical layers tested, and persisted throughout development.

Reelin^{+} cells are primarily neurogliaform cells (Rudy *et al.*, 2011), which are known to form connections not only with pyramidal cortical neurons, but also other interneurons, including PV^{+} fast-spiking interneurons (Simon *et al.*, 2005). Through targeted dendritic inhibition and disinhibitory feedback onto PV^{+} interneurons, neurogliaform neurons play an important role in dendritic integration in the somatosensory cortex (Chittajallu, Pelkey and McBain, 2013). To my knowledge, no study has reported changes in the abundance or function of reelin^{+} interneurons in *Fmr1*$^{-/y}$ animals, while dendritic integration is known to be excessive in *Fmr1*$^{-/y}$ mice (Domanski *et al.*, 2019). Therefore, it is unlikely that the reelin^{+} cell population is driving these deficits in the *Fmr1*$^{-/y}$ cortex.

The density of PV^{+} cells as well as their precursors has previously been found to be decreased in the cingulate cortex, motor cortex and S1 of *Fmr1*$^{-/y}$ mice and in FXS individuals (Selby, Zhang and Sun, 2007; Lee *et al.*, 2019; Kourdougli *et al.*, 2023). In contrast, my data indicates no change in the PV^{+} cell population in the S1 of *Fmr1*$^{-/y}$ rats, suggesting that some interneuron diversity changes in an FMRP-deficient cortex could be species-dependent. In *Fmr1*$^{-/y}$ mice, a decrease in PV interneuron density is underlain by their hypoactivity in early development (Kourdougli *et al.*, 2023). As PV interneuron function has not been explicitly tested in *Fmr1*$^{-/y}$ rats, it is unclear whether they are likewise functionally deficient. Indeed, the function and maturation of PV interneurons may be differentially affected by the loss of FMRP

across species, including mice and rats. Alternatively, the timing of PV interneuron maturation and hypoactivity may not be conserved between species, such that they are not coincident with the elimination of excess interneurons in rats, thus resulting in the typical PV interneuron density observed here. Furthermore, as PV^+ cell density was only tested in later development, it is unclear whether the onset of PV expression is comparable between WT and *Fmr1*$^{-/y}$ animals. Considering that PV is expressed in an activity-dependent manner (Moissidis *et al.*, 2025), and that PV interneurons were previously found to be hypoactive in *Fmr1*$^{-/y}$ mice (Goel *et al.*, 2018; Domanski *et al.*, 2019; Kourdougli *et al.*, 2023), it is possible that PV expression is developmentally delayed in the absence of FMRP.

In addition to a decrease in the density and activity of PV^+ cells, Kourdougli *et al.* (2023) found an increase in the density of Sst^+ interneurons and a transcriptomic upregulation of *Sst* in the S1 of juvenile and adult *Fmr1*$^{-/y}$ mice. As PV^+ and Sst^+ interneuron classes are both derived from the medial ganglionic eminence (MGE) during embryonic development, (Kourdougli *et al.*, 2023) suggested that an increase in Sst^+ interneurons could arise as a compensatory mechanism due to the hypoactivity of PV^+ interneurons. PV-expressing interneurons are typically fast-spiking cells that provide FFI in cortical circuits (Rudy *et al.*, 2011; Delevich *et al.*, 2015). Indeed, FFI has been found to be dysfunctional in the *Fmr1*$^{-/y}$ mice, with reduced connectivity between fast-spiking interneurons and L4 SCs and altered, ineffective FFI in the developing barrel cortex of *Fmr1*$^{-/y}$ mice (Domanski *et al.*, 2019). As inhibitory function is not addressed in this thesis, it is unclear whether similar changes to FFI are present in the *Fmr1*$^{-/y}$ rats. If so, they would likely be driven by altered electrophysiological properties of PV^+ INs, rather than their lower abundance in the cortex. Additionally, Kourdougli *et al.* speculate that an increase in the Sst^+ population could come at the expense of MGE-derived interneurons that would have otherwise become PV^+, thus explaining the deficit in PV^+ cell density. The data presented in this chapter appear to directly contradict this hypothesis, as no changes in the PV^+ cell density were found despite an increase in Sst^+ cells. Whether PV^+ interneurons are functionally impaired in *Fmr1*$^{-/y}$ rats and thus unable to respond to changes in activity in the developing S1 remains uncertain. Instead, increased

Sst-14$^+$ cell density likely plays a compensatory role to stabilize the network output in response to L4 SC hyperexcitability. Sst$^+$ interneurons might be preferentially selected to control activity in the circuit, as the expression of Sst receptors is known to increase immediately following seizure activity in order to effectively counteract hyperexcitability in the brain (Iwasawa, Narita and Tamura, 2019). Moreover, an increase in Sst-14$^+$ cell density may not be restricted to the interneuron population. Although Sst expression is not typically found in excitatory neurons, it may be induced in response to high levels of activity, such as chemically-evoked seizures (Hashimoto and Obata, 1991). As such, it is possible that the intrinsic hyperexcitability of S1 neurons could be sufficient to induce ectopic Sst expression in excitatory neurons. While at the transcriptomic level Sst expression was only found in the interneuron population (Chapter 6), the identity of Sst-expressing cells could be verified further by investigating the co-expression of Sst-14 with interneuron markers such as VGAT.

An increase in Sst-expressing cells raises interesting questions for the function of S1 in *Fmr1*$^{-/y}$ rats. Typically, Sst$^+$ interneurons release Sst in addition to GABA as an inhibitory neurotransmitter (Morrison *et al.*, 1983; Tapia-Arancibia and Astier, 1989). Sst then exerts its functions by binding onto somatostatin receptors (SSTR), which exist in 5 distinct isoforms (Schulz *et al.*, 2000). While it is unclear whether Sst signalling is upregulated in the *Fmr1*$^{-/y}$ rats, an increase in Sst release could have significant repercussions for cortical function. Excitatory neurons in the cortex express two SSTR isoforms postsynaptically - SSTR2 and SSTR4, both of which are G-protein coupled receptors that function by inhibiting adenylate cyclase (Patel *et al.*, 1994; Schulz *et al.*, 2000). Therefore, an increase in Sst signalling could lead to lower cAMP levels in L4 SCs. A reduction in the levels of cAMP is a well-described phenotype of FXS individuals that is conserved across species (Berry-Kravis, Hicar and Ciurlionis, 1995; Kelley *et al.*, 2007), that arises as a result of several phosphodiesterases (PDEs) being direct targets of FMRP (Darnell *et al.*, 2011). However, decreased cAMP has been shown to directly contribute to L4 SC hyperexcitability through its effects on I_h current (Booker *et al.*, 2019). Therefore, a specific increase in Sst$^+$ interneuron density could play a role in stabilizing the activity of L4 SCs, but an associated increase in Sst signalling could further exacerbate their intrinsic hyperexcitability (Figure 4.6). While

I did not find definitive evidence of I_h deficits in the *Fmr1*$^{-/y}$ rats, future work should address the role of Sst-mediated signalling to elucidate whether it arises as a compensatory mechanism that could play a role in cortical hyperexcitability during development. Furthermore, in addition to inhibiting adenylate cyclase, Sst signalling mediates dendritic inhibition by activating K^+ conductance via GIRK1 channels and inhibiting Ca^{2+} currents, as well as influencing gene expression downstream of GPCR activation via cAMP/MAPK signalling (see Section 1.4), leading to long-term suppression of neuronal activity, and even morphological changes such as a reduction in dendritic spine density (Chen *et al.*, 1990; Kreienkamp, Hönck and Richter, 1997; Schweitzer, Madamba and Siggins, 1998; Hou and Yu, 2013).

However, it is important to note that Sst expression is itself activity-dependent and induced through the cAMP/PKA/CREB pathway (Montminy *et al.*, 1986; Sánchez-Muñoz *et al.*, 2010). Thus, increased activity and reduced cAMP levels in Sst^+ interneurons could regulate Sst-mediated signalling in opposite directions. As such, a detailed investigation of Sst^+ interneuron function is necessary to identify the mechanisms driving this upregulation of Sst expression in the cortex. For example, extracellular field recordings combined with optogenetic stimulation of Sst interneurons and targeted pharmacology to inhibit Sst signalling (e.g., Sst receptor antagonist cyclosomatostatin) could be used to elucidate the role of Sst-mediated signalling in cortical dysfunction of *Fmr1*$^{-/y}$ rats.

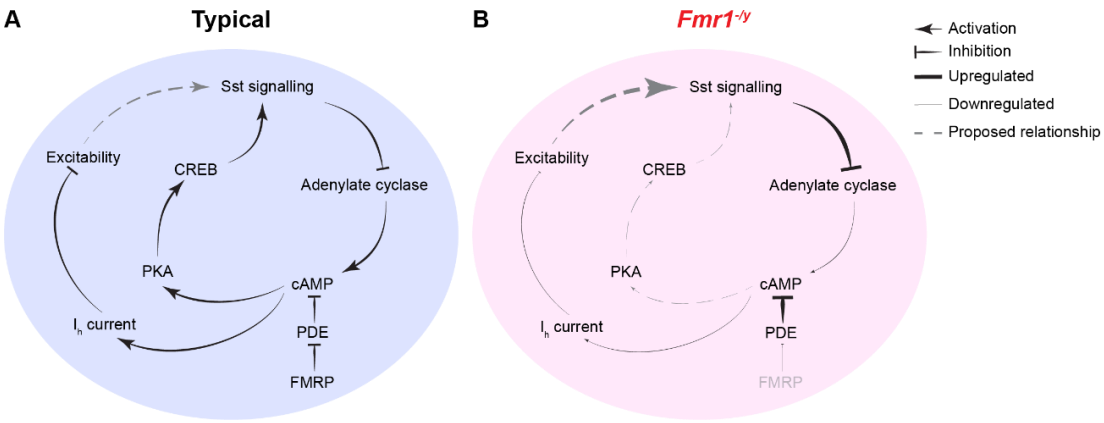

Figure 4.6. Diagram of proposed mechanism of Sst signalling in FXS. A. In a typical brain FMRP regulates cAMP levels through PDE. cAMP then affects Sst signalling via the PKA/CREB pathway. Additionally, I_h current is dependent on cAMP levels and contributes to typical excitability in neurons. Sst signalling could be induced with neuronal activity, inhibiting adenylate cyclase and thus further regulating cAMP. **B.** In the *Fmr1*$^{-/y}$, the loss of FMRP leads to excessive degradation of cAMP by PDE. A reduction in cAMP contributes to decreased I_h current, leading to hyperexcitability. Such hyperexcitability could drive an upregulation of Sst signalling and excessive inhibition of adenylate cyclase. This in turn would further decrease cAMP levels. However, reduced cAMP signalling could downregulate Sst expression through the PKA/CREB pathway.

It is worth mentioning that the three subtypes investigated in this chapter are not necessarily distinct classes of interneurons, as some degree of overlap in the expression of markers can occur. For example, reelin$^+$ interneurons have been found to also express neuropeptide Y, PV, Sst, calbindin and others (Pohlkamp *et al.*, 2014). The tendency towards an increase in the density of L2/3 reelin$^+$ interneurons could thus represent an increase in the reelin$^+$ interneurons which also co-express Sst. Similarly, a subset of PV$^+$ interneurons co-expresses Sst (Rudy *et al.*, 2011). Nevertheless, this overlap is unlikely to affect the overall conclusions as only one subtype was affected in the presented dataset.

In summary, I found that while interneuron diversity is altered during S1 development of *Fmr1*$^{-/y}$ rats, this is specific to the Sst$^+$ subtype, rather than presenting a broad change in all interneuron populations. Future work should address whether cell-type specific changes in interneuron populations are also associated with inhibitory dysfunction, contributing to an altered developmental trajectory in the *Fmr1*$^{-/y}$ rats.

4.4.4 Summary

The data presented in this chapter support the hypothesis that the loss of FMRP leads to an altered developmental trajectory in the rat S1. This occurs in the form of both transient and permanent anatomical changes in the cortex, in addition to the elevated intrinsic hyperexcitability discussed in the previous chapter. Like the physiological changes, these are established in early development and could have consequences for cortical function. A reduction in the dendritic complexity of *Fmr1*$^{-/y}$ L4 SCs co-occurs with their hyperexcitability and could directly underlie it. Similarly, the inhibitory cytoarchitecture is disrupted in the absence of FMRP, possibly as a compensatory mechanism in order to normalize the output of a hyperexcitable circuit. While the morphological deficit of L4 SCs is transient, the increase in Sst-14^{+} cell density persists throughout development. As the activity-dependent pruning of excess interneurons occurs only during the second postnatal week (Southwell *et al.*, 2012; Priya *et al.*, 2018), such changes in inhibitory cytoarchitecture could become permanent during development and remain into adulthood. While elevated cortical excitability could be pharmacologically targeted, anatomical changes such as an increased interneuron density would likely not be corrected with treatment in adulthood, thus limiting its efficacy. This could have significant implications for potential treatment options for FXS, suggesting that early treatment, before such changes are solidified during development, could provide a more effective, long-term rescue. Furthermore, the phenotypes identified in this chapter, i.e. reduced dendritic complexity and elevated Sst-14^{+} cell density could be used as biomarkers when evaluating the effectiveness of potential therapeutic interventions preclinically to ensure a consistent and multimodal rescue of disease-relevant phenotypes.

Overall, the data presented in this chapter paint a more complex picture of cortical dysfunction in early development of the *Fmr1*$^{-/y}$ rats. Once again, the *Fmr1*$^{-/y}$ rats replicate some, but not all of the phenotypes previously described in the mouse model, suggesting species differences. Notably, while ineffective inhibition has frequently been reported to contribute to cortical dysfunction in the *Fmr1*$^{-/y}$ mice, it is unclear whether such deficits are likewise present in the rats. As the data presented

here point to interneurons being affected by the loss of FMRP, inhibitory function in the cortex of *Fmr1*$^{-/y}$ rats should be explored further. Future work should also address whether an increase in Sst-14^{+} cell density translates into elevated Sst signalling, which could become a maladaptive mechanism further driving the FMRP-deficient neurons into hyperexcitability.

Chapter 5

Pharmacological rescue of *Fmr1*$^{-/y}$ L4 SC development through BPN14770 treatment

5.1 Introduction

Despite extensive research into the pathophysiology of FXS, currently there are no FDA-approved targeted treatments for FXS (Berry-Kravis *et al.*, 2018; Lee *et al.*, 2018). As such, FXS individuals often receive medication aimed at managing the associated symptoms, such as inattention, aggression, seizures, anxiety or sleep problems, rather than their underlying mechanisms (Hagerman *et al.*, 2009; Lee *et al.*, 2018). Several treatments that have shown a rescue of behavioural and physiological deficits in *Fmr1*$^{-/y}$ mice (e.g. arbaclofen, mavoglurant) have later failed when tested in clinical trials against placebo (reviewed in Berry-Kravis *et al.,* 2018). Therefore, it is crucial to better understand the mechanisms through which cortical dysfunction emerges in development and effectively target it therapeutically, as it can underlie a wide range of symptoms in FXS individuals.

A reduction in cAMP levels is a common feature shared across several models of FXS, including drosophila and mouse, as well as FXS individuals (Berry-Kravis, Hicar and Ciurlionis, 1995; Kelley *et al.*, 2007). Several isoforms of phosphodiesterases (PDEs), which degrade cAMP, are direct targets of FMRP (Darnell *et al.*, 2011). In an FMRP-deficient brain, PDEs such as PDE2A are upregulated and overactive, leading to a decrease in available cAMP (Maurin *et al.*, 2018, 2019). As such, addressing the cAMP reduction, most commonly through PDE inhibitors, has been proposed as a potential treatment for FXS in a so-called cAMP theory of FXS (Kelley *et al.*, 2008;

Bardoni, Gwizdek and Maurin, 2025). Indeed, restoring cAMP levels has been shown to rescue long-term memory deficits in the drosophila model of FXS as well as hippocampal synaptic plasticity and novel object recognition in *Fmr1*$^{-/y}$ mice (Choi *et al.*, 2016; Costa *et al.*, 2018). However, non-specific PDE inhibitors which showed promising results preclinically (e.g. rolipram) have significant gastrointestinal side effects which precluded their use in FXS individuals (Berry-Kravis, 2022). As such, it was suggested that PDE inhibitors specific to brain-dominant isoforms could confer therapeutic benefits while avoiding the gastrointestinal side effects. PDE4D is an isoform of the cAMP-specific PDE4 which is highly expressed throughout the brain, particularly the cerebral cortex and hippocampus, with a role in cognitive functions such as learning and memory (Pérez-Torres *et al.*, 2000; Lakics, Karran and Boess, 2010; Choi *et al.*, 2016; Wakabayashi *et al.*, 2020). Thus, the PDE4D-specific allosteric inhibitor, BPN14770 has been proposed as a potential treatment for FXS (Gurney *et al.*, 2019). In *Fmr1*$^{-/y}$ mice, BPN14770 rescues deficits in behaviours such as marble burying, nesting and social interactions, with detectable improvements even 2 weeks after the original treatment (Gurney *et al.*, 2017; Rosenheck *et al.*, 2021), suggesting that BPN14770 could produce lasting effects on cellular and circuit-level function. BPN14770 has been tested in adult FXS individuals in a randomized, double blind phase 2 clinical trial, where it showed improvement in cognitive performance and no severe adverse effects (Berry-Kravis, Harnett, *et al.*, 2021). As this study included a crossover design, persistent effects were found lasting beyond the original treatment period, suggesting that similarly to *Fmr1*$^{-/y}$ mice, BPN14770 could provide a more long-lasting rescue in FXS individuals than previously expected.

In Chapters 3 and 4 I have identified changes in the developmental trajectory of the somatosensory cortex in *Fmr1*$^{-/y}$ rats. These include intrinsic hyperexcitability and morphology deficits in L4 SCs that are already present during the second postnatal week. However, it is unclear what role these early life changes play in the emergence of cortical dysfunction in later development. As reduced cAMP has been shown to contribute to L4 SC hyperexcitability in *Fmr1*$^{-/y}$ mice (Zhang *et al.*, 2014; Booker *et al.*, 2019), I hypothesize that increasing endogenous cAMP levels could rescue L4 SC hyperexcitability in *Fmr1*$^{-/y}$ rats. Therefore, in this chapter I will test the

hypothesis that the altered developmental trajectory in *Fmr1*$^{-/y}$ rats is amenable to therapeutic intervention through a brief administration of the PDE4D inhibitor, BPN14770 in the first postnatal week. Additionally, I will assess whether this early life intervention can provide long-term benefits and restore the typical development of L4 SCs in the *Fmr1*$^{-/y}$ rats.

5.2 BPN14770 treatment partially corrects *Fmr1*$^{-/y}$ development at P10-14

5.2.1 *Fmr1*$^{-/y}$ L4 SC depolarization block but not passive intrinsic properties are rescued by BPN14770 treatment

Having characterized the electrophysiological properties of L4 SCs during development, I have identified that hyperexcitability and changes in the intrinsic properties of *Fmr1*$^{-/y}$ rats are present from the earliest developmental stages tested i.e., P9-12 and undergo developmental regulation (Chapter 3). In order to determine whether a brief, early treatment with BPN14770 can rescue the hyperexcitability of *Fmr1*$^{-/y}$ L4 SCs during early development, BPN14770 or vehicle was administered to WT and *Fmr1*$^{-/y}$ rats through modified oral gavage daily from P5-9. BPN14770 was administered at a dose of 1 mg/kg, which was previously shown to be sufficient to significantly increase cAMP levels in WT mice (C. Zhang *et al.*, 2018). I then performed whole-cell patch clamp recordings in WT and *Fmr1*$^{-/y}$ L4 SCs at P10-14, to characterize their AP firing and intrinsic properties (Figure 5.1A). Like previously, the injection of current steps from 0 to +400 pA resulted in firing of APs in all groups (Figure 5.1B). The AP firing was increased in vehicle-treated *Fmr1*$^{-/y}$ L4 SCs. This increased firing in *Fmr1*$^{-/y}$ cells appeared to be rescued to WT levels after BPN14770 treatment (Figure 5.1C). In the vehicle-treated animals, the mean F-I slope was 28% higher in the *Fmr1*$^{-/y}$ compared to WT (Vehicle; WT: 0.081 ± 0.005; *Fmr1*$^{-/y}$: 0.104 ± 0.005). In contrast, the F-I slopes of BPN14770-treated animals the F-I slopes appeared comparable between WT and *Fmr1*$^{-/y}$ (BPN14770; WT: 0.078 ± 0.005; *Fmr1*$^{-/y}$: 0.084 ± 0.004). However, there was no significant effect of treatment or genotype and no interaction, when accounting for animal ID as a random effect (Figure 5.1D). The F-I slope decreased with age in all groups except vehicle-treated *Fmr1*$^{-/y}$, while the slope of the linear regression trended towards a significant difference between groups (Figure 5.1L), suggesting that BPN14770 treatment could restore the developmental trajectory of AP firing in *Fmr1*$^{-/y}$ L4 SCs. Similarly, I found no significant difference in rheobase between genotypes and treatments (Figure 5.1E), although rheobase increased with age in all groups except BPN14770-treated WT, with a trend towards

significance in linear regression slopes (Figure 5.1M). There was no genotype or treatment effect on the maximum number of APs fired (Figure 5.1F). Finally, the proportion of cells showing depolarization block was higher in the vehicle-treated *Fmr1*$^{-/y}$ rats compared to WT (p=0.0012). This was rescued with BPN14770 treatment, as the proportion was reduced in BPN14770-treated *Fmr1*$^{-/y}$ rats (p=0.017), with no difference between WT and *Fmr1*$^{-/y}$ in the BPN14770-treated group (p=0.43) and no effect of treatment on WT animals (p=0.58; Figure 5.1G).

I next investigated the passive intrinsic properties of L4 SCs of WT and *Fmr1*$^{-/y}$ rats after vehicle or BPN14770 treatment. The RMP was not different between genotypes, but tended to be more hyperpolarized with BPN14770 treatment (Figure 5.1H). Input resistance showed a trend towards a decrease with BPN14770 treatment, with no significant difference between the genotypes and no interaction of treatment and genotype (Figure 5.1I). The mean input resistance of L4 SCs was 16% higher in the vehicle-treated *Fmr1*$^{-/y}$ compared to WT (Vehicle; WT: 353.12 ± 22.08 MΩ; *Fmr1*$^{-/y}$: 409.32 ± 23.52 MΩ) and appeared comparable between genotypes in the BPN14770-treated group (BPN14770; WT: 326.95 ± 21.51 MΩ; *Fmr1*$^{-/y}$: 334.60 ± 19.44 MΩ). However, when input resistance was plotted by age, I found no difference in the linear regression slopes between the groups (Figure 5.1N), suggesting that input resistance does not differ between genotypes and treatments even when the animal's age is considered. The membrane time constant tended to decrease with BPN14770 but was not different between genotypes (Figure 5.1J). Finally, membrane capacitance showed a trend towards an interaction of genotype and treatment (Figure 5.1K) as it was 10% lower in the vehicle-treated *Fmr1*$^{-/y}$ rats compared to WT (Vehicle; WT: 81.02 ± 2.69 pF; *Fmr1*$^{-/y}$: 72.87 ± 3.38 pF) and comparable between genotypes when treated with BPN14770 (BPN1770; WT: 73.74 ± 3.11 pF; *Fmr1*$^{-/y}$: 78.09 ± 2.83 pF).

In conclusion, the passive intrinsic properties of L4 SCs did not significantly differ between genotypes and treatments, although BPN14770 shows a tendency towards reduced input resistance and τ_m overall and increased capacitance in the *Fmr1*$^{-/y}$ rats. Nevertheless, BPN14770 does rescue the increased proportion of cells with depolarization block in *Fmr1*$^{-/y}$ rats.

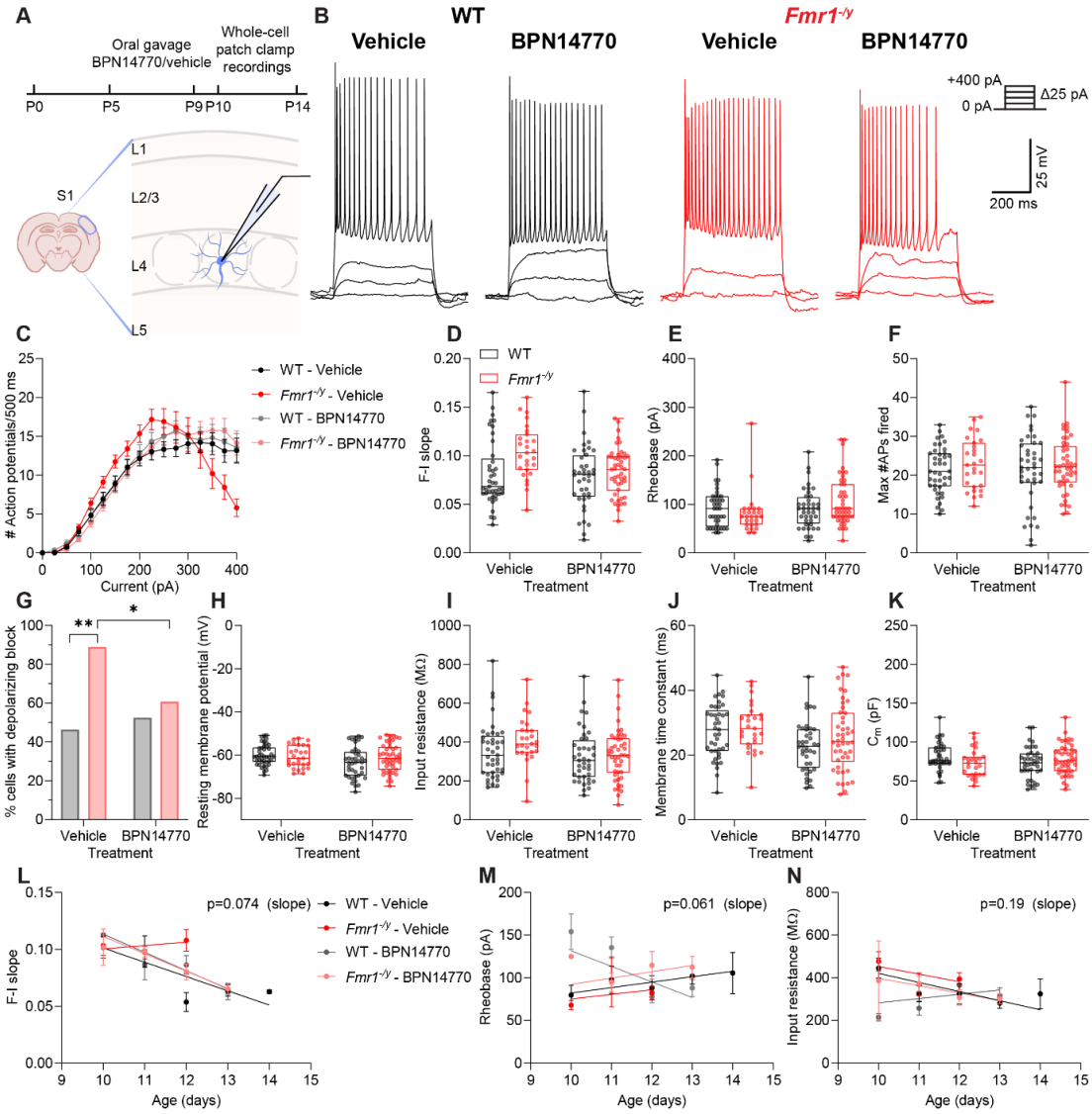
A
Oral gavage
BPN14770/vehicle
Whole-cell
patch clamp
recordings
P0
P5
P9
P10
P14
S1
L1
L2/3
L4
L5
B
WT
Fmr1-/y
Vehicle
BPN14770
Vehicle
BPN14770
+400 pA
0 pA
Δ25 pA
25 mV
200 ms
C
Action potentials/500 ms
Current (pA)
WT - Vehicle
Fmr1-/y - Vehicle
WT - BPN14770
Fmr1-/y - BPN14770
D
F-I slope
WT
Fmr1-/y
Vehicle
BPN14770
Treatment
E
Rheobase (pA)
F
Max #APs fired
G
% cells with depolarizing block
**
*
H
Resting membrane potential (mV)
I
Input resistance (MΩ)
J
Membrane time constant (ms)
K
Cm (pF)
L
F-I slope
p=0.074 (slope)
Age (days)
M
Rheobase (pA)
p=0.061 (slope)
N
Input resistance (MΩ)
p=0.19 (slope)

Figure 5.1. BPN14770 treatment rescues the depolarization block but not the intrinsic properties of *Fmr1*$^{-/y}$ L4 SCs at P10-14. A. Schematic of experimental timeline and recording setup. WT and *Fmr1*$^{-/y}$ littermate rats were dosed with vehicle or 1 mg/kg BPN14770 daily via modified oral gavage from P5-P9. Whole-cell patch clamp recordings were performed in WT and *Fmr1*$^{-/y}$ S1 L4 SCs at P10-14. **B.** Representative traces from WT (black) and *Fmr1*$^{-/y}$ L4 SCs treated with vehicle or BPN14770. Current steps were applied from 0 pA to +400 pA in 25 pA increments. **C.** Current-frequency plots suggest that *Fmr1*$^{-/y}$ L4 SCs fire more APs than WT, which is reduced with BPN14770 treatment. **D.** F-I slope shows no difference between genotypes and treatments. No interaction was found (GLMM; treatment: F=1.05, p=0.31; genotype: F=2.69, p=0.11; treatment × genotype: F=1.50, p=0.23). **E.** Rheobase did not differ between genotypes and treatments (GLMM; treatment: F=2.12, p=0.17; genotype: F=0.0098, p=0.92; treatment × genotype: F=2.68, p=0.12; log-transformed). **F.** Maximum number of APs fired was not different between genotypes and treatments (GLMM; treatment: F=0.61, p=0.81; genotype: F=0.94, p=0.34; treatment × genotype: F=0.0094, p=0.92). **G.** The proportion of cells showing depolarization block is increased in vehicle-treated *Fmr1*$^{-/y}$ (p=0.0012) and rescued with BPN14770 treatment (p=0.017) (Binomial GLM; treatment: X^2=1.46, p=0.23; genotype: X^2=7.72, p=0.0055; treatment × genotype: X^2=6.04, p=0.014). **H.** Resting membrane potential is consistent between genotypes but tends to be more hyperpolarized with BPN14770 (GLMM; treatment: F=3.58, p=0.071, genotype: F=0.57, p=0.46; treatment × genotype: F=1.75, p=0.20). **I.** Input resistance shows a tendency to decrease with BPN14770 but does not differ between genotypes (GLMM; treatment: F=3.15, p=0.08; genotype: F=1.72, p=0.20; treatment × genotype: F=0.47, p=0.50). **J.** Membrane time constant tends to decrease with BPN14770 treatment but shows no effect of genotype (GLMM; treatment: F=3.82, p=0.064; genotype: F=1.65, p=0.21; treatment × genotype: F=0.44, p=0.51). **K.** Membrane capacitance shows a trend towards an interaction between treatment and genotype (GLMM; treatment: F=0.067, p=0.80; genotype: F=0.26, p=0.61; treatment × genotype: F=3.62, p=0.069). **L.** F-I slope trends towards a difference in linear regression slope (p=0.074). **M.** Rheobase trends towards a difference in linear regression slope (p=0.061). **N.** Input resistance does not differ between the genotypes and treatments in terms of linear regression slope (p=0.19). Vehicle: WT: n=41 cells from N=10 animals; *Fmr1*$^{-/y}$: n=27 cells from N=5 animals; BPN14770: WT: n=40 cells from N=10 animals; *Fmr1*$^{-/y}$: n=46 cells from N=12 animals.

5.2.2 AP kinetics are not affected by BPN14770 treatment

In Chapter 3 I found that *Fmr1*$^{-/y}$ L4 SCs show altered active intrinsic properties, with deficits during the rising phase of the AP. Thus, I next asked whether early treatment with BPN14770 could rescue the AP kinetic properties of *Fmr1*$^{-/y}$ L4 SCs. I measured the first AP fired at rheobase in WT and *Fmr1*$^{-/y}$ L4 SCs of rats treated with either vehicle or BPN14770 (Figure 5.2A). AP phase plots suggest no difference in AP kinetics between WT and *Fmr1*$^{-/y}$ in either treatment (Figure 5.2B). V_{thresh} showed a tendency to be more depolarized in *Fmr1*$^{-/y}$ regardless of treatment, but there is no effect of treatment (Figure 5.2C). AP amplitude was not affected by treatment and did not differ between genotypes (Figure 5.2D). Similarly, the half-height duration did not differ between genotypes nor treatments (Figure 5.2E). Likewise, the rise time showed no effect of genotype and treatment (Figure 5.2F). Finally, there was no difference between genotypes and treatments in the maximum rise rate (Figure 5.2G) nor the maximum decay rate (Figure 5.2H). Overall, the data suggest no significant differences between WT and *Fmr1*$^{-/y}$ rats in terms of AP kinetics of L4 SCs, and no effect of BPN14770 treatment.

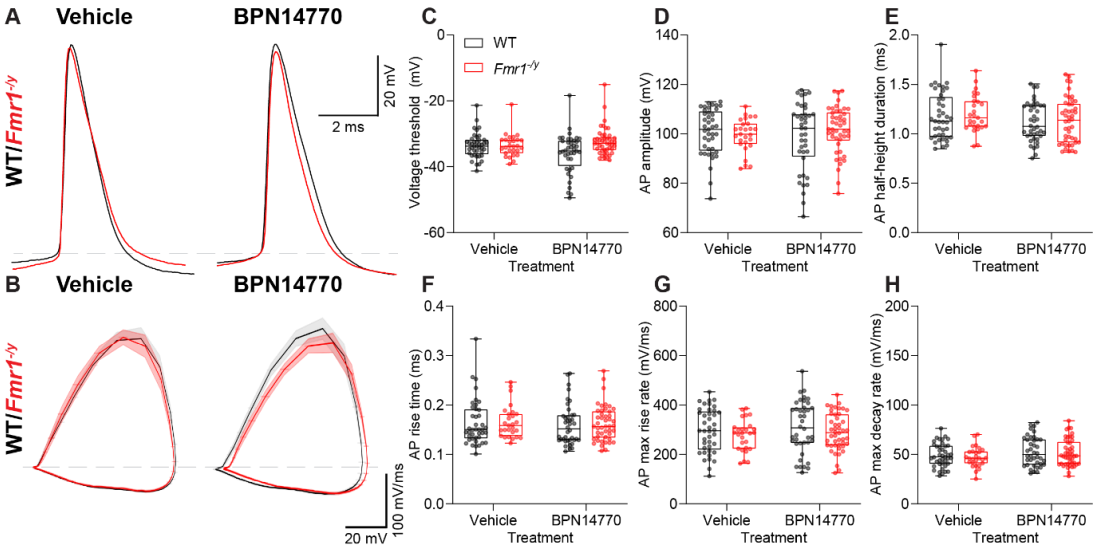

Figure 5.2. AP kinetics are not significantly affected by BPN14770 treatment at P10-14. A. Representative traces from WT (black) and *Fmr1*$^{-/y}$ (red) L4 SCs after treatment with vehicle (left) or BPN14770 (right). Grey dashed line indicates voltage threshold. **B.** AP phase plots from WT and *Fmr1*$^{-/y}$ cells treated with vehicle or BPN14770. Grey dashed line indicates baseline. **C.** Voltage threshold tends to be more depolarized in *Fmr1*$^{-/y}$ but does not differ between treatments (GLMM; treatment: F=0.29, p=0.59; genotype: F=3.43, p=0.077; treatment × genotype: F=2.55, p=0.12). **D.** AP amplitude is not affected by genotype or treatment (GLMM; treatment: F=0.014, p=0.91; genotype: F=0.39, p=0.54; treatment × genotype: F=1.23, p=0.28). **E.** AP half-height duration shows no difference between genotypes and treatments (GLMM; treatment: F=0.52, p=0.48; genotype: F=0.015, p=0.90; treatment × genotype: F=0.0091, p=0.92). **F.** AP rise time is not affected by genotype or treatment (GLMM; treatment: F=0.020, p=0.89; genotype: F=0.017, p=0.90; treatment × genotype: F=0.0024, p=0.96). **G.** AP max rise rate does not differ between genotypes and treatments (GLMM; treatment: F=0.088, p=0.77; genotype: F=0.24, p=0.63; treatment × genotype: F=0.025, p=0.88). **H.** Max decay rate is not affected by treatment and does not differ between WT and *Fmr1*$^{-/y}$ (GLMM; treatment: F=0.56, p=0.46; genotype: F=0.020, p=0.89; treatment × genotype: F=0.018, p=0.89). Vehicle: WT: n=41 cells from N=10 animals; *Fmr1*$^{-/y}$: n=27 cells from N=5 animals; BPN14770: WT: n=40 cells from N=10 animals; *Fmr1*$^{-/y}$: n=46 cells from N=12 animals.

5.2.3 BPN14770 rescues dendritic morphology of *Fmr1*$^{-/y}$ L4 SCs

In the previous chapter I discussed the reduced dendritic complexity of *Fmr1*$^{-/y}$ L4 SCs during the second postnatal week. Consequently, I inquired whether such a deficit could be amenable to therapeutic intervention with BPN14770 by reconstructing the dendritic arbours of WT and *Fmr1*$^{-/y}$ L4 SCs after treatment with vehicle or BPN14770 (Figure 5.3A). I then performed Sholl analysis and found that *Fmr1*$^{-/y}$ L4 SCs have a reduced dendritic complexity compared to WT when treated with vehicle, in agreement with Chapter 4 results. BPN14770 treatment rescued this deficit in the *Fmr1*$^{-/y}$, but reduced the dendritic complexity of WT L4 SCs. (Figure 5.3B). The total number of Sholl intersections did not differ between genotypes nor treatments (Figure 5.3C). L4 SCs showed a reduction in the Sholl peak that was rescued with BPN14770 treatment. Conversely, Sholl peak was decreased in WT when treated with BPN14770 compared to vehicle (Figure 5.3D). The Sholl span showed a tendency to increase with BPN14770 treatment, but did not differ between genotypes (Figure 5.3E). The total number of dendrites was not affected by genotype or treatment (Figure 5.3F). Finally, there was no genotype or treatment difference in the total dendritic length of L4 SCs (Figure 5.3G). These data suggest that L4 SCs have a reduced dendritic complexity in the *Fmr1*$^{-/y}$ rats, as indicated by Sholl analysis and a lower Sholl peak. BPN14770 treatment rescues this deficit, although it has the opposite effect of reducing the dendritic complexity of WT L4 SCs.

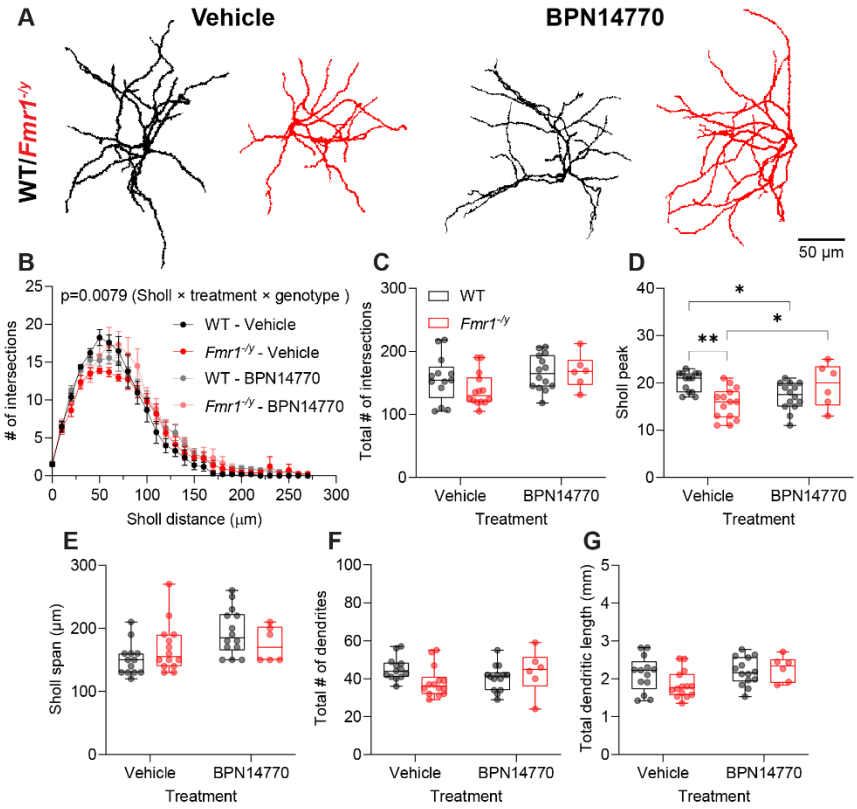

Figure 5.3. BPN14770 treatment rescues reduced dendritic complexity in *Fmr1*$^{-/y}$ L4 SCs at P10-14. A. Representative dendritic arbour reconstructions from WT (black) and *Fmr1*$^{-/y}$ (red) L4 SCs after treatment with vehicle or BPN14770. **B.** *Fmr1*$^{-/y}$ L4 SCs have reduced dendritic complexity, which is rescued with BPN14770 (3-way repeated measures ANOVA on animal average values; Sholl: F=209.5, p<0.0001; treatment: F=1.96, p=0.19; genotype: F=0.0012, p=0.97; Sholl × treatment × genotype: F=1.84, p=0.0079). **C.** Total number of Sholl intersections does not differ between genotypes and treatments (GLMM; treatment: F=2.98, p=0.11; genotype: F=0.24, p=0.63; treatment × genotype: F=0.73, p=0.41). **D.** Sholl peak is reduced in *Fmr1*$^{-/y}$ compared to WT (p=0.0039) and is rescued with BPN14770 (p=0.022). Sholl peak is reduced in WT after BPN14770 treatment (p=0.035) (GLMM; treatment: F=0.16, p=0.69; genotype: F=1.34, p=0.25; treatment × genotype: F=13.00, p=0.00080). **E.** Sholl span shows a tendency towards an increase with BPN14770 treatment (GLMM; treatment: F=4.28, p=0.057; genotype: F=0.0012, p=0.97; treatment × genotype: F=2.12, p=0.17). **F.** Total number of dendrites is not different between genotypes and treatments (GLMM; treatment: F=0.0005, p=0.98; genotype: F=0.19, p=0.67; treatment × genotype: F=1.70, p=0.22). **G.** Total dendrite length does not differ between genotypes and treatments (GLMM; treatment: F=2.63, p=0.13; genotype: F=0.23, p=0.64; treatment × genotype: F=1.27, p=0.28). Vehicle: WT: n=13 cells from N=5 animals; *Fmr1*$^{-/y}$: n=14 cells from N=4 animals; BPN14770: WT: n=14 cells from N=4 animals; *Fmr1*$^{-/y}$: n=6 cells from N=3 animals.

5.3 Early BPN14770 treatment does not rescue *Fmr1*$^{-/y}$ L4 SC hyperexcitability at P25-28

5.3.1 Intrinsic physiology of L4 SCs is minimally affected by BPN14770

Having found that BPN14770 treatment could have some beneficial effects on the AP firing and morphology of L4 SCs, I next asked whether an early intervention could provide long-lasting effects extending beyond the treatment window. In order to determine whether early BPN14770 treatment could provide a persistent rescue of *Fmr1*$^{-/y}$ hyperexcitability, I performed whole-cell patch clamp recordings in WT and *Fmr1*$^{-/y}$ L4 SCs of P25-28 rats that were treated with vehicle or BPN14770 at P5-P9 (Figure 5.4A-B). L4 SCs fired more APs in the *Fmr1*$^{-/y}$ rats regardless of treatment, in a manner consistent with hyperexcitability (Figure 5.4C). However, the F-I slope was not significantly different between the genotypes and showed no effect of treatment (Figure 5.4D). The rheobase was likewise comparable between genotypes and treatments (Figure 5.4E). On the other hand, the maximum number of APs was increased in the *Fmr1*$^{-/y}$ L4 SCs, indicating that the cells are hyperexcitable (Figure 5.4F). This was not rescued with BPN14770, as there was no effect of treatment. The resting membrane potential did not differ between genotypes nor treatments (Figure 5.4G). Input resistance was not different between WT and *Fmr1*$^{-/y}$ rats, but increased with BPN14770 treatment regardless of genotype (Figure 5.4H). There was no genotype or treatment effect on the membrane time constant (Figure 5.4I). Finally, membrane capacitance did not differ between the genotypes, but decreased with BPN14770 treatment (Figure 5.4J).

In summary, *Fmr1*$^{-/y}$ L4 SCs are hyperexcitable at P25-28, as indicated by an increase in peak firing. However, BPN14770 does not have an effect on the AP firing of L4 SCs and their passive intrinsic properties, except for input resistance and membrane capacitance, suggesting no long-term rescue of hyperexcitability.

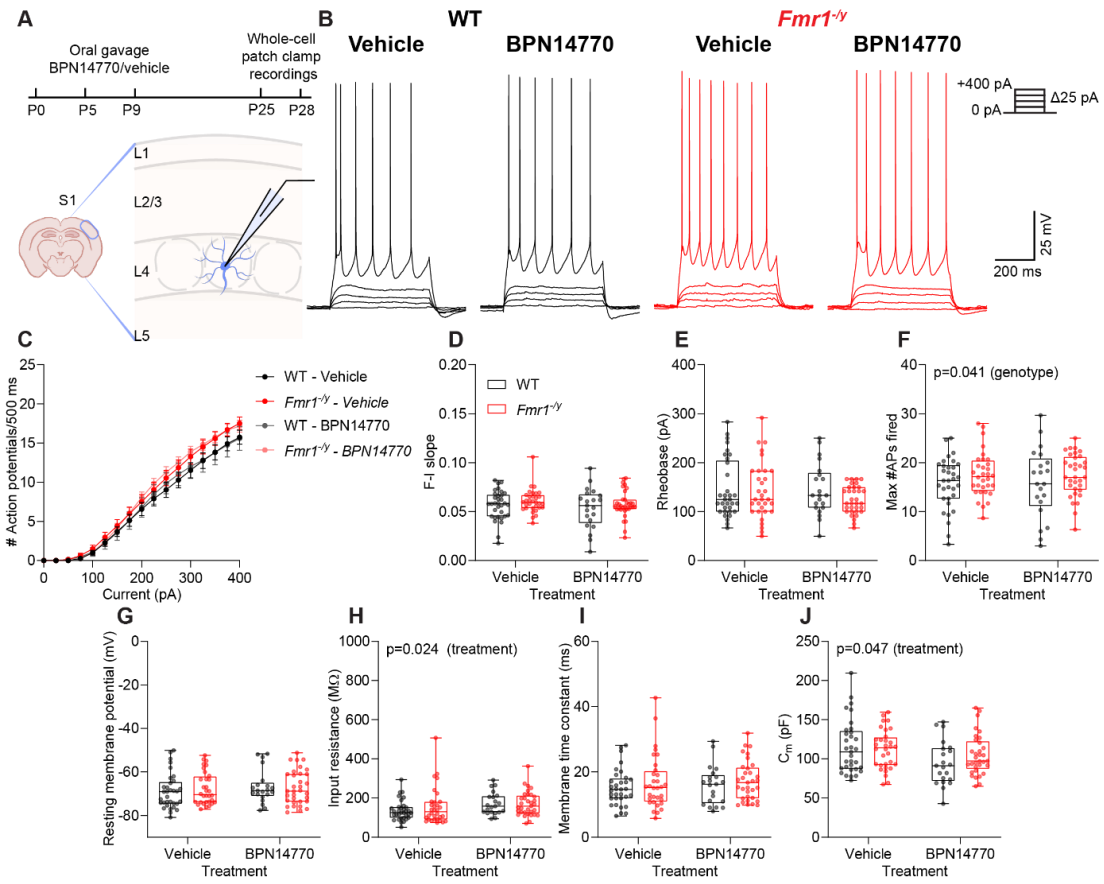

Figure 5.4. BPN14770 treatment does not rescue the AP firing and intrinsic properties of L4 SCs at P25-28. A. Schematic of experimental timeline and recording setup. WT and *Fmr1*$^{-/y}$ littermate rats were dosed with vehicle or 1mg/kg BPN14770 daily via modified oral gavage from P5-P9. Whole cell patch clamp recordings were performed in WT and *Fmr1*$^{-/y}$ L4 SCs at P25-28. **B.** Representative traces from WT (black) and *Fmr1*$^{-/y}$ (red) L4 SCs treated with vehicle or BPN14770. **C.** Current-frequency plots suggest AP firing is minimally increased in *Fmr1*$^{-/y}$ but comparable between treatments. **D.** F-I slope shows no difference between genotypes and treatments (GLMM; treatment: F=1.04, p=0.32; genotype: F=1.96, p=0.17; treatment × genotype: F=0.0095, p=0.92). **E.** Rheobase is not affected by genotype or treatment (GLMM; treatment: F=1.14, p=0.30; genotype: F=1.70, p=0.20; treatment × genotype: F=0.29, p=0.59). **F.** Maximum number of APs fired is increased in the *Fmr1*$^{-/y}$ regardless of treatment (GLMM; treatment: F=0.059, p=0.81; genotype: F=4.29, p=0.041; treatment × genotype: F=0.036, p=0.85; square root-transformed). **G.** Resting membrane potential shows no change between genotypes and treatments (GLMM; treatment: F=0.67, p=0.42; genotype: F=0.0002, p=0.99; treatment × genotype: F=0.015, p=0.90). **H.** Input resistance is increased with BPN14770 treatment regardless of genotype (GLMM; treatment: F=5.53, p=0.024; genotype: F=0.056, p=0.81; treatment × genotype: F=0.099, p=0.76; log-transformed). **I.** Membrane time constant is not affected by genotype or treatment (GLMM; treatment: F=0.56, p=0.46; genotype: F=0.57, p=0.46; treatment × genotype: F=0.090, p=0.77). **J.** Membrane capacitance decreases with BPN14770 treatment, but does not differ between WT and *Fmr1*$^{-/y}$ (GLMM; treatment: F=4.24, p=0.047; genotype: F=0.62, p=0.43; treatment × genotype: F=1.22, p=0.28; log-transformed). Vehicle: WT: n=33 cells from N=10 animals; *Fmr1*$^{-/y}$: n=32 cells from N=11 animals; BPN14770: WT: n=21 cells from N=8 animals; *Fmr1*$^{-/y}$: n=33 cells from N=10

5.3.2 AP kinetics

While BPN14770 treatment could improve some measures of *Fmr1*$^{-/y}$ L4 SC hyperexcitability at P10-14, it does not have any effect on the AP kinetics of these neurons. Thus, I next investigated the AP kinetics of vehicle- and BPN14770-treated WT and *Fmr1*$^{-/y}$ L4 SCs at P25-28 to test whether this is also the case in later development (Figure 5.5A). Phase plots suggest no changes in the AP kinetics of WT and *Fmr1*$^{-/y}$ L4 SCs. BPN14770 treatment did not appear to influence the AP dynamics in either genotype (Figure 5.5 B). Voltage threshold was not different between WT and *Fmr1*$^{-/y}$ cells and there was no effect of treatment (Figure 5.5C). Similarly, the AP amplitude (Figure 5.5D) and half-height duration (Figure 5.5E) were not affected by genotype nor treatment. The AP rise time showed a tendency towards an increase in the *Fmr1*$^{-/y}$ rats, regardless of treatment (Figure 5.5F). Finally, there was no change in the maximum rate of rise (Figure 5.5G) and decay (Figure 5.5H) between the genotypes and treatments.

Overall, with the exception of rise time, the AP kinetics do not appear to be significantly affected in the *Fmr1*$^{-/y}$ L4 SCs at P25-28, and BPN14770 treatment does not influence any of the active intrinsic properties.

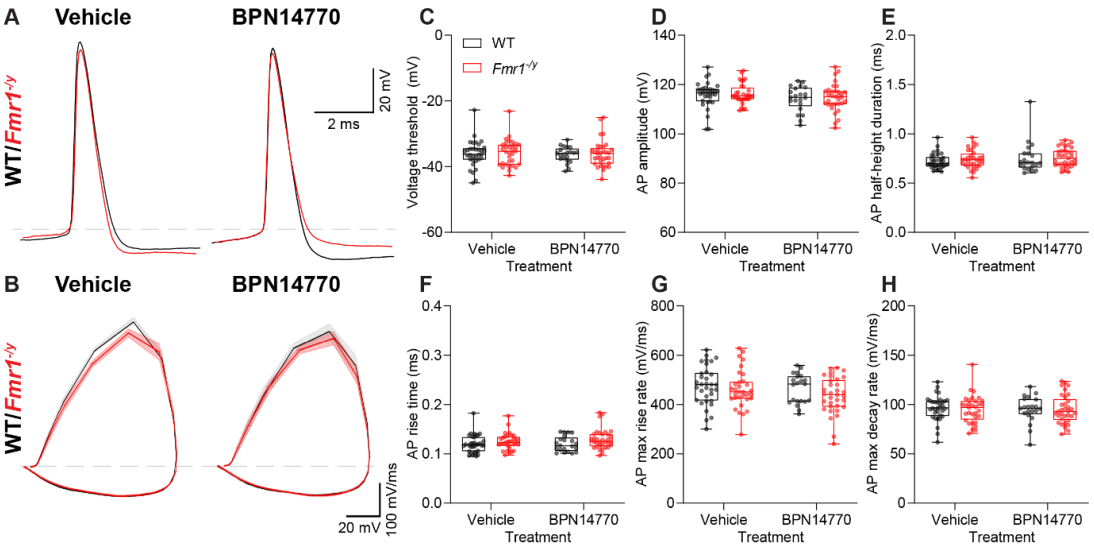

Figure 5.5. BPN14770 treatment does not affect AP kinetics at P25-28. A. Representative AP traces from P25-28 WT (black) and *Fmr1*$^{-/y}$ (red) L4 SCs after treatment with vehicle (left) or BPN14770 (right). Grey dashed line indicates voltage threshold. **B.** AP phase plots from WT and *Fmr1*$^{-/y}$ cells treated with vehicle or BPN14770. Grey dashed line indicates baseline. **C.** Voltage threshold does not differ between genotypes and treatments (GLMM; treatment: F=0.40, p=0.53; genotype: F=0.24, p=0.63; treatment × genotype: F=0.0039, p=0.95). **D.** AP amplitude is not affected by genotype or treatment (GLMM; treatment: F=0.87, p=0.36; genotype: F=0.55, p=0.47; treatment × genotype: F=0.015, p=0.90). **E.** AP half-height duration shows no difference between genotypes and treatments (GLMM; treatment: F=1.31, p=0.26; genotype: F=0.68, p=0.41; treatment × genotype: F=0.041, p=0.84). **F.** AP rise time shows a tendency towards an increase in *Fmr1*$^{-/y}$ but is not affected by BPN14770 treatment (GLMM; treatment: F=0.40, p=0.53; genotype: F=2.98, p=0.094; treatment × genotype: F=0.60, p=0.45; log-transformed). **G.** AP max rise rate does not differ between genotypes and treatments (GLMM; treatment: F=0.97, p=0.33; genotype: F=1.39, p=0.25; treatment × genotype: F=0.36, p=0.55). **H.** Max decay rate is not affected by treatment and does not differ between WT and *Fmr1*$^{-/y}$ (GLMM; treatment: F=0.074, p=0.79; genotype: F=0.14, p=0.71; treatment × genotype: F=0.010, p=0.92). Vehicle: WT: n=33 cells from N=10 animals; *Fmr1*$^{-/y}$: n=32 cells from N=11 animals; BPN14770: WT: n=21 cells from N=8 animals; *Fmr1*$^{-/y}$: n=33 cells from N=10 animals.

5.3.3 Morphology

Finally, I set out to test whether early treatment with BPN14770 could have lasting effects on the dendritic morphology of L4 SCs. Like previously, I have reconstructed the dendritic arbours of WT and *Fmr1*$^{-/y}$ L4 SCs (Figure 5.6A). Sholl analysis revealed no significant differences in the dendritic complexity of WT and *Fmr1*$^{-/y}$ L4 SCs, regardless of treatment (Figure 5.6B). Accordingly, there were no genotype or treatment effects in the associated measures i.e., the total number of Sholl intersections (Figure 5.6C), Sholl peak (Figure 5.6D), as well as the Sholl span (Figure 5.6E). In addition to typical dendritic complexity, the WT and *Fmr1*$^{-/y}$ L4 SCs exhibited similar overall sizes in the vehicle and BPN14770-treated groups, as evidenced by their comparable total dendrite number (Figure 5.6F) and length (Figure 5.6G). In summary, the dendritic morphology of L4 SCs does not differ between WT and *Fmr1*$^{-/y}$ rats at P25-28 and is not affected by BPN14770 treatment.

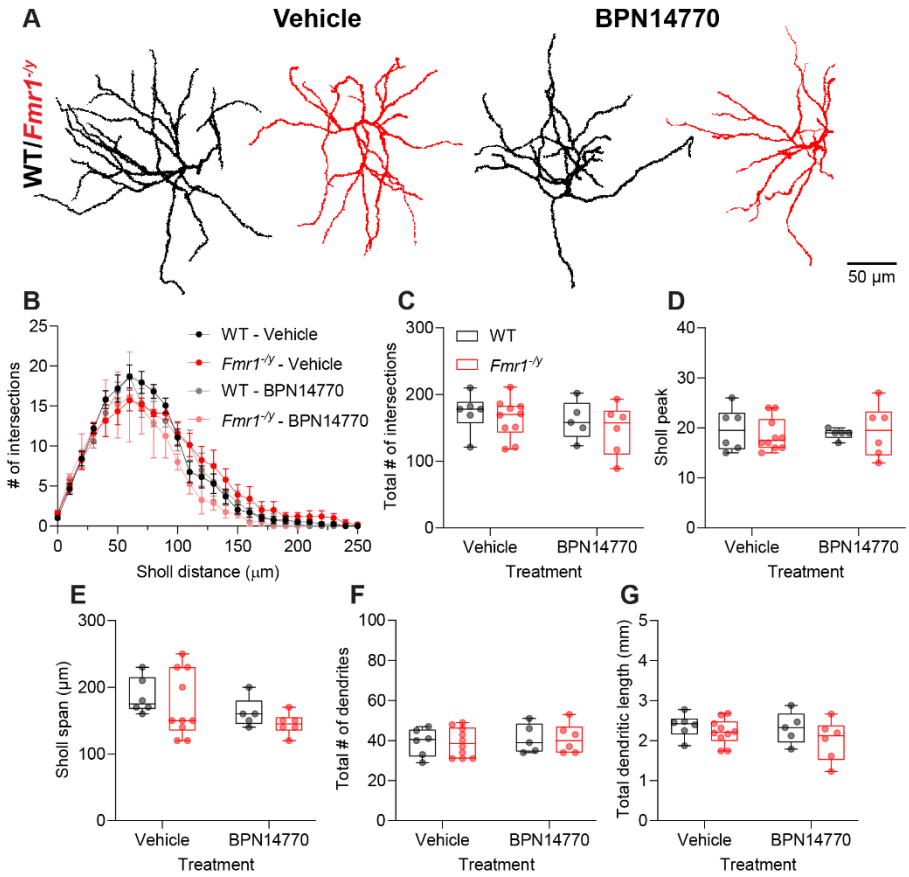

Figure 5.6. BPN14770 treatment does not affect L4 SC morphology at P25-28. A. Representative dendritic arbour reconstructions from P25-28 WT (black) and *Fmr1*$^{-/y}$ L4 SCs after treatment with vehicle (left) or BPN14770 (right). **B.** Sholl analysis shows no change in dendritic complexity regardless of treatment and genotype (3-way ANOVA on animal average values; Sholl: F=107.1, p<0.0001, treatment: F=1.73, p=0.21; genotype: F=0.41, p=0.53; Sholl × treatment × genotype: F=1.39, p=0.27). **C.** Total number of Sholl intersections does not differ between genotypes and treatments (GLMM; treatment: F=1.36, p=0.27; genotype: F=0.69, p=0.43; treatment × genotype: F=0.31, p=0.59). **D.** Sholl peak shows no effect of treatment and genotype (GLMM; treatment: F=0.009, p=0.93; genotype: F=0.23, p=0.64; treatment × genotype: F=0.08, p=0.78). **E.** Sholl span is unchanged between WT and *Fmr1*$^{-/y}$ and is not affected by BPN14770 (GLMM; treatment: F=3.23, p=0.11; genotype: F=0.54, p=0.48; treatment × genotype: F=0.13, p=0.72). **F.** The total number of dendrites is not different regardless of genotype and treatment (GLMM; treatment: F=0.44, p=0.51; genotype: F=0.0008, p=0.98; treatment × genotype: F=0.0008, p=0.98). **G.** Total dendritic length shows no effect of genotype and treatment (GLMM; treatment: F=0.93, p=0.36; genotype: F=1.93, p=0.20; treatment × genotype: F=0.61, p=0.46). Vehicle: WT: n=6 cells from N=4 animals; *Fmr1*$^{-/y}$: n=10 cells from N=5 animals; BPN14770: WT: n=5 cells from N=4 animals; *Fmr1*$^{-/y}$: n=6 cells from N=2 animals.

5.4 Discussion

The loss of FMRP leads to intrinsic hyperexcitability and reduced dendritic complexity of L4 SCs in early development of *Fmr1*$^{-/y}$ rats. Consequently, in this chapter I investigated the hypothesis that this altered developmental trajectory of *Fmr1*$^{-/y}$ L4 SCs could be amenable to therapeutic intervention. Reduced cAMP levels have previously been reported to underlie L4 SC hyperexcitability in young *Fmr1*$^{-/y}$ mice (Booker *et al.*, 2019) and constitute one of the most conserved phenotypes shared between models of FXS and individuals (Berry-Kravis, Hicar and Ciurlionis, 1995; Kelley *et al.*, 2007). In order to restore cAMP levels a PDE4D inhibitor – BPN14770 – was administered to WT and *Fmr1*$^{-/y}$ rat pups during their first postnatal week to test whether an intervention in early life could rescue S1 development with long-term results.

Table 5.1. Summary of Chapter 5 results.

Age	**P10-14**		**P25-28**	
Treatment	**Vehicle**	**BPN14770**	**Vehicle**	**BPN14770**
Excitability	↑	=	↑	↑
AP kinetics	=	=	=	=
Dendritic complexity	↓	=	=	=

5.4.1 BPN14770 treatment in early development

In line with previous data, *Fmr1*$^{-/y}$ L4 SCs were hyperexcitable after dosing with vehicle, which appeared to be improved after BPN14770 treatment. Namely, *Fmr1*$^{-/y}$ rats had a significantly higher proportion of cells exhibiting depolarization block, which was rescued with BPN14770. However, this treatment provided only a partial rescue, as intrinsic properties such as input resistance were mildly affected by BPN14770 without achieving statistical significance. While I did not find strong evidence implicating reduced I_h current in *Fmr1*$^{-/y}$ rats at this age (Chapter 3), previous studies suggest that altered I_h directly underlies neuronal hyperexcitability in *Fmr1*$^{-/y}$ mice through a cAMP-dependent mechanism (Zhang *et al.*, 2014; Booker *et al.*, 2019). cAMP signalling modulates the function and gating properties of

multiple ion channels by binding to the channel directly (e.g. HCN channels), or by activating PKA, leading to increased phosphorylation of channels such as Ca^{2+} and K^+-permeable ion channels (Hell *et al.*, 1995; Kavalali, Hwang and Plummer, 1997; Hoffman and Johnston, 1998; Wainger *et al.*, 2001). BPN14770 could therefore normalize the AP firing of L4 SCs by restoring cAMP to typical levels, through its effects on I_h or another cAMP-dependent mechanism. Furthermore, at P10-14 *Fmr1*$^{-/y}$ L4 SCs showed reduced dendritic complexity that was fully rescued when BPN14770 was administered, suggesting that reduced cAMP could underlie this morphological deficit. Indeed, cAMP signalling has previously been shown to play a role in dendritic arborisation of hippocampal neurons, and increasing cAMP levels is sufficient to increase dendritic length and complexity *in vitro* by influencing gene expression via CREB phosphorylation (Fujioka, Fujioka and Duman, 2004). Therefore, this developmental delay in the maturation of dendritic morphology in *Fmr1*$^{-/y}$ rats could plausibly arise as a result of reduced cAMP and is thus rescued through PDE4D inhibition with BPN14770. This in turn could underlie the partial rescue of excitability, as dendritic complexity can contribute to neuronal excitability through input resistance (as discussed in Section 4.4.1). Thus, these data support the hypothesis that reduced dendritic complexity underlies *Fmr1*$^{-/y}$ hyperexcitability during the second postnatal week. Nevertheless, this was not sufficient to fully restore the developmental trajectory, as *Fmr1*$^{-/y}$ L4 SCs were still hyperexcitable at P25-28, regardless of treatment. Therefore, while a brief treatment with BPN14770 may provide a rescue of L4 SC hyperexcitability in early development, it is not able to prevent hyperexcitability in later life. While it is unclear exactly why BPN14770 only provides a short term rescue of *Fmr1*$^{-/y}$ hyperexcitability, any of the following explanations are possible:

1. Hyperexcitability at P25-28 arises independently of previous developmental changes or through a different mechanism. Therefore, rescuing neuronal activity at P10-14 cannot affect the process through which hyperexcitability arises in later life as the two are separate. While additional factors (e.g. I_h) could contribute to hyperexcitability during the second postnatal week, a developmental delay in dendritic morphology at this age supports the idea

that L4 SC hyperexcitability at P10-14 and P25-28 could arise due to different mechanisms.

2. Hyperexcitability at P25-28 arises as a result of the altered developmental trajectory in *Fmr1*$^{-/y}$ rat S1. However, the brief and early BPN14770 treatment tested here (i.e., P5-9) can rescue hyperexcitability on more immediate timescales, but does not affect the overall developmental trajectory enough to produce long-lasting results. While the AP firing of *Fmr1*$^{-/y}$ neurons was restored, their intrinsic properties were not significantly affected, suggesting that the BPN14770 treatment in its current form is insufficient to provide a substantial rescue of *Fmr1*$^{-/y}$ deficits in development. Consequently, a different or wider treatment window (e.g. from birth) may be better positioned to provide a sustained correction of the developmental trajectory.
3. Loss of FMRP leads to reduced cAMP levels through dysregulation of its direct targets - PDE2A, PDE8B and PDE4B (Berry-Kravis, Hicar and Ciurlionis, 1995; Darnell *et al.*, 2011). This results in intrinsic hyperexcitability of *Fmr1*$^{-/y}$ neurons via I_h or another cAMP-dependent mechanism, which can be corrected by restoring cAMP levels. However, as FMRP expression is constitutively lost in *Fmr1*$^{-/y}$ neurons, any intervention targeting cAMP must necessarily be continuous and ongoing to successfully restore typical neuronal excitability.

It would thus be particularly interesting to further investigate the role of cAMP in cortical development of *Fmr1*$^{-/y}$ rats as well as explore alternative therapeutic windows to further disentangle the mechanisms involved in the development of cortical hyperexcitability. A crucial experiment to address the first and third hypothesis would be to administer BPN14770 right before P25, in order to test whether this second period of hyperexcitability is also cAMP-sensitive.

5.4.2 Limitations

The data presented in this chapter show that BPN14770 administered in early development can improve the hyperexcitability and reduced morphology of *Fmr1*$^{-/y}$ L4 SCs. Despite this, no measures of intrinsic physiology reached statistical significance and the treatment failed to produce a long-term rescue in *Fmr1*$^{-/y}$ rats.

One possible explanation for why BPN14770 treatment only significantly rescued the AP output, but not the intrinsic properties of L4 SCs in *Fmr1*$^{-/y}$ rats at P10-14 is the sample size. In particular, the *Fmr1*$^{-/y}$ vehicle-treated group included far fewer animals that the other groups (5 vs 10-12), due to the double blind experimental design. Such uneven powering could obscure biologically relevant effects, especially when the intra-animal variability is high. Therefore, increasing the sample size could benefit this analysis to more definitively test whether BPN14770 has an effect on the intrinsic properties of L4 SCs. Likewise, BPN14770 had no effects on L4 SC morphology beyond the second postnatal week, with no genotype or treatment effects at P25-28. It is worth noting that this P25-28 morphology dataset is preliminary with particularly small sample sizes which preclude any definitive conclusions about the long-term effect of BPN14770 on L4 SC morphology. However, there is no previous indication that dendritic morphology could be affected at this age, as in the *Fmr1*$^{-/y}$ rats the deficit in dendritic complexity is likely a developmental delay that is normalized by the fourth postnatal week (Chapter 4).

Unlike the data presented in Chapter 3, the cells in the P10-14 group were recorded under different conditions, allowing for the implementation of Patch-seq (discussed in Chapter 7). This included a modified internal solution to achieve a lower osmolarity, as well as the addition of an RNase inhibitor to the internal solution. I found that these conditions can significantly affect some (e.g., input resistance), but not all intrinsic properties of L4 SCs, especially in the WT (discussed in depth in Chapter 7; Figure 7.1). Thus, these factors need to be taken into consideration, as the two datasets are not directly comparable. This limitation does not apply to the P25-28 group however, as those recordings were performed under typical conditions, identical to Chapter 3.

Although the treatment started in early postnatal development (P5), it was only given for 5 days before experiments. Thus, it is possible that 5 days of treatment could simply be insufficient to produce a significant correction of the intrinsic properties of *Fmr1*$^{-/y}$ L4 SCs. A similar treatment with BPN14770 in adult mice has previously been shown to rescue the behavioural phenotypes (hyperactivity, reduced nesting, marble burying and social interactions) of *Fmr1*$^{-/y}$ mice, although it is unclear whether the electrophysiological properties of neurons were affected (Gurney *et al.*, 2017). In this case however, BPN14770 was administered in later life, for 14 days and at a lower dose (0.3 mg/kg). Some of the behavioural benefits, such as rescued nesting behaviour, marble burying and social interactions, persisted even 14 days after the treatment, but hyperactivity re-emerged in the washout period. This indicates that the administration of BPN14770 can have some long-term benefits for behaviour, even if this rescue is limited. Similarly, when BPN14770 was tested on adult FXS individuals in a phase 2 clinical trial with a crossover design, carryover effects were observed in participants who received BPN14770 in the first phase of the trial (Berry-Kravis, Harnett, *et al.*, 2021). This was attributed to low amounts BPN14770 still being present in the plasma even 12 weeks after the last dose. BPN14770 has a half-life of 8-10 hours in the mouse blood and brain (C. Zhang *et al.*, 2018), although the same has not been explicitly tested in rats. As the experiments presented in this chapter were conducted at least 24 hours after the last administration, one could expect that only a fraction of the original concentration of BPN14770 was present in the brain at that point. Although the concentration of BPN14770 in the brain is not addressed here, it would be especially interesting to test whether the degree of rescue of intrinsic properties correlates with the concentration of BPN14770. Indeed, a phase 2 clinical trial showed that in FXS individuals the correction of event-related auditory potentials in response to auditory stimuli was correlated with plasma concentration of BPN14770 (Norris *et al.*, 2024). Additionally, some long term effects of BPN14770 treatment were found at P25-28, namely increased input resistance and reduced capacitance. It is possible that these were caused by BPN14770 directly especially considering the aforementioned studies found effects lasting beyond the original treatment window and unexpectedly long washout periods (Gurney *et al.*, 2017; Berry-Kravis, Harnett, *et al.*, 2021). However,

as these effects were oriented in the opposite direction of the immediate findings (i.e. trend towards reduced input resistance at P10-14 vs increase at P25-28), it is more likely that they are caused by changes to the developmental trajectory of L4 SCs as a result of rescued early hyperexcitability, rather than BPN14770 directly. Likewise, due to time constraints this thesis does not address whether the levels of cAMP are indeed reduced in the *Fmr1*$^{-/y}$ rats and rescued with BPN14770, posing a significant limitation to the interpretability of the data presented in this chapter. However, during dissection, additional brain tissue and trunk blood were preserved to directly address these questions at a later timepoint. Thus, mass spectrometry and enzyme-linked immunosorbent assay (ELISA) could be used to determine the levels of BPN14770 and cAMP respectively in the blood and the brain of these animals at the time of experiment.

Daily handling represents a major confounding factor when comparing these results to the data discussed in Chapter 3. Unlike the previous chapters, here all of the animals were handled every day for weighing and dosing through modified oral gavage, which contributes to their different sensory experience in early life. This could be addressed through an alternative mode of drug administration, such as in food. However, it is not possible to implement such a solution at such early developmental stages i.e., before weaning. Additionally, while administering the drug through food minimizes the experimenter's contact with the animals, it also makes it impossible to control each animal's individual intake. Such a solution can still produce meaningful results, as a similarly designed trial of lovastatin was shown to rescue the behavioural and synaptic plasticity deficits of adult *Fmr1*$^{-/y}$ rats (Asiminas *et al.*, 2019). Nevertheless, for early treatment, modified oral gavage is likely the most viable option, although changes in sensory experience as a result of handling should be taken into account. It is likely that handling does have an effect on the intrinsic properties of L4 SCs, as the some of the values obtained here do not match the control ones discussed in Chapter 3, even when the rats only received vehicle (Table 5.2).

Table 5.2. Comparison of selected intrinsic properties for P9-12 control (Chapter 3) and P10-14 vehicle and BPN1770-treated L4 SCs.

	Control (P9-12)		Vehicle (P10-14)		BPN14770 (P10-14)	
	WT	***Fmr1*$^{-/y}$**	**WT**	***Fmr1*$^{-/y}$**	**WT**	***Fmr1*$^{-/y}$**
F-I slope	0.071 ±0.005	0.094 ±0.006	0.081 ±0.005	0.104 ±0.005	0.078 ±0.005	0.084 ±0.004
Rheobase	92.42 ±4.71	83.00 ±5.35	92.28 ±5.92	81.79 ±8.41	91.46 ±6.28	105.98 ±7.28
RMP	-61.90 ±1.24	-60.34 ±1.08	-59.99 ±0.74	-60.65 ±1.00	-63.50 ±1.11	-61.21 ±0.95
IR	281.83 ±18.76	406.88 ±22.88	353.12 ±22.08	409.316 ±23.52	326.95 ±21.51	334.60 ±19.44
MTC	26.54 ±2.00	28.83 ±1.75	27.41 ±1.28	28.50 ±1.41	22.76 ±1.22	25.47 ±1.53
C_m	96.14 ±6.35	73.31 ±4.08	81.07 ±2.69	72.87 ±3.38	73.74 ±3.11	78.09 ±2.83
Rise time	0.15± 0.006	0.19± 0.009	0.16± 0.007	0.17± 0.006	0.16± 0.006	0.16± 0.005
Max rise rate	321.79 ±14.95	255.72 ±13.43	297.30 ±13.79	276.85 ±12.04	309.92 ±16.53	290.77 ±11.10

Daily handling could influence the development of the S1, as sensory experience plays an important role in developmental regulation of S1 circuit function, especially during the first and second postnatal weeks, coincident with the critical period for L4 to L2/3 synaptic plasticity, which underlies the fine tuning of whisker receptive fields during development (Fox, 1992; Lendvai *et al.*, 2000; Stern, Maravall and Svoboda, 2001). Sensory deprivation during this critical period has previously been shown to induce changes in connectivity, but not intrinsic properties of L2/3 and L4 neurons in S1 (Fox, 1992; Maravall, Stern and Svoboda, 2004). In adult rats, sensory stimulation through environmental enrichment can induce plasticity in L4 and L2/3 neurons, increasing their response to whisker stimulation (Rema *et al.*, 2006). It also leads to enhanced spatial acuity and adjacent whisker tuning in L2/3 (Zheng *et al.*, 2021). In the auditory cortex, developmental sensory experience plays a role in establishing a balance between cortical excitation and inhibition (Dorrn *et al.*, 2010). While it is unclear what effect increased sensory stimulation during early development could have on the intrinsic properties of L4 SCs, it can be expected to

be a confounding factor in these data. This effect could be particularly prominent in WT animals, as FMRP expression is known to be upregulated in response to environmental enrichment (Irwin *et al.*, 2000, 2005). Consequently, a detailed examination of the role of sensory experience in the S1 development of *Fmr1*$^{-/y}$ rats, through both sensory deprivation and enrichment, could provide crucial insight into its contribution to the development of hyperexcitability in the S1. As such, whether sensory modulation could itself be used therapeutically, on its own or in conjunction with a pharmacological intervention such as BPN14770 is a fascinating question that warrants further investigation.

5.4.3 Summary

Overall, the data presented in this chapter indicate that early treatment with BPN14770 could have some beneficial effects on *Fmr1*$^{-/y}$ L4 SC excitability and morphology. It does not however provide a robust correction of intrinsic properties nor a long-term rescue of excitability for these neurons. An in-depth exploration of the role of sensory experience in these deficits as well as alternative therapeutic windows for pharmacological intervention could provide crucial, translationally-relevant insight into cortical development in FXS.

Chapter 6

Transcriptomic characterization of S1 development in *Fmr1*$^{-/y}$ rats

6.1 Introduction

Loss of FMRP expression leads to a wide range of functional and structural changes in the brain, including impaired synaptic function and plasticity, altered oscillatory activity, dendritic spine morphology or axon initial segment length (Irwin *et al.*, 2001; Huber *et al.*, 2002; Pan *et al.*, 2010; van der Molen, Stam and van der Molen, 2014; Till *et al.*, 2015; Booker *et al.*, 2019).

In the FMRP-deficient somatosensory cortex, intrinsic hyperexcitability of excitatory neurons (Chapter 3; Booker et al., 2019; Domanski et al., 2019), deficits in dendritic morphology development as well as altered inhibitory cytoarchitecture (Chapter 4; Till *et al*., 2012; Kourdougli *et al*., 2023), and a shift in the critical period for plasticity (Harlow *et al.*, 2010) contribute to its altered developmental trajectory and dysfunction. While FMRP primarily functions as a translational repressor for 100s of targets (Li, 2001; Darnell *et al.*, 2011), it can also be involved in processes such as mRNA editing, stability and alternative splicing (Zalfa *et al.*, 2007; Filippini *et al.*, 2017; Zhou *et al.*, 2017; F. Zhang *et al.*, 2018). Additionally, homeostatic plasticity mechanisms may compensate for some of the effects of FMRP loss to stabilize circuit-level activity, while further dysregulating cellular function (Antoine *et al.*, 2019; Booker *et al.*, 2020). As such, the consequences of FMRP loss can extend beyond its direct targets. Indeed, translatome profiling of *Fmr1*$^{-/y}$ mouse hippocampal neurons revealed differential translation in mRNAs that included, but were not exclusive to direct FMRP targets (Thomson *et al.*, 2017). In cortical forebrain organoids the loss of FMRP significantly impairs their development, leading to excessive synapse

formation and hyperexcitability, reduced proliferation of neural progenitor cells and premature neuronal differentiation (Kang *et al.*, 2021). These phenotypes are underlain by broad differences in gene expression, which disrupt the typical developmental trajectory, similarly to FXS fetal brain tissue. Likewise, previous work in the developing cortex of *Fmr1*$^{-/y}$ mice found widespread changes on the transcriptomic level, including an upregulation in the expression of genes involved in ribogenesis and protein translation (Donnard, Shu and Garber, 2022). Indeed, excessive ribogenesis, translation and proteostasis have been identified as a key phenotype which underlies neuronal dysfunction in the hippocampus and inferior colliculus of *Fmr1*$^{-/y}$ mice (Osterweil *et al.*, 2010; Seo *et al.*, 2022; Louros *et al.*, 2023). However, the cortex contains multiple cell types with distinct transcriptomes that could be differentially affected by the loss of FMRP (Scala *et al.*, 2019; Siletti *et al.*, 2023; Yao *et al.*, 2023). In fact, Donnard, Shu and Garber (2022) found that the same pathways (e.g., translation and mitochondrial function) could be dysregulated in opposite directions in excitatory vs inhibitory neurons. However, no subtype-specific changes were assessed, despite the fact both excitatory and inhibitory neurons in the cortex form several transcriptomically distinct subtypes with different functions (Scala *et al.*, 2019).

In the previous chapters I have identified significant changes in the developmental trajectory of L4 SCs in the S1 of *Fmr1*$^{-/y}$ rats, including increased excitability and morphological deficits. Additionally, changes in the density of specific interneuron subtypes imply that the loss of FMRP could have cell type and subtype-specific effects, which could be supported by distinct changes in gene expression. Furthermore, to my knowledge, no transcriptomic investigation has been performed in the rat model of FXS, which replicates some, but not all phenotypes seen in the *Fmr1*$^{-/y}$ mice, highlighting species-specific differences in cortical development in the absence of FMRP. Thus, it is currently unclear how the transcriptomes of cortical cells are affected by the loss of FMRP on an individual cell level in the *Fmr1*$^{-/y}$ rats. Therefore, in this chapter I will use single nucleus RNA sequencing (snRNAseq) to investigate the cell-type specific transcriptomic changes in

the S1 of WT and *Fmr1*$^{-/y}$ rats at P9, a key stage in the early postnatal development of the somatosensory cortex.

6.2 Transcriptomic characterization of developing S1 in *Fmr1*$^{-/y}$ rats

6.2.1 Clustering of single nuclei transcriptomes

In order to investigate whether the transcriptomes of individual cells are altered during S1 development in *Fmr1*$^{-/y}$ rats, single nucleus RNA sequencing (snRNAseq) was performed. Nuclei were isolated from S1 cortical sections of 3 WT and 3 *Fmr1*$^{-/y}$ littermate rats at P9. Following sequencing, 169838 cells were detected. Low quality transcriptomes were identified as outliers based on high and low features, high and low counts (i.e. transcripts) as well as high mitochondrial RNA (see Section 2.7.1), and removed. Likewise, doublets were identified and removed to ensure single cell transcriptomes. After outlier and doublet filtering (see Section 2.7.1), 129669 cells remained (WT: 58221; *Fmr1*$^{-/y}$: 71488), expressing 25629 unique features (i.e., genes). I then performed unsupervised Louvain clustering on the remaining cells, which grouped them into 18 clusters, visualized using uniform manifold approximation and projection (UMAP; Figure 6.1A). Cluster composition by sample is summarized in Figure 6.1B-C. Note that sample 4 contains fewer nuclei overall and in cluster 0 in particular due to unsuccessful sample preparation.

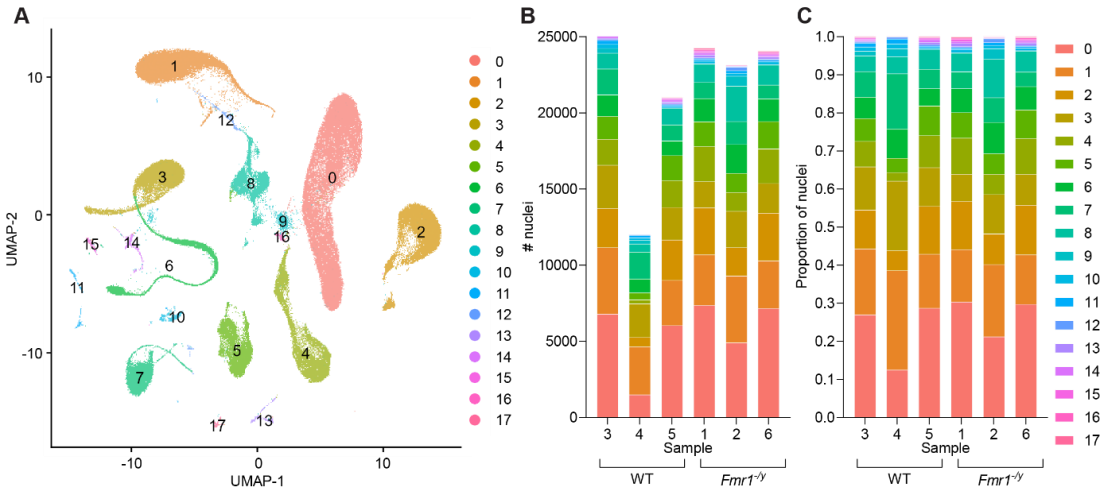

Figure 6.1. Unsupervised clustering divides S1 cells into 18 clusters. A. UMAP plot of S1 single-nucleus transcriptomes from WT and *Fmr1*$^{-/y}$ rats at P9. **B.** Number of nuclei by sample and cluster. **C.** Proportion of nuclei by sample and cluster. Colours indicate the cluster. WT: samples 3-5, *Fmr1*$^{-/y}$: samples 1,2 and 6.

6.2.2 Cell type composition of the S1 does not differ between WT and Fmr1$^{-/y}$

Cell type identities were individually assigned to each cell based on the expression of established gene markers for major cortical cell types (see Section 2.7.1). A summary of cell numbers by type is provided in Table 6.1. In both genotypes, excitatory neurons comprised the largest group, at 42-48% overall (Figure 6.2A). Astrocytes were the second, with 15-18% of the total. Inhibitory neurons formed 11-14% of all the cells. OPCs and oligodendrocytes contributed 9-13% and 5-6% respectively, while microglia added 5-8%. Vascular cells (endothelial cells and pericytes) and vascular leptomeningeal cells (VLMCs) were the least common cell types, contributing less than 2% of the overall population. As the overall cell type distribution in the *Fmr1*$^{-/y}$ did not appear to match the WT, I next investigated the relative proportion of each cell type in WT and *Fmr1*$^{-/y}$ by sample to include individual biological replicates. I found no differences in the abundance of any cell type, indicating that the cell type composition of the S1 is not affected in the *Fmr1*$^{-/y}$ at P9 (Figure 6.2B).

Table 6.1. Cell numbers by cell type and genotype.

	WT	***Fmr1*$^{-/y}$**	**Total**
Excitatory neuron	24428	34303	58731
Inhibitory neuron	6530	9927	16457
Astrocyte	10593	11029	21622
OPC	7572	6411	13983
Oligodendrocyte	3147	4727	7874
Microglia	4643	3632	8275
Endothelial cell	269	222	491
Pericyte	286	236	522
VLMC	438	528	966
Unknown	315	433	748
Total	58221	71488	129669

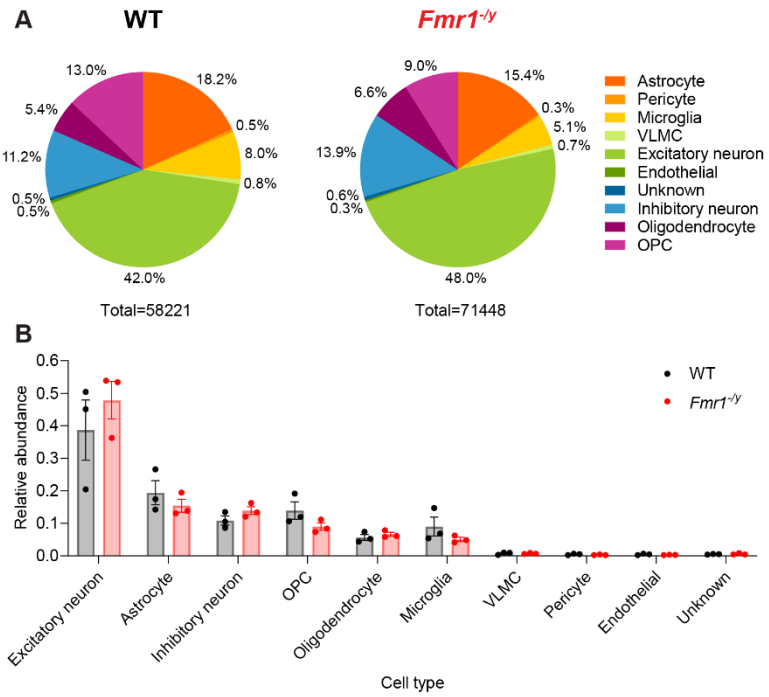

Figure 6.2. *Fmr1*$^{-/y}$ S1 does not differ in cell type composition at P9. A. Proportion of cells by type in WT (left) and *Fmr1*$^{-/y}$ (red) S1 at P9. Colours indicate cell type. **B.** Relative proportions of cells are not different between WT (black) and *Fmr1*$^{-/y}$ rats regardless of cell type (Two-way ANOVA; cell type: F=43.53, p<0.0001; genotype: F=0.00, p>0.99; interaction: F=1.05, p=0.42).

6.2.3 Cell type identification by cluster

The selected gene markers showed distinct patterns of expression between clusters (Figure 6.4), allowing to assign cell type identity to each cluster (Figure 6.3). Excitatory neurons expressing *Slc17a7* and *Satb2* belonged to clusters 0, 2, 4, 13 and 16. Inhibitory neurons were present in clusters 5 and 8, and expressed *Gad1* and *Gad2*. Cluster 1 was positive for *Aqp4* and *Aldh1l1*, and was thus identified as astrocytes. Cluster 1 had a non-uniform shape with a tail that was enriched in *Gfap* expression, suggesting the presence of reactive astrocytes (Wilhelmsson *et al.*, 2006). Clusters 3 and 6 also formed an elongated shape and expressed *Sox10*, while *Pdgfra* expression was restricted to cluster 3. Cluster 6 also expressed *Mbp* and *Plp1* throughout as well as *Mog* in a subset of cells. As *Mbp* expression increases along cluster 6, while the end of cluster 6 tail strongly expresses *Mog*, the elongated shape of cluster 3 and 6 could represent the transition from oligodendrocyte precursor cells (OPCs) to mature oligodendrocytes (Kuhn *et al.*, 2019). Hence, clusters 3 and 6 were identified as OPCs and oligodendrocytes, respectively. Microglia belonged to cluster

7, which was positive for *Csf1r*, *P2ry12* and *Aif1*. Finally, several types of vascular-associated cells were identified. Endothelial cells expressing *Vwf* and *Flt1*, as well as pericytes expressing *Pla1a* and *Cox4i2* were found in cluster 11. As endothelial cells and pericytes clustered together, for further analysis they were collapsed into one category termed 'Vascular cell'. VLMCs were present in cluster 10, positive for *Dcn*, *Lum* and *Ptgds*. Clusters 9, 12, 14 and 15 were small clusters that contained a mixture of cell types, or cells that expressed conflicting markers (e.g., *Slc17a7* and *Gad1*), and thus were classified as unknown. Expression of gene markers by cell type cluster is summarized in Figure 6.5.

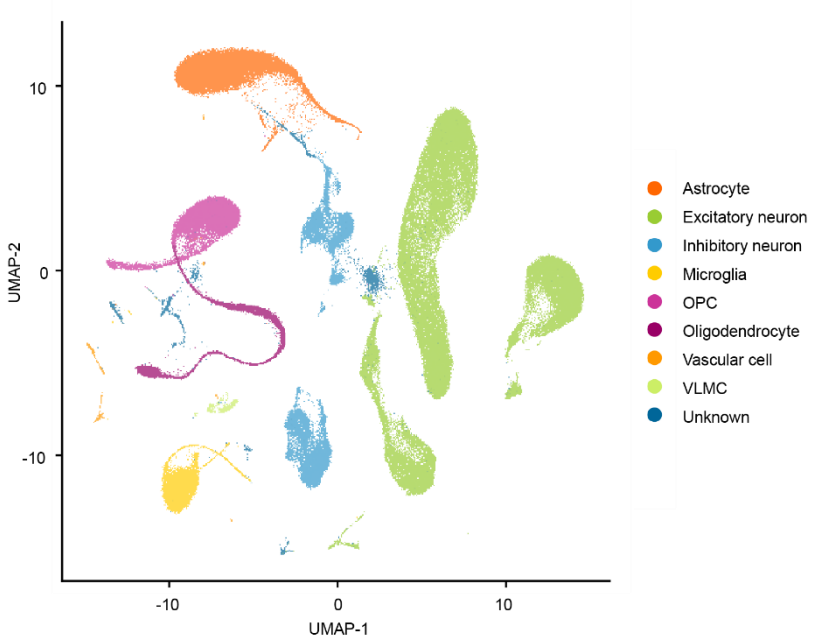

Figure 6.3. Transcriptomic clusters represent distinct cell types in the S1. UMAP plot of S1 nuclei from WT and *Fmr1*$^{-/y}$ rat S1 at P9. Colours indicate the most abundant cell type within the cluster.

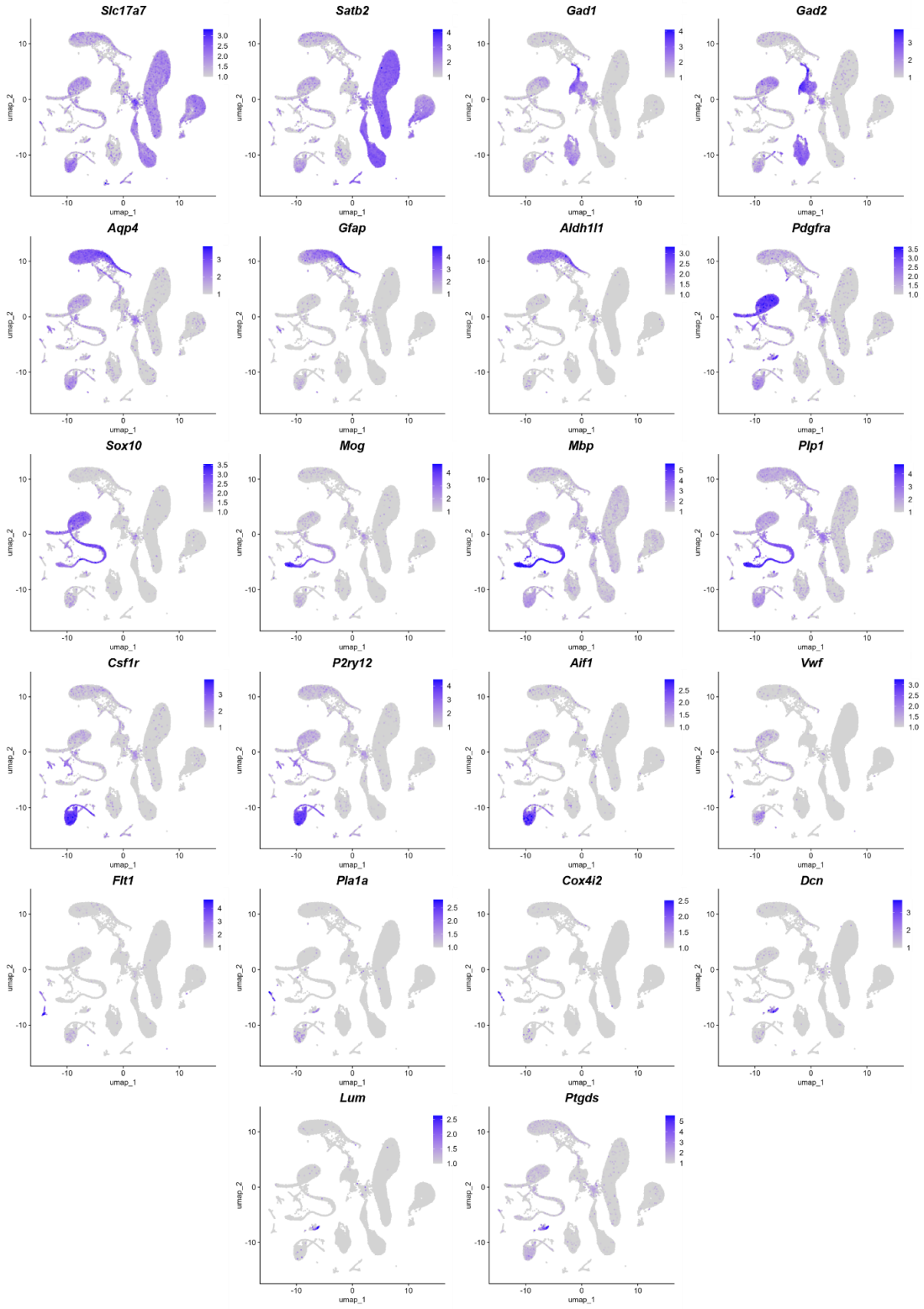

Figure 6.4. Feature UMAP plots of selected gene marker expression. Excitatory neurons: *Slc17a7, Satb2*; Inhibitory neurons: *Gad1, Gad2*; Astrocytes: *Aqp4, Gfap, Aldh1l1*; OPCs: *Pdgfra, Sox10*; Oligodendrocytes: *Mog, Mbp, Plp1*; Microglia: *Csf1r, P2ry12, Aif1*; Endothelial cells: *Vwf, Flt1*; Pericytes: *Pla1a, Cox4i2*; VLMCs: *Dcn, Lum, Ptgds*.

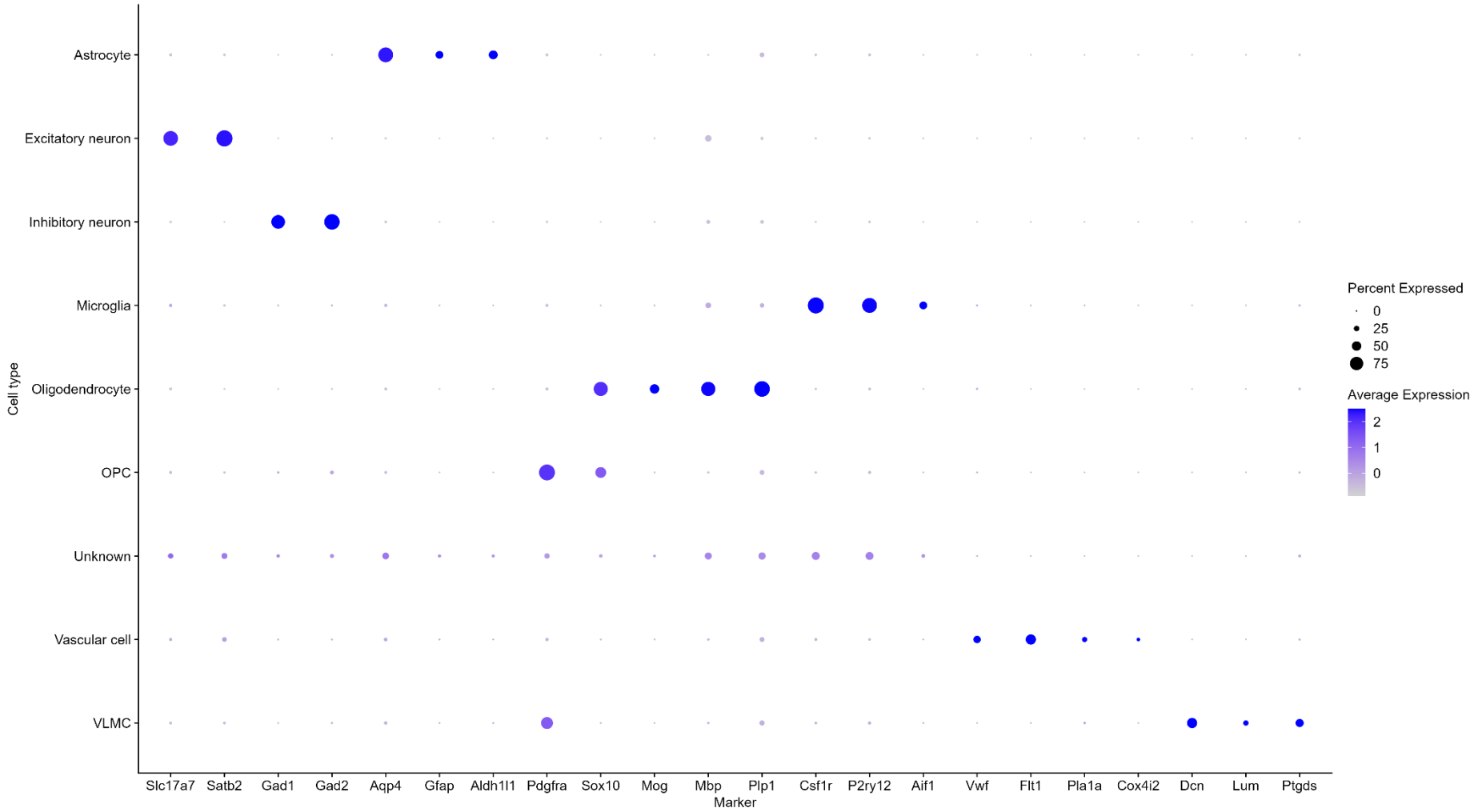

Figure 6.5. Summary of gene marker expression by cell type cluster. Dot size represents % cells expressing the gene, colour intensity shows average normalized expression level.

6.2.4 Differential gene expression analysis identifies neurons as the most affected cell type in *Fmr1*$^{-/y}$ cortex

Following the identification of the major cell types I performed pseudobulk differential gene expression analysis (Lun and Marioni, 2017; Squair *et al.*, 2021) to compare the gene expression patterns (i.e., relative abundance of mRNA transcripts) between WT and *Fmr1*$^{-/y}$ in each cell type (Figure 6.6A). Excitatory neurons were the most affected in the *Fmr1*$^{-/y}$, with a total of 141 differentially expressed genes (DEGs) relative to WT. Similarly, inhibitory neurons differentially expressed 93 genes in the *Fmr1*$^{-/y}$. Astrocytes, microglia and OPCs showed a lower number of DEGs, while oligodendrocytes, vascular cells, VLMCs and unknown cells only had one downregulated gene, which was *Fmr1*. Indeed, *Fmr1* was the most (or only) downregulated gene in every cell type, confirming the intended global knockout in *Fmr1*$^{-/y}$ rats. Since excitatory and inhibitory neurons were identified as the most affected cell types in the developing *Fmr1*$^{-/y}$ rat brain, I further investigated their transcriptomic changes. A full list of all DEGs in excitatory and inhibitory neurons is provided in Appendix 9.2. Excitatory neurons showed upregulation in 16 genes involved in mitochondrial respiratory chain function, including 9 mitochondrially-encoded genes (in order of significance: *Mt-nd1, Mt-nd5, Mt-co2, Mt-cyb, Mt-atp6, Mt-co3, Mt-co1, Mt-nd2, Mt-nd4* and *Mt-nd6*; Figure 6.6B). 14 genes encoding both the small and large ribosomal subunit proteins were significantly upregulated (*Rplp0, Rpl28, Rps16, Rps9, Rps11, Rps13, Rps2, Rpl32l5, Rpl10, Rps19, Rpsa, Mrps34, Rpl19, Rpl3*), together with a gene regulating ribosome assembly (*Sbds*). Indeed, gene ontology (GO) analysis on upregulated genes confirmed enrichment in terms related to mitochondrial energy production and ribosome assembly, as well as cellular stress responses in *Fmr1*$^{-/y}$ excitatory neurons (Figure 6.6C). The most downregulated genes in excitatory neurons included *Syt17, Ror2, Kcp* and *Tshz2*, as well as genes responsible for the regulation of cellular size and shape through neurite outgrowth (*Gprin3, Unc5a, Arhgap15, Epb41l2, Dgkg, Kel, Ntng2*; Figure 6.6B). However, no significant GO terms were found for excitatory neuron downregulated genes. In inhibitory neurons, top upregulated genes included *Strip2, Ccdc180, Rasgrp1, Gpr88* and *Itpka* (Figure 6.6D). GO analysis revealed enrichment in learning, dopamine

metabolism, calcium signalling and postsynaptic structure terms (Figure 6.6E). *Nudt7* and *Itga8* were among the top downregulated genes, with no significant GO terms identified. Notably, *Sst* was found to be upregulated in the *Fmr1*$^{-/y}$ interneurons, due to an increase in the average expression, and a minor increase in the proportion of *Sst*$^{+}$ cells (Figure 6.6F-H), in agreement with increased Sst-14 labelling discussed in Chapter 4. Therefore, in the developing somatosensory cortex, *Fmr1*$^{-/y}$ neurons exhibit distinct transcriptomic signatures, with excitatory neurons showing enrichment in genes suggesting increased energy demand, ribosomal translation and cellular stress, while inhibitory neurons differentially express genes related to synaptic function, development and cellular signalling.

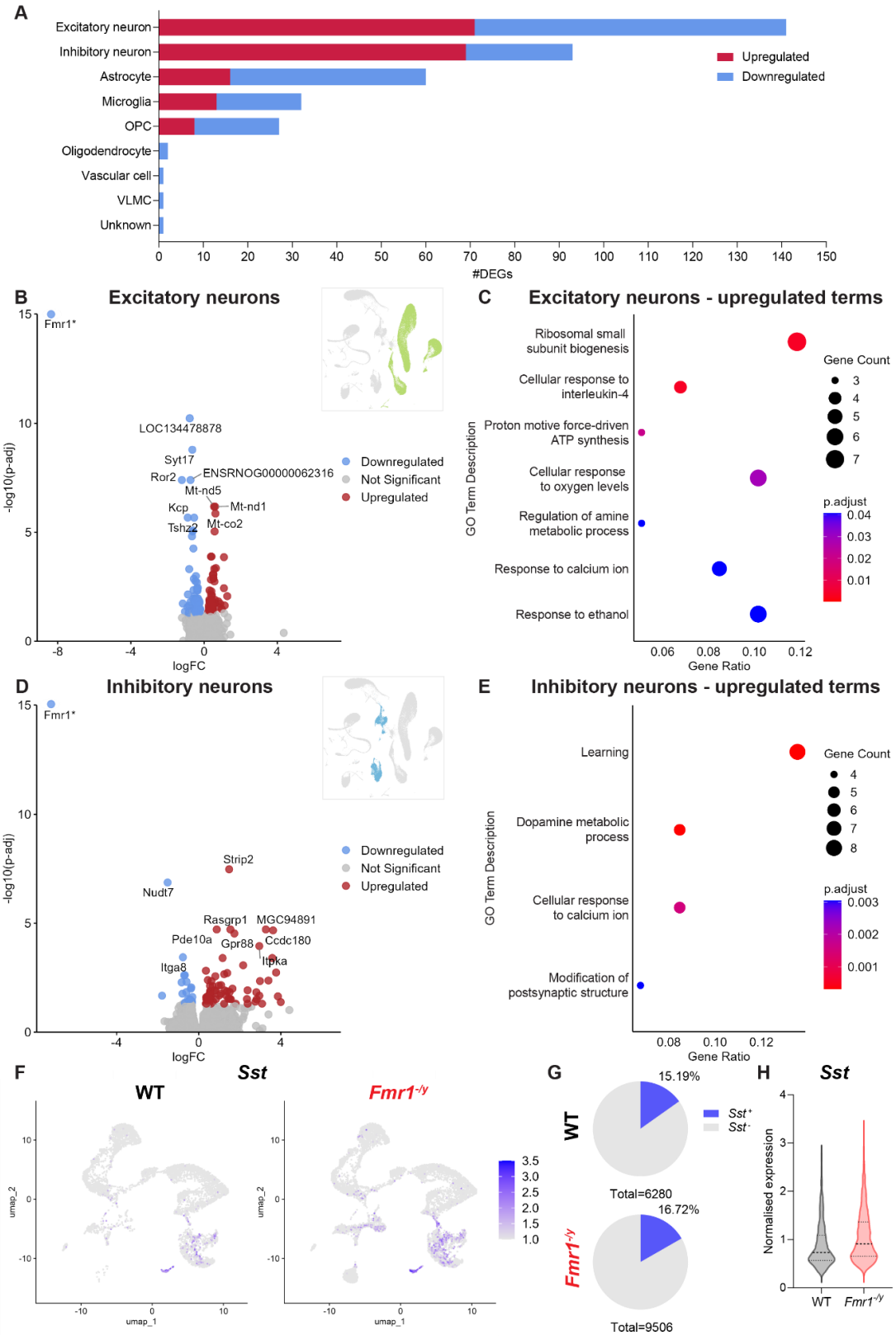
A
Excitatory neuron
Inhibitory neuron
Astrocyte
Microglia
OPC
Oligodendrocyte
Vascular cell
VLMC
Unknown
Upregulated
Downregulated
#DEGs
B
Excitatory neurons
Fmr1*
LOC134478878
Syt17
Ror2
ENSRNOG00000062316
Mt-nd5
Kcp
Mt-nd1
Tsha2
Mt-co2
Downregulated
Not Significant
Upregulated
-log10(p-adj)
logFC
C
Excitatory neurons - upregulated terms
Ribosomal small subunit biogenesis
Cellular response to interleukin-4
Proton motive force-driven ATP synthesis
Cellular response to oxygen levels
Regulation of amine metabolic process
Response to calcium ion
Response to ethanol
GO Term Description
Gene Ratio
Gene Count
p.adjust
D
Inhibitory neurons
Fmr1*
Strip2
Nudt7
Rasgrp1
MGC94891
Pde10a
Gpr88
Ccdc180
Itga8
Itpka
Downregulated
Not Significant
Upregulated
-log10(p-adj)
logFC
E
Inhibitory neurons - upregulated terms
Learning
Dopamine metabolic process
Cellular response to calcium ion
Modification of postsynaptic structure
GO Term Description
Gene Ratio
Gene Count
p.adjust
F
Sst
WT
Fmr1-/y
umap_1
umap_2
G
WT
15.19%
Sst+
Sst-
Total=6280
Fmr1-/y
16.72%
Total=9506
H
Sst
Normalised expression
WT
Fmr1-/y

Figure 6.6. Differential gene expression analysis reveals cell-type specific patterns of altered gene expression in *Fmr1*$^{-/y}$ S1. A. Number of differentially expressed genes (DEGs) by cell type. **B.** Volcano plot of differential gene expression in *Fmr1*$^{-/y}$ excitatory neurons showing upregulated (red) and downregulated genes (blue) with 10 most differentially expressed genes labelled. * -log10(p-adj) for *Fmr1* was capped at 15 for presentation purposes (actual -log10(p-adj)>1000). **C.** Gene ontology analysis for genes upregulated in *Fmr1*$^{-/y}$ excitatory neurons. Dot size indicates number of genes, colour shows the adjusted p-value. **D.** Volcano plot of differentially expressed genes in *Fmr1*$^{-/y}$ inhibitory neurons with 10 most differentially expressed genes labelled. * -log10(p-adj) for *Fmr1* capped at 15 for presentation purposes (actual -log10(p-adj)=175.5). **E.** Gene ontology analysis for genes upregulated in *Fmr1*$^{-/y}$ inhibitory neurons. **F.** UMAP feature plot of Sst expression in WT and *Fmr1*$^{-/y}$ inhibitory neurons. Colour indicates normalized expression. **G.** Proportion of cells expressing *Sst* in WT (top) and *Fmr1*$^{-/y}$ (bottom) inhibitory neurons. *Fmr1*$^{-/y}$ inhibitory neurons have a higher proportion of *Sst*$^{+}$ cells compared to WT (Chi-square test; X^2=17.18, p<0.0001). **H.** Normalized *Sst* expression is upregulated in *Fmr1*$^{-/y}$ inhibitory neurons. Only cells with normalized *Sst* expression > 0 were included.

6.2.5 Excitatory neuron subclusters show cortical lamination

In order to investigate the transcriptome of excitatory neurons in more detail, excitatory neuron clusters were extracted and re-clustered to produce 7 subclusters (Figure 6.7A). Although each sample contained cells in each subcluster, sample 4 contributed fewer cells in total and had a smaller proportion of cells in subcluster 1 (Figure 6.7B-C). Excitatory neuron subclusters likely represent different types of glutamatergic neurons across the cortical layers, as the subclusters separate based on their expression of cortical layer markers (Figure 6.7D-E; Kwan *et al.,* 2008; Rosenberg *et al*., 2018; Qian *et al*., 2024). Subclusters 1,2 and 6 are upper layer neurons, as evidenced by the expression of *Cux2*. The L4 marker *Rorb* was highly expressed in subcluster 2, which thus likely contains primarily L4 SCs, whose development was characterized in the previous chapters. As subclusters 1 and 6 only partially expressed *Rorb*, they are likely enriched in L2/3 neurons, which are mostly *Rorb*-negative (Oishi, Aramaki and Nakajima, 2016). Finally, subclusters 3-5 and 7 are deep cortical layer neurons, with a high expression of *Sox5.* Subclusters 3 and 5 express *Foxp2* and *Tle4*, which are associated with L5 and L6 neurons. Subcluster 4 strongly expressed *Il1rapl2,* which is not a cortical layer marker *per se*, but has recently been associated with a subtype of L5 neurons (Liu *et al.*, 2025). Subcluster 5 was positive for the L5A marker *Etv1*, while subcluster 3 expressed *Syt6*, a marker for L6. A summary of cell numbers in each excitatory neuron subcluster in WT and *Fmr1*$^{-/y}$ is provided in Table 6.2.

Table 6.2. Number of excitatory neurons by subcluster and genotype.

	WT	***Fmr1*$^{-/y}$**	**Total**
Excitatory neuron 1	6261	7846	14107
Excitatory neuron 2	8073	11578	19651
Excitatory neuron 3	5388	7585	12973
Excitatory neuron 4	3726	5796	9522
Excitatory neuron 5	460	479	939
Excitatory neuron 6	213	403	616
Excitatory neuron 7	74	225	299

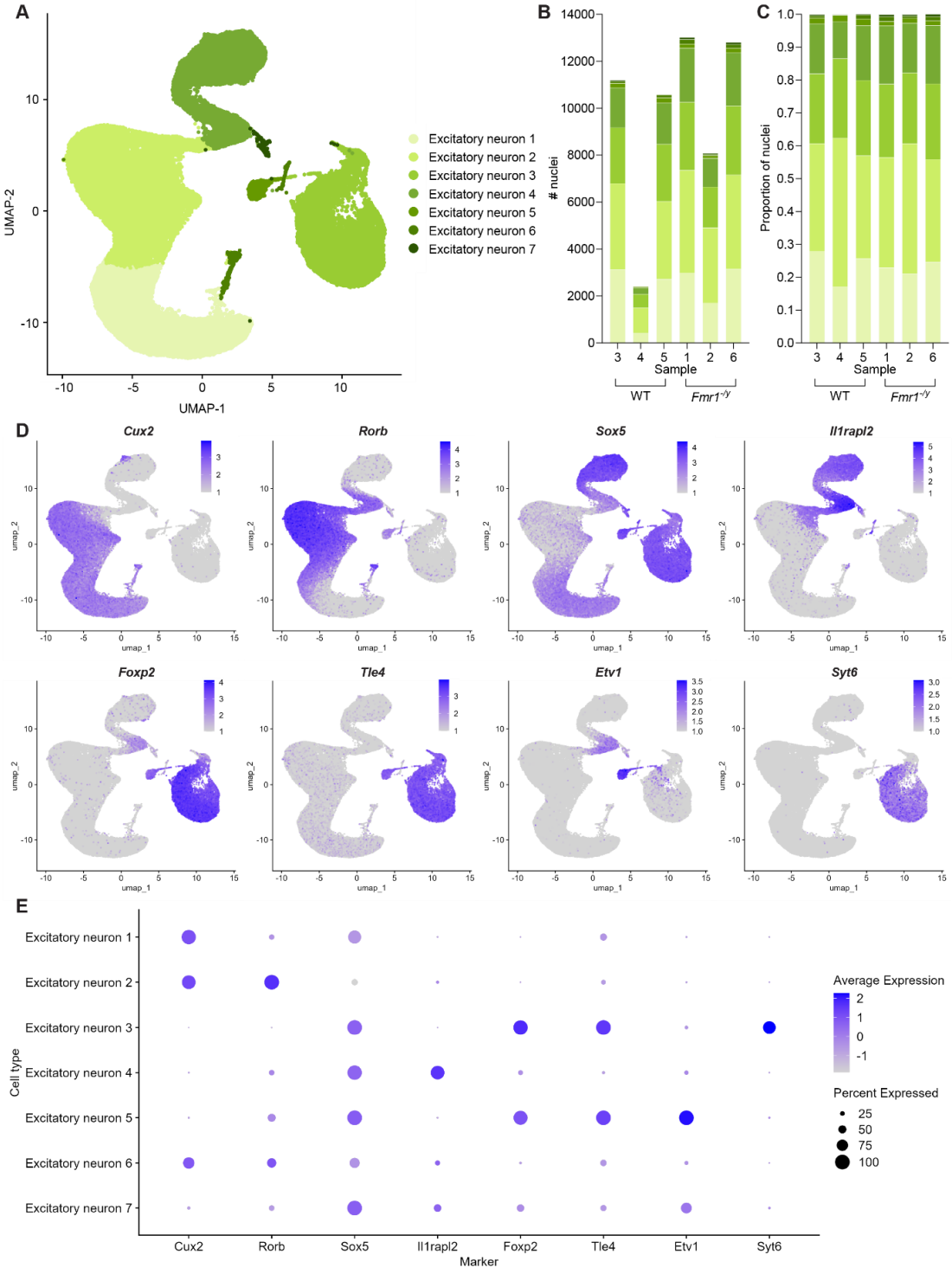

Figure 6.7. Excitatory neuron subclusters show evidence of cortical layers. A. UMAP plot of excitatory neuron subclusters from WT and *Fmr1*$^{-/y}$ rat S1 at P9. Shades of green indicate subcluster. **B.** Excitatory neuron subcluster composition in each sample. **C.** Proportion of nuclei in each excitatory neuron subcluster by sample. **D.** UMAP feature plots of selected cortical layer gene markers. L2-4: *Cux1, Cux2*; L4: *Rorb*; L5: *Il1rapl2*; L5-6: *Sox5, Foxp2, Tle4*; L5A: *Etv1*; L6: *Syt6*. **E.** Summary of cortical layer gene marker expression by excitatory neuron subcluster.

6.2.6 Excitatory neuron transcriptomes differ by subtype

Pseudobulk DGE analysis was performed like previously to identify the transcriptomic changes in *Fmr1*$^{-/y}$ excitatory neurons by subtype. Excitatory neuron subclusters 1-4 showed a high number of DEGs (Figure 6.8A), with putative L4 SCs in subcluster 2 having the highest number of DEGs (139), suggesting they could be the most vulnerable to the loss of FMRP at this age. Excitatory neuron 6 subcluster showed upregulation of the transcriptional regulator *Tox*, which plays a role in neuronal differentiation, proliferation and neurite outgrowth (Artegiani *et al.*, 2015). Subclusters 5, 6 and 7 only had 1 downregulated gene – *Fmr1*. As such, subclusters 5-7 are not included in further analysis. I next investigated the overlap in DEGs between subclusters to identify common changes in excitatory neuron subtypes (Figure 6.8B). L2-4 neurons in subclusters 1 and 2 had the highest degree of overlap, with 24 DEGs shared between the two groups and 7 more shared with subcluster 3 or 4. In addition to the shared DEGs, each excitatory neuron subcluster showed unique transcriptome differences in the *Fmr1*$^{-/y}$ rats. L2/3 neurons in subcluster 1 differentially expressed 45 unique genes, while L4 SCs in subcluster 2 had 101 DEGs unique to this cell type.

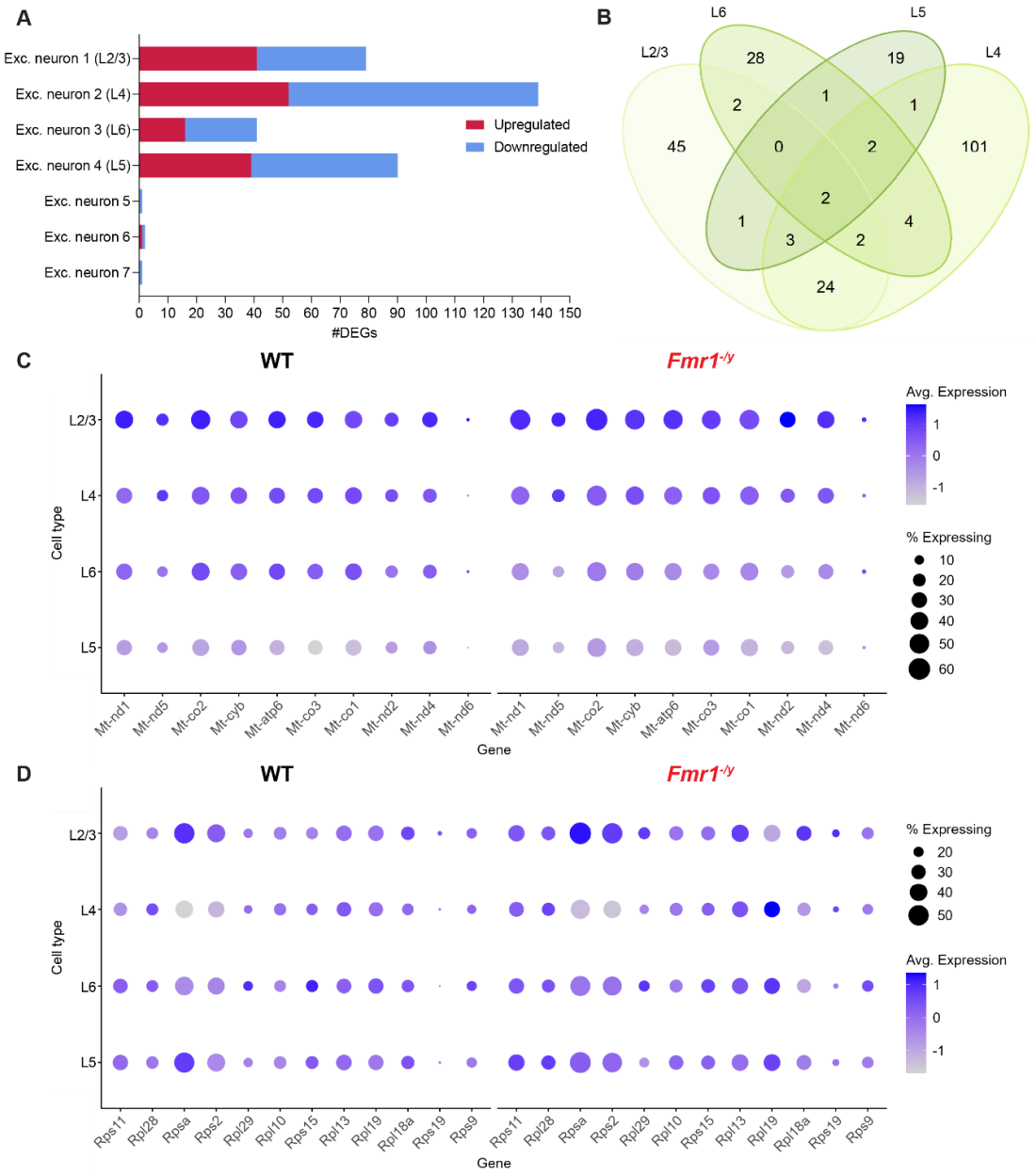

Figure 6.8. Excitatory neurons show subtype-specific differences in differentially expressed genes in *Fmr1*$^{-/y}$ S1. **A.** Number of DEGs by excitatory neuron subtype. Upregulated genes indicated in red, downregulated in blue. **B.** DGE overlap between excitatory neuron subtypes. Shades of green indicate excitatory neuron subtype; numbers show the number of genes in each group. **C.** Dot plot of selected mitochondrial gene expression in WT and *Fmr1*$^{-/y}$ excitatory neuron subtypes. Dot size shows proportion of cells, colour indicates normalized expression. **D.** Dot plot of ribosomal gene expression in WT and *Fmr1*$^{-/y}$ excitatory neuron subtypes.

Upper layer neurons showed upregulation in mitochondrial and ribosomal protein genes, most of which overlapped between the subclusters. These included the same 9 upregulated mitochondrial genes discussed in Section 6.2.4 (Figure 6.8C), as well as upregulated ribosomal protein genes *Rps11, Rpl28, Rpsa* and *Rps2* (Figure 6.8D). In addition to the shared DEGs, L2/3 neurons uniquely overexpressed mitochondrial respiratory chain genes *Mt-nd4l, Cox4i1* and *Cox7c*, and ribosomal genes *Rpl29, Rpl10, Rps15, Rpl13* (Figure 6.9A). GO terms related to ribosome biogenesis and assembly were enriched in L2/3 neurons (Figure 6.9B). Genes such as *Dlc1, Frmd4b, Igsf3, Map7,* and *Arhgef28* were downregulated in this subtype, typically contributing to the regulation of neuronal morphological development. Additionally, L2/3 neurons showed downregulation in cAMP-related genes *Adcy8* and *Ppargc1b*. However, no significant GO terms were identified in downregulated genes in L2/3 neurons. Similarly, the L4 neuron subcluster showed upregulation in unique ribosome protein genes that were not significantly affected in any other excitatory neuron subtype (Figure 6.9C). These included *Rpl19*, *Rpl18a, Rps19, Rps9*. Indeed, ribosomal small unit biogenesis and cytoplasmic translation were among the top GO terms in L4 upregulated genes (Figure 6.9D). Again, downregulated DEGs included several genes involved in cell adhesion and morphological development, such as *Cdh13* (Figure 6.9C). GO analysis confirmed enrichment in a single term – cell-cell adhesion mediated by cadherin (not shown; p=0.019, gene count=4, gene ratio=0.06). Therefore, while upper layer neurons show upregulation of genes encoding ribosome proteins, the exact set of genes is partially unique to each subcluster. Likewise, both subclusters downregulate genes affecting neuronal morphology, but there is little overlap in the specific genes.

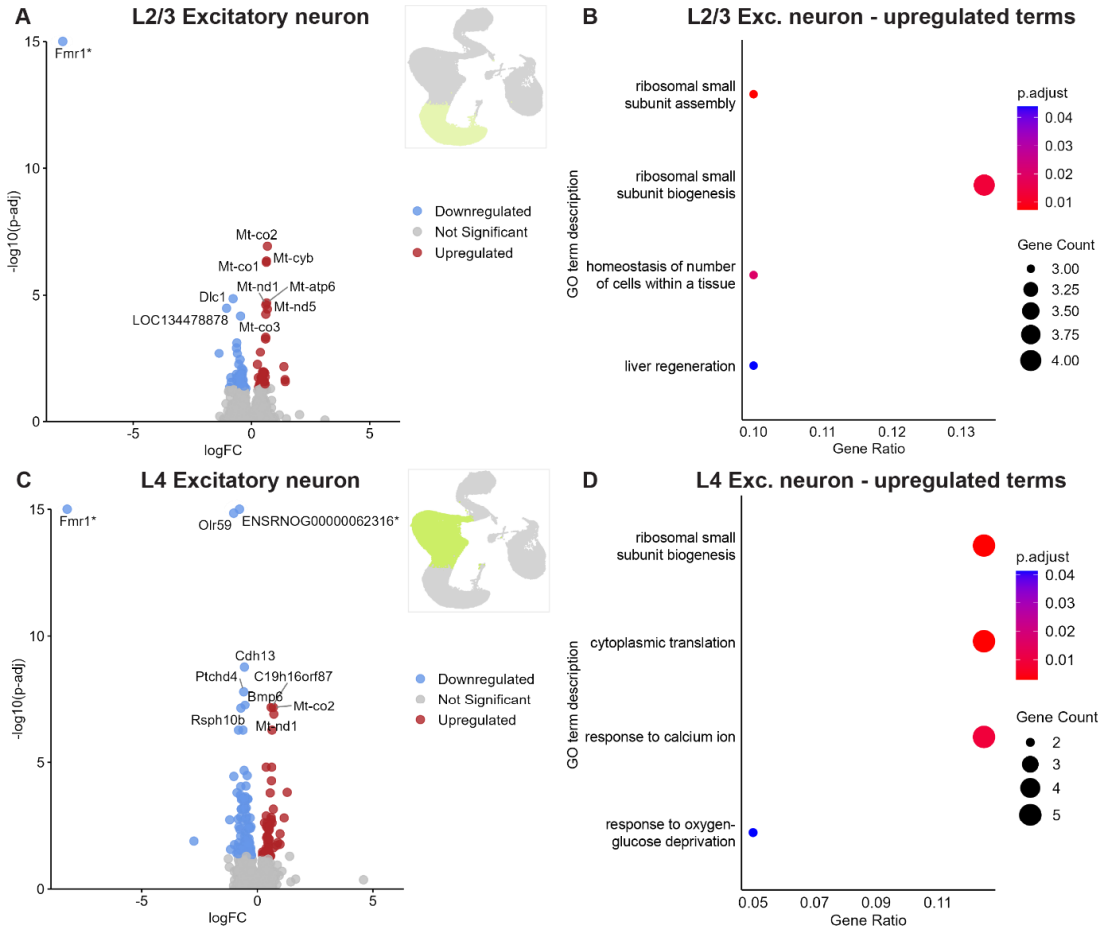

Figure 6.9. Upper layer excitatory neurons differentially express mitochondrial, ribosomal and cell morphology genes. A. Volcano plot of L2/3 excitatory neuron differential gene expression with 10 most differentially expressed genes labelled. Downregulated genes labelled in blue, upregulated in red. * -log10(p-adj) for *Fmr1* was capped at 15 for presentation (actual -log10(p-adj)=142.0) **B.** Gene ontology analysis of upregulated genes in the L2/3 excitatory neuron subcluster. Dot size indicates number of genes, colour shows the adjusted p-value. **C.** Volcano plot of L4 excitatory neuron DEGs. * To improve resolution around other genes, -log10(p-adj) was capped at 15 for *Fmr1* (actual -log10(p-adj)=210.2) and *ENSRNOG00000062316* (actual -log10(p-adj)=15.2). **D.** GO analysis for L4 excitatory neuron upregulated genes.

In contrast to the other subtypes, L6 excitatory neurons showed upregulation in neuronal developmental genes (*Vstm2a, Tenm3, Fstl1, Nhs*; Figure 6.10A) and downregulation in genes involved in regulating AMPA receptor trafficking and function (*Syndig1, Cnih3*). GO analysis on upregulated genes identified enrichment in cellular response to bone morphogenic protein (BMP) stimulus (not shown; p=0.02, gene count=4, gene ratio=0.27), suggesting that BMP signalling could be affected in this cell type. Downregulated genes showed enrichment in GO terms pertaining to synaptic structure and neurotransmission, as well as VEGF signalling (Figure 6.10B). L5 neurons upregulated the transcription factor *Egr1*, as well as *Slc1a2*, which controls glutamate reuptake at synapses (Figure 6.10C). L5 neurons upregulated the GO terms cellular response to oxygen levels (not shown; p=0.04, gene count=5, gene

ratio=0.16) and homeostasis of number of cells within a tissue (not shown; p=0.04, gene count=3, gene ratio=0.09). Excitatory neurons in L5 showed downregulation in morphological development genes such as *Robo1, Sdk1,* and *Chd4* and GO terms such as axon guidance, VEGF signalling and synaptic vesicle transport (Figure 6.10D). In conclusion, upper layer excitatory neurons show dysregulation in similar functions which suggest increased energy production and protein translation, as well as impaired morphological development, while deep cortical neurons exhibit changes in genes responsible for synaptic function and development.

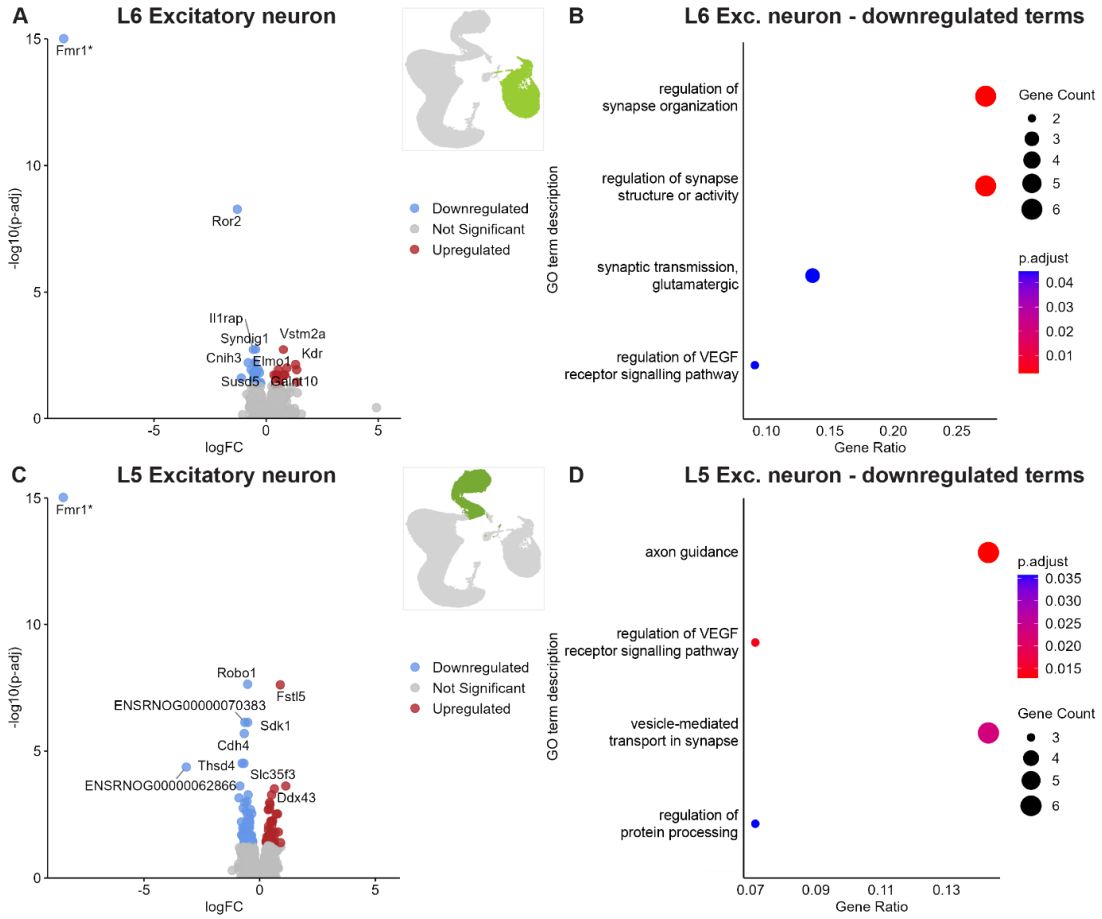

Figure 6.10. Deep layer excitatory neuron subclusters differentially express synaptic and developmental genes. **A.** Volcano plot of differentially expressed genes in the L6 excitatory neuron subcluster with top 10 genes labelled. Downregulated genes labelled in blue, upregulated in red. * -log10(p-adj) for *Fmr1* capped at 15 for presentation (actual -log10(p-adj)=78.2). **B.** Gene ontology analysis for downregulated genes in the L6 excitatory neuron subcluster. Number of genes is indicated by dot size; colour indicates the adjusted p-value. **C.** Volcano plot of differentially expressed genes in the L5 excitatory neuron subcluster with 10 most differentially expressed genes labelled. * -log10(p-adj) for *Fmr1* capped at 15 for presentation purposes (actual -log10(p-adj)=88.4). **D.** GO analysis results for genes downregulated in the L5 excitatory neuron subcluster.

6.2.7 Inhibitory neurons separate into subtype clusters

Inhibitory neurons were extracted and re-clustered to produce 8 distinct subclusters (Figure 6.11A). Like previously, sample 4 contributed fewer inhibitory neurons per subcluster and overall (Figure 6.11B), but showed a similar proportional distribution of inhibitory neurons per subcluster (Figure 6.11C). In contrast, sample 2 had a higher proportion of cells in subcluster 5 and 6 compared to other samples. In order to identify the interneuron types in each subcluster, I examined the expression of established interneuron markers (Figure 6.11D-E; Rudy et al., 2011; Shi et al., 2021). *Sst* was weakly expressed in some cells within the inhibitory neuron 4 and 5 subclusters, as well as strongly expressed throughout subcluster 8. *Reln* expression was not associated with any particular subclusters, but rather expressed in a portion of all subclusters, with the strongest expression in subcluster 3 and 7. In subcluster 4 and 8, *Reln* expression overlapped with *Sst*, in agreement with studies showing co-expression of these two markers in some interneurons (Pohlkamp *et al.*, 2014). *Vip*-expressing interneurons formed the majority of subcluster 2, while *Meis2* expression was restricted to subclusters 5 and 6. *Cck* expression was found in subclusters 2,3 and 5, where it overlapped with *Vip*. *Calb1* was co-expressed with *Sst* and *Reln* in subcluster 4 and 8, and with *Reln* alone in subcluster 1. Similarly, *Calb2* was present in subcluster 2 and 5. Subclusters 1,4 and 8 as well as portions of subclusters 3 and 5 were positive for *Sox6,* which is a marker for MGE-derived interneurons i.e., *Pvalb* and *Sst*-expressing interneurons (Batista-Brito *et al.*, 2009). While *Pvalb* is a marker for the most abundant class of interneurons, it is typically not expressed in rodent cortex until P14 (Lecea, del Ri´o and Soriano, 1995). Indeed, no *Pvalb* expression was found in any of the inhibitory neuron subclusters. However, as subcluster 1 is the largest subcluster, and expresses the MGE-derived interneuron marker *Sox6*, but not *Sst,* it most likely contains the future *Pvalb*-expressing interneurons. Summary of cell numbers in each subcluster is provided in Table 6.3.

Table 6.3. Number of inhibitory neurons by subcluster and genotype.

	WT	***Fmr1*$^{-/y}$**	**Total**
Inhibitory neuron 1	2197	2615	4812
Inhibitory neuron 2	1284	1428	2712
Inhibitory neuron 3	1191	1455	2646
Inhibitory neuron 4	1070	1503	2573
Inhibitory neuron 5	318	1418	1736
Inhibitory neuron 6	16	831	847
Inhibitory neuron 7	128	108	236
Inhibitory neuron 8	76	148	224

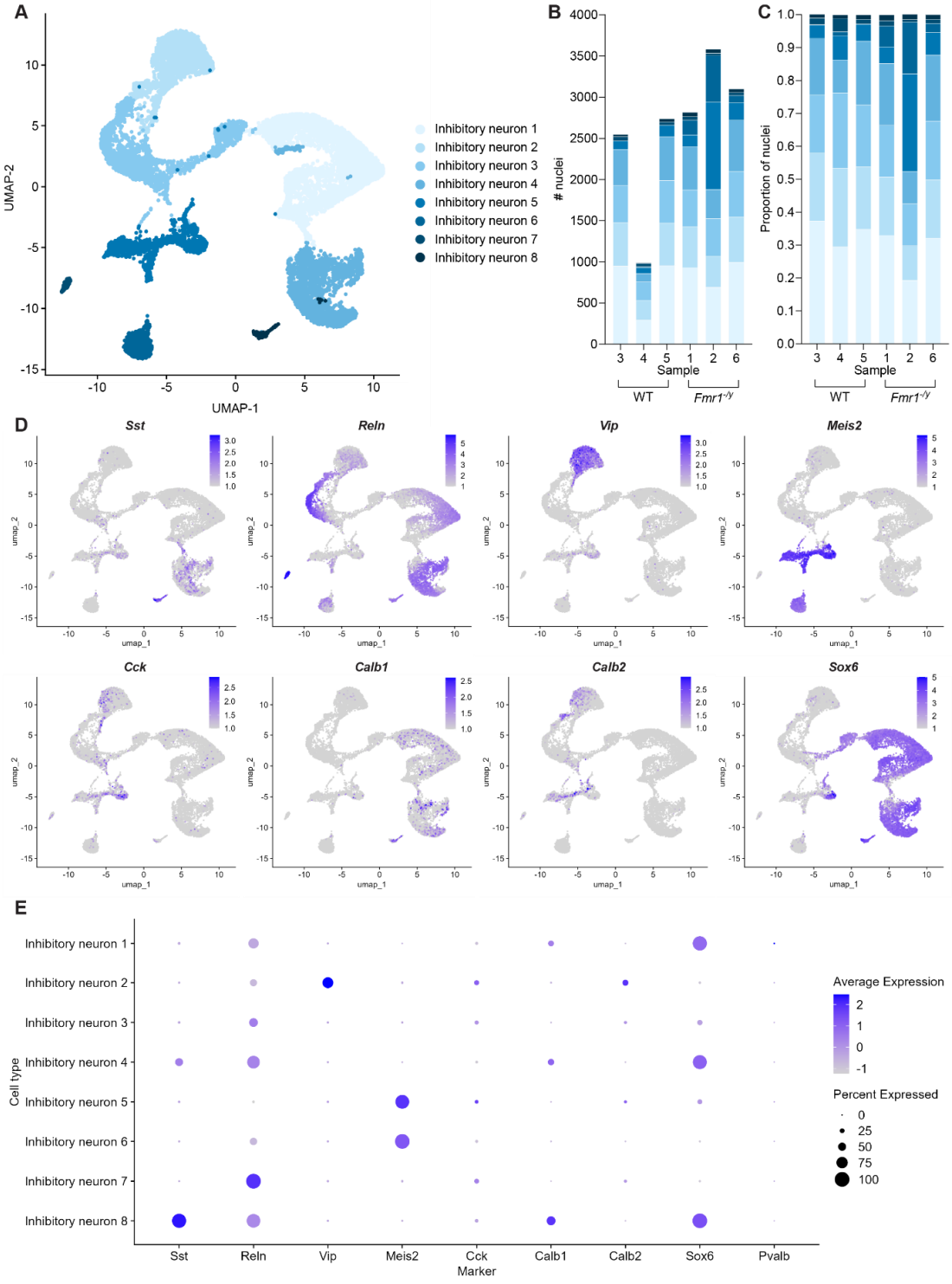

Figure 6.11. Inhibitory neuron subclusters contain several distinct classes of interneurons. A. UMAP plot of inhibitory neuron subclusters from WT and *Fmr1*$^{-/y}$ rat S1 at P9. Shades of blue indicate subcluster. **B.** Inhibitory neuron subcluster composition in each sample. **C.** Proportion of nuclei in each inhibitory neuron subcluster by sample. **D.** UMAP feature plots of selected interneuron subtype gene markers. **E.** Summary of interneuron subtype gene marker expression by inhibitory neuron subcluster. Dot size indicates proportion of cells expressing the gene, colour shows average normalized expression.

6.2.8 Inhibitory neurons show subtype-specific gene expression changes in *Fmr1*$^{-/y}$

Finally, to identify subtype-specific changes in gene expression in *Fmr1*$^{-/y}$ interneurons, I performed DGE analysis in each inhibitory neuron subcluster. DGE analysis on inhibitory neuron subtype level identified fewer DEGs than when all inhibitory neurons were considered as a whole. With the exception of *Fmr1*, DEGs tended to be unique to each subcluster. Putative *PV*$^{+}$ interneurons in the inhibitory neuron 1 subcluster showed the highest number of DEGs (31), which included upregulation in genes involved in establishing and organizing neuronal projections and connectivity (*Tenm3, Dscam, Lrp12, Pcdh15, Brinp1;* Figure 6.12A) as well as mitochondrial genes (*Mt-co2, Mt-co1, Mt-nd1, Mt-cyb*). GO analysis on upregulated genes identified enrichment in one term - homophilic cell adhesion via plasma membrane adhesion molecules (not shown; p=0.03, gene count=3, gene ratio=0.23), and no terms in downregulated genes. *Vip*$^{+}$ interneurons in the inhibitory neuron 2 subcluster showed upregulation in only 3 genes – *Cadps2*, responsible for synaptic vesicle exocytosis, *Col25a,* involved in axonogenesis, and *Vcan*, which has functions in brain development, cell adhesion and intracellular signalling (Figure 6.12B). *Itga8*, which controls the organization of cell projections, was downregulated in subclusters 1 and 3 (Figure 6.12C). Inhibitory neuron 4 subcluster, which contains the MGE-derived *Sst*$^{+}$ and *Reln*$^{+}$ interneurons, downregulated the ciliary intracellular transport protein *Dnah11* and the chromatin organizer *L3mbtl4* (Figure 6.12D). *Meis2*$^{+}$ interneurons in subcluster 5 overexpressed the voltage-gated potassium channel *Kcnc2* and the transcription factor *Zfp521* and downregulated *Grik1*, a serine/threonine protein kinase (Figure 6.12E). The *Reln*$^{+}$ subcluster 7 showed downregulation in *Cntn5* and *Plcl1*, which regulate neurite outgrowth and GABAergic synaptic neurotransmission respectively (Figure 6.12F). Inhibitory neuron subclusters 6 and 8 showed no changes in gene expression. Overall, *Fmr1*$^{-/y}$ inhibitory neurons show minor subtype-specific transcriptomic changes reflecting altered synaptic function and connectivity.

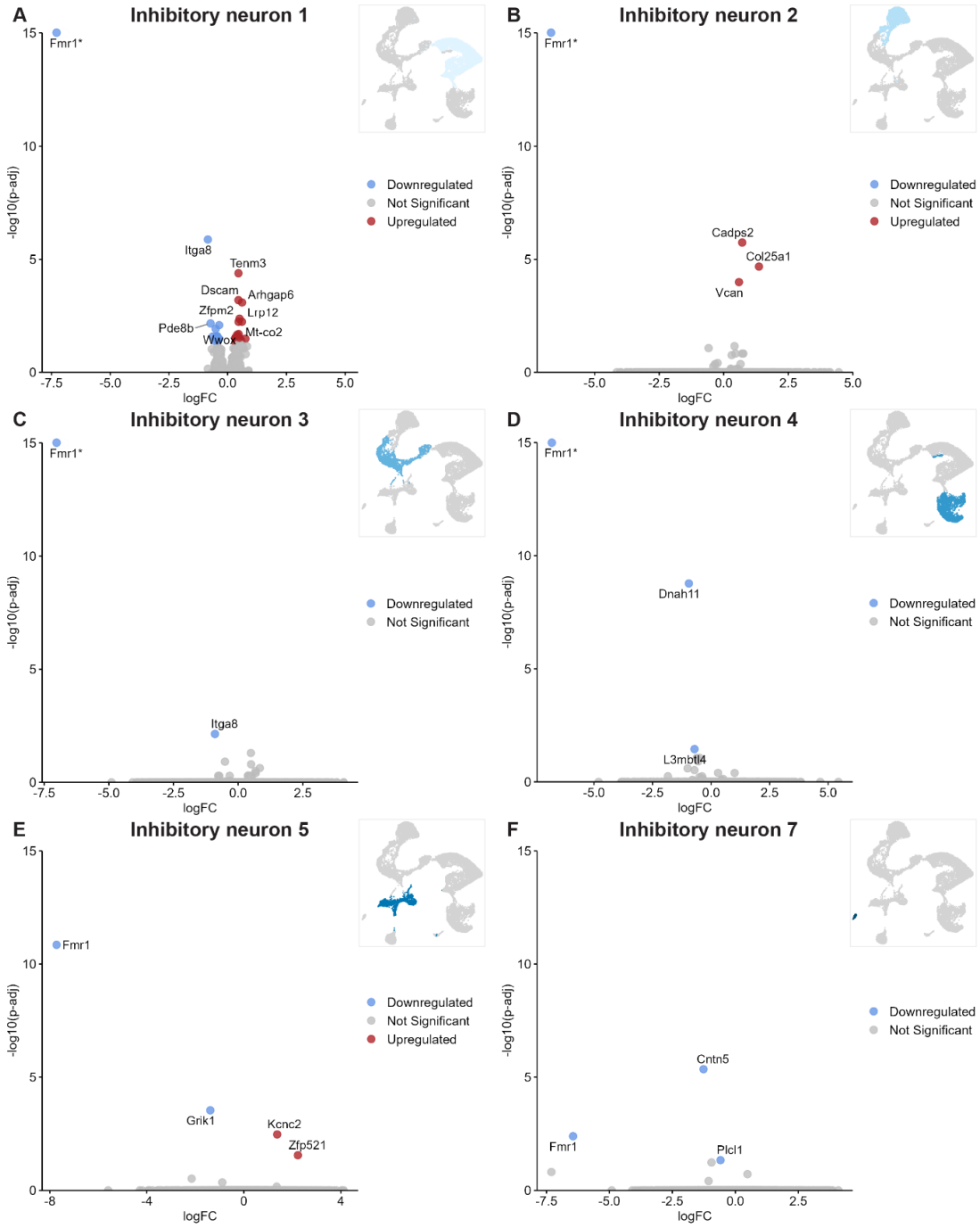

Figure 6.12. *Fmr1*$^{-/y}$ inhibitory neurons show subtype-specific changes in gene expression. A. Volcano plot of inhibitory neuron 1 differential gene expression with 10 most differentially expressed genes labelled. Downregulated genes labelled in blue, upregulated genes in red. * -log10(p-adj) for *Fmr1* capped at 15 for presentation (actual -log10(p-adj)=68.2). **B.** Volcano plot of differential gene expression in the inhibitory neuron 2 subcluster. * -log10(p-adj) for *Fmr1* capped at 15 for presentation (actual -log10(p-adj)=31.1). **C.** Volcano plot of differential gene expression in the inhibitory neuron 3 subcluster. * -log10(p-adj) for *Fmr1* capped at 15 for presentation (actual -log10(p-adj)=30.5). **D.** Volcano plot of differential gene expression in the inhibitory neuron 4 subcluster. * -log10(p-adj) for *Fmr1* capped at 15 for presentation (actual -log10(p-adj)=36.4). **E.** Volcano plot of differential gene expression in the inhibitory neuron 5 subcluster. **F.** Volcano plot of differential gene expression in the inhibitory neuron 7 subcluster.

6.3 Discussion

The second postnatal week is a key stage in the development of the S1 cortex, during which *Fmr1*$^{-/y}$ rats show significant alterations in the function (Chapter 3) and structure of S1 excitatory neurons (Chapter 4), as well as density of a specific subtype of inhibitory interneurons (Chapter 4). I hypothesized that these diverse changes could be underlain by cell type-specific differences in gene expression, that are not caused by the loss of FMRP directly. In this chapter, I have investigated single-cell level transcriptomic changes in the developing S1 of *Fmr1*$^{-/y}$ rats at P9. These changes differed based on cell type, suggesting that the loss of FMRP can have a range of consequences that are not universal.

6.3.1 Excitatory neurons

In line with FMRP typically being highly expressed in neurons (Till *et al.*, 2012; Gholizadeh, Halder and Hampson, 2015; Seo *et al.*, 2022), excitatory neurons were the most affected cell type, with common pathways – such as mitochondrial and ribosomal gene upregulation – affected in upper layer (L2-4) neuronal subtypes, while deep layer (L5-6) neurons shared changes in synaptic and developmental genes. Neurons in the upper cortical layers, and especially L4 SCs could be particularly sensitive to the loss of FMRP, as they show the highest number of differentially expressed genes relative to WT. Upregulation in mitochondrial genes was prevalent across upper layer excitatory neuronal clusters, in agreement with a similar proteomic finding in the hippocampal neurons of juvenile *Fmr1*$^{-/y}$ mice (Seo *et al.*, 2022). In Chapter 3 I have shown that L4 SCs are hyperexcitable during the second postnatal week in *Fmr1*$^{-/y}$ rats. Thus, mitochondrial genes could be upregulated in the hyperexcitable excitatory neurons to match their increased energy demand, as mitochondrial gene expression is known to be regulated by neuronal activity (Hevner and Wong-Riley, 1993; Zhang and Wong-Riley, 2000). Therefore, in order to verify this connection, it would be interesting to test whether rescuing hyperexcitability in these neurons could have an effect on their mitochondrial function and vice versa. However, mitochondrial function is itself deficient in the absence of FMRP, as mitochondrial Ca^{2+} homeostasis is disrupted in *Fmr1*$^{-/y}$ mouse neurons, alongside

inefficient respiration and elevated production of reactive oxygen species (El Bekay *et al.*, 2007; Griffiths *et al.*, 2020; Geng *et al.*, 2023). Therefore, the upregulation of inefficient energy production in neurons could further disrupt neuronal function through oxidative stress, supported by the significant enrichment in GO terms such as cellular response to oxygen levels I found in *Fmr1*$^{-/y}$ excitatory neurons (Figure 6.6C).

Ribosomal subunit genes were upregulated in excitatory neurons overall, as well as in several excitatory neuron subtypes, suggesting that ribosomal production could be increased in the *Fmr1*$^{-/y}$, likely in conjunction with protein translation. This in turn could affect processes such as synaptic plasticity. Indeed, elevated ribogenesis and protein production have previously been shown to contribute to the excessive mGluR-LTD in the CA1 of 4-5 week old *Fmr1*$^{-/y}$ mice and rats, a key phenotype underlying their hippocampal dysfunction (Huber *et al.*, 2002; Osterweil *et al.*, 2010; Till *et al.*, 2015; Seo *et al.*, 2022). Such an increase in the rate of translation does not lead to the accumulation of excess proteins within the cell, since is it matched by a compensatory upregulation of protein degradation via the ubiquitin proteasome system (UPS; Louros *et al.*, 2023). Excessive proteostasis is in itself pathological however, as inhibiting UPS activity is able to restore typical protein synthesis levels in the hippocampus and rescue neuronal function in the inferior colliculus of *Fmr1*$^{-/y}$ mice, preventing audiogenic seizures and providing a direct link between proteostasis and neuronal hyperexcitability. However, it is currently unclear whether protein degradation is similarly affected in the S1 of *Fmr1*$^{-/y}$ rats. At a transcriptomic level, excitatory neurons in the presented dataset showed upregulation in the proteasome component gene *Psma4* but downregulation in some genes involved in the regulation of protein degradation e.g., *Arrdc4, Cbfa2t3*. Thus, a direct investigation of protein translation and degradation rates should be performed to verify whether similar changes are also present in *Fmr1*$^{-/y}$ rat S1. Nevertheless, the upregulation of ribogenesis and translation, as well as protein degradation could likely be a common mechanism in the *Fmr1*$^{-/y}$ brain, present across multiple brain areas and species. Furthermore, the data presented in this chapter suggest that ribogenesis is upregulated in postnatal development, earlier than previously reported, with

changes arising at the transcriptomic level. Whether these changes are causative to, or a side effect of the intrinsic hyperexcitability of L4 SCs is unclear, and should be explored further. Such an investigation could further solidify protein synthesis and degradation pathways as valid therapeutic targets or biomarkers for FXS.

Downregulated genes in excitatory neurons include regulators of neurite outgrowth, in agreement with the reduction in dendritic complexity at this age discussed in Chapter 4. Indeed, previous work has identified downregulation in pathways regulating morphological development and axon guidance in *Fmr1*$^{-/y}$ mice and in FXS iPSC-derived neuronal cultures, both at a transcriptome and translatome level, leading to a reduction in neurite outgrowth, dendritic length and branching (Doers *et al.*, 2014; Utami *et al.*, 2020; Donnard, Shu and Garber, 2022). In Chapter 5 I have shown that the dendritic complexity deficits of *Fmr1*$^{-/y}$ L4 SCs can be rescued through a brief treatment with the PDE4D inhibitor BPN14770. Therefore, it would be interesting to test whether such treatment also provides a rescue at the transcriptomic level, addressing the downregulation of morphogenic genes in these cells. At the same time, excitatory neurons differentially expressed several genes encoding cell adhesion molecules (e.g., *Tenm3, Robo1, Unc5a, Cdh13*), which play an important role in establishing circuit connectivity by providing axon guidance and self-avoidance cues, as well as regulating synapse development (Paradis *et al.*, 2007; Purohit *et al.*, 2012; Leyva-Díaz *et al.*, 2014; Berns *et al.*, 2018; Pederick *et al.*, 2021). Therefore, it is possible that the morphological development of excitatory neurons in the *Fmr1*$^{-/y}$ cortex is impaired beyond just dendritic complexity, but also in terms of axonal outgrowth and connectivity.

Deep cortical layer excitatory neurons show downregulation in genes responsible for synapse assembly and function, in particular relating to AMPAR function. Therefore, it would be interesting to test whether AMPAR-mediated currents are particularly affected in L5/6 neurons in *Fmr1*$^{-/y}$ rats. A downregulation in AMPAR function could imply an alteration in the NMDA/AMPA ratio in L5/6 excitatory neurons, which has been shown in L4 SCs and CA1 pyramidal neurons of *Fmr1*$^{-/y}$ mice (Pilpel *et al.*, 2009; Booker *et al.*, 2019). This in turn could lead to an increase in the density of silent synapses and impair synaptic plasticity processes such as LTP, leading

to changes in the processing of sensory stimuli in the deep cortical layers. In fact, L5/6 neurons of juvenile *Fmr1*$^{-/y}$ mice are significantly less responsive to whisker stimulation, with a higher threshold for sensory-driven neuronal recruitment and impaired homeostatic plasticity in response to sensory deprivation (Lakhani *et al.*, 2025). Additionally, the downregulation of VEGF signalling in deep cortical layer excitatory neurons, could affect their connectivity, as intracellular signalling via VEGF receptors typically influences neuronal morphology by promoting neurite extension and axonal outgrowth (Rosenstein *et al.*, 2003). While L4 is the primary recipient of direct thalamocortical inputs, L5 and L6 neurons also receive a portion of the same afferents (Constantinople and Bruno, 2013). In addition to innervating other cortical regions, a specific subtype of L6 neurons, the infrabarrel corticothalamic neurons, send out their axonal projections into the thalamus, forming a feedback loop (Crandall *et al.*, 2017). In this way, changes in the synaptic properties of L6 neurons could paradoxically influence the thalamic inputs onto L4 SCs, further disrupting sensory processing in the barrel cortex of *Fmr1*$^{-/y}$ rats. However, very little is known about the function of L6 neurons in models of FXS, as research typically focuses on the upper cortical layers L2-4. Therefore, these findings warrant further functional validation e.g., through whole-cell patch clamp recordings in L6 neurons to investigate their synaptic properties and connectivity.

6.3.2 Inhibitory neurons

The interneuron subcluster with the highest number of DEGs was inhibitory neuron 1, which I hypothesize could consist of future PV^{+} interneurons. Although this was not confirmed explicitly as PV is not expressed at P9, if true, PV^{+} interneurons could be the interneuron subtype that is the most affected by the loss of FMRP. In the visual cortex of *Fmr1*$^{-/y}$ mice, PV^{+} interneuron dysfunction drives deficits in a visual discrimination task (Goel *et al.*, 2018). In S1, PV^{+} interneurons and their precursors have been shown to be particularly vulnerable during cortical development, showing intrinsic and whisker-evoked hypoactivity, which drives some of the circuit-level deficits and E/I imbalance of the somatosensory cortex in *Fmr1*$^{-/y}$ mice (Kourdougli *et al.*, 2023). In the second postnatal week, fast-spiking (putative

PV$^+$) interneurons of *Fmr1*$^{-/y}$ mice exhibit altered intrinsic properties and reduced functional connectivity, which gives rise to mistimed and ineffective feedforward inhibition and ultimately – impaired sensory processing in L4 of the barrel cortex (Domanski *et al.*, 2019). However, here the inhibitory neuron 1 subcluster showed upregulation in genes promoting cell adhesion, connectivity and neuronal projections, as well as developmental genes, in opposition to what is known about PV$^+$ interneurons in the *Fmr1*$^{-/y}$. Upregulation of connectivity-regulating genes in interneurons, and especially fast-spiking PV$^+$ interneurons, could constitute a homeostatic compensatory response to the hyperexcitability of excitatory neurons such as L4 SCs in an attempt to quench excess activity and restore E/I balance (Antoine *et al.*, 2019). It is however unclear if this upregulation translates into a real increase in synaptic connections between interneurons and their target excitatory neurons, as well as functional connectivity, which could still be impaired despite an increase in the expression of connectivity-regulating genes.

Additionally, I found that *Sst* was upregulated in inhibitory neurons as a whole, but not in any particular interneuron subcluster, suggesting mild but diffuse overexpression. This falls in line with *Sst* upregulation in the bulk transcriptome of *Fmr1*$^{-/y}$ mice identified by Kourdougli *et al.* (2023), and supports the increased Sst-14$^+$ cell density described in Chapter 4, while implying that in the *Fmr1*$^{-/y}$ rats, *Sst* could be broadly overexpressed in multiple transcriptomic types of interneurons, rather than caused by an increase in expression a particular subgroup, as *Sst*-expressing interneurons were present in multiple transcriptomically distinct subclusters. *Sst* was not found to be expressed in non-interneuron cell types (not shown), further suggesting that the increase in Sst-14$^+$ cell density (Chapter 4) likely corresponds to a true shift in Sst interneuron abundance in the developing S1 of *Fmr1*$^{-/y}$ rats.

6.3.3 General and non-neuronal changes

I have identified multiple differentially expressed genes in the astrocytes, microglia and OPCs of *Fmr1*$^{-/y}$ rats. While the function of non-neuronal cells in the FMRP-deficient brain is beyond the scope of this thesis, it would be interesting to

investigate these in more detail. *FMR1*-KO iPSC-derived cortical organoids have an increased number of GFAP$^+$ astrocytes, similarly to *Fmr1*$^{-/y}$ mice (Lee *et al.*, 2019; Brighi *et al.*, 2021). Astrocytes have been shown to contribute to neuronal hyperexcitability in *Fmr1*$^{-/y}$ cell cultures in a cell non-autonomous manner via S100β (Sharma *et al.*, 2023) and in *Fmr1*$^{-/y}$ mouse hippocampus via reduced K^+ reuptake through Kir4.1 channels (Bataveljic *et al.*, 2024). As such, astrocytes can significantly affect the activity and function of neurons, highlighting the need to further investigate the astrocyte-specific changes in *Fmr1*$^{-/y}$ rats. Likewise, loss of FMRP has previously been associated with changes in myelination, with white matter abnormalities and a delay in myelination during the early brain development of *Fmr1*$^{-/y}$ mice (Pacey *et al.*, 2013; Shi *et al.*, 2019). Therefore, a further investigation of the transcriptomic changes in OPCs could help to verify the mechanisms through which such a delay could arise, if likewise present in *Fmr1*$^{-/y}$ rats.

It is important to consider that rather than influencing transcription, FMRP canonically acts as a translational repressor (Darnell *et al.*, 2011). Transcriptomic approaches such as snRNAseq are thus not able to reliably detect alterations in the expression of direct FMRP targets, which are repressed at a translational level. Therefore, any transcriptomic changes discussed here form compensatory mechanisms and are unlikely to be caused by the loss of FMRP directly. Cell type-specific phenotypes in models of FXS have previously been suggested to arise due to FMRP having different functions in various cell types (Kalmbach, Johnston and Brager, 2015; Brandalise *et al.*, 2020). However, it is also likely that these changes are caused by different mechanisms used by specific types of cells to compensate for the loss of FMRP, which can include transcriptomic changes. Ultimately, a major limitation of this dataset is that it can only describe changes in the expression of genes in individual cells, but it is not able to show how these changes could relate to function. One potential approach to address this issue is Patch-seq, which enables the direct correlation of a neuron's intrinsic physiological properties with its transcriptome (Cadwell *et al.*, 2016; Fuzik *et al.*, 2016). As such, the implementation of Patch-seq to explore the developmental changes in *Fmr1*$^{-/y}$ neurons will be discussed in Chapter 7.

6.3.4 Summary

In summary, in this chapter I have uncovered cell-type specific transcriptomic changes in the developing barrel cortex of *Fmr1*$^{-/y}$ rats, some of which agree with previous findings in the mouse, while others are entirely novel. I have identified common mechanisms that could play an important role in the emergence cortical dysfunction of the *Fmr1*$^{-/y}$ rats, such as elevated expression of genes required for ribogenesis and mitochondrial energy production. Future work should focus on identifying a direct link between these transcriptomic changes and cortical function, to better understand their role in the developing *Fmr1*$^{-/y}$ cortex.

Chapter 7

Detailed Patch-seq protocol & optimization in S1 L4 SCs

7.1 Introduction

The relationship between a neuron's functional properties and its transcriptome is a question that has significant ramifications for our understanding of cellular diversity within the brain, as well as changes that occur when processes such as neuronal development are disrupted. Single-cell transcriptomic approaches can be used to uncover gene expression changes within cell types, subtypes and individual cells. Nevertheless, extensive validation is necessary to confirm the functional implications of any transcriptomic changes, but even with such validation it is not possible to directly compare an individual cell's transcriptome with its physiology. To address this, a technique called Patch-seq has been developed (Cadwell *et al.*, 2016), which allows mRNA samples to be obtained from individual neurons following a whole-cell patch clamp recording in the same cell. This technique enables the direct comparison of a cell's transcriptome with its physiology, and occasionally even morphology. In previous years, Patch-seq has been implemented in large research centres such as the Allen Brain Institute to deeply profile the cell diversity of the human and mouse brains (Cadwell *et al.*, 2016; Fuzik *et al.*, 2016; Muñoz-Manchado *et al.*, 2018; Gouwens *et al.*, 2020; Scala *et al.*, 2021). In these studies, hundreds of neurons were recorded and sequenced, giving rise to detailed transcriptomic, electrophysiological and morphological classifications of neuronal subtypes. In the previous chapters, I have identified the functional, anatomical and transcriptomic changes that occur during the somatosensory cortex development in *Fmr1*$^{/y}$ rats. Additionally, in Chapter 5, I discussed how a brief treatment with BPN14770 can rescue some, but not all aspects of the disrupted developmental

trajectory of L4 SCs in *Fmr1*$^{-/y}$ rats. However, it is unclear what mechanisms underlie this selective rescue for some phenotypes like morphology, and lack thereof for others e.g., intrinsic properties. In order to bridge this gap, I aimed to implement Patch-seq as part of the BPN14770 treatment experiments, to test whether the degree of physiological rescue within individual neurons correlates with changes in their transcriptome. However, Patch-seq is a non-trivial and highly skilled technique, while existing Patch-seq protocols are often insufficient to directly implement without extensive optimization to adapt for the chosen context – such as developing L4 SCs. In this chapter I will discuss the steps I have taken to implement and optimize the Patch-seq protocol, from recording, sample processing, library preparation until sequencing.

7.2 Recording and sample collection

While Patch-seq protocols vary in their exact details and application, the overall approach remains similar (Lipovsek *et al.*, 2021) Whole-cell patch clamp recordings are performed to investigate the neuron's activity pattern and intrinsic properties, followed by cell extraction, cDNA library preparation and sequencing to assess the neuron's transcriptome (Figure 7.1).

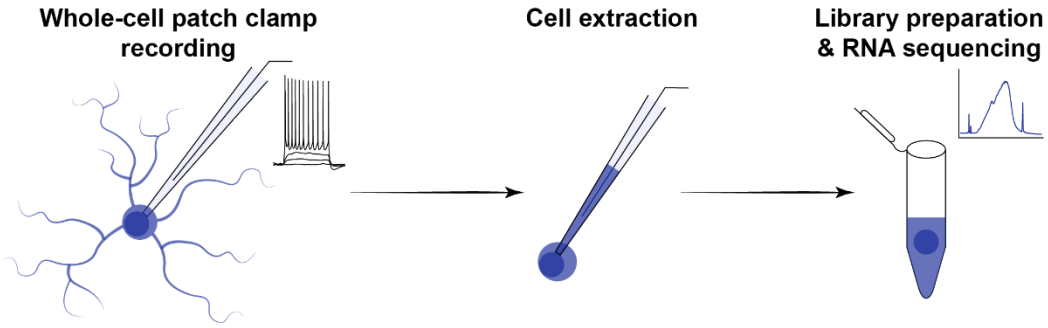

Figure 7.1. Diagram of the Patch-seq workflow. Whole-cell patch clamp recordings are performed to assess the electrophysiological properties of L4 SCs. Following a recording, the cell is extracted to be used for cDNA library preparation and RNA sequencing.

For Patch-seq recording and sample collection I followed the published protocol from Lipovsek, Browne and Grubb (2020), which was developed for small interneurons within the olfactory bulb, thus more suitable for the small L4 SCs. Whole-cell patch clamp recordings were obtained from WT and *Fmr1*$^{-/y}$ rat L4 SCs at P9-12 and BPN14770/vehicle-treated WT and *Fmr1*$^{-/y}$ rat L4 SCs at P10-13 (data presented in Chapter 5). Untreated samples were primarily used in the protocol optimization, while BPN14770-treated samples were used for sequencing (see Section 7.5). Whole-cell patch clamp recordings were performed like previously (Section 2.2), with modifications to provide a clean, RNase-free environment and avoid contamination of samples during collection. Specifically, the 8 mM Cl^- K-gluconate internal solution was modified to account for the change in osmolarity after the addition of an RNase inhibitor (295-315 mOsm with RNase inhibitor, 245-265 mOsm without; Table 7.1), which was necessary to prevent RNA degradation during the recording (Cadwell *et al.*, 2016). The internal solution was made in a PCR cabinet using nuclease-free water and molecular biology-grade reagents. 8µl/ml of SUPERaseIn RNase inhibitor (final concentration – 0.16 U/µl; AM2696, Invitrogen)

was added prior to the recording. All equipment was thoroughly wiped with RNase-Zap (AM9780, Invitrogen), the electrode holder was rinsed with RNase-Zap, 70% ethanol and nuclease free water. All glassware was autoclaved before every use. Recording ACSF was prepared according to previous protocols (Chapter 2; Table 2.1) using Patch-seq-dedicated molecular biology-grade reagents (in nuclease-free solution form where possible) and autoclaved double-deionized water. Glass capillaries were autoclaved and pulled in a dedicated RNase-free puller immediately before each recording. Recording pipettes used were smaller than usual, typically of 5-8 MΩ resistance, which was necessary for the nuclear corking approach (Lipovsek, Browne and Grubb, 2020). Sterile filters were applied to the tubing and changed after every extraction.

Table 7.1. Composition of modified 8 mM Cl^- potassium gluconate internal solution used for Patch-seq recordings.

	Concentration (mM)
K-Gluconate	110
KCl	4
EGTA	0.5
HEPES	10
$MgCl_2$	2
Na_2ATP	2
Na_2GTP	0.3
Na_2Phosphocreatine	10
Biocytin	5.4

I applied the same quality control criteria as in standard whole-cell patch clamp recordings: R_a<30 and changed <20% from beginning to end of the recording, RMP<-50 mV, at least one AP fired exceeding 0 mV. Previous reports suggest that measurements obtained under Patch-seq conditions are comparable to those recorded under standard whole-cell patch clamp, with minor changes reflective of the adjustments in internal solution composition (Lee *et al.*, 2021). As such, I compared intrinsic physiology measurements from P9-12 WT and *Fmr1*$^{-/y}$ L4 SCs recorded in traditional whole-cell patch clamp conditions (presented in Chapter 3) to

Patch-seq (Figure 7.2A). Surprisingly, I found that Patch-seq conditions significantly affect some, but not all intrinsic properties of L4 SCs. The overall AP firing pattern (including depolarization block in *Fmr1*$^{-/y}$ but not WT cells), resting membrane potential and rheobase were not affected by Patch-seq (Figure 7.2B-D), in accordance with previous reports (Cadwell *et al.*, 2016; Lee *et al.*, 2021). While Patch-seq conditions had no effect on the input resistance of *Fmr1*$^{-/y}$ cells, they significantly increased the input resistance of WT neurons, entirely abolishing the genotype difference seen under standard recording conditions (Figure 7.2E). Likewise, the voltage threshold and AP amplitude were increased in Patch-seq recordings in both genotypes (Figure 7.2F-G). Patch-seq conditions also affected the AP kinetics, eradicating the genotype differences during the rising phase in standard whole-cell patch clamp recordings, while having no effect on the decay (Figure 7.2H-J). Other electrophysiological properties, such as the membrane time constant, F-I slope and AP half-height duration (not shown) were not affected by the recording conditions and were comparable between standard whole-cell patch clamp and Patch-seq.

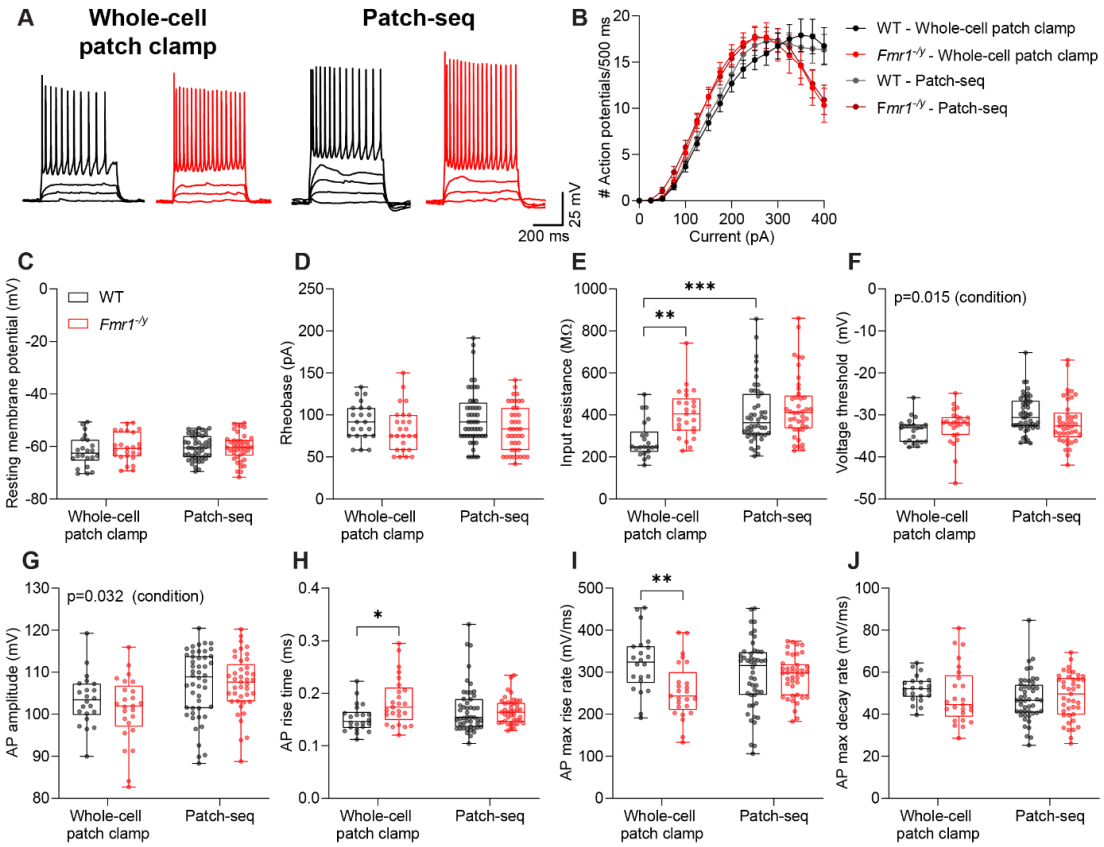

Figure 7.2. Patch-seq recording conditions significantly affect several intrinsic physiology parameters in L4 SCs. **A.** Representative AP firing traces from WT (black) and *Fmr1*$^{-/y}$ S1 L4 SCs recorded under standard whole-cell patch clamp (left) and Patch-seq conditions. **B.** Patch-seq does not affect the overall AP firing pattern of L4 SCs in either genotype. **C.** Resting membrane potential is not affected by recording condition and genotype (GLMM; condition: F=0.82, p=0.37; genotype: F=0.02, p=0.88; condition × genotype: F=0.02, p=0.89). **D.** Rheobase does not differ between conditions and trends towards a decrease in *Fmr1*$^{-/y}$ (GLMM; condition: F=0.32, p=0.57; genotype: F=4.22, p=0.052; condition × genotype: F=0.02, p=0.89). **E.** Patch-seq selectively increases the input resistance of WT L4 SCs (GLMM; condition: F=10.89, p=0.003; genotype: F=13.32, p=0.001; condition × genotype: F=5.98, p=0.021; log-transformed). **F.** Voltage threshold is more depolarized in Patch-seq recordings (GLMM; condition: F=6.71, p=0.015; genotype: F=0.44, p=0.51; condition × genotype: F=0.41, p=0.53). **G.** AP amplitude is increased in Patch-seq recordings (GLMM; condition: F=11.00, p=0.003, genotype: F=1.16, p=0.29; condition × genotype: F=1.20, p=0.29). **H.** AP rise time shows a significant interaction between recording condition and genotype and a tendency towards an increase in *Fmr1*$^{-/y}$ (p=0.063) between recording conditions (GLMM; condition: F=0.21, p=0.65; genotype: F=3.59, p=0.071; condition × genotype: F=4.81, p=0.039). **I.** The maximum rise rate shows a significant interaction between recording condition and genotype and a tendency towards an increase in *Fmr1*$^{-/y}$ (p=0.064) between recording conditions (GLMM; condition: F=0.09, p=0.76; genotype: F=5.59, p=0.027; condition × genotype: F=4.38, p=0.047). **J.** The maximum decay rate is not affected by recording condition and genotype (GLMM; condition: F=0.70, p=0.41; genotype: F=0.59, p=0.46; condition × genotype: F=1.13, p=0.30). Whole-cell patch clamp: WT: n=22 cells from N=6 animals, *Fmr1*$^{-/y}$: n=25 cells from N=10 animals; Patch-seq: WT: n=48 cells from N=9 animals, *Fmr1*$^{-/y}$: n=41 cells from N=10 animals.

Following a successful recording, I began applying negative pressure to aspirate the cytoplasmic contents into the recording pipette until the soma was noticeably smaller and the nucleus was visible. The cell's nucleus and contents were then extracted from the slice using continuous negative pressure while the electrode was slowly retracted from the slice. This allowed the nucleus to follow the electrode while the electrical seal was maintained throughout the extraction. Many cells failed at this stage, due to a rupture in the membrane and loss of the electrical seal, particularly at the last stage of retracting the pipette from the surface of the slice. Once the membrane was resealed (as evidenced by a gigaOhm seal), I removed the pipette from the bath and carefully broke the tip into the bottom of a pre-labelled PCR tube containing the storage buffer and expelled the remaining solution. The tube was immediately snap-frozen on dry ice. Each extraction was given a score based on criteria delineated in the Lipovsek *et al.* protocol (Table 7.2). 'Perfect' samples were extracted in <5 minutes from the end of recording, with a nucleus present at the tip of the recording pipette, no debris and an electrical seal stably maintained throughout the extraction (Figure 7.3A). In contrast, 'bad' samples did not contain the nucleus and/or had visible debris present at the recording pipette, while the electrical seal was entirely lost during extraction (Figure 7.3B). Collected samples were stored at -80°C until processing. Only samples with a 'perfect' or 'very good' extraction score were used for further processing and sequencing.

Table 7.2. Summary of criteria for assessing Patch-seq extraction quality. From Lipovsek *et al.* 2020.

Nucleus	**Electrical seal**	**Debris**	**Extraction time**	**Tip touch**	**Extraction score**
At tip	Perfect	No debris	<5 min	No touch	Perfect
At tip/ In pipette	Perfect/ Unstable	No debris	<10 min	No touch	Very good
At tip/ In pipette	Unstable/ High I_{leak}	No debris	<10 min	No touch	Good
In pipette/ Absent	High I_{leak}/lost	Some debris	>10 min	No touch	Poor
Absent	Lost	Debris present	>10 min	Touch	Bad

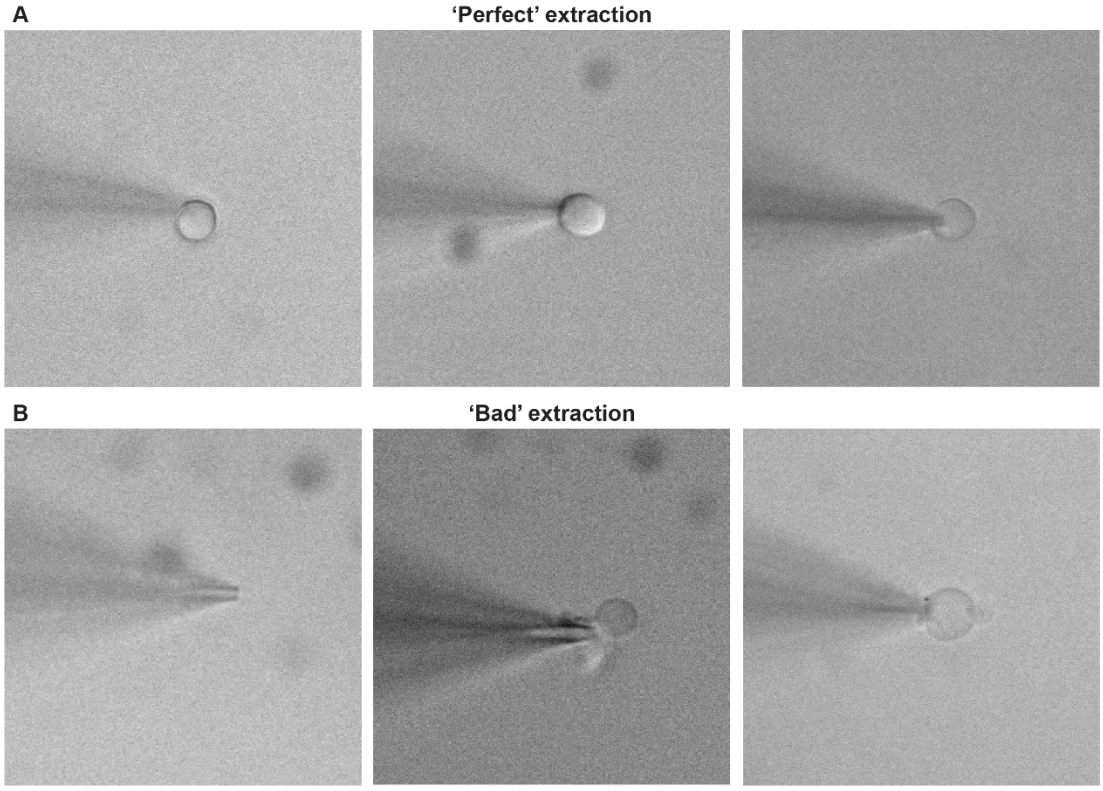

Figure 7.3. Example Patch-seq cell extractions. A. Example images of L4 SCs with a 'perfect' extraction score. Nucleus is present at the tip of the recording pipette with no debris present. **B.** Example images of L4 SCs with a 'bad' extraction score. Nucleus is not present and/or debris are visible at the tip of the recording pipette.

7.3 Sample processing optimization

A vast majority of published Patch-seq studies uses the SMART-seq workflow for cDNA synthesis and library preparation, due to its high sensitivity even with minimal input material (reviewed in Lipovsek *et al.,* 2021). The inclusion of unique molecular identifiers (UMIs) was preferable, as it allows to control for amplification bias and improve the quantification accuracy (Kivioja *et al.*, 2012). Therefore, for Patch-seq sample processing I used the Takara Bio SMART-seq mRNA LP (with UMIs) kit (634765, Takara Bio). As this kit is typically used for library preparation from FACS-sorted cells, adapting it to the Patch-seq protocol required optimization. I used gel electrophoresis for a qualitative assessment of each step's results.

7.3.1 Sample lysis and storage buffer

Positive and negative controls were included during each step of sample processing. For positive control, 4 µl total mouse brain RNA (kit component) was used at a 10 pg/µl dilution. Negative control was an equivalent volume of nuclease-free water. Samples were thawed on ice, mixed by vortexing and centrifuged. Initially I stored the samples in 2 µl of the kit's recommended storage buffer, BD FACS Pre-sort buffer (563503, BD Biosciences), with lysis as the first stage of the sample processing protocol:

Table 7.3. Sample preparation. Adapted from Takara Bio.

	Sample	**+ve ctrl**	**-ve ctrl**
10X Reaction Buffer[1]	1 µl	1 µl	1 µl
Nuclease-free water	5.5 µl	5.5 µl	9.5 µl
Diluted control RNA	-	4 µl	-
Sample[2]	4 µl	-	-
Total	10.5 µl	10.5 µl	10.5 µl

[1]10X Reaction Buffer:19 µl 10X Lysis Buffer + 1 µl RNase inhibitor

[2]Sample: 2 µl internal solution (containing sample) + 2 µl storage buffer

However, as most published Patch-seq protocols recommend storing samples in a lysis buffer, I also trialled the 10x Lysis Buffer (635013, Takara Bio) to make a storage buffer (Table 7.4), allowing to proceed immediately into the incubation with Oligo-dT and first-strand cDNA synthesis (Figure 7.4A):

Table 7.4. Composition of the lysis storage buffer.

	Volume per sample (µl)
10x Lysis Buffer	0.95
SUPERaseIn RNase inhibitor	0.05
Nuclease-free water	7.5
Total	8.5

In this case, 2 µl of internal solution containing the sample was expelled into 8.5 µl of storage buffer, now equivalent to the product from Table 7.1. Positive and negative controls were prepared according to Table 7.1 regardless of the buffer used for sample storage. Direct comparison of storage buffers showed that while cDNA can be obtained when BD FACS Pre-sort buffer is used, using a lysis buffer gives better results, with a larger proportion of longer cDNA fragments (>766 bp; Figure 7.4B). Therefore, the lysis buffer was used for all subsequent recordings.

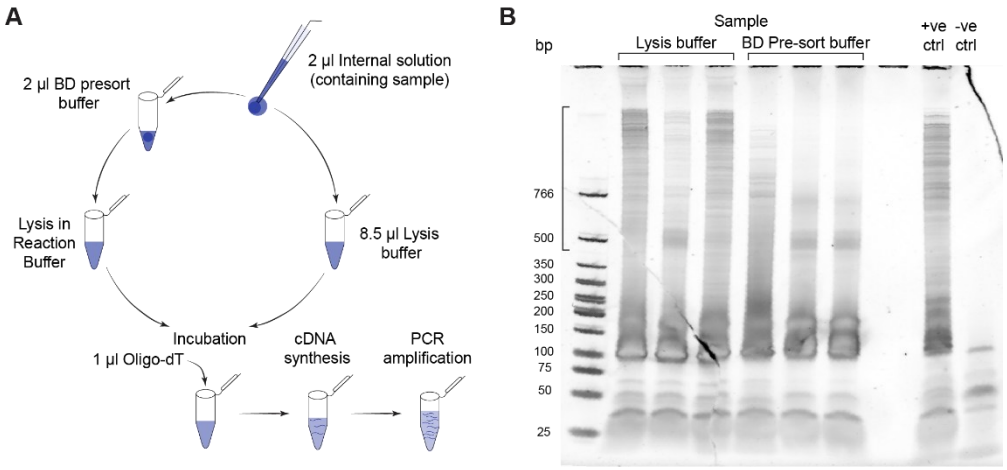

Figure 7.4. Storage buffer optimization. A. Schematic of differences in workflow when the BD FACS Pre-sort buffer or the lysis buffer are used. **B.** Samples stored in lysis buffer show larger cDNA fragments compared to BD FACS Pre-sort buffer. Presented samples were not purified after PCR amplification. Bracket shows the desired size range.

7.3.2 First-strand cDNA synthesis

1 µl of SMART-Seq mRNA Oligo-dT was added to each sample. Prepared samples were mixed by vortexing, centrifuged and immediately incubated in a pre-heated thermal cycler at 72°C for 3 minutes and placed on ice afterwards for 2-10 mins. During the incubation RT-PCR master mix was prepared:

Table 7.5. Composition of the RT master mix.

	Volume per sample (µl)
5X Ultra Low First-Strand Buffer	4
SMART-Seq mRNA UMI TSO (50 µM)	1
GTP (20 mM)	1
RNase Inhibitor (40 U/µl)	0.5
SMARTScribe Reverse Transcriptase (100 U/µl)	2
Total	8.5

8.5 µl of the RT master mix was added to each sample, contents mixed by vortexing and centrifuged. Samples were then placed in a thermal cycler and the following program was run:

Table 7.6. RT-PCR program setup.

Temperature (°C)	**Time (mins)**
42	90
70	10
4	forever

7.3.3 cDNA amplification by PCR

In order to amplify the cDNA, 30 µl of the PCR master mix was added to each sample:

Table 7.7. Composition of the PCR master mix.

	Volume per sample (µl)
SeqAmp CB PCR Buffer	25
SMART-Seq mRNA PCR Primer Mix	1.2
Nuclease-free water	2.8
SeqAmp DNA Polymerase	1
Total	30

The samples were placed in a preheated thermal cycler and the following program was run:

Table 7.8. PCR program setup.

Temperature (°C)	**Time**	
95	1 min	
98	10 sec	
65	30 sec	**x cycles**
68	3 min	
72	10 min	
4	forever	

To optimize the PCR step, I tested 26-30 of PCR cycles using the positive control (Figure 7.5A). 30 cycles consistently yielded a range of cDNA sizes with the most reproducible results. Consequently, I tested whether 30 PCR cycles is sufficient to produce a similar size range in 9 Patch-seq samples (Figure 7.5B). While some samples (e.g., 1-2) failed (n=5), some produced a range of cDNA fragments, including larger fragments >766 bp (n=4). As 30 PCR cycles gave the most consistent results both in +ve control and Patch-seq samples, I used 30 cycles for the remainder of the samples.

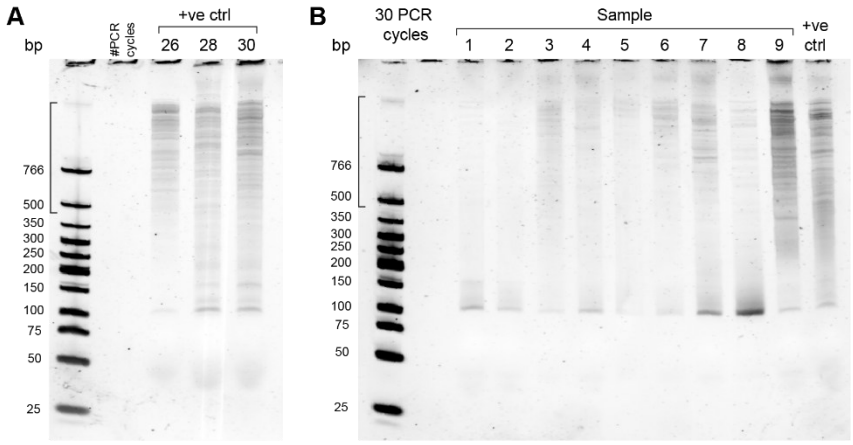

Figure 7.5. PCR cycle number optimization. A. Representative image of PCR optimization results. 26-30 PCR cycles were tested using the positive control. **B.** PCR was tested on Patch-seq samples (1-9) and positive control at 30 cycles. Presented samples were purified using AMPure XP SPRI beads at 0.7x bead:sample ratio. Bracket indicates the expected size range.

7.3.4 Bead purification

To purify the amplified cDNA and remove PCR primers, I used AMPure XP SPRI beads (A63881, Beckman Coulter) according to the manufacturer protocol, aiming to remove cDNA fragments <200 bp. In order to optimize the bead:sample ratio, I tested a range of bead concentrations on 5 µl of Low molecular weight DNA ladder diluted in 45 µl H_2O (N3233S, New England Biolabs; Figure 7.6A). As 0.7x and 0.6x were able to remove the smaller cDNA fragments, I next tested these concentrations using the +ve control (Figure 7.6B). Bead:sample ratio of 0.7x removed most cDNA fragments <200 bp without compromising cDNA quantity, and was thus used for all subsequent experiments.

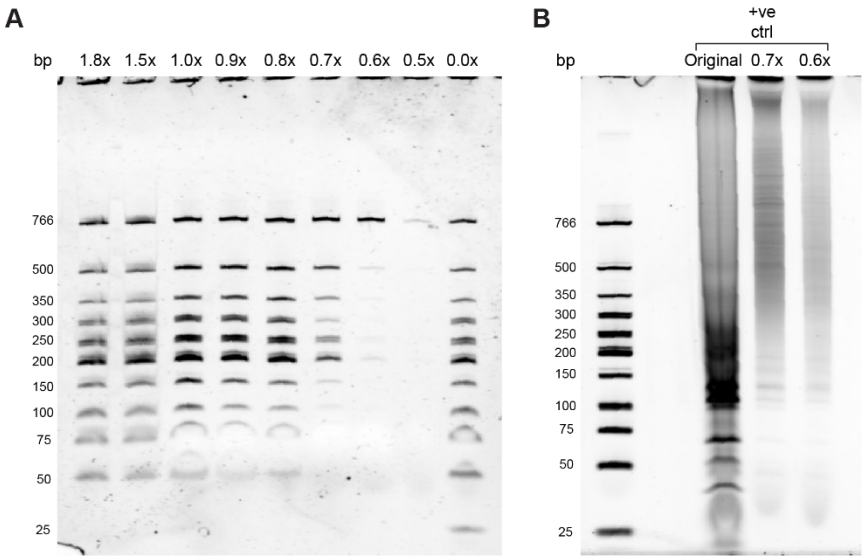

Figure 7.6. Bead concentration optimization. A. A range of bead:sample ratios was tested using the Low Molecular Weight DNA ladder. **B.** Comparison of no bead purification (original, left), 0.7x (middle) and 0.6x (right) bead:sample ratios using +ve control.

7.3.5 Selecting samples for library preparation

Since many samples failed at each stage of the protocol, for each sample I ran a downsized test PCR at 30 cycles using 2 µl of pre-amplified cDNA and 18 µl of an adjusted PCR master mix:

Table 7.9. Composition of the adjusted test PCR master mix.

	Volume per sample (µl)
SeqAmp CB PCR Buffer	10
SMART-Seq mRNA PCR Primer Mix	0.48
Nuclease-free water	7.12
SeqAmp DNA Polymerase	0.4
Total	18

After visualizing each sample using gel electrophoresis, I selected the successful samples and ran a final 30 cycle PCR using 10 µl of the remaining pre-amplified cDNA and 15 µl of PCR master mix:

Table 7.10. Composition of the PCR master mix for the final PCR.

	Volume per sample (µl)
SeqAmp CB PCR Buffer	12.5
SMART-Seq mRNA PCR Primer Mix	0.6
Nuclease-free water	1.4
SeqAmp DNA Polymerase	0.5
Total	15

All remaining samples were then quantified using the Agilent 2100 Bioanalyzer with a High Sensitivity DNA kit (NC1738319, Agilent). While the majority of samples failed to produce cDNA at this stage, I selected 8 successful samples to be used for library preparation, based on the presence of visible peaks within the expected 400 bp to 5,000 bp range (Figure 7.7). For each successful sample the cDNA concentration was quantified within a 200 bp to 3,000 bp range.

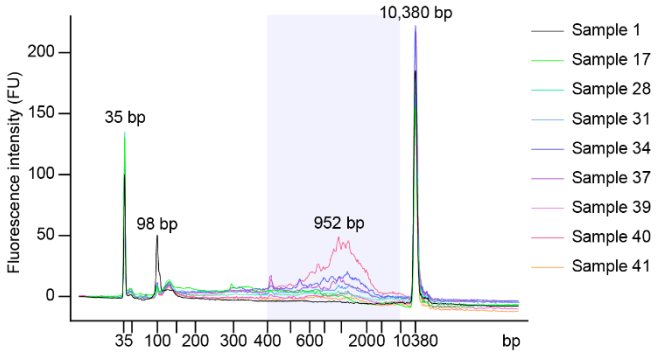

Figure 7.7. Quantification of cDNA quality. Agilent 2100 Bioanalyzer traces of a failed Patch-seq sample (Sample 1, black) and 8 successful samples (coloured). Peaks at 35bp and 10,380 bp represent the lower and upper markers respectively. Shaded area indicates the expected size range.

7.4 Library preparation

Samples were diluted in Elution Buffer (kit component) to a fixed concentration of 0.125 ng/µl and 8 µl of each diluted sample was added to tubes containing 4 µl Stem-Loop Adapters. 8 µl of Elution Buffer was used as a negative control. 4 µl of 10x FE was diluted in 36 µl FE Dilution Buffer to prepare 1x FE. 10.5 µl of Library Prep master mix was added to each sample:

Table 7.11. Composition of the Library Prep master mix.

	Volume per sample (µl)
Library Prep Buffer	4
Rxn Enhancer	3.5
Library Prep Enzyme	2
1x FE	1
Total	10.5

Samples were mixed by vortexing and centrifuged before being placed in a thermal cycler for the library preparation reaction:

Table 7.12. Library preparation program setup.

Temperature (°C)	**Time (mins)**
20	40
85	10
4	forever

For library amplification, 25.5 µl of the Library Amplification master mix was added to each sample:

Table 7.13. Composition of the Library Amplification master mix.

	Volume per sample (µl)
Amplification Buffer	21.5
PrimeSTAR HS DNA Polymerase	1
Nuclease-free water	3

2 µl of a different index from the Unique Dual Index Kit (634756, Takara Bio) was added to each sample, mixed by vortexing and centrifuged. Library amplification was performed in a thermal cycler using the following program:

Table 7.14. Library amplification program setup.

Temperature (°C)	Time	
72	3 min	
85	2 min	
98	2 min	
98	20 sec	**x cycles**
60	75 sec	
68	5 min	
4	forever	

The amplified libraries were purified individually using AMPure XP SPRI beads at 0.8x bead:sample ratio according to the manufacturer protocol. Initially I amplified the libraries using the protocol's recommended 16 cycles. However, having visualized the libraries using gel electrophoresis, I found that they were overamplified (Figure 7.8A). Thus, to optimize the library amplification, I re-ran the library preparation and amplification on the positive control using 10, 12 and 14 PCR cycles. I quantified the prepared libraries using the Agilent 2100 Bioanalyzer and found that 10 cycles were sufficient to amplify the libraries (Figure 7.8B).

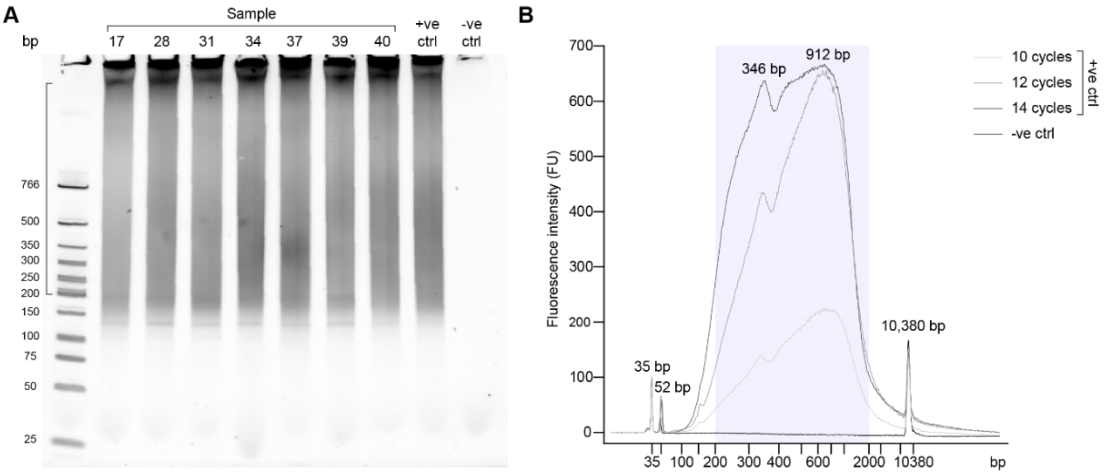

Figure 7.8. Library amplification optimization. A. Prepared libraries of Patch-seq samples and +ve control were overamplified after 16 PCR cycles. Bracket indicates the expected size range. **B.** Agilent 2100 Bioanalyzer traces of +ve control libraries amplified at 10, 12 and 14 cycles (shades of grey). Black trace shows -ve control. Shaded area indicates the expected size range.

Finally, I performed library preparation and amplification on the same Patch-seq samples at 10 PCR cycles. Amplified libraries were purified individually using AMPure XP SPRI beads at a 0.8x bead:sample ratio using the standard manufacturer protocol and eluted in 25 µl of nuclease-free water. Library quality was assessed using the Agilent 2100 Bioanalyzer with a High Sensitivity DNA kit (Figure 7.9A) before equimolar pooling of all samples (Figure 7.9B).

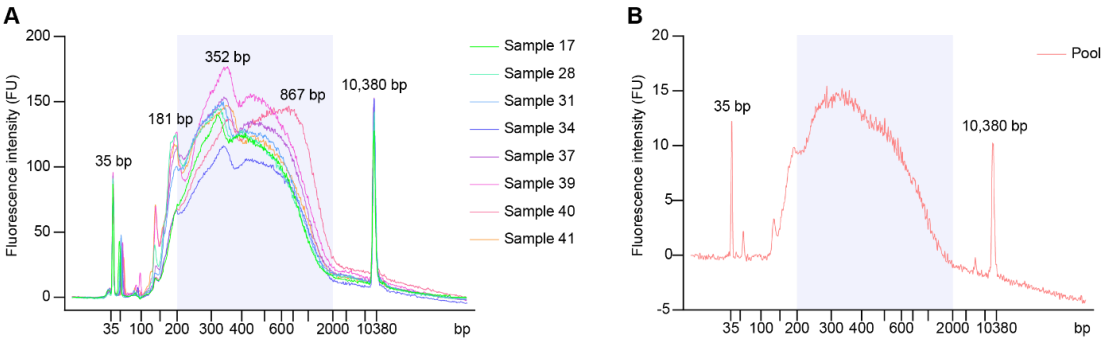

Figure 7.9. Final library quantification. A. Agilent 2100 Bioanalyzer traces of amplified Patch-seq sample libraries. **B.** Agilent 2100 Bioanalyzer trace of the pooled Patch-seq library. Shaded area indicates the expected size range.

7.5 Sequencing

The pooled library was sequenced with assistance from Dr Jamie Toombs on a MiSeq Sequencing System using a 150-cycle MiSeq Reagent kit v3 (MS-102-3001, Illumina) according to the manufacturer protocol. 3.3 million reads were obtained in total, with per sample reads ranging from 290 to 570 thousand (Table 7.15). In the interest of time, further analysis was not performed.

Table 7.15. Summary of amplified cDNA concentration, average size and reads obtained from Patch-seq samples.

Sample	cDNA concentration (ng/µl)	Average size (bp)	Reads
17	5.76	466	302,207
28	5.89	450	534,658
31	6.22	465	477,032
34	4.36	490	446,390
37	6.37	476	362,093
39	6.63	487	291,055
40	5.24	547	569,671
41	6.18	475	340,376
Total			**3,323,482**

7.6 Discussion

Patch-seq has previously been used to characterize neurons in *ex vivo* slices from various brain areas and species, identifying diverse neuronal subtypes based on their combined electrophysiological and transcriptomic features (reviewed in Lipovsek *et al*., 2021). In this chapter I detailed the steps I have taken to implement the Patch-seq technique as part of the characterization of the developmental differences in L4 SCs of *Fmr1*$^{-/y}$ rats. Following multiple optimization steps, I was able to successfully implement the Patch-seq workflow to obtain transcriptomic reads from 8 neurons following electrophysiological recordings.

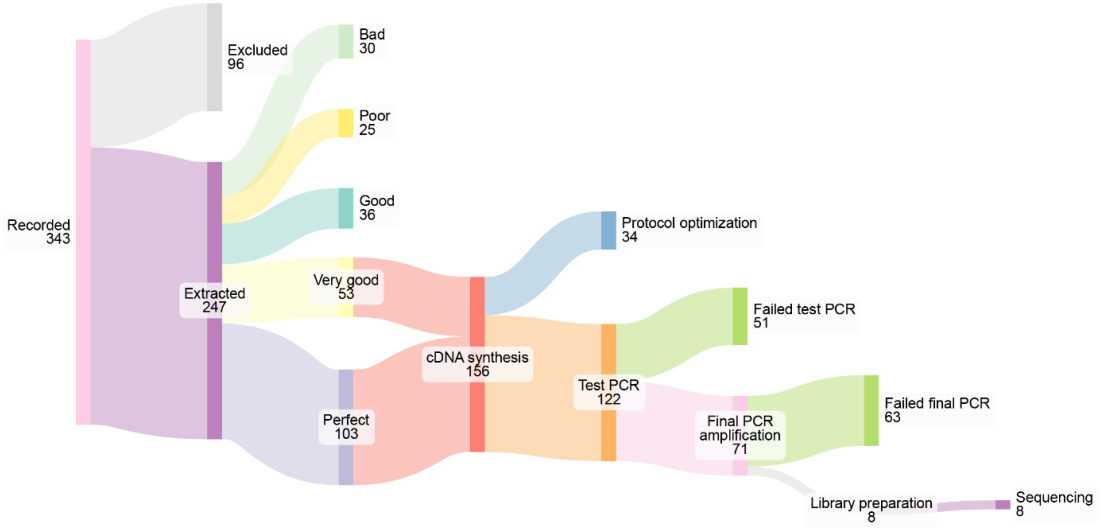

Figure 7.10. Sankey plot of Patch-seq samples showing the number of cells at each step of the protocol. From 343 recorded neurons only 8 were successfully sequenced.

I found that at each stage a large proportion of samples were unsuccessful, dramatically reducing the final yield (Figure 7.10). I was able to sequence only 8 cells, which comprised 2.3% of the total cells recorded. This was primarily due to a majority of the collected samples failing to produce good quality cDNA, despite only using cells with a 'perfect' and 'very good' extraction score for cDNA synthesis. Previously published studies included as few as 8 to as many as 4270 neurons sequenced (reviewed in Lipovsek *et al.,* 2021). However, many studies do not report how many samples were excluded and how many recordings were performed to achieve these sample sizes. Lipovsek, Browne and Grubb (2020) reported that nearly 50% of all recording attempts resulted in good quality samples, however it is not clear whether that includes all collected or sequenced samples. On the other hand, Cadwell *et al*.

(2016) claim that 80-90% of all collected samples yielded good quality cDNA. Overall, I have not been able to achieve a comparable success rate to published studies, highlighting the need for further optimization, particularly during sample collection. Additionally, the quality and quantity of cDNA obtained in this experiment likely does not match that of published studies. Amplified cDNA typically showed product with a peak at 952 bp, significantly shorter than 2,000 bp obtained in published protocols, but within the recommended range of 400-9,000 bp (Cadwell *et al.*, 2017; van den Hurk *et al.*, 2018; Lipovsek, Browne and Grubb, 2020). I also achieved fewer reads per cell (300-500 thousand) compared to the 1 million typically obtained in Patch-seq studies (Gouwens *et al.*, 2020; Lipovsek, Browne and Grubb, 2020). Likewise, the cDNA had to be amplified a lot more (30 PCR cycles) than in published protocols and studies (typically 18-20 cycles) in order to generate any product in the desired size range. This could lead to significant PCR amplification bias, where some transcripts are amplified more than others (Acinas *et al.*, 2005; Sun *et al.*, 2024). UMIs, which were included in this experiment, can be used to control for PCR bias and capture real changes in gene expression (Kivioja *et al.*, 2012). Additionally, with further optimization it may be possible to improve the success rate, as well as quality and quantity of obtained cDNA so that fewer PCR cycles are sufficient.

Few studies directly compare electrophysiological parameters obtained from standard whole-cell patch clamp recordings to Patch-seq. The main difference between a standard whole-cell patch clamp recording and Patch-seq is the presence of RNase inhibitors in the internal solution, which is necessary to prevent mRNA degradation and improve the final cDNA yield (Cadwell *et al.*, 2016). In my experience, the inclusion of RNase inhibitor in the internal solution negatively affected the health of neurons during recording, making them unstable (qualitative observation), despite using the same RNase inhibitor concentration as a published Patch-seq protocol (Lipovsek, Browne and Grubb, 2020). Cadwell *et al*. (2016) showed that the presence of RNase inhibitors does not impact the resting membrane potential of neurons over the course of recording, similarly to data presented in this chapter. Lee *et al.* (2021) found that electrophysiological data obtained from Patch-seq recordings in mouse and human cortical neurons are largely consistent with data from the traditional

whole-cell patch clamp approach, although a small shift in some features such as AP width was present. In contrast, I found that several key intrinsic properties were significantly affected by the Patch-seq conditions, including input resistance, AP amplitude and voltage threshold. Additionally, some of these changes were genotype-specific, such as the increase in input resistance in WT cells, which entirely abolished any genotype differences between WT and *Fmr1*$^{-/y}$ rats in Patch-seq recordings. It is possible that RNase inhibitors may have different effects on WT and *Fmr1*$^{-/y}$ cells due to inherent changes in RNA stability and the transcriptional milieu in the absence of FMRP expression, which has widespread roles in RNA metabolism, editing and alternative splicing (Zalfa *et al.*, 2007; Filippini *et al.*, 2017; Zhou *et al.*, 2017; F. Zhang *et al.*, 2018). Finally, it is unclear whether the Patch-seq protocol itself may influence a cell's transcriptome. While the use of RNase inhibitors during recording is necessary to preserve the mRNA sample, it could indirectly alter transcription within the cell due to changes in mRNA transcript turnover and cellular stress responses. Nevertheless, commercially available RNase inhibitors such as SUPERaseIn are not known to interfere with transcription directly (Life Technologies, 2013) and with a recording time of less than 5 mins it is likely that these effects are minor.

The overall AP firing pattern was not affected, suggesting that it could be reliably used for cell type classification, similarly to previous work (Cadwell *et al.*, 2016). However, it is important to consider that with such significant and genotype-specific changes in electrophysiology, perhaps Patch-seq is not a suitable technique to investigate specific changes in disease models. It is possible that with additional protocol optimization, these issues could be improved, but electrophysiological data obtained using Patch-seq might not be directly comparable to standard whole-cell patch clamp recording, especially when making conclusions about disease-related phenotypes, as opposed to classifying neurons based on their correlated electrophysiological and transcriptomic signatures. It would be interesting to test whether differences in the exact composition of the internal solution used and cell types recorded could contribute to the discrepancy between presented data and findings from Lee *et al*. (2021). Nevertheless, perhaps Patch-seq might be better

suited for exploring the cellular subtype diversity within the brain, rather than identifying mechanisms underlying altered functional states in disease models. In summary, although powerful, Patch-seq remains an expensive, labour-intensive and extremely low-throughput technique. Implementing this approach in a new context requires significant expertise, as well as extensive optimization, even when following a published protocol. These challenges can make Patch-seq inaccessible to many smaller research labs. While I was able to follow each stage of the workflow, further optimization is necessary to improve the success rate and quality of collected samples. Finally, considering that the modified recording conditions could significantly affect the electrophysiological properties of neurons, great caution should be exercised when comparing the properties assayed through Patch-seq to traditional whole-cell patch clamp recordings.

Chapter 8

General discussion

8.1 Summary of findings

Cortical development relies on a complex interplay of a range of genetically-encoded and activity-dependent mechanisms, which fine-tune the emergent circuit into one that is capable of learning, processing information and adapting to novel conditions (Van der Loos and Woolsey, 1973; Killackey and Belford, 1979; Crair and Malenka, 1995; Feldman *et al.*, 1998; Fukuchi-Shimogori and Grove, 2001; O'Leary and Sahara, 2008). In the absence of FMRP, this developmental fine-tuning of cortical circuits such as S1 is disrupted, leading to hyperexcitability and impaired functionality (Gibson *et al.*, 2008; Harlow *et al.*, 2010; Till *et al.*, 2012; He *et al.*, 2017; Booker *et al.*, 2019; Domanski *et al.*, 2019; Kourdougli *et al.*, 2023). Here, a detailed investigation of the developmental trajectory of the S1 in *Fmr1*$^{-/y}$ rats revealed that hyperexcitability does not arise in a linear fashion, but rather in multiple distinct phases (Figure 8.1). During the second postnatal week, cells within L4 of the S1 are intrinsically hyperexcitable which is associated with a delay in the morphological development of the dendritic arbour. At the same time, an increase in the density of Sst-14^{+} interneurons could function to balance this hyperexcitability and normalize the circuit-level activity. While the hyperexcitability subsides as the dendritic complexity matures, the altered inhibitory cytoarchitecture persists. In the fourth postnatal week the hyperexcitability emerges once again, albeit likely through a different mechanism. This previously unknown dynamic nature of altered cortical development in the *Fmr1*$^{-/y}$ rats became apparent thanks to the high temporal resolution of the characterization presented in this thesis, underscoring the importance of longitudinal analysis in studies of cortical development, with implications for other NDDs.

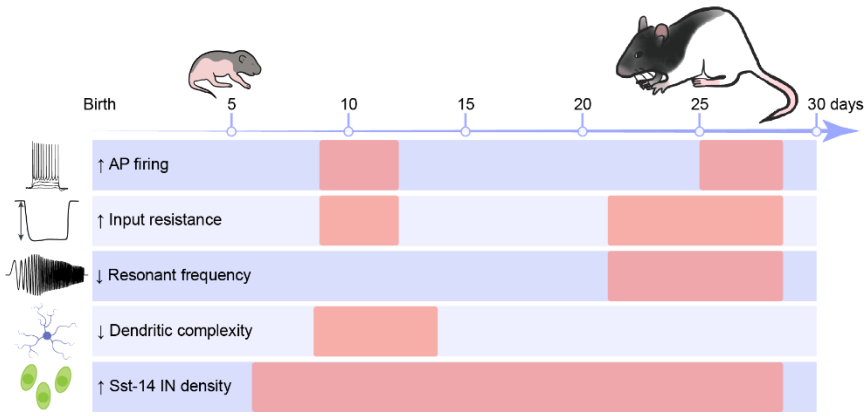

Figure 8.1. Summary of key findings. *Fmr1*$^{-/y}$ exhibit differences in their S1 development with two periods of excessive AP firing underlain by an increase in input resistance. This is underlain by a deficit in dendritic complexity in the second postnatal week and a reduction in resonant frequency in the fourth postnatal week. The density of Sst-14^{+} interneurons is increased throughout this developmental period.

Single cell transcriptomic analysis revealed cell-type specific differences in the developing S1 of *Fmr1*$^{-/y}$ rats. Upper layer excitatory neurons showed upregulation in mitochondrial and ribosomal genes, in agreement with previous studies showing elevated ribogenesis protein translation in the CA1 of adolescent *Fmr1*$^{-/y}$ mice, which underlies their altered synaptic plasticity (Osterweil *et al.*, 2010; Seo *et al.*, 2022; Louros *et al.*, 2023). Therefore, increased protein translation could be a key mechanism driving synaptic dysfunction in the *Fmr1*$^{-/y}$ brain, which arises in early development. Moreover, the same upper layer neurons downregulated genes responsible for neuronal morphogenesis, suggesting that morphological deficits in L4 SCs are likely driven by transcriptomic changes in the *Fmr1*$^{-/y}$ rats.

8.2 Role of homeostatic compensation in FXS

Despite significant structural and functional deficits at molecular, cellular and circuit levels, which individually could be predicted to have more severe downstream consequences, *Fmr1*$^{-/y}$ mouse and rat models only show some, arguably minor, behavioural phenotypes, such as learning deficits (Krueger *et al.*, 2011; Ding, Sethna and Wang, 2014; Till *et al.*, 2015; Tian *et al.*, 2017; Asiminas *et al.*, 2019; Borreca *et al.*, 2023; Ntoulas *et al.*, 2024). Moreover, *Fmr1*$^{-/y}$ mice have an increased propensity for audiogenic seizures, but no seizures at rest, despite their cortical hyperexcitability (Chen and Toth, 2001; Ding, Sethna and Wang, 2014). This suggests that effective homeostatic compensation likely takes place during development, which allows the cortical circuit to function almost normally, at least under baseline conditions.

Compensatory mechanisms are likely an inherent part of the altered developmental trajectory of S1 in the absence of FMRP. Intrinsic hyperexcitability of L4 SCs arises in early life and is consistent with a developmental delay in maturation of their dendritic arbours (Chapter 3-4). Since the morphology of *Fmr1*$^{-/y}$ L4 SCs can be rescued with a brief treatment with BPN14770 (Chapter 5), this delay is likely driven by a cAMP-dependent mechanism. This can be directly caused by the loss of FMRP – which normally inhibits the translation of several PDEs – thus leading to a broad decrease in cAMP levels in FXS (Berry-Kravis, Hicar and Ciurlionis, 1995; Kelley *et al.*, 2007; Darnell *et al.*, 2011). Additionally, upper cortical layer excitatory neurons, including L4 SCs show significant downregulation in several genes responsible for neuronal morphogenesis and neurite outgrowth, thus likely contributing to the morphological deficits of L4 SCs in *Fmr1*$^{-/y}$ rats (Chapter 6). Since FMRP primarily affects translation, any transcriptomic differences in an FMRP-deficient brain may not be caused by the loss of FMRP directly, but rather constitute compensatory changes, or arise as a result of disrupted downstream intracellular signalling cascades, including the cAMP signalling pathway, which exerts direct control of gene expression by interacting with multiple transcription factors (Sassone-Corsi, 2012). As such, impaired cAMP signalling in *Fmr1*$^{-/y}$ rat L4 SCs could give rise to their morphological deficits and consequently – intrinsic hyperexcitability by altering the expression of key genes involved in the morphological development of these neurons. Notably, as

the morphology of L4 SCs catches up to WT levels, the intrinsic hyperexcitability subsides, which could explain why the hyperexcitability at P9-12 is temporary and immediately followed by a period of typical excitability.

In addition to L4 SC hyperexcitability, the loss of FMRP has important downstream consequences on a circuit level. Previous data from the *Fmr1*$^{-/y}$ mice indicate that PV^{+} interneurons may be especially vulnerable to the loss of FMRP, which leads to their hypoactivity and hypoconnectivity, giving rise to ineffective feed-forward inhibition in the developing S1 (Goel *et al.*, 2018; Domanski *et al.*, 2019; Kourdougli *et al.*, 2023). In this thesis I showed that putative PV interneurons are uniquely impaired on a transcriptomic level, showing upregulation in multiple genes involved in regulating neuronal connectivity (Chapter 6). This could reflect a developmental delay in PV interneuron development, such that in the absence of FMRP the connectivity of PV interneurons with their targets is established and matures in later life, which has previously been found in the *Fmr1*$^{-/y}$ mouse model (Nomura *et al.*, 2017). Such a delay could thus manifest as upregulation in connectivity genes at P9 and underlie the ineffective feed-forward inhibition during the second postnatal week. The lack of changes in PV^{+} cell density could suggest that in the rat model of FXS PV interneurons are not hypoactive (like in *Fmr1*$^{-/y}$ mice), or that such hypoactivity is not temporally aligned with the activity-dependent apoptosis of excess interneurons. Furthermore Domanski *et al*. (2019) showed that in the *Fmr1*$^{-/y}$ mice PV interneurons are intrinsically hyperexcitable on immediate timescales, but hypoactive and unable to maintain firing during sustained activity, which gives rise to the inefficient FFI on a circuit level. As inhibitory function was not directly assayed in this thesis, further work is necessary to confirm whether this is also the case in *Fmr1*$^{-/y}$ rats. Nevertheless, if PV interneurons are indeed unable to provide sufficient inhibitory control in the developing S1 of *Fmr1*$^{-/y}$ rats, this deficit in inhibition could compound with the intrinsic hyperexcitability of L4 SCs to bring about an extremely overactive network. While it is likely that the developing S1 of *Fmr1*$^{-/y}$ rats could be hyperexcitable on a circuit level to an extent, compensatory changes in inhibition likely occur to stabilize the output of the S1, in line with similar findings in the ventral hippocampus of *Fmr1*$^{-/y}$ rats (Leontiadis *et al.*, 2023). In the developing S1,

this compensatory inhibitory function could be taken over by Sst^+ interneurons, which could upregulate their activity in early life (e.g. P9-12) to control network output. This however could disrupt the activity-dependent apoptosis of excess interneurons which occurs in the second postnatal week (Southwell *et al.*, 2012; Priya *et al.*, 2018), giving rise to the increased density of Sst-14 interneurons seen in *Fmr1*$^{-/y}$ rats (Chapter 4) and mice (Kourdougli *et al.*, 2023). Therefore, early life hyperexcitability in the absence of FMRP expression could drive circuit-level compensatory changes to the activity and abundance of Sst-14 interneurons in the S1. Beyond the second postnatal week there may no longer be a mechanism to allow for the selective adjustment of interneuron numbers, meaning that this change is likely permanent, supported by the fact that an increase in Sst^+ interneurons was also reported in the S1 of adult *Fmr1*$^{-/y}$ mice (Kourdougli *et al.*, 2023). However, especially if accompanied by an increase in Sst-14-mediated signalling, this increase could paradoxically further drive hyperexcitability of L4 SCs in a dysregulated feedback loop (Chapter 4). As such, I propose that the second period of intrinsic hyperexcitability in *Fmr1*$^{-/y}$ L4 SCs during the fourth postnatal week could arise as a result of excessive Sst-mediated signalling, which together with the loss of FMRP's control of PDE expression, contribute to a reduction in intracellular cAMP levels. This in turn could disrupt the activation and kinetics of the I_h current, in line with similar findings in *Fmr1*$^{-/y}$ mouse L4 SCs (Booker *et al.*, 2019). As such, changes which originally arise in the S1 of *Fmr1*$^{-/y}$ rats as a compensatory mechanism in response to increased intrinsic excitability in early development could themselves disrupt cortical function in later life.

8.3 Species differences and future considerations

Whether driven by the loss of FMRP directly, or indirectly through compensatory mechanisms, the developmental trajectory of S1 in *Fmr1*$^{-/y}$ rats is indeed altered. Notably, while the data presented in this thesis fall largely in agreement with published findings from the *Fmr1*$^{-/y}$ mice, the rat model of FXS does not replicate all of the phenotypes described in the mouse. For example, rather than due to a change in I_h (Booker *et al.*, 2019), cortical hyperexcitability during the second postnatal week appears to arise from a morphological deficit of L4 SCs, contrary to published findings in the *Fmr1*$^{-/y}$ mice (Till *et al.*, 2012). Furthermore, I found no change in the density of PV interneurons in the developing S1, unlike the reduction seen in *Fmr1*$^{-/y}$ mice (Selby, Zhang and Sun, 2007; Lee *et al.*, 2019; Kourdougli *et al.*, 2023). As the underlying mechanisms of altered S1 development appear to differ between *Fmr1*$^{-/y}$ mice and rats, the periodic nature of cortical hyperexcitability, or the timing of these changes could thus be specific to rat development. This suggests that the loss of FMRP may affect cortical development in different ways or drive the cells towards divergent compensatory mechanisms in each species. Indeed, the observed species differences could be representative of different downstream mechanisms compensating for the loss of FMRP rather than the absence of FMRP expression *per se.* Consequently, it is unclear what the effect of FMRP loss would be on the developmental trajectory of the human brain, potentially explaining why many treatments that provide a rescue in the mouse model of FXS ultimately failed to show robust effects in clinical trials. As such, cross-species investigations could prove crucial in identifying conserved functions of FMRP and consequently – key phenotypes which could be targeted therapeutically.

The findings presented in this thesis raise novel questions about cortical development in the absence of FMRP. To confirm whether the proposed model of altered developmental trajectory in *Fmr1*$^{-/y}$ rats is correct, future work should address the following:

- Is the hyperexcitability at P25-28 indeed underlain by changes in I_h kinetics and can it be rescued with a longer treatment, e.g. using BPN14770? Is the hyperexcitability arising at P25-28 a permanent feature of the *Fmr1*$^{-/y}$ S1 beyond 4 weeks of life, lasting into adulthood?
- Is the function of PV interneurons impaired in early development similarly to *Fmr1*$^{-/y}$ mice? Does rescuing PV interneuron function also restore the developmental trajectory of the S1?
- Are Sst interneurons overactive in the developing S1 and does their increased density translate into increased Sst-14-mediated signalling in *Fmr1*$^{-/y}$ rats? If so, does the elevated Sst-14 signalling impair the function of L4 SCs?
- Is the processing of sensory stimuli impaired in *Fmr1*$^{-/y}$ rats due to this altered developmental trajectory giving rise to altered tactile responses and whisker-dependent behaviours?

8.4 Therapeutic perspective in FXS

Is the loss of FMRP an issue of neurodevelopment or neuromaintenance? With FMRP both conveying developmental roles and contributing to typical neuronal function via its synaptic protein targets (Till, 2010; Darnell *et al.*, 2011; Sidorov, Auerbach and Bear, 2013), perhaps the answer lies somewhere in the middle. In this thesis, I aimed to explore the idea of critical periods for therapeutic intervention to test whether treatment might be more effective during particular periods in life. While early pharmacological treatment with BPN14770 during the critical period of S1 development conveys some immediate benefits, such as a rescue of morphological deficits and depolarization block in *Fmr1*$^{-/y}$ SCs, it is not sufficient to fully restore the typical developmental trajectory of the S1 (Chapter 5). On the other hand, restoring FMRP expression postnatally can reduce audiogenic seizure incidence (Wong *et al.*, 2023) and intrinsic properties of CA1 pyramidal neurons in *Fmr1*$^{-/y}$ mice (Booker lab, unpublished observations), suggesting a neuromaintenance function. However, preliminary data suggest that postnatal FMRP re-expression is likely not sufficient to rescue physiological deficits such as exaggerated mGluR-LTD (Appendix 9.3) and elevated protein translation (Susana Ribeiro dos Louros, unpublished), which could thus be neurodevelopmental. These findings suggest that perhaps FXS might not be an ideal candidate for gene therapy, which has previously proven successful preclinically in other monogenic NDDs such as Rett Syndrome (Guy *et al.*, 2007; Palmieri, Pozzer and Landsberger, 2023). It is thus likely that in the case of FXS, chronic pharmacological treatment might be the most viable option, since a true critical period for therapeutic intervention (assuming one indeed exists), which is sufficient to fully restore the developmental trajectory, likely takes place in prenatal development, making it inaccessible for targeted treatment – unless genetic screening and therapy can commence prenatally. Furthermore, in preclinical research it is critical to assess the effectiveness of interventions across multiple modalities, as rescue of one phenotype e.g., dendritic morphology or intrinsic physiology does not necessarily make the treatment successful when other, key features such as synaptic plasticity may still be affected.

8.5 Limitations

Fmr1$^{-/y}$ mice and rats are commonly used, but imperfect models of FXS. A full *Fmr1* knockout model represents a binary scenario in which FMRP expression is missing from conception, while in the actual condition of Fragile X Syndrome, the loss of FMRP expression develops gradually. In fact, FMRP is still expressed during embryonic development in full mutation embryos until 10-12 weeks of gestation (Willemsen *et al.*, 2002). Additionally, while outbred rats provide a more diverse genetic background compared to inbred mice, they are not sufficient to replicate the complexity of FXS. FXS is a diverse condition, with a wide range of factors, such as CGG repeat length, methylation status and mosaicism contributing to its variable severity (Willemsen, Levenga and Oostra, 2011; Pretto *et al.*, 2014). To truly understand FXS it is imperative to study the impact of these factors on brain development and function, which is not possible in a simple *Fmr1*$^{-/y}$ model.

This thesis does not address arguably the most important outcome of disrupted cortical development – behaviour. *Fmr1*$^{-/y}$ mice are known to exhibit behavioural deficits, such as hyperactivity, spatial and contextual memory deficits, altered social behaviours as well as increased anxiety and susceptibility to audiogenic seizures (Spencer *et al.*, 2005; Krueger *et al.*, 2011; Kramvis *et al.*, 2013; Ding, Sethna and Wang, 2014). Similarly, *Fmr1*$^{-/y}$ rats show impaired novel object recognition and social interaction as well as hyperactivity, which could be underlain by a dysregulation of excitatory and inhibitory neurotransmission, oscillatory activity and experience-dependent plasticity (Till *et al.*, 2015; Wong *et al.*, 2020; Asiminas *et al.*, 2022; Ntoulas *et al.*, 2024). The administration of lovastatin in adolescence has been shown to correct these associative learning deficits of *Fmr1*$^{-/y}$ rats (Asiminas *et al.*, 2019). As such, future work should address whether treatment with BPN14770 is able to rescue such behavioural deficits in *Fmr1*$^{-/y}$ rats, and whether a brief treatment can convey long-lasting effects, in line with similar findings in *Fmr1*$^{-/y}$ mice, and in *Fmr1*$^{-/y}$ rats following the administration of lovastatin (Gurney *et al.*, 2017; C. Zhang *et al.*, 2018; Asiminas *et al.*, 2019). Such studies are currently ongoing in the Booker lab, guided by the key findings presented in this thesis.

To allow the direct comparison of WT and *Fmr1*$^{-/y}$ littermates, only male rats were used in this thesis. Since FXS is an X-linked condition, it is twice as common in males over females. However, female FXS individuals are often overlooked in research (Bartholomay *et al.*, 2019) and typically present differently than males, with generally less severe autism and ID, attention deficits and behavioural issues. Instead, female FXS individuals tend to experience learning disabilities and mental health problems (Keysor and Mazzocco, 2002; Bartholomay *et al.*, 2019). Since most studies on animal models of FXS only use males, little is known about the sex-specific effects of the loss of FMRP. (Wong *et al.*, 2020) found that female WT rats show higher power in awake EEG compared to males, a difference which was not present in the *Fmr1*$^{-/y}$ and *Fmr1*$^{-/-}$ rats. While male, but not female, *Fmr1*$^{-/y}$ rats exhibited higher gamma band activity during sleep, female *Fmr1*$^{-/-}$ rats had lower theta power in the awake state. Furthermore, sexually dimorphic differences in behaviour were found, with male *Fmr1*$^{-/y}$ showing increased repetitive behaviours such as wood chewing and female *Fmr1*$^{-/-}$ exhibiting exaggerated fear responses. Thus, it would be interesting to test whether such sex-specific differences in the FMRP-deficient brains already arise at cellular level, as such an investigation could better inform potential therapeutic approaches for all FXS individuals, regardless of their sex.

8.6 Conclusion

In conclusion, this thesis provides a first of its kind comprehensive multi-modal characterization of the postnatal development of the primary somatosensory cortex of the rat model of FXS. I have identified an alternate developmental trajectory which takes place in the FMRP-deficient cortex. By using a combination of electrophysiology, imaging and transcriptomics, I have discovered a wide range of changes which occur as a result of the loss of FMRP, leading to the identification of potential targets and points of divergence which could inform future therapeutic approaches.

Appendix

9.1 Detailed statistics

9.1.1 Chapter 3 – Electrophysiology

Table 9.1. Summary of GLMM results for L4 SC electrophysiological properties. Statistically significant results indicated in bold.

	P9-12 Mean ± SEM		**P25-28 Mean ± SEM**		**Age**		**Genotype**		**Age × Genotype**	
	WT	***Fmr1*$^{-/y}$**	**WT**	***Fmr1*$^{-/y}$**	**F**	**p**	**F**	**p**	**F**	**p**
F-I slope	0.071 ±0.005	0.094± 0.006	0.056± 0.003	0.054 ±0.003	7.98	**2.49 ×10^{-5}**	6.02	**0.017**	1.45	0.23
Rheobase	92.42 ±4.71	83.00 ±5.35	182.53 ±10.03	137.88 ±11.45	20.78	**2.92 ×10^{-9}**	8.25	**0.007**	0.87	0.49
Max #APs	20.88 ±1.29	22.71 ±0.96	13.69± 1.067	16.52 ±1.10	8.51	**1.87 ×10^{-5}**	5.86	**0.019**	0.08	0.99
RMP	-61.90 ±1.24	-60.34 ±1.08	-68.36 ±1.42	-67.68 ±1.56	6.36	**2.42 ×10^{-4}**	0.002	0.96	0.35	0.84
IR	281.83 ±18.76	406.88 ±22.88	111.67 ±6.99	158.98 ±8.94	38.61	**9.15 ×10^{-16}**	12.03	**9.86 ×10^{-4}**	3.14	**0.021**
τ_m	26.54 ±2.00	28.83 ±1.75	12.60 ±0.67	18.56 ±1.29	10.63	**1.32 ×10^{-6}**	7.50	**0.008**	1.28	0.29
C_m	96.14 ±6.35	73.31 ±4.08	118.36 ±6.48	118.39 ±5.87	8.78	**1.64 ×10^{-5}**	0.00	>0.99	1.32	0.27
V_{thresh}	-33.70 ±0.62	-32.69 ±0.87	-33.75 ±0.64	-35.37 ±0.82	0.88	0.49	0.14	0.71	1.27	0.30
AP amplitude	103.42 ±1.31	101.11 ±1.58	119.78 ±0.82	113.44 ±1.69	13.49	**6.13 ×10^{-8}**	1.13	0.29	2.60	**0.044**
½ height duration	1.10 ±0.03	1.23 ±0.06	0.66 ±0.02	0.72 ±0.02	40.30	**2.80 ×10^{-15}**	5.51	**0.033**	1.63	0.18
Rise time	0.15± 0.006	0.19± 0.009	0.10± 0.003	0.13± 0.004	16.42	**7.22 ×10^{-9}**	14.44	**3.66 ×10^{-4}**	1.07	0.38

Max rise rate	321.79 ±14.95	255.72 ±11.72	555.52 ±19.10	448.03 ±15.31	28.50	**8.76 ×10^{-13}**	15.83	**2.06 ×10^{-4}**	1.13	0.35
Max decay rate	52.16 ±1.34	49.12 ±2.76	101.98 ±2.74	96.06 ±3.094	45.44	**<2.00 ×10^{-16}**	0.74	0.39	1.32	0.27
mAHP	-18.00 ±0.71	-16.03 ±0.87	-19.53 ±0.57	-18.26 ±0.84	1.52	0.22	3.64	0.065	0.55	0.70
Sag	-5.67 ±0.37	-6.91 ±0.39	-2.08 ±0.13	-2.20 ±0.22	30.03	**7.60 ×10^{-12}**	2.79	0.10	0.41	0.80
Sag (% max)	21.80 ±1.72	20.23 ±1.11	16.33 ±0.71	14.00 ±1.67	4.08	**0.006**	0.02	0.88	1.79	0.14
Rebound	4.53 ±0.35	6.39 ±0.46	2.10 ±0.14	1.99 ±0.24	20.81	**3.01 ×10^{-10}**	3.47	0.07	1.20	0.32
Rebound slope	-0.036 ±0.003	-0.047 ±0.003	-0.014 ±0.001	-0.013 ±0.002	25.74	**1.30 ×10^{-11}**	2.50	0.12	0.90	0.47
R_f	1.02 ±0.14	1.67 ±0.17	1.96 ±0.21	1.27 ±0.19	0.50	0.74	0.33	0.57	3.52	**0.017**
Peak impedance	130.75 ±10.53	151.91 ±8.72	68.025 ±4.41	93.48 ±8.58	4.58	**0.002 7**	3.35	0.072	0.71	0.59
Q	1.14 ±0.02	1.08 ±0.01	1.11 ±0.016	1.13 ±0.041	0.53	0.71	0.82	0.37	1.43	0.24
R_f (resonating cells)	1.28 ±0.23	1.81 ±0.18	2.25 ±0.22	1.40 ±0.27	1.35	0.27	2.70	0.11	3.35	**0.017**
Peak impedance (resonating cells)	106.46 ±10.97	154.31 ±10.18	66.86 ±5.20	91.74 ±11.78	3.27	**0.018**	2.79	0.10	0.96	0.44
Q (resonating cells)	1.08± 0.019	1.07 ±0.010	1.095 ±0.01	1.10 ±0.40	0.58	0.68	0.71	0.40	1.48	0.22
sEPSC frequency	6.79 ±0.66	6.05 ±0.94	8.48 ±0.67	8.80 ±0.66	2.67	**0.041**	0.03	0.86	0.46	0.76
sEPSC amplitude	-17.07 0.89	-17.21 ±1.52	-12.75 ±0.95	-12.15 ±1.090	5.93	**5.25× 10^{-4}**	0.10	0.76	0.27	0.89

9.1.2 Chapter 4 – Anatomy

Table 9.2. Summary of 2-way ANOVA results for L4 SC morphology. Statistically significant results indicated in bold.

	P9-14 Mean ± SEM		P21-28 Mean ± SEM		Age		Genotype		Age × Genotype	
	WT	***Fmr1*$^{-}$ /y**	**WT**	***Fmr1*$^{-}$ /y**	**F**	**p**	**F**	**p**	**F**	**p**
Total Sholl intersections	149.76 ±7.31	131.00 ±8.10	150.87 ±8.18	159.48 ±6.91	3.74	**0.033**	1.25	0.27	1.15	0.33
Sholl peak	19.24 ±1.02	17.41 ±0.84	20.27 ±1.02	21.78 ±0.86	3.64	**0.033**	1.34	0.25	1.62	0.088
Sholl span	148.57 ±7.63	135.29 ±7.48	145.33 ±10.37	157.04 ±8.33	2.55	0.088	0.22	0.64	0.81	0.45
Total # dendrites	47.52 ±2.93	41.18 ±2.45	42.4 ±2.16	44.42 ±1.40	0.26	0.77	1.25	0.27	1.53	0.23
Total dendrite length	2.11 ±0.10	1.78 ±0.10	2.22 ±0.12	2.29 ±0.09	6.40	**0.0052**	2.60	0.12	1.60	0.22

Table 9.3. Summary of GLMM results for L4 SC dendritic spine density. Statistically significant results indicated in bold.

	P9-14 Mean ± SEM		P32-38 Mean ± SEM		Age		Genotype		Age × Genotype	
	WT	***Fmr1*$^{-/y}$**	**WT**	***Fmr1*$^{-/y}$**	**F**	**p**	**F**	**p**	**F**	**p**
Spine density	4.93 ±0.49	5.52 ±0.91	11.16 ±0.44	10.81 ±0.97	14.09	**1.64 ×10^{-6}**	2.44	0.13	0.91	0.45

Table 9.4. Summary of 2-way ANOVA results for PV^{+} cell density. Statistically significant results indicated in bold.

	P15-21 Mean ± SEM		**P32-38 Mean ± SEM**		**Age**		**Genotype**		**Age × Genotype**	
Layer	**WT**	***Fmr1*$^{-/y}$**	**WT**	***Fmr1*$^{-/y}$**	**F**	**p**	**F**	**p**	**F**	**p**
L1	171.98 ±61.31	36.27 ±36.27	211.31 ±88.30	159.13 ±53.91	1.54	0.24	3.42	0.08	0.21	0.81
L2/3	4007.8 ±326.4	4054.9 ±429.2	3227.5± 242.7	2561.2 ±448.4	2.25	0.13	1.81 ×10^{-5}	>0.99	1.05	0.37
L4	6944.3 ±1279.5	7002.2 ±1283.9	4861.93 ±464.7	4051.6 ±845.1	3.58	**0.045**	0.58	0.45	1.81	0.19

Table 9.5. Summary of 2-way ANOVA results for reelin^{+} cell density.

	P6-14 Mean ± SEM		**P22-28 Mean ± SEM**		**Age**		**Genotype**		**Age × Genotype**	
Layer	**WT**	***Fmr1*$^{-/y}$**	**WT**	***Fmr1*$^{-/y}$**	**F**	**p**	**F**	**p**	**F**	**p**
L1	6704.9 ±1318.2	8310.2 ±1394.2	5226.1 ±453.2	6347.1± 635.3	2.27	0.12	0.48	0.49	0.52	0.60
L2/3	4510.5 ±574.8	5717.5 ±812.5	3232.5 ±363.0	4669.6± 639.2	2.08	0.14	3.55	0.07	0.25	0.78
L4	7284.7 ±928.3	7954.4 ±1629.6	5012.0 ±892.0	7200.5± 1246.2	0.84	0.44	1.16	0.29	0.84	0.44

Table 9.6. Summary of 2-way ANOVA results for Sst-14^{+} cell density. Statistically significant results indicated in bold.

	P6-14 Mean ± SEM		**P22-28 Mean ± SEM**		**Age**		**Genotype**		**Age × Genotype**	
Layer	**WT**	***Fmr1*$^{-/y}$**	**WT**	***Fmr1*$^{-/y}$**	**F**	**p**	**F**	**p**	**F**	**p**
L1	171.5± 92.3	1095.8 ±536.3	38.73 ±38.73	1765.2± 1167.1	0.92	0.41	8.86	**0.0045**	1.01	0.37
L2/3	3319.8 ±421.4	4079.7 ±667.2	1989.4 ±201.0	4748.2± 849.4	1.96	0.15	13.28	**0.0006**	1.34	0.27
L4	2981.7 ±418.5	6361.9 ±908.4	1472.9 ±322.5	7131.7± 2131.2	0.45	0.64	29.97	**<0.0001**	2.07	0.14

9.1.3 Chapter 5 – BPN14770 treatment

Table 9.7. Summary of GLMM results for intrinsic properties of L4 SCs at P10-14 after vehicle or BPN14770 treatment.

	Vehicle		BPN14770		Treatment		Genotype		Treatment × Genotype	
Property	**WT**	***Fmr1*$^{-/y}$**	**WT**	***Fmr1*$^{-/y}$**	**F**	**P**	**F**	**p**	**F**	**p**
F-I slope	0.081 ±0.005	0.104 ±0.005	0.078 ±0.005	0.084 ±0.004	1.05	0.31	2.69	0.11	1.50	0.23
Rheobase	92.28 ±5.92	81.79 ±8.41	91.46 ±6.28	105.98 ±7.28	2.12	0.17	0.0098	0.92	2.68	0.12
Max #APs	21.31 ±0.92	22.89 ±1.26	21.31 ±1.42	22.53 ±1.04	0.61	0.81	0.94	0.34	0.0094	0.92
RMP	-59.99 ±0.74	-60.65 ±1.00	-63.50 ±1.11	-61.21 ±0.95	3.58	0.071	0.57	0.46	1.75	0.20
IR	353.12 ±22.08	409.32 ±23.52	326.95 ±21.51	334.60 ±19.43	3.15	0.08	1.72	0.20	0.47	0.50
τ_m	27.41 ±1.28	28.50 ±1.41	22.76 ±1.22	25.47 ±1.53	3.82	0.064	1.65	0.21	0.44	0.51
C_m	81.07 ±2.69	72.87 ±3.38	73.74 ±3.11	78.09 ±2.83	0.07	0.80	0.26	0.61	3.62	0.069
V_{thresh}	-33.59 ±0.59	-33.55 ±0.67	-35.98 ±0.96	-32.35 ±0.62	0.29	0.59	3.43	0.077	2.55	0.12
AP amplitude	100.68 ±1.46	99.44 ±1.29	98.78 ±2.16	101.48 ±1.39	0.01	0.91	0.39	0.54	1.23	0.28
½ height duration	1.18 ±0.04	1.20 ±0.04	1.12 ±0.03	1.13 ±0.03	0.52	0.48	0.02	0.90	0.009	0.92
Rise time	0.16± 0.007	0.17± 0.006	0.16± 0.006	0.16± 0.005	0.02	0.89	0.02	0.90	0.002	0.96
Max rise rate	297.30 ±13.79	276.85 ±12.04	309.92 ±16.53	290.77 ±11.10	0.09	0.77	0.24	0.63	0.03	0.88
Max decay rate	49.22 ±1.88	47.36 ±1.97	53.04 ±2.33	51.80 ±1.98	0.56	0.46	0.02	0.89	0.02	0.89

Table 9.8. Summary of 2-way ANOVA results for L4 SC morphology at P10-14 after treatment with vehicle or BPN14770. Statistically significant results indicated in bold.

	Vehicle Mean ± SEM		**BPN14770 Mean ± SEM**		**Treatment**		**Genotype**		**Treatment × Genotype**	
	WT	***Fmr1*$^{-}$ /y**	**WT**	***Fmr1*$^{-}$ /y**	**F**	**p**	**F**	**p**	**F**	**p**
Total Sholl intersections	156.31 ±10.08	138.93 ±7.15	166.36 ±7.45	168.17 ±11.05	2.98	0.11	0.24	0.63	0.73	0.41
Sholl peak	20.23 ±0.59	15.64 ±0.88	17.14 ±0.79	19.50 ±1.88	0.16	0.69	1.34	0.25	13.00	**0.0008**
Sholl span	150.77 ±7.20	169.29 ±10.40	194.29 ±9.82	175.00 ±11.48	4.28	0.057	0.0012	0.97	2.12	0.17
Total # dendrites	45.31 ±1.69	38.36 ±2.17	40.50 ±1.81	43.67 ±4.72	0.0005	0.98	0.19	0.67	1.70	0.22
Total dendrite length	2.13 ±0.13	1.85 ±0.10	2.19 ±0.10	2.27 ±0.14	2.63	0.13	0.23	0.64	1.27	0.28

Table 9.9. Summary of GLMM results for intrinsic properties of L4 SCs at P25-28 after BPN14770 treatment. Statistically significant results indicated in bold.

	Vehicle		**BPN14770**		**Treatment**		**Genotype**		**Treatment × Genotype**	
Property	**WT**	***Fmr1*$^{-/y}$**	**WT**	***Fmr1*$^{-/y}$**	**F**	**P**	**F**	**p**	**F**	**p**
F-I slope	0.057 ±0.003	0.061 ±0.002	0.054 ±0.005	0.057 ±0.002	1.04	0.32	1.96	0.17	0.01	0.92
Rheobase	145.71 ±10.37	141.93 ±10.23	145.24 ±11.51	124.24 ±4.98	1.14	0.30	1.70	0.20	0.29	0.59
Max #APs	15.79 ±0.90	17.52 ±0.80	15.78 ±1.55	17.48 ±0.75	0.06	0.81	4.29	**0.041**	0.04	0.85
RMP	-68.90 ±1.40	-67.67 ±1.31	-66.80 ±1.67	-67.13 ±1.35	0.67	0.42	0.0002	0.99	0.02	0.90
IR	136.92 ±8.94	157.27 ±16.63	171.69 ±12.33	170.43 ±10.88	5.53	**0.024**	0.06	0.81	0.10	0.76
τ_m	15.18 ±0.97	16.79 ±1.47	15.86 ±1.30	17.32 ±1.05	0.56	0.46	0.57	0.46	0.09	0.77
C_m	115.11 ±5.94	111.99 ±4.40	94.89 ±6.16	105.07 ±4.48	4.24	**0.047**	0.62	0.44	1.22	0.28
V_{thresh}	-36.11 ±0.72	-35.80 ±0.70	-36.38 ±0.53	-36.08 ±0.71	0.40	0.53	0.24	0.63	0.004	0.95
AP amplitude	115.86 ±0.92	116.13 ±0.73	114.22 ±1.11	114.73 ±0.96	0.87	0.36	0.55	0.47	0.02	0.90
½ height duration	0.72 ±0.01	0.74 ±0.02	0.75 ±0.04	0.76 ±0.02	1.31	0.26	0.68	0.41	0.04	0.84
Rise time	0.12± 0.003	0.13± 0.003	0.12± 0.003	0.13± 0.004	0.40	0.53	2.98	0.094	0.60	0.45
Max rise rate	476.27 ±13.83	461.57 ±13.64	464.40 ±13.14	436.17 ±12.91	0.97	0.33	1.39	0.25	0.36	0.55
Max decay rate	96.40 ±2.20	95.30 ±2.50	95.13 ±2.92	95.07 ±2.51	0.07	0.79	0.14	0.71	0.01	0.92

Table 9.10. Summary of 2-way ANOVA results for L4 SC morphology at P25-28 after treatment with vehicle or BPN14770.

	Vehicle Mean ± SEM		**BPN14770 Mean ± SEM**		**Treatment**		**Genotype**		**Treatment × Genotype**	
	WT	***Fmr1*$^{-/y}$**	**WT**	***Fmr1*$^{-/y}$**	**F**	**p**	**F**	**p**	**F**	**p**
Total Sholl intersections	173.00±11.86	163.80±9.22	161.20±13.04	147.33±15.57	1.36	0.27	0.69	0.43	0.31	0.59
Sholl peak	19.67 ±1.76	18.60 ±1.04	18.80 ±0.49	19.33 ±2.14	0.009	0.93	0.23	0.64	0.08	0.78
Sholl span	186.67±11.16	174.00±15.43	162.00±10.20	145.00±6.71	3.23	0.11	0.54	0.48	0.13	0.72
Total # dendrites	39.17 ±2.83	39.00 ±2.28	41.00 ±3.27	41.00 ±3.04	0.44	0.51	0.0008	0.98	0.0008	0.98
Total dendrite length	2.37 ±0.12	2.22 ±0.10	2.32 ±0.18	2.01 ±0.21	0.93	0.36	1.93	0.20	0.61	0.46

9.1.4 Chapter 7 – Patch-seq

Table 9.11. Summary of GLMM results for intrinsic properties of P9-12 L4 SCs recorded under standard whole-cell patch clamp or Patch-seq conditions. Statistically significant results indicated in bold.

	Whole-cell patch clamp		**Patch-seq**		**Condition**		**Genotype**		**Condition × Genotype**	
Property	**WT**	***Fmr1*$^{-/y}$**	**WT**	***Fmr1*$^{-/y}$**	**F**	**P**	**F**	**p**	**F**	**p**
RMP	-61.90 ±1.24	-60.34 ±1.08	-60.39 ±0.66	-60.29 ±0.81	0.82	0.37	0.02	0.88	0.02	0.89
Rheobase	92.42 ±4.71	83.00 ±5.35	97.05 ±4.81	83.54 ±4.34	0.32	0.57	4.22	0.052	0.02	0.89
IR	281.83 ±18.76	406.88 ±22.88	403.48 ±20.67	436.55 ±23.48	10.89	**0.003**	13.32	**0.001**	5.89	**0.021**
V_{thresh}	-33.70 ±0.62	-32.69 ±0.87	-29.84 ±0.64	-31.70 ±0.84	6.71	**0.015**	0.44	0.51	0.41	0.53
AP amplitude	103.42 ±1.31	101.11 ±1.58	107.16 ±1.16	107.24 ±1.05	11.00	**0.003**	1.16	0.29	1.20	0.29
Rise time	0.15± 0.006	0.19± 0.009	0.17± 0.007	0.17± 0.004	0.21	0.65	3.59	0.071	4.81	**0.039**
Max rise rate	321.79 ±14.95	255.72 ±13.43	294.21 ±11.89	290.97 ±7.73	0.09	0.76	5.59	**0.027**	4.38	**0.047**
Max decay rate	52.16 ±1.34	49.12 ±2.76	47.52 ±1.56	48.48 ±1.69	0.70	0.41	0.59	0.46	1.13	0.30

9.2 Differentially expressed gene list

9.2.1 Excitatory neurons

Table 9.12. Upregulated genes in excitatory neurons – Figure 6.6B.

Gene	Log2FC	p-adj	Function
Mt-nd1	0.597482	6.70×10^{-7}	Mitochondrial respiratory chain – NADH dehydrogenase
Mt-nd5	0.539944	6.70×10^{-7}	Mitochondrial respiratory chain –NADH dehydrogenase
Mt-co2	0.621154	1.39×10^{-6}	Mitochondrial respiratory chain – cytochrome c oxidase
Mt-cyb	0.575426	9.20×10^{-6}	Mitochondrial respiratory chain – cytochrome b-c1 complex
Dgcr6	0.402684	0.00013	Development
Rplp0	0.374325	0.00013	Ribosomal protein – large 60S subunit
Ccn2	1.084053	0.000138	Cell adhesion, development
Tacr3	0.643085	0.000438	G protein-coupled receptor
Mt-atp6	0.547111	0.000478	Mitochondrial respiratory chain – ATP synthase
Map1lc3a	0.477912	0.000847	Microtubule-associated protein, autophagosome
Mt-co3	0.514677	0.000847	Mitochondrial respiratory chain – cytochrome c oxidase
Mt-co1	0.515579	0.001281	Mitochondrial respiratory chain – cytochrome c oxidase
Mt-nd2	0.502197	0.001312	Mitochondrial respiratory chain – NADH dehydrogenase
Fth1	0.374971	0.001461	Iron homeostasis
Mt-nd4	0.563973	0.001799	Mitochondrial respiratory chain – cytochrome c oxidase
Fos	1.083376	0.003684	Transcription factor
Sbds	0.298537	0.004616	Ribosome biogenesis
Ttc9b	0.396148	0.005092	Protein binding
Tuba1a	0.385078	0.007324	Cytoskeleton component
Rpl28	0.432905	0.007862	Ribosomal protein – large 60S subunit
Tedc1	1.262365	0.008557	Ciliary hedgehog signalling
Hcfc1r1	0.378705	0.012369	HCFC1 receptor
Psma4	0.593812	0.012608	20S proteasome core component
Rps16	0.405425	0.01266	Ribosomal protein – small 40S subunit
Zdhhc3	0.284112	0.01266	Protein palmitoylation
Marcks	0.35767	0.013013	Cytoskeleton, development
Flt3lg	0.415115	0.014247	Protein binding
Rps9	0.434544	0.014269	Ribosomal protein – small 40S subunit
Rprm	0.399564	0.014269	Cell cycle regulation

Hint1-ps1	0.776839	0.014832	Endoplasmic reticulum to Golgi vesicle transport
Commd4	0.29493	0.01519	Protein binding, DNA repair
Rps11	0.414742	0.016835	Ribosomal protein – small 40S subunit
Galnt10	0.595648	0.017591	Protein binding
Rps13	0.391433	0.018638	Ribosomal protein – small 40S subunit
Lgr5	0.880289	0.018846	G protein-coupled receptor, Wnt signalling
Rps2	0.44172	0.019211	Ribosomal protein – small 40S subunit
Arpc4	0.350502	0.020718	Cytoskeleton component
Kdr	1.124499	0.022958	MAP kinase signalling, AKT1 signalling
Mif	0.487015	0.022958	Protein binding, cytokine activity
Atp5mc1	0.45335	0.023064	Mitochondrial respiratory chain – ATP synthase
Hmgcr	0.257237	0.023307	Cholesterol homeostasis
Atp5f1d	0.41032	0.023307	Mitochondrial respiratory chain – ATP synthase
Scand1	0.403555	0.025027	Transcriptional regulation, protein binding
Rpl32l5	0.461592	0.026976	Ribosomal protein – large 60S subunit
Rpl10	0.358596	0.026976	Ribosomal protein – large 60S subunit
Mt-nd6	0.79341	0.026976	Mitochondrial respiratory chain – NADH dehydrogenase
Rps19	0.438636	0.027646	Ribosomal protein – small 40S subunit
Rpsa	0.382161	0.029076	Ribosome biogenesis – small 40S subunit
Cox6a1	0.418447	0.029076	Mitochondrial respiratory chain – cytochrome c oxidase
Vps28	0.340207	0.029741	Vesicle transport
Oaz1	0.359501	0.029741	Ubiquitin-independent polyamine degradation
Atp6v1g1	0.260446	0.029844	ATPase, proton homeostasis
Adam32	0.443516	0.032021	Brain development
Sh3bgrl3	0.477926	0.032827	Cytoskeleton
Cox4i1	0.328008	0.033126	Mitochondrial respiratory chain – cytochrome c oxidase
Bmpr1b	0.958598	0.033498	Serine/threonine kinase receptor
Pebp1	0.438016	0.034088	Protein/ATP binding, intracellular signalling
Mrps34	0.384994	0.035093	Mitoribosomal protein – small 28S subunit
Gsta6	0.424832	0.035199	Glutathione transferase
H3f3b	0.422099	0.035199	H3 histone
Smdt1	0.348107	0.037394	Mitochondrial Ca^{2+} homeostasis, Ca^{2+} signalling
Atp5mc3	0.435742	0.039347	Mitochondrial respiratory chain – ATP synthase
Rpl19	0.40184	0.04034	Ribosomal protein – large 60S subunit
Rpl3	0.281485	0.040423	Ribosomal protein – large 60S subunit
Acaa2	0.480304	0.040423	Mitochondrial respiratory chain – acetyl-CoA transferase
Calm3	0.389184	0.040784	Ca^{2+} signalling

Myl6	0.368133	0.042536	Myosin light chain, protein binding
Arl6ip4	0.325836	0.04292	RNA splicing
Slc20a1	0.227073	0.043856	Metabolism, intracellular signalling
Tubb2a	0.30359	0.043856	Microtubule component
Hspa5	0.271167	0.049851	Cellular stress response

Table 9.13. Downregulated genes in excitatory neurons – Figure 6.6B.

Gene	Log2FC	p-adj	Function
Fmr1	-8.35922	0	Translational repressor
LOC134478878	-0.78432	5.93×10^{-11}	Not yet characterized
Syt17	-0.64266	1.63×10^{-9}	Ca^{2+} signalling, dendrite extension, postsynaptic neurotransmitter receptor internalisation
Ror2	-1.21631	4.01×10^{-8}	Tyrosine-protein kinase receptor
ENSRNOG00000062316	-0.74333	4.01×10^{-8}	lncRNA
Kcp	-0.89619	2.13×10^{-6}	BMP signalling
Tshz2	-0.54417	2.15×10^{-6}	Transcription factor
Olr59	-0.60786	8.26×10^{-6}	G protein-coupled receptor
Thsd4	-0.63001	9.20×10^{-6}	TGFB signalling, extracellular matrix assembly
Kcnip1	-0.66408	1.53×10^{-5}	A-type K channel subunit
Plch2	-0.58527	5.55×10^{-5}	IP3 signalling, neuronal function
Gprin3	-0.8124	0.000483	Neurite outgrowth
Colgalt2	-0.44819	0.001007	Extracellular matrix assembly
Dnah5	-0.56409	0.001351	Microtubule motor activity
Mri1	-0.47461	0.00173	Protein binding
Rsph10b	-0.39748	0.001976	Cell projection, cilia structure
Arhgef17	-0.33666	0.003543	GTPase, cytoskeleton
Plekha7	-0.39138	0.003684	Cell adhesion
Glis3	-0.58108	0.004496	Transcription factor
Tmem266	-0.3563	0.004694	Voltage sensor
Slc38a7	-0.37444	0.004694	Na^{+}/amino acid transporter, mTORC1 activation
Rarb	-0.88673	0.007156	Development, neurogenesis, DNA binding
Septin9	-0.5154	0.0084	GTPase, cytoskeleton
Ltbp1	-0.46604	0.010913	Extracellular matrix assembly
Map2k6	-0.32883	0.010913	MAP kinase signalling
Rbms3	-0.59353	0.011397	RNA-binding, translational regulator
Unc5a	-0.29402	0.01266	Netrin signalling, axon guidance, neurite outgrowth
Epha10	-0.49811	0.013578	Ephrin receptor
Rnf144a	-0.33987	0.014269	Ubiquitin ligase regulation
Spetex2gl1	-0.25698	0.014656	Not yet characterized
AABR07069821.1	-0.52842	0.014832	lincRNA
Hpse2	-0.3715	0.014905	Extracellular matrix assembly, cell proliferation
Ptchd4	-0.47262	0.015729	Canonical hedgehog signalling repressor

Car4	-0.74095	0.015818	pH regulation
Nim1k	-0.32578	0.017579	Serine/threonine protein kinase
Arhgap15	-0.25216	0.017579	GTPase activator, regulation of cell shape
Kcnc2	-0.34275	0.017591	Voltage-gated K^+ channel
Mreg	-0.48875	0.017591	Microtubule transport
Zfp536	-1.16396	0.018638	Transcription factor, neuronal differentiation repressor
Elfn2	-0.40602	0.018638	Phosphatase inhibitor
Epb41l2	-0.29919	0.020702	Cytoskeleton, regulation of cell shape
Man2b1	-0.27339	0.02102	Protein modification
Bmp6	-0.38365	0.021217	BMP signalling, development, cell differentiation, gene expression regulation
Car12	-0.81742	0.023307	Carbonate dehydratase
Dgkg	-0.48544	0.023657	Intracellular signalling, neuron development, dendrite development regulation
Arrdc4	-0.39231	0.026976	Ubiquitin ligase regulation
Kel	-0.90918	0.026976	K^+ transport, regulation of cell size
Sel1l3	-0.31939	0.029741	Protein binding
Cyp7b1	-0.32406	0.031265	G protein-coupled receptor, memory, response to cAMP
Ahdc1	-0.21384	0.032827	Transcription factor, cell differentiation
Ppargc1b	-0.33105	0.032827	RNA binding, transcription factor regulation, response to cAMP
Mettl21a	-0.48603	0.033167	Protein methylation
Vstm2l	-0.32059	0.034088	Negative regulation of neuronal apoptosis
Cbfa2t3	-0.405	0.034822	Transcriptional corepressor, ubiquitination and proteasome regulation
Ntng2	-0.30279	0.035093	Neurite outgrowth, neuronal migration, circuit formation, synapse assembly
Ano10	-0.29409	0.035093	Ca^{2+}-activated Cl^- channel
Stat5b	-0.28058	0.035199	Transcription factor, intracellular signalling
Fam13c	-0.21159	0.035199	Not yet characterized
Zbbx	-0.35372	0.039463	Zn^{2+} binding
Adgb	-0.78447	0.04034	Oxygen-binding
Asb5	-0.4526	0.040784	Ubiquitin ligase regulation, intracellular signalling
Vwa5al1	-0.46306	0.041852	Tumour suppressor
Col6a2	-0.50098	0.042536	Extracellular matrix assembly, cell adhesion
Sptb	-0.2578	0.042841	Cytoskeleton
Albfm1	-1.04425	0.043862	Not yet characterized
Lrrc3b	-0.23365	0.043862	Tumour suppressor
Foxo3	-0.25518	0.046261	Transcription factor, Wnt signalling
Cdk18	-0.83608	0.049223	ATP binding, intracellular signalling
Htr4	-0.45793	0.049712	G protein-coupled receptor, serotonin receptor
Impa2	-0.36929	0.049851	Inositol metabolism

9.2.2 Inhibitory neurons

Table 9.14. Upregulated genes in inhibitory neurons – Figure 6.6D.

Gene	Log2FC	p-adj	Function
Strip2	1.483222	3.34E-08	Regulation of cell shape, cell migration, cytoskeleton
MGC94891	3.270579	1.93E-05	Not yet characterized
Pde10a	0.876051	1.93E-05	cAMP signalling, phosphodiesterase
Rasgrp1	1.543659	1.93E-05	MAP kinase signalling, cell differentiation, vesicle transport
Ccdc180	3.619461	2.12E-05	Cilia motility
Gpr88	1.738096	2.96E-05	G protein-coupled receptor, learning
Itpka	2.951369	0.000112	Inositol metabolism, cytoskeleton, Ca^{2+} signalling, dendritic spine maintenance
Slc35d3	3.58303	0.000396	Dopamine signalling, energy homeostasis
Inf2	1.164034	0.000396	Cytoskeleton
Cbr3	2.165864	0.000851	NADPH binding, metabolism, cognition
Kcnab1	0.352811	0.001512	Voltage-gated K^+ channel
Il20ra	3.771412	0.001837	Cytokine activity, apoptosis signalling
Penk	1.388121	0.001926	Neuropeptide synaptic signalling, cellular stress response, response to cAMP
Pde1b	1.239478	0.002186	cAMP signalling, phosphodiesterase
Htr2c	0.810748	0.002721	G protein-coupled receptor, serotonin receptor
Car11	0.444749	0.004048	MAP kinase signalling
Casq2	3.396022	0.004256	Ca^{2+} binding, Ca^{2+} homeostasis
Ddc	2.984881	0.004507	Serotonin biosynthesis
Gng4	0.617383	0.004507	G protein-coupled receptor, cell growth repressor
Echdc2	1.089016	0.00692	Fatty acid metabolism
Syt6	0.982452	0.007197	Synaptic vesicle exocytosis, Ca^{2+} sensor, synaptic transmission
Chn2	0.55384	0.00745	Cellular signalling
Phyhip	0.679935	0.007797	Protein tyrosine kinase binding
Drd2	1.643233	0.010049	Dopamine receptor, axonogenesis, interneuron migration, intracellular signalling, synaptic transmission
Rxrg	2.379063	0.01193	Brain development, neuronal differentiation
Gprin3	0.765227	0.012068	Neurite outgrowth
Frem2	0.810012	0.012212	Extracellular matrix assembly, cell adhesion
Itpr2	1.275744	0.012212	Inositol receptor, response to cAMP
Slc4a4	0.560356	0.012706	Na^+/HCO_3^- transporter, pH regulation, membrane potential
Erf	1.379892	0.013426	Transcriptional repressor

Spata13	1.503795	0.014439	Cell migration, intracellular signalling
Rgs9	2.808967	0.014752	GTPase, intracellular signalling, brain development
Fras1	0.551801	0.014752	Extracellular matrix assembly
ENSRNOG00000062316	1.078255	0.016977	lncRNA
Schip1	0.54219	0.017515	Node of Ranvier/AIS molecular complex organization
Icam5	1.004038	0.02057	Cell adhesion, synapse assembly
Rasgef1b	0.616121	0.020918	GTPase signalling
Sst	0.579172	0.021107	Somatostatin signalling
Tgfa	2.955078	0.021197	Cell proliferation
B3gnt2	1.345012	0.021197	Axon guidance
Mt-cyb	0.429827	0.022772	Mitochondrial respiratory chain – cytochrome b-c1 complex
Neurod2	3.857911	0.022779	Transcription factor, brain development, synapse function
Cplx2	0.367326	0.024659	Synaptic vesicle exocytosis
Marcks	0.494988	0.025755	Cytoskeleton, development
Mt-nd1	0.387501	0.027104	Mitochondrial respiratory chain – NADH dehydrogenase
Cchcr1	1.442613	0.02934	Cell differentiation
Strn	0.567249	0.030166	Intracellular signalling, dendrite development
Fos	1.51911	0.030166	Transcription factor
Sh3rf2	2.349565	0.030166	Ubiquitin ligase activity
Rps16	0.45154	0.030693	Ribosomal protein – small 40S subunit
Emid1	0.83528	0.030693	Cell proliferation
Drd1	1.561528	0.030693	Dopamine receptor, interneuron migration, learning
Cacna2d3	0.37217	0.030693	Voltage-gated Ca^{2+} channel, presynapse organization
Asb2	2.820781	0.031354	Ubiquitination, cytoskeleton, intracellular signalling
Slc35f3	0.466036	0.036229	Thiamine transporter
Mt-co2	0.405292	0.036229	Mitochondrial respiratory chain – cytochrome c oxidase
Chst11	0.701636	0.040011	Development, apoptosis inhibition, cell proliferation
Kremen1	2.765798	0.040011	Wnt signalling
Rarb	3.996319	0.041808	Development, neurogenesis, DNA binding
LOC102551114	0.585433	0.044388	ncRNA
Rpl18a	0.516393	0.044795	Ribosomal protein – large 60S subunit
Slc22a3	3.084939	0.049358	Voltage-dependent transporter

ENSRNOG00000067970	0.418089	0.049358	Not yet characterized
Six3	2.384623	0.049358	Wnt signalling, brain development
Tuba1a	0.350067	0.049358	Cytoskeleton component
Ccdc3	1.804039	0.049358	Cell signalling, gene expression repressor
Gpr6	1.234094	0.049358	G protein-coupled receptor, cAMP signalling
Cpne5	0.593477	0.049358	Cell differentiation, dendrite extension
Mt-co1	0.374542	0.049358	Mitochondrial respiratory chain – cytochrome c oxidase

Table 9.15. Downregulated genes in inhibitory neurons – Figure 6.6D.

Gene	Log2FC	p-adj	Function
Fmr1	-7.21685	3.2E-176	Translational repressor
Nudt7	-1.51518	1.35E-07	Metabolism
Itga8	-0.76956	0.000365	Extracellular matrix assembly, brain development
Tns3	-0.67884	0.002393	Cell proliferation
LOC134478878	-0.70506	0.00246	Not yet characterized
Myof	-0.59244	0.004905	VEGF signalling
Fgd5	-0.83405	0.005179	VEGF signalling
Cdh4	-0.3661	0.008838	Axon guidance, axon extension, cell adhesion
Fat4	-0.38293	0.010049	Cell adhesion, brain development, neurogenesis
Eln	-0.6053	0.014578	Extracellular matrix assembly
Hmcn1	-0.79412	0.017075	Cytoskeleton
Lhx9	-1.78665	0.021107	DNA binding, cell proliferation
Spetex2gl1	-0.30711	0.024479	Not yet characterized
Septin9	-0.51818	0.03068	Cytoskeleton
Wwox	-0.42863	0.030693	Wnt signalling, apoptosis signalling
Jph1	-0.38198	0.036229	Junctional membrane complex component
Nxph2	-0.46149	0.037963	Cell signalling receptor
Necab1.1	-0.32442	0.040011	Ca^{2+} binding, protein binding
Bcl7c	-0.32794	0.044388	Apoptosis inhibitor, cell proliferation
Gpd1	-0.67701	0.044795	Response to cAMP
Dnah11	-0.6639	0.048615	Cilia motility
Suclg2	-0.43739	0.049358	Citric acid cycle
Arhgap15	-0.45586	0.049358	GTPase activator, regulation of cell shape
Grpr	-0.65047	0.049358	G protein-coupled receptor, neuropeptide binding

9.3 *FMR1* gene re-expression in mouse hippocampus

FMR1 re-expression through an AAV9 viral vector was tested in collaboration with Cobb Lab. WT and *Fmr1*$^{-/y}$ littermate FVB mice received an intracerebroventricular injection of PBS or 3e11vg of AAV9 vector containing the human *FMR1* isoform 7 (FXS6; Cobb lab) at P0-2 (Figure 9.1A). Extracellular field recordings were performed in the CA1 region at P28-35. Acute horizontal hippocampal slices were prepared like previously (see Section 2.2.1). CA3 was severed prior to recording. Extracellular field EPSPs were recorded from the *stratum radiatum* in CA1 while stimulating the Schaffer collaterals (Figure 9.1B). After 20 mins of a stable baseline, 25 mM S-DHPG was applied for 5 mins to induce mGluR-LTD (Figure 9.1B-D). LTD was quantified from the last 10 mins of the recording relative to the last 10 mins of baseline. The % of LTD showed a tendency towards a difference between the groups, because *Fmr1*$^{-/y}$ appeared to exhibit exaggerated LTD compared to WT, regardless of treatment. Confirmation of FMRP re-expression within the CA1 was validated separately by members of the Cobb lab (unpublished).

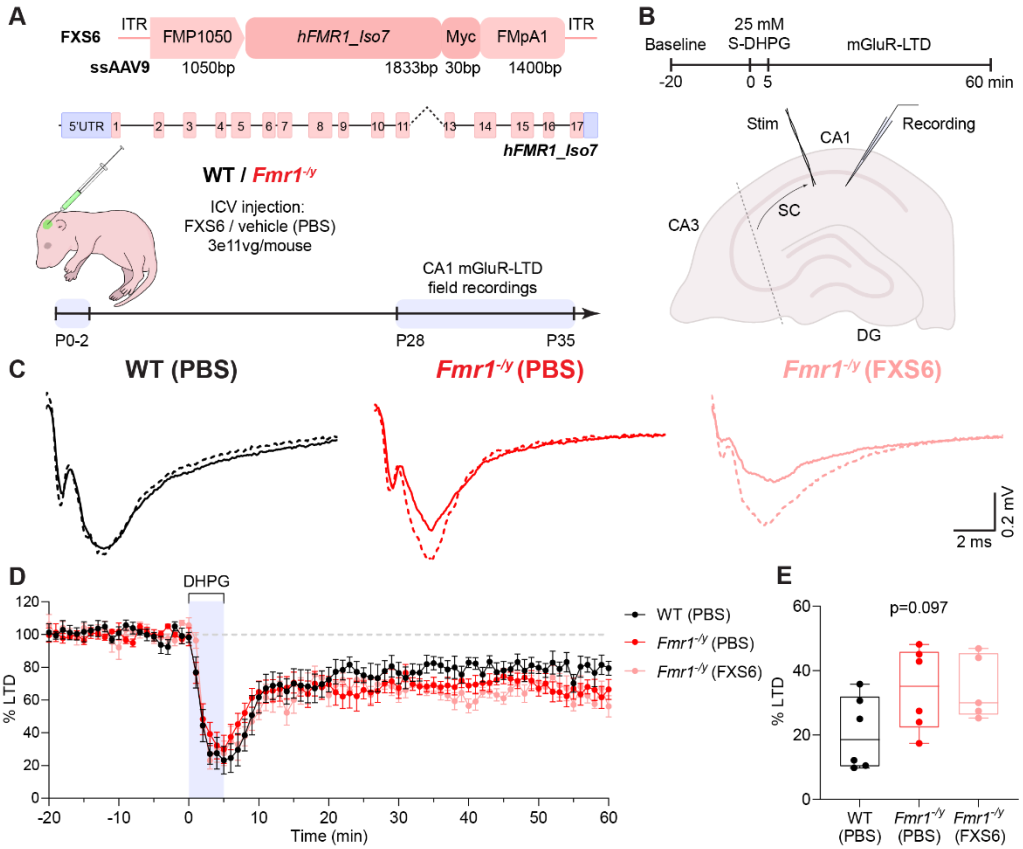

Figure 9.1. *FMR1* re-expression in the CA1 does not rescue exaggerated LTD in *Fmr1*$^{-/y}$ mice. A. Top: schematic of the FXS6 construct (not to scale). Single-stranded AAV9 was used to deliver the human *FMR1* isoform 7 under the endogenous promoter and flanked by a Myc tag and a 1400bp fragment of the endogenous 3'UTR (FMpA1). Middle: schematic of the human *FMR1* isoform 7, drawn to scale. Boxes denote exons, lines indicate introns. *FMR1* isoform 7 does not contain exon 12 due to alternative splicing (dashed line). Bottom: WT and *Fmr1*$^{-/y}$ received intracerebroventricular injections (ICV) of the FXS6 construct (3e11vg/mouse) or vehicle (PBS) at P0-2. CA1 mGluR-LTD field recordings were performed at P28-35. **B.** Top: Schematic timecourse of the recordings. 20 mins of stable baseline were obtained before the application of 25 mM of S-DHPG for 5 minutes. Extracellular field responses were recorded for 60 mins from the time of application. Bottom: diagram of the CA1 mGluR-LTD recordings. Stimulating electrode was placed within the Schaffer collaterals (SC) and extracellular field responses were recorded from the stratum radiatum of the CA1 region. CA3 was severed prior to recording (dashed line). DG – dentate gyrus. **C.** Representative traces of field EPSPs from WT and *Fmr1*$^{-/y}$ mice after vehicle or FXS6 injection. Dashed line indicates baseline response, solid line shows the response after mGluR-LTD induction. **D.** Averaged timecourses of CA1 mGluR-LTD recordings from WT and *Fmr1*$^{-/y}$ mice after FXS6 injection. Shaded region indicates DHPG application. **E.** % LTD trends towards a difference between the groups (1-way ANOVA; F=2.767, p=0.097). WT: n=6 animals, *Fmr1*$^{-/y}$ (PBS): n=6 animals; *Fmr1*$^{-/y}$ (FXS6): n=5 animals.

References

Acinas, S.G. *et al.* (2005) 'PCR-Induced Sequence Artifacts and Bias: Insights from Comparison of Two 16S rRNA Clone Libraries Constructed from the Same Sample', *Applied and Environmental Microbiology*, 71(12), pp. 8966–8969. Available at: https://doi.org/10.1128/AEM.71.12.8966-8969.2005.

American Psychiatric Association (2022) 'Neurodevelopmental Disorders', in *Diagnostic and Statistical Manual of Mental Disorders - Text Revision*. American Psychiatric Association Publishing. Available at: https://doi.org/10.1176/appi.books.9780890425787.x01_Neurodevelopmental_Disorders.

Amiet, C. *et al.* (2008) 'Epilepsy in Autism is Associated with Intellectual Disability and Gender: Evidence from a Meta-Analysis', *Biological Psychiatry*, 64(7), pp. 577–582. Available at: https://doi.org/10.1016/j.biopsych.2008.04.030.

Anney, R. *et al.* (2010) 'A genome-wide scan for common alleles affecting risk for autism', *Human Molecular Genetics*, 19(20), pp. 4072–4082. Available at: https://doi.org/10.1093/hmg/ddq307.

Anney, R. *et al.* (2012) 'Individual common variants exert weak effects on the risk for autism spectrum disorders', *Human Molecular Genetics*, 21(21), pp. 4781–4792. Available at: https://doi.org/10.1093/hmg/dds301.

Anney, R. and The Autism Spectrum Disorders Working Group of The Psychiatric Genomics Consortium (2017) 'Meta-analysis of GWAS of over 16,000 individuals with autism spectrum disorder highlights a novel locus at 10q24.32 and a significant overlap with schizophrenia', *Molecular Autism*, 8(1), p. 21. Available at: https://doi.org/10.1186/s13229-017-0137-9.

Antar, L.N. *et al.* (2004) 'Metabotropic Glutamate Receptor Activation Regulates Fragile X Mental Retardation Protein and *Fmr1* mRNA Localization Differentially in Dendrites and at Synapses', *The Journal of Neuroscience*, 24(11), pp. 2648–2655. Available at: https://doi.org/10.1523/JNEUROSCI.0099-04.2004.

Antar, L.N. *et al.* (2006) 'Local functions for FMRP in axon growth cone motility and activity-dependent regulation of filopodia and spine synapses', *Molecular and Cellular Neuroscience*, 32(1–2), pp. 37–48. Available at: https://doi.org/10.1016/j.mcn.2006.02.001.

Antoine, M.W. *et al.* (2019) 'Increased Excitation-Inhibition Ratio Stabilizes Synapse and Circuit Excitability in Four Autism Mouse Models', *Neuron*, 101(4), pp. 648-661.e4. Available at: https://doi.org/10.1016/j.neuron.2018.12.026.

Arpi, M.N.T. and Simpson, T.I. (2022) 'SFARI genes and where to find them; modelling Autism Spectrum Disorder specific gene expression dysregulation with RNA-seq data',

Scientific Reports, 12(1), p. 10158. Available at: https://doi.org/10.1038/s41598-022-14077-1.

Artegiani, B. *et al.* (2015) 'Tox: a multifunctional transcription factor and novel regulator of mammalian corticogenesis', *The EMBO Journal*, 34(7), pp. 896–910. Available at: https://doi.org/10.15252/embj.201490061.

Ashby, M.C. and Isaac, J.T.R. (2011) 'Maturation of a Recurrent Excitatory Neocortical Circuit by Experience-Dependent Unsilencing of Newly Formed Dendritic Spines', *Neuron*, 70(3), pp. 510–521. Available at: https://doi.org/10.1016/j.neuron.2011.02.057.

Asiminas, A. *et al.* (2019) 'Sustained correction of associative learning deficits after brief, early treatment in a rat model of Fragile X Syndrome', *Science Translational Medicine*, 11(494). Available at: https://doi.org/10.1126/scitranslmed.aao0498.

Asiminas, A. *et al.* (2022) 'Experience-dependent changes in hippocampal spatial activity and hippocampal circuit function are disrupted in a rat model of Fragile X Syndrome', *Molecular Autism*, 13(1), p. 49. Available at: https://doi.org/10.1186/s13229-022-00528-z.

Athar, Y.M. and Joseph, S. (2020) 'RNA-Binding Specificity of the Human Fragile X Mental Retardation Protein', *Journal of Molecular Biology*, 432(13), pp. 3851–3868. Available at: https://doi.org/10.1016/j.jmb.2020.04.021.

Bailey, A. *et al.* (1995) 'Autism as a strongly genetic disorder: evidence from a British twin study', *Psychological Medicine*, 25(1), pp. 63–77. Available at: https://doi.org/10.1017/S0033291700028099.

Baird, G. *et al.* (2006) 'Prevalence of disorders of the autism spectrum in a population cohort of children in South Thames: the Special Needs and Autism Project (SNAP)', *The Lancet*, 368(9531), pp. 210–215. Available at: https://doi.org/10.1016/S0140-6736(06)69041-7.

Baker, K.B. *et al.* (2010) 'Male and female *Fmr1* knockout mice on C57 albino background exhibit spatial learning and memory impairments', *Genes, Brain and Behavior*, 9(6), pp. 562–574. Available at: https://doi.org/10.1111/j.1601-183X.2010.00585.x.

Baranek, G.T. *et al.* (2008) 'Developmental Trajectories and Correlates of Sensory Processing in Young Boys with Fragile X Syndrome', *Physical & Occupational Therapy In Pediatrics*, 28(1), pp. 79–98. Available at: https://doi.org/10.1300/J006v28n01_06.

Bardoni, B., Gwizdek, C. and Maurin, T. (2025) 'How close are we to a cAMP- and cGMP-theory-based pharmacological therapy for fragile X syndrome?', *Cell Reports Medicine*, 6(2), p. 101972. Available at: https://doi.org/10.1016/j.xcrm.2025.101972.

Barnea-Goraly, N. *et al.* (2003) 'White matter tract alterations in fragile X syndrome: Preliminary evidence from diffusion tensor imaging', *American Journal of Medical Genetics*

Part B: Neuropsychiatric Genetics, 118B(1), pp. 81–88. Available at: https://doi.org/10.1002/ajmg.b.10035.

Barnes, S.A. *et al.* (2015) 'Convergence of Hippocampal Pathophysiology in *Syngap* +/− and *Fmr1* −/ *y* Mice', *The Journal of Neuroscience*, 35(45), pp. 15073–15081. Available at: https://doi.org/10.1523/JNEUROSCI.1087-15.2015.

Bartholomay, K. *et al.* (2019) 'Closing the Gender Gap in Fragile X Syndrome: Review of Females with Fragile X Syndrome and Preliminary Research Findings', *Brain Sciences*, 9(1), p. 11. Available at: https://doi.org/10.3390/brainsci9010011.

Bataveljic, D. *et al.* (2024) 'Astroglial Kir4.1 potassium channel deficit drives neuronal hyperexcitability and behavioral defects in Fragile X syndrome mouse model', *Nature Communications*, 15(1), p. 3583. Available at: https://doi.org/10.1038/s41467-024-47681-y.

Batista-Brito, R. *et al.* (2009) 'The Cell-Intrinsic Requirement of Sox6 for Cortical Interneuron Development', *Neuron*, 63(4), pp. 466–481. Available at: https://doi.org/10.1016/j.neuron.2009.08.005.

Bean, B.P. (2007) 'The action potential in mammalian central neurons', *Nature Reviews Neuroscience*, 8(6), pp. 451–465. Available at: https://doi.org/10.1038/nrn2148.

Bear, M.F., Huber, K.M. and Warren, S.T. (2004) 'The mGluR theory of fragile X mental retardation', *Trends in Neurosciences*, 27(7), pp. 370–377. Available at: https://doi.org/10.1016/j.tins.2004.04.009.

El Bekay, R. *et al.* (2007) 'Enhanced markers of oxidative stress, altered antioxidants and NADPH-oxidase activation in brains from Fragile X mental retardation 1-deficient mice, a pathological model for Fragile X syndrome', *European Journal of Neuroscience*, 26(11), pp. 3169–3180. Available at: https://doi.org/10.1111/j.1460-9568.2007.05939.x.

Bell, M.V. *et al.* (1991) 'Physical mapping across the fragile X: Hypermethylation and clinical expression of the fragile X syndrome', *Cell*, 64(4), pp. 861–866. Available at: https://doi.org/10.1016/0092-8674(91)90514-Y.

Berns, D.S. *et al.* (2018) 'Teneurin-3 controls topographic circuit assembly in the hippocampus', *Nature*, 554(7692), pp. 328–333. Available at: https://doi.org/10.1038/nature25463.

Berry-Kravis, E. (2002) 'Epilepsy in fragile X syndrome', *Developmental Medicine & Child Neurology*, 44(11). Available at: https://doi.org/10.1017/S0012162201002833.

Berry-Kravis, E., Harnett, M.D., *et al.* (2021) 'Inhibition of phosphodiesterase-4D in adults with fragile X syndrome: a randomized, placebo-controlled, phase 2 clinical trial', *Nature Medicine*, 27(5), pp. 862–870. Available at: https://doi.org/10.1038/s41591-021-01321-w.

Berry-Kravis, E., Filipink, R.A., *et al.* (2021) 'Seizures in Fragile X Syndrome: Associations and Longitudinal Analysis of a Large Clinic-Based Cohort', *Frontiers in Pediatrics*, 9. Available at: https://doi.org/10.3389/fped.2021.736255.

Berry-Kravis, E. (2022) 'Disease-Targeted Treatment Translation in Fragile X Syndrome as a Model for Neurodevelopmental Disorders', *Journal of Child Neurology*, 37(10–11), pp. 797–812. Available at: https://doi.org/10.1177/08830738221089740.

Berry-Kravis, E., Hicar, M. and Ciurlionis, R. (1995) 'Reduced Cyclic AMP Production in Fragile X Syndrome: Cytogenetic and Molecular Correlations', *Pediatric Research*, 38(5), pp. 638–643. Available at: https://doi.org/10.1203/00006450-199511000-00002.

Berry-Kravis, E.M. *et al.* (2018) 'Drug development for neurodevelopmental disorders: lessons learned from fragile X syndrome', *Nature Reviews Drug Discovery*, 17(4), pp. 280–299. Available at: https://doi.org/10.1038/nrd.2017.221.

Berzhanskaya, J. *et al.* (2016) 'Sensory hypo-excitability in a rat model of fetal development in Fragile X Syndrome', *Scientific Reports*, 6(1), p. 30769. Available at: https://doi.org/10.1038/srep30769.

Bhattacharyya, A. and Zhao, X. (2016) 'Human pluripotent stem cell models of Fragile X syndrome', *Molecular and Cellular Neuroscience*, 73, pp. 43–51. Available at: https://doi.org/10.1016/j.mcn.2015.11.011.

Bianchi, D. *et al.* (2012) 'On the mechanisms underlying the depolarization block in the spiking dynamics of CA1 pyramidal neurons', *Journal of Computational Neuroscience*, 33(2), pp. 207–225. Available at: https://doi.org/10.1007/s10827-012-0383-y.

Bland, K.M. *et al.* (2021) 'FMRP regulates the subcellular distribution of cortical dendritic spine density in a non-cell-autonomous manner', *Neurobiology of Disease*, 150, p. 105253. Available at: https://doi.org/10.1016/j.nbd.2021.105253.

Bonanno, G. *et al.* (1991) 'Somatostatin Release from Rat Cerebral Cortex Synaptosomes', *Journal of Neurochemistry*, 57(4), pp. 1258–1264. Available at: https://doi.org/10.1111/j.1471-4159.1991.tb08287.x.

Booker, S.A. *et al.* (2019) 'Altered dendritic spine function and integration in a mouse model of fragile X syndrome', *Nature Communications*, 10(1), p. 4813. Available at: https://doi.org/10.1038/s41467-019-11891-6.

Booker, S.A. *et al.* (2020) 'Input-Output Relationship of CA1 Pyramidal Neurons Reveals Intact Homeostatic Mechanisms in a Mouse Model of Fragile X Syndrome', *Cell Reports*, 32(6), p. 107988. Available at: https://doi.org/10.1016/j.celrep.2020.107988.

Borreca, A. *et al.* (2023) 'Fmr1-KO mice failure to detect object novelty associates with a post-test decrease of structural and synaptic plasticity upstream of the hippocampus', *Scientific Reports*, 13(1), p. 755. Available at: https://doi.org/10.1038/s41598-023-27991-9.

Bowling, H. *et al.* (2019) 'Altered steady state and activity-dependent de novo protein expression in fragile X syndrome', *Nature Communications*, 10(1), p. 1710. Available at: https://doi.org/10.1038/s41467-019-09553-8.

Brandalise, F. *et al.* (2020) 'Fragile X Mental Retardation Protein Bidirectionally Controls Dendritic Ih in a Cell Type-Specific Manner between Mouse Hippocampus and Prefrontal Cortex', *The Journal of Neuroscience*, 40(27), pp. 5327–5340. Available at: https://doi.org/10.1523/JNEUROSCI.1670-19.2020.

Bridi, M.C.D. and Peixoto, L. (2025) 'Excitatory/Inhibitory imbalance as a mechanism linking autism and sleep problems', *Current Opinion in Neurobiology*, 90, p. 102968. Available at: https://doi.org/10.1016/j.conb.2024.102968.

Brighi, C. *et al.* (2021) 'Novel fragile X syndrome 2D and 3D brain models based on human isogenic FMRP-KO iPSCs', *Cell Death & Disease*, 12(5), p. 498. Available at: https://doi.org/10.1038/s41419-021-03776-8.

Brown, C.O. *et al.* (2024) 'Disruption of the autism-associated gene SCN2A alters synaptic development and neuronal signaling in patient iPSC-glutamatergic neurons', *Frontiers in Cellular Neuroscience*, 17. Available at: https://doi.org/10.3389/fncel.2023.1239069.

Brown, D.L. (2017) 'Bias in image analysis and its solution: unbiased stereology', *Journal of Toxicologic Pathology*, 30(3), pp. 183–191. Available at: https://doi.org/10.1293/tox.2017-0013.

Brown, V. *et al.* (2001) 'Microarray Identification of FMRP-Associated Brain mRNAs and Altered mRNA Translational Profiles in Fragile X Syndrome', *Cell*, 107(4), pp. 477–487. Available at: https://doi.org/10.1016/S0092-8674(01)00568-2.

Bryant, A. *et al.* (2023) 'Endothelial Cells Are Heterogeneous in Different Brain Regions and Are Dramatically Altered in Alzheimer's Disease', *The Journal of Neuroscience*, 43(24), pp. 4541–4557. Available at: https://doi.org/10.1523/JNEUROSCI.0237-23.2023.

Budimirovic, D.B. *et al.* (2022) 'Sleep problems in fragile X syndrome: Cross-sectional analysis of a large clinic-based cohort', *American Journal of Medical Genetics Part A*, 188(4), pp. 1029–1039. Available at: https://doi.org/10.1002/ajmg.a.62601.

Bureau, I., Shepherd, G.M.G. and Svoboda, K. (2008) 'Circuit and Plasticity Defects in the Developing Somatosensory Cortex of Fmr1 Knock-Out Mice', *The Journal of Neuroscience*, 28(20), pp. 5178–5188. Available at: https://doi.org/10.1523/JNEUROSCI.1076-08.2008.

Butovsky, O. and Weiner, H.L. (2018) 'Microglial signatures and their role in health and disease', *Nature Reviews Neuroscience*, 19(10), pp. 622–635. Available at: https://doi.org/10.1038/s41583-018-0057-5.

C Yuen, R.K. *et al.* (2017) 'Whole genome sequencing resource identifies 18 new candidate genes for autism spectrum disorder', *Nature Neuroscience*, 20(4), pp. 602–611. Available at: https://doi.org/10.1038/nn.4524.

Cadwell, C.R. *et al.* (2016) 'Electrophysiological, transcriptomic and morphologic profiling of single neurons using Patch-seq', *Nature Biotechnology*, 34(2), pp. 199–203. Available at: https://doi.org/10.1038/nbt.3445.

Cadwell, C.R. *et al.* (2017) 'Multimodal profiling of single-cell morphology, electrophysiology, and gene expression using Patch-seq', *Nature Protocols*, 12(12), pp. 2531–2553. Available at: https://doi.org/10.1038/nprot.2017.120.

Casingal, C.R. *et al.* (2020) 'Identification of FMRP target mRNAs in the developmental brain: FMRP might coordinate Ras/MAPK, Wnt/β-catenin, and mTOR signaling during corticogenesis', *Molecular Brain*, 13(1), p. 167. Available at: https://doi.org/10.1186/s13041-020-00706-1.

Cea-Del Rio, C.A. *et al.* (2020) 'Disrupted inhibitory plasticity and homeostasis in Fragile X syndrome', *Neurobiology of Disease*, 142, p. 104959. Available at: https://doi.org/10.1016/j.nbd.2020.104959.

Chen, C. *et al.* (1990) 'Two types of voltage-dependent calcium current in rat somatotrophs are reduced by somatostatin.', *The Journal of Physiology*, 425(1), pp. 29–42. Available at: https://doi.org/10.1113/jphysiol.1990.sp018090.

Chen, L. and Toth, M. (2001) 'Fragile X mice develop sensory hyperreactivity to auditory stimuli', *Neuroscience*, 103(4), pp. 1043–1050. Available at: https://doi.org/10.1016/S0306-4522(01)00036-7.

Chittajallu, R., Pelkey, K.A. and McBain, C.J. (2013) 'Neurogliaform cells dynamically regulate somatosensory integration via synapse-specific modulation', *Nature Neuroscience*, 16(1), pp. 13–15. Available at: https://doi.org/10.1038/nn.3284.

Choi, C.H. *et al.* (2015) 'PDE-4 Inhibition Rescues Aberrant Synaptic Plasticity in *Drosophila* and Mouse Models of Fragile X Syndrome', *The Journal of Neuroscience*, 35(1), pp. 396–408. Available at: https://doi.org/10.1523/JNEUROSCI.1356-12.2015.

Choi, C.H. *et al.* (2016) 'Multiple Drug Treatments That Increase cAMP Signaling Restore Long-Term Memory and Aberrant Signaling in Fragile X Syndrome Models', *Frontiers in Behavioral Neuroscience*, 10. Available at: https://doi.org/10.3389/fnbeh.2016.00136.

Chudley, A.E. and Hagerman, R.J. (1987) 'Fragile X syndrome', *The Journal of Pediatrics*, 110(6), pp. 821–831. Available at: https://doi.org/10.1016/S0022-3476(87)80392-X.

Ciganok-Hückels, N. *et al.* (2023) 'Postnatal development of electrophysiological and morphological properties in layer 2/3 and layer 5 pyramidal neurons in the mouse primary

visual cortex', *Cerebral Cortex*, 33(10), pp. 5875–5884. Available at: https://doi.org/10.1093/cercor/bhac467.

Clements, J.D. and Bekkers, J.M. (1997) 'Detection of spontaneous synaptic events with an optimally scaled template', *Biophysical Journal*, 73(1), pp. 220–229. Available at: https://doi.org/10.1016/S0006-3495(97)78062-7.

Clifford, S. *et al.* (2007) 'Autism Spectrum Phenotype in Males and Females with Fragile X Full Mutation and Premutation', *Journal of Autism and Developmental Disorders*, 37(4), pp. 738–747. Available at: https://doi.org/10.1007/s10803-006-0205-z.

Coffee, B. *et al.* (2008) 'Mosaic *FMR1* deletion causes fragile X syndrome and can lead to molecular misdiagnosis: A case report and review of the literature', *American Journal of Medical Genetics Part A*, 146A(10), pp. 1358–1367. Available at: https://doi.org/10.1002/ajmg.a.32261.

Comery, T.A. *et al.* (1997) 'Abnormal dendritic spines in fragile X knockout mice: Maturation and pruning deficits', *Proceedings of the National Academy of Sciences*, 94(10), pp. 5401–5404. Available at: https://doi.org/10.1073/pnas.94.10.5401.

Constantinople, C.M. and Bruno, R.M. (2013) 'Deep Cortical Layers Are Activated Directly by Thalamus', *Science*, 340(6140), pp. 1591–1594. Available at: https://doi.org/10.1126/science.1236425.

Cordeiro, L. *et al.* (2011) 'Clinical assessment of DSM-IV anxiety disorders in fragile X syndrome: prevalence and characterization', *Journal of Neurodevelopmental Disorders*, 3(1), pp. 57–67. Available at: https://doi.org/10.1007/s11689-010-9067-y.

Cornish, K., Munir, F. and Cross, G. (1999) 'Spatial Cognition in Males With Fragile-X Syndrome: Evidence for a Neuropsychological Phenotype', *Cortex*, 35(2), pp. 263–271. Available at: https://doi.org/10.1016/S0010-9452(08)70799-8.

Costa, L. *et al.* (2018) 'Activation of Serotonin 5-HT7 Receptors Modulates Hippocampal Synaptic Plasticity by Stimulation of Adenylate Cyclases and Rescues Learning and Behavior in a Mouse Model of Fragile X Syndrome', *Frontiers in Molecular Neuroscience*, 11. Available at: https://doi.org/10.3389/fnmol.2018.00353.

Crair, M.C. and Malenka, R.C. (1995) 'A critical period for long-term potentiation at thalamocortical synapses', *Nature*, 375(6529), pp. 325–328. Available at: https://doi.org/10.1038/375325a0.

Crandall, S.R. *et al.* (2017) 'Infrabarrels Are Layer 6 Circuit Modules in the Barrel Cortex that Link Long-Range Inputs and Outputs', *Cell Reports*, 21(11), pp. 3065–3078. Available at: https://doi.org/10.1016/j.celrep.2017.11.049.

Crawford, D.C., Acuña, J.M. and Sherman, S.L. (2001) 'FMR1 and the fragile X syndrome: Human genome epidemiology review', *Genetics in Medicine*, 3(5), pp. 359–371. Available at: https://doi.org/10.1097/00125817-200109000-00006.

Crawford, H. *et al.* (2020) 'Fragile X syndrome: an overview of cause, characteristics, assessment and management', *Paediatrics and Child Health*, 30(11), pp. 400–403. Available at: https://doi.org/10.1016/j.paed.2020.08.007.

Cregenzán-Royo, O., Brun-Gasca, C. and Fornieles-Deu, A. (2022) 'Behavior Problems and Social Competence in Fragile X Syndrome: A Systematic Review', *Genes*, 13(2), p. 280. Available at: https://doi.org/10.3390/genes13020280.

Dahlhaus, R. (2018) 'Of Men and Mice: Modeling the Fragile X Syndrome', *Frontiers in Molecular Neuroscience*, 11. Available at: https://doi.org/10.3389/fnmol.2018.00041.

Darnell, J.C. *et al.* (2011) 'FMRP Stalls Ribosomal Translocation on mRNAs Linked to Synaptic Function and Autism', *Cell*, 146(2), pp. 247–261. Available at: https://doi.org/10.1016/j.cell.2011.06.013.

Delevich, K. *et al.* (2015) 'The Mediodorsal Thalamus Drives Feedforward Inhibition in the Anterior Cingulate Cortex via Parvalbumin Interneurons', *The Journal of Neuroscience*, 35(14), pp. 5743–5753. Available at: https://doi.org/10.1523/JNEUROSCI.4565-14.2015.

Deng, P.-Y. *et al.* (2013) 'FMRP Regulates Neurotransmitter Release and Synaptic Information Transmission by Modulating Action Potential Duration via BK Channels', *Neuron*, 77(4), pp. 696–711. Available at: https://doi.org/10.1016/j.neuron.2012.12.018.

Deng, P.-Y. *et al.* (2019) 'Voltage-Independent SK-Channel Dysfunction Causes Neuronal Hyperexcitability in the Hippocampus of Fmr1 Knock-Out Mice', *The Journal of Neuroscience*, 39(1), pp. 28–43. Available at: https://doi.org/10.1523/JNEUROSCI.1593-18.2018.

Deng, P.-Y. and Klyachko, V.A. (2016) 'Increased Persistent Sodium Current Causes Neuronal Hyperexcitability in the Entorhinal Cortex of Fmr1 Knockout Mice', *Cell Reports*, 16(12), pp. 3157–3166. Available at: https://doi.org/10.1016/j.celrep.2016.08.046.

Deng, W. *et al.* (2015) 'The Relationship Among Genetic Heritability, Environmental Effects, and Autism Spectrum Disorders', *Journal of Child Neurology*, 30(13), pp. 1794–1799. Available at: https://doi.org/10.1177/0883073815580645.

Desai, N.S. *et al.* (2006) 'Early Postnatal Plasticity in Neocortex of *Fmr1* Knockout Mice', *Journal of Neurophysiology*, 96(4), pp. 1734–1745. Available at: https://doi.org/10.1152/jn.00221.2006.

Devlin, B. and Scherer, S.W. (2012) 'Genetic architecture in autism spectrum disorder', *Current Opinion in Genetics & Development*, 22(3), pp. 229–237. Available at: https://doi.org/10.1016/j.gde.2012.03.002.

D'Hooge, R. *et al.* (1997) 'Mildly impaired water maze performance in maleFmr1 knockout mice', *Neuroscience*, 76(2), pp. 367–376. Available at: https://doi.org/10.1016/S0306-4522(96)00224-2.

D'Incal, C.P. *et al.* (2025) 'A missense variant in the KH0-domain of FMRP downregulates the protein in a patient with the clinical hallmarks of fragile X syndrome', *European Journal of Human Genetics* [Preprint]. Available at: https://doi.org/10.1038/s41431-025-01967-x.

Ding, Q., Sethna, F. and Wang, H. (2014) 'Behavioral analysis of male and female Fmr1 knockout mice on C57BL/6 background', *Behavioural Brain Research*, 271, pp. 72–78. Available at: https://doi.org/10.1016/j.bbr.2014.05.046.

Doers, M.E. *et al.* (2014) 'iPSC-Derived Forebrain Neurons from FXS Individuals Show Defects in Initial Neurite Outgrowth', *Stem Cells and Development*, 23(15), pp. 1777–1787. Available at: https://doi.org/10.1089/scd.2014.0030.

Dolan, B.M. *et al.* (2013) 'Rescue of fragile X syndrome phenotypes in Fmr1 KO mice by the small-molecule PAK inhibitor FRAX486', *Proceedings of the National Academy of Sciences*, 110(14), pp. 5671–5676. Available at: https://doi.org/10.1073/pnas.1219383110.

Doll, C.A. and Broadie, K. (2015) 'Activity-dependent FMRP requirements in development of the neural circuitry of learning and memory', *Development*, 142(7), pp. 1346–1356. Available at: https://doi.org/10.1242/dev.117127.

Domanski, A.P.F. *et al.* (2019) 'Cellular and synaptic phenotypes lead to disrupted information processing in Fmr1-KO mouse layer 4 barrel cortex', *Nature Communications*, 10(1), p. 4814. Available at: https://doi.org/10.1038/s41467-019-12736-y.

Donnard, E., Shu, H. and Garber, M. (2022) 'Single cell transcriptomics reveals dysregulated cellular and molecular networks in a fragile X syndrome model', *PLOS Genetics*, 18(6), p. e1010221. Available at: https://doi.org/10.1371/journal.pgen.1010221.

Dorrn, A.L. *et al.* (2010) 'Developmental sensory experience balances cortical excitation and inhibition', *Nature*, 465(7300), pp. 932–936. Available at: https://doi.org/10.1038/nature09119.

Drozd, M., Bardoni, B. and Capovilla, M. (2018) 'Modeling Fragile X Syndrome in Drosophila', *Frontiers in Molecular Neuroscience*, 11. Available at: https://doi.org/10.3389/fnmol.2018.00124.

Eadie, B.D. *et al.* (2009) 'Fmr1 knockout mice show reduced anxiety and alterations in neurogenesis that are specific to the ventral dentate gyrus', *Neurobiology of Disease*, 36(2), pp. 361–373. Available at: https://doi.org/10.1016/j.nbd.2009.08.001.

Egger, V., Nevian, T. and Bruno, R.M. (2008) 'Subcolumnar Dendritic and Axonal Organization of Spiny Stellate and Star Pyramid Neurons within a Barrel in Rat Somatosensory

Cortex', *Cerebral Cortex*, 18(4), pp. 876–889. Available at: https://doi.org/10.1093/cercor/bhm126.

Eleftheriou, C. *et al.* (2025) 'Better statistical reporting does not lead to statistical rigour: lessons from two decades of pseudoreplication in mouse-model studies of neurological disorders', *Molecular Autism*, 16(1), p. 30. Available at: https://doi.org/10.1186/s13229-025-00663-3.

Ellingford, R.A. *et al.* (2021) 'Cell-type-specific synaptic imbalance and disrupted homeostatic plasticity in cortical circuits of ASD-associated Chd8 haploinsufficient mice', *Molecular Psychiatry*, 26(7), pp. 3614–3624. Available at: https://doi.org/10.1038/s41380-021-01070-9.

Engineer, C.T. *et al.* (2014) 'Degraded speech sound processing in a rat model of fragile X syndrome', *Brain Research*, 1564, pp. 72–84. Available at: https://doi.org/10.1016/j.brainres.2014.03.049.

Epelbaum, J. (1986) 'Somatostatin in the central nervous system: Physiology and pathological modifications', *Progress in Neurobiology*, 27(1), pp. 63–100. Available at: https://doi.org/10.1016/0301-0082(86)90012-2.

Ethridge, L.E. *et al.* (2016) 'Reduced habituation of auditory evoked potentials indicate cortical hyper-excitability in Fragile X Syndrome', *Translational Psychiatry*, 6(4), pp. e787–e787. Available at: https://doi.org/10.1038/tp.2016.48.

Ethridge, L.E. *et al.* (2017) 'Neural synchronization deficits linked to cortical hyper-excitability and auditory hypersensitivity in fragile X syndrome', *Molecular Autism*, 8(1), p. 22. Available at: https://doi.org/10.1186/s13229-017-0140-1.

Feldman, D.E. *et al.* (1998) 'Long-Term Depression at Thalamocortical Synapses in Developing Rat Somatosensory Cortex', *Neuron*, 21(2), pp. 347–357. Available at: https://doi.org/10.1016/S0896-6273(00)80544-9.

Feldmeyer, D. (2012) 'Excitatory neuronal connectivity in the barrel cortex', *Frontiers in Neuroanatomy*, 6. Available at: https://doi.org/10.3389/fnana.2012.00024.

Feldmeyer, D. *et al.* (2018) 'Inhibitory Interneurons and their Circuit Motifs in the Many Layers of the Barrel Cortex', *Neuroscience*, 368, pp. 132–151. Available at: https://doi.org/10.1016/j.neuroscience.2017.05.027.

Ferri, R. *et al.* (1994) 'BIT-mapped somatosensory evoked potentials in the fragile X syndrome', *Neurophysiologie Clinique/Clinical Neurophysiology*, 24(6), pp. 413–426. Available at: https://doi.org/10.1016/S0987-7053(05)80074-7.

Filippini, A. *et al.* (2017) 'Absence of the Fragile X Mental Retardation Protein results in defects of RNA editing of neuronal mRNAs in mouse', *RNA Biology*, 14(11), pp. 1580–1591. Available at: https://doi.org/10.1080/15476286.2017.1338232.

Fox, K. (1992) ‘A critical period for experience-dependent synaptic plasticity in rat barrel cortex’, *The Journal of Neuroscience*, 12(5), pp. 1826–1838. Available at: https://doi.org/10.1523/JNEUROSCI.12-05-01826.1992.

Francés, L. *et al.* (2022) ‘Current state of knowledge on the prevalence of neurodevelopmental disorders in childhood according to the DSM-5: a systematic review in accordance with the PRISMA criteria’, *Child and Adolescent Psychiatry and Mental Health*, 16(1), p. 27. Available at: https://doi.org/10.1186/s13034-022-00462-1.

Francés, L. *et al.* (2023) ‘Prevalence, comorbidities, and profiles of neurodevelopmental disorders according to the DSM-5-TR in children aged 6 years old in a European region’, *Frontiers in Psychiatry*, 14. Available at: https://doi.org/10.3389/fpsyt.2023.1260747.

Fujioka, T., Fujioka, A. and Duman, R.S. (2004) ‘Activation of cAMP Signaling Facilitates the Morphological Maturation of Newborn Neurons in Adult Hippocampus’, *The Journal of Neuroscience*, 24(2), pp. 319–328. Available at: https://doi.org/10.1523/JNEUROSCI.1065.03.2004.

Fukuchi-Shimogori, T. and Grove, E.A. (2001) ‘Neocortex Patterning by the Secreted Signaling Molecule FGF8’, *Science*, 294(5544), pp. 1071–1074. Available at: https://doi.org/10.1126/science.1064252.

Fuzik, J. *et al.* (2016) ‘Integration of electrophysiological recordings with single-cell RNA-seq data identifies neuronal subtypes’, *Nature Biotechnology*, 34(2), pp. 175–183. Available at: https://doi.org/10.1038/nbt.3443.

Gabel, L.A. *et al.* (2004) ‘Visual Experience Regulates Transient Expression and Dendritic Localization of Fragile X Mental Retardation Protein’, *The Journal of Neuroscience*, 24(47), pp. 10579–10583. Available at: https://doi.org/10.1523/JNEUROSCI.2185-04.2004.

Galvez, R., Gopal, A.R. and Greenough, W.T. (2003) ‘Somatosensory cortical barrel dendritic abnormalities in a mouse model of the fragile X mental retardation syndrome’, *Brain Research*, 971(1), pp. 83–89. Available at: https://doi.org/10.1016/S0006-8993(03)02363-1.

Galvez, R. and Greenough, W.T. (2005) ‘Sequence of abnormal dendritic spine development in primary somatosensory cortex of a mouse model of the fragile X mental retardation syndrome’, *American Journal of Medical Genetics Part A*, 135A(2), pp. 155–160. Available at: https://doi.org/10.1002/ajmg.a.30709.

Geng, J. *et al.* (2023) ‘Deregulation of ER-mitochondria contact formation and mitochondrial calcium homeostasis mediated by VDAC in fragile X syndrome’, *Developmental Cell*, 58(7), pp. 597-615.e10. Available at: https://doi.org/10.1016/j.devcel.2023.03.002.

Germain, P.-L. *et al.* (2022) 'Doublet identification in single-cell sequencing data using scDblFinder', *F1000Research*, 10, p. 979. Available at: https://doi.org/10.12688/f1000research.73600.2.

Gholizadeh, S., Halder, S.K. and Hampson, D.R. (2015) 'Expression of fragile X mental retardation protein in neurons and glia of the developing and adult mouse brain', *Brain Research*, 1596, pp. 22–30. Available at: https://doi.org/10.1016/j.brainres.2014.11.023.

Gibson, J.R. *et al.* (2008) 'Imbalance of Neocortical Excitation and Inhibition and Altered UP States Reflect Network Hyperexcitability in the Mouse Model of Fragile X Syndrome', *Journal of Neurophysiology*, 100(5), pp. 2615–2626. Available at: https://doi.org/10.1152/jn.90752.2008.

Giri, S. *et al.* (2019) 'Generation of a FMR1 homozygous knockout human embryonic stem cell line (WAe009-A-16) by CRISPR/Cas9 editing', *Stem Cell Research*, 39, p. 101494. Available at: https://doi.org/10.1016/j.scr.2019.101494.

Goel, A. *et al.* (2018) 'Impaired perceptual learning in a mouse model of Fragile X syndrome is mediated by parvalbumin neuron dysfunction and is reversible', *Nature Neuroscience*, 21(10), pp. 1404–1411. Available at: https://doi.org/10.1038/s41593-018-0231-0.

Golowasch, J. *et al.* (2009) 'Membrane Capacitance Measurements Revisited: Dependence of Capacitance Value on Measurement Method in Nonisopotential Neurons', *Journal of Neurophysiology*, 102(4), pp. 2161–2175. Available at: https://doi.org/10.1152/jn.00160.2009.

Gonçalves, J.T. *et al.* (2013) 'Circuit level defects in the developing neocortex of Fragile X mice', *Nature Neuroscience*, 16(7), pp. 903–909. Available at: https://doi.org/10.1038/nn.3415.

Goswami, S. *et al.* (2019) 'Local cortical circuit correlates of altered EEG in the mouse model of Fragile X syndrome', *Neurobiology of Disease*, 124, pp. 563–572. Available at: https://doi.org/10.1016/j.nbd.2019.01.002.

Gouwens, N.W. *et al.* (2020) 'Integrated Morphoelectric and Transcriptomic Classification of Cortical GABAergic Cells', *Cell*, 183(4), pp. 935-953.e19. Available at: https://doi.org/10.1016/j.cell.2020.09.057.

Greco, C.M. *et al.* (2011) 'Neuropathologic features in the hippocampus and cerebellum of three older men with fragile X syndrome', *Molecular Autism*, 2(1), p. 2. Available at: https://doi.org/10.1186/2040-2392-2-2.

Greenough, W.T. and Chang, F.-L.F. (1988) 'Dendritic pattern formation involves both oriented regression and oriented growth in the barrels of mouse somatosensory cortex', *Developmental Brain Research*, 43(1), pp. 148–152. Available at: https://doi.org/10.1016/0165-3806(88)90160-5.

Griffiths, K.K. *et al.* (2020) 'Inefficient thermogenic mitochondrial respiration due to futile proton leak in a mouse model of fragile X syndrome', *The FASEB Journal*, 34(6), pp. 7404–7426. Available at: https://doi.org/10.1096/fj.202000283RR.

Grove, J. *et al.* (2019) 'Identification of common genetic risk variants for autism spectrum disorder', *Nature Genetics*, 51(3), pp. 431–444. Available at: https://doi.org/10.1038/s41588-019-0344-8.

Gundersen, H.J.G. *et al.* (1988) 'The new stereological tools: Disector, fractionator, nucleator and point sampled intercepts and their use in pathological research and diagnosis', *APMIS*, 96(7–12), pp. 857–881. Available at: https://doi.org/10.1111/j.1699-0463.1988.tb00954.x.

Gurney, M.E. *et al.* (2017) 'Multiple Behavior Phenotypes of the Fragile-X Syndrome Mouse Model Respond to Chronic Inhibition of Phosphodiesterase-4D (PDE4D)', *Scientific Reports*, 7(1), p. 14653. Available at: https://doi.org/10.1038/s41598-017-15028-x.

Gurney, M.E. *et al.* (2019) 'Design and Synthesis of Selective Phosphodiesterase 4D (PDE4D) Allosteric Inhibitors for the Treatment of Fragile X Syndrome and Other Brain Disorders', *Journal of Medicinal Chemistry*, 62(10), pp. 4884–4901. Available at: https://doi.org/10.1021/acs.jmedchem.9b00193.

Haberl, M.G. *et al.* (2015) 'Structural-functional connectivity deficits of neocortical circuits in the *Fmr1 −/y* mouse model of autism', *Science Advances*, 1(10). Available at: https://doi.org/10.1126/sciadv.1500775.

Hagerman, R.J. *et al.* (2009) 'Advances in the Treatment of Fragile X Syndrome', *Pediatrics*, 123(1), pp. 378–390. Available at: https://doi.org/10.1542/peds.2008-0317.

Hall, S.S. *et al.* (2013) 'Identifying Large-Scale Brain Networks in Fragile X Syndrome', *JAMA Psychiatry*, 70(11), p. 1215. Available at: https://doi.org/10.1001/jamapsychiatry.2013.247.

Hall, S.S., Dougherty, R.F. and Reiss, A.L. (2016) 'Profiles of aberrant white matter microstructure in fragile X syndrome', *NeuroImage: Clinical*, 11, pp. 133–138. Available at: https://doi.org/10.1016/j.nicl.2016.01.013.

Hallmayer, J. (2011) 'Genetic Heritability and Shared Environmental Factors Among Twin Pairs With Autism', *Archives of General Psychiatry*, 68(11), p. 1095. Available at: https://doi.org/10.1001/archgenpsychiatry.2011.76.

Hamilton, S.M. *et al.* (2014) 'Fmr1 and Nlgn3 knockout rats: Novel tools for investigating autism spectrum disorders.', *Behavioral Neuroscience*, 128(2), pp. 103–109. Available at: https://doi.org/10.1037/a0035988.

Hammond, L.S. *et al.* (1997) 'Fragile X syndrome and deletions in FMR1: New case and review of the literature', *American Journal of Medical Genetics*, 72(4), pp. 430–434.

Available at: https://doi.org/10.1002/(SICI)1096-8628(19971112)72:4<430::AID-AJMG11>3.0.CO;2-S.

Handt, M. *et al.* (2014) 'Point mutation frequency in the FMR1 gene as revealed by fragile X syndrome screening', *Molecular and Cellular Probes*, 28(5–6), pp. 279–283. Available at: https://doi.org/10.1016/j.mcp.2014.08.003.

Hao, Y. *et al.* (2024) 'Dictionary learning for integrative, multimodal and scalable single-cell analysis', *Nature Biotechnology*, 42(2), pp. 293–304. Available at: https://doi.org/10.1038/s41587-023-01767-y.

Harlow, E.G. *et al.* (2010) 'Critical Period Plasticity Is Disrupted in the Barrel Cortex of Fmr1 Knockout Mice', *Neuron*, 65(3), pp. 385–398. Available at: https://doi.org/10.1016/j.neuron.2010.01.024.

Harris, S.W. *et al.* (2008) 'Autism Profiles of Males With Fragile X Syndrome', *American Journal on Mental Retardation*, 113(6), pp. 427–438. Available at: https://doi.org/10.1352/2008.113:427-438.

Hashimoto, T. and Obata, K. (1991) 'Induction of somatostatin by kainic acid in pyramidal and granule cells of the rat hippocampus', *Neuroscience Research*, 12(4), pp. 514–527. Available at: https://doi.org/10.1016/S0168-0102(09)80004-7.

Hayashi, M.L. *et al.* (2007) 'Inhibition of p21-activated kinase rescues symptoms of fragile X syndrome in mice', *Proceedings of the National Academy of Sciences*, 104(27), pp. 11489–11494. Available at: https://doi.org/10.1073/pnas.0705003104.

He, C.X. *et al.* (2017) 'Tactile Defensiveness and Impaired Adaptation of Neuronal Activity in the *Fmr1* Knock-Out Mouse Model of Autism', *The Journal of Neuroscience*, 37(27), pp. 6475–6487. Available at: https://doi.org/10.1523/JNEUROSCI.0651-17.2017.

He, Q. *et al.* (2019) 'Critical period inhibition of NKCC1 rectifies synapse plasticity in the somatosensory cortex and restores adult tactile response maps in fragile X mice', *Molecular Psychiatry*, 24(11), pp. 1732–1747. Available at: https://doi.org/10.1038/s41380-018-0048-y.

Hell, J.W. *et al.* (1995) 'Phosphorylation of presynaptic and postsynaptic calcium channels by cAMP-dependent protein kinase in hippocampal neurons.', *The EMBO Journal*, 14(13), pp. 3036–3044. Available at: https://doi.org/10.1002/j.1460-2075.1995.tb07306.x.

Hendry, S. *et al.* (1987) 'Numbers and proportions of GABA-immunoreactive neurons in different areas of monkey cerebral cortex', *The Journal of Neuroscience*, 7(5), pp. 1503–1519. Available at: https://doi.org/10.1523/JNEUROSCI.07-05-01503.1987.

Hernandez, R.N. *et al.* (2009) 'Autism spectrum disorder in fragile X syndrome: A longitudinal evaluation', *American Journal of Medical Genetics Part A*, 149A(6), pp. 1125–1137. Available at: https://doi.org/10.1002/ajmg.a.32848.

Hessl, D. *et al.* (2009) 'A solution to limitations of cognitive testing in children with intellectual disabilities: the case of fragile X syndrome', *Journal of Neurodevelopmental Disorders*, 1(1), pp. 33–45. Available at: https://doi.org/10.1007/s11689-008-9001-8.

Hessl, D., Rivera, S.M. and Reiss, A.L. (2004) 'The neuroanatomy and neuroendocrinology of fragile X syndrome', *Mental Retardation and Developmental Disabilities Research Reviews*, 10(1), pp. 17–24. Available at: https://doi.org/10.1002/mrdd.20004.

Hevner, R. and Wong-Riley, M. (1993) 'Mitochondrial and nuclear gene expression for cytochrome oxidase subunits are disproportionately regulated by functional activity in neurons', *The Journal of Neuroscience*, 13(5), pp. 1805–1819. Available at: https://doi.org/10.1523/JNEUROSCI.13-05-01805.1993.

Hinton, V.J. *et al.* (1991) 'Analysis of neocortex in three males with the fragile X syndrome', *American Journal of Medical Genetics*, 41(3), pp. 289–294. Available at: https://doi.org/10.1002/ajmg.1320410306.

Hodgkin, A.L. and Huxley, A.F. (1952) 'A quantitative description of membrane current and its application to conduction and excitation in nerve', *The Journal of Physiology*, 117(4), pp. 500–544. Available at: https://doi.org/10.1113/jphysiol.1952.sp004764.

Hoeft, F. *et al.* (2010) 'Region-specific alterations in brain development in one- to three-year-old boys with fragile X syndrome', *Proceedings of the National Academy of Sciences*, 107(20), pp. 9335–9339. Available at: https://doi.org/10.1073/pnas.1002762107.

Hoffman, D.A. and Johnston, D. (1998) 'Downregulation of Transient K + Channels in Dendrites of Hippocampal CA1 Pyramidal Neurons by Activation of PKA and PKC', *The Journal of Neuroscience*, 18(10), pp. 3521–3528. Available at: https://doi.org/10.1523/JNEUROSCI.18-10-03521.1998.

Hou, L. *et al.* (2006) 'Dynamic Translational and Proteasomal Regulation of Fragile X Mental Retardation Protein Controls mGluR-Dependent Long-Term Depression', *Neuron*, 51(4), pp. 441–454. Available at: https://doi.org/10.1016/j.neuron.2006.07.005.

Hou, Z.-H. and Yu, X. (2013) 'Activity-regulated Somatostatin Expression Reduces Dendritic Spine Density and Lowers Excitatory Synaptic Transmission via Postsynaptic Somatostatin Receptor 4', *Journal of Biological Chemistry*, 288(4), pp. 2501–2509. Available at: https://doi.org/10.1074/jbc.M112.419051.

Hubel, D.H. and Wiesel, T.N. (1963) 'Receptive Fields of Cells in Striate Cortex of Very Young, Visually Inexperienced Kittens', *Journal of Neurophysiology*, 26(6), pp. 994–1002. Available at: https://doi.org/10.1152/jn.1963.26.6.994.

Hubel, D.H. and Wiesel, T.N. (1970) 'The period of susceptibility to the physiological effects of unilateral eye closure in kittens', *The Journal of Physiology*, 206(2), pp. 419–436. Available at: https://doi.org/10.1113/jphysiol.1970.sp009022.

Huber, K.M. *et al.* (2002) 'Altered synaptic plasticity in a mouse model of fragile X mental retardation', *Proceedings of the National Academy of Sciences*, 99(11), pp. 7746–7750. Available at: https://doi.org/10.1073/pnas.122205699.

van den Hurk, M. *et al.* (2018) 'Patch-Seq Protocol to Analyze the Electrophysiology, Morphology and Transcriptome of Whole Single Neurons Derived From Human Pluripotent Stem Cells', *Frontiers in Molecular Neuroscience*, 11. Available at: https://doi.org/10.3389/fnmol.2018.00261.

Hutcheon, B. and Yarom, Y. (2000) 'Resonance, oscillation and the intrinsic frequency preferences of neurons', *Trends in Neurosciences*, 23(5), pp. 216–222. Available at: https://doi.org/10.1016/S0166-2236(00)01547-2.

Hutsler, J.J. and Zhang, H. (2010) 'Increased dendritic spine densities on cortical projection neurons in autism spectrum disorders', *Brain Research*, 1309, pp. 83–94. Available at: https://doi.org/10.1016/j.brainres.2009.09.120.

Irwin, S.A. *et al.* (2000) 'Evidence for Altered Fragile-X Mental Retardation Protein Expression in Response to Behavioral Stimulation', *Neurobiology of Learning and Memory*, 73(1), pp. 87–93. Available at: https://doi.org/10.1006/nlme.1999.3914.

Irwin, S.A. *et al.* (2001) 'Abnormal dendritic spine characteristics in the temporal and visual cortices of patients with fragile-X syndrome: A quantitative examination', *American Journal of Medical Genetics*, 98(2), pp. 161–167. Available at: https://doi.org/10.1002/1096-8628(20010115)98:2<161::AID-AJMG1025>3.0.CO;2-B.

Irwin, S.A. *et al.* (2005) 'Fragile X mental retardation protein levels increase following complex environment exposure in rat brain regions undergoing active synaptogenesis', *Neurobiology of Learning and Memory*, 83(3), pp. 180–187. Available at: https://doi.org/10.1016/j.nlm.2004.11.004.

Iwasawa, C., Narita, M. and Tamura, H. (2019) 'Regional and temporal regulation and role of somatostatin receptor subtypes in the mouse brain following systemic kainate-induced acute seizures', *Neuroscience Research*, 149, pp. 38–49. Available at: https://doi.org/10.1016/j.neures.2019.01.004.

Jaffe, D.B. and Carnevale, N.T. (1999) 'Passive Normalization of Synaptic Integration Influenced by Dendritic Architecture', *Journal of Neurophysiology*, 82(6), pp. 3268–3285. Available at: https://doi.org/10.1152/jn.1999.82.6.3268.

Jonak, C.R. *et al.* (2021) 'The PDE10A Inhibitor TAK-063 Reverses Sound-Evoked EEG Abnormalities in a Mouse Model of Fragile X Syndrome', *Neurotherapeutics*, 18(2), pp. 1175–1187. Available at: https://doi.org/10.1007/s13311-021-01005-w.

Jonak, C.R. *et al.* (2024) 'Phenotypic analysis of multielectrode array EEG biomarkers in developing and adult male Fmr1 KO mice', *Neurobiology of Disease*, 195, p. 106496. Available at: https://doi.org/10.1016/j.nbd.2024.106496.

Juczewski, K. *et al.* (2016) 'Somatosensory map expansion and altered processing of tactile inputs in a mouse model of fragile X syndrome', *Neurobiology of Disease*, 96, pp. 201–215. Available at: https://doi.org/10.1016/j.nbd.2016.09.007.

Jurga, A.M. *et al.* (2021) 'Beyond the GFAP-Astrocyte Protein Markers in the Brain', *Biomolecules*, 11(9), p. 1361. Available at: https://doi.org/10.3390/biom11091361.

Kalmbach, B.E., Johnston, D. and Brager, D.H. (2015) 'Cell-Type Specific Channelopathies in the Prefrontal Cortex of the fmr1-/y Mouse Model of Fragile X Syndrome', *eneuro*, 2(6), p. ENEURO.0114-15.2015. Available at: https://doi.org/10.1523/ENEURO.0114-15.2015.

Kang, M. *et al.* (2025) 'Screening and Identification of Brain Pericyte-Selective Markers', *CNS Neuroscience & Therapeutics*, 31(2). Available at: https://doi.org/10.1111/cns.70247.

Kang, Y. *et al.* (2021) 'A human forebrain organoid model of fragile X syndrome exhibits altered neurogenesis and highlights new treatment strategies', *Nature Neuroscience*, 24(10), pp. 1377–1391. Available at: https://doi.org/10.1038/s41593-021-00913-6.

Karimi, P. *et al.* (2017) 'Environmental factors influencing the risk of autism', *Journal of Research in Medical Sciences*, 22(1), p. 27. Available at: https://doi.org/10.4103/1735-1995.200272.

Kaufmann, W.E. *et al.* (2004) 'Autism spectrum disorder in fragile X syndrome: Communication, social interaction, and specific behaviors', *American Journal of Medical Genetics Part A*, 129A(3), pp. 225–234. Available at: https://doi.org/10.1002/ajmg.a.30229.

Kaufmann, W.E. *et al.* (2017) 'Autism Spectrum Disorder in Fragile X Syndrome: Cooccurring Conditions and Current Treatment', *Pediatrics*, 139(Supplement_3), pp. S194–S206. Available at: https://doi.org/10.1542/peds.2016-1159F.

Kaufmann, W.E. and Reiss, A.L. (1999) 'Molecular and cellular genetics of fragile X syndrome', *American Journal of Medical Genetics*, 88(1), pp. 11–24. Available at: https://doi.org/10.1002/(SICI)1096-8628(19990205)88:1<11::AID-AJMG3>3.0.CO;2-O.

Kavalali, E.T., Hwang, K.S. and Plummer, M.R. (1997) 'cAMP-Dependent Enhancement of Dihydropyridine-Sensitive Calcium Channel Availability in Hippocampal Neurons', *The Journal of Neuroscience*, 17(14), pp. 5334–5348. Available at: https://doi.org/10.1523/JNEUROSCI.17-14-05334.1997.

Kazdoba, T.M. *et al.* (2014) 'Modeling fragile X syndrome in the Fmr1 knockout mouse', *Intractable & Rare Diseases Research*, 3(4), pp. 118–133. Available at: https://doi.org/10.5582/irdr.2014.01024.

Kelley, D. *et al.* (2008) 'The cyclic AMP phenotype of fragile X and autism', *Neuroscience & Biobehavioral Reviews*, 32(8), pp. 1533–1543. Available at: https://doi.org/10.1016/j.neubiorev.2008.06.005.

Kelley, D.J. *et al.* (2007) 'The Cyclic AMP Cascade Is Altered in the Fragile X Nervous System', *PLoS ONE*, 2(9), p. e931. Available at: https://doi.org/10.1371/journal.pone.0000931.

Keysor, C.S. and Mazzocco, M.M.M. (2002) 'A developmental approach to understanding Fragile X syndrome in females', *Microscopy Research and Technique*, 57(3), pp. 179–186. Available at: https://doi.org/10.1002/jemt.10070.

Khachadourian, V. *et al.* (2023) 'Comorbidities in autism spectrum disorder and their etiologies', *Translational Psychiatry*, 13(1), p. 71. Available at: https://doi.org/10.1038/s41398-023-02374-w.

Khayachi, A. *et al.* (2018) 'Sumoylation regulates FMRP-mediated dendritic spine elimination and maturation', *Nature Communications*, 9(1), p. 757. Available at: https://doi.org/10.1038/s41467-018-03222-y.

Killackey, H.P. and Belford, G.R. (1979) 'The formation of afferent patterns in the somatosensory cortex of the neonatal rat', *Journal of Comparative Neurology*, 183(2), pp. 285–303. Available at: https://doi.org/10.1002/cne.901830206.

Kim, U. and Ebner, F.F. (1999) 'Barrels and septa: Separate circuits in rat barrel field cortex', *The Journal of Comparative Neurology*, 408(4), pp. 489–505. Available at: https://doi.org/10.1002/(SICI)1096-9861(19990614)408:4<489::AID-CNE4>3.0.CO;2-E.

Kimm, T., Khaliq, Z.M. and Bean, B.P. (2015) 'Differential Regulation of Action Potential Shape and Burst-Frequency Firing by BK and Kv2 Channels in Substantia Nigra Dopaminergic Neurons', *The Journal of Neuroscience*, 35(50), pp. 16404–16417. Available at: https://doi.org/10.1523/JNEUROSCI.5291-14.2015.

Kivioja, T. *et al.* (2012) 'Counting absolute numbers of molecules using unique molecular identifiers', *Nature Methods*, 9(1), pp. 72–74. Available at: https://doi.org/10.1038/nmeth.1778.

Kogan, C.S. (2003) 'Differential impact of the FMR1 gene on visual processing in fragile X syndrome', *Brain*, 127(3), pp. 591–601. Available at: https://doi.org/10.1093/brain/awh069.

Köhler, I. *et al.* (2025) 'Chemogenetic activation of Gq signaling modulates dendritic development of cortical neurons in a time- and layer-specific manner', *Frontiers in Cellular Neuroscience*, 19. Available at: https://doi.org/10.3389/fncel.2025.1524470.

Kole, M.H.P., Letzkus, J.J. and Stuart, G.J. (2007) 'Axon Initial Segment Kv1 Channels Control Axonal Action Potential Waveform and Synaptic Efficacy', *Neuron*, 55(4), pp. 633–647. Available at: https://doi.org/10.1016/j.neuron.2007.07.031.

Kooy, R.F. *et al.* (1996) 'Transgenic mouse model for the fragile X syndrome', *American Journal of Medical Genetics*, 64(2), pp. 241–245. Available at: https://doi.org/10.1002/(SICI)1096-8628(19960809)64:2<241::AID-AJMG1>3.0.CO;2-X.

Kourdougli, N. *et al.* (2023) 'Improvement of sensory deficits in fragile X mice by increasing cortical interneuron activity after the critical period', *Neuron*, 111(18), pp. 2863-2880.e6. Available at: https://doi.org/10.1016/j.neuron.2023.06.009.

Kozono, N. *et al.* (2020) 'Gamma power abnormalities in a Fmr1-targeted transgenic rat model of fragile X syndrome', *Scientific Reports*, 10(1), p. 18799. Available at: https://doi.org/10.1038/s41598-020-75893-x.

Kramvis, I. *et al.* (2013) 'Hyperactivity, perseveration and increased responding during attentional rule acquisition in the Fragile X mouse model', *Frontiers in Behavioral Neuroscience*, 7. Available at: https://doi.org/10.3389/fnbeh.2013.00172.

Kreienkamp, H.-J., Hönck, H.-H. and Richter, D. (1997) 'Coupling of rat somatostatin receptor subtypes to a G-protein gated inwardly rectifying potassium channel (GIRK1)', *FEBS Letters*, 419(1), pp. 92–94. Available at: https://doi.org/10.1016/S0014-5793(97)01437-3.

Krueger, D.D. *et al.* (2011) 'Cognitive dysfunction and prefrontal synaptic abnormalities in a mouse model of fragile X syndrome', *Proceedings of the National Academy of Sciences*, 108(6), pp. 2587–2592. Available at: https://doi.org/10.1073/pnas.1013855108.

Kuhn, S. *et al.* (2019) 'Oligodendrocytes in Development, Myelin Generation and Beyond', *Cells*, 8(11), p. 1424. Available at: https://doi.org/10.3390/cells8111424.

Kwan, K.Y. *et al.* (2008) 'SOX5 postmitotically regulates migration, postmigratory differentiation, and projections of subplate and deep-layer neocortical neurons', *Proceedings of the National Academy of Sciences*, 105(41), pp. 16021–16026. Available at: https://doi.org/10.1073/pnas.0806791105.

Lake, B.B. *et al.* (2016) 'Neuronal subtypes and diversity revealed by single-nucleus RNA sequencing of the human brain', *Science*, 352(6293), pp. 1586–1590. Available at: https://doi.org/10.1126/science.aaf1204.

Lakhani, A. *et al.* (2025) 'Impairment in the homeostatic recruitment of layer 5/6 neurons following whisker stimulation in Fmr1 KO mice', *Neurobiology of Disease*, 207, p. 106837. Available at: https://doi.org/10.1016/j.nbd.2025.106837.

Lakics, V., Karran, E.H. and Boess, F.G. (2010) 'Quantitative comparison of phosphodiesterase mRNA distribution in human brain and peripheral tissues',

Neuropharmacology, 59(6), pp. 367–374. Available at: https://doi.org/10.1016/j.neuropharm.2010.05.004.

Land, P.W. and Erickson, S.L. (2005) 'Subbarrel domains in rat somatosensory (S1) cortex', *Journal of Comparative Neurology*, 490(4), pp. 414–426. Available at: https://doi.org/10.1002/cne.20677.

Lecea, L. de, del Ri´o, J. and Soriano, E. (1995) 'Developmental expression of parvalbumin mRNA in the cerebral cortex and hippocampus of the rat', *Molecular Brain Research*, 32(1), pp. 1–13. Available at: https://doi.org/10.1016/0169-328X(95)00056-X.

Lee, A.D. *et al.* (2007) '3D pattern of brain abnormalities in Fragile X syndrome visualized using tensor-based morphometry', *NeuroImage*, 34(3), pp. 924–938. Available at: https://doi.org/10.1016/j.neuroimage.2006.09.043.

Lee, A.W. *et al.* (2018) 'Clinical Development of Targeted Fragile X Syndrome Treatments: An Industry Perspective', *Brain Sciences*, 8(12), p. 214. Available at: https://doi.org/10.3390/brainsci8120214.

Lee, B.H., Smith, T. and Paciorkowski, A.R. (2015) 'Autism spectrum disorder and epilepsy: Disorders with a shared biology', *Epilepsy & Behavior*, 47, pp. 191–201. Available at: https://doi.org/10.1016/j.yebeh.2015.03.017.

Lee, B.R. *et al.* (2021) 'Scaled, high fidelity electrophysiological, morphological, and transcriptomic cell characterization', *eLife*, 10. Available at: https://doi.org/10.7554/eLife.65482.

Lee, F.H.F. *et al.* (2019) 'Altered cortical Cytoarchitecture in the Fmr1 knockout mouse', *Molecular Brain*, 12(1), p. 56. Available at: https://doi.org/10.1186/s13041-019-0478-8.

Lee, J.-I. *et al.* (2024) 'Membrane depolarization mediates both the inhibition of neural activity and cell-type-differences in response to high-frequency stimulation', *Communications Biology*, 7(1), p. 734. Available at: https://doi.org/10.1038/s42003-024-06359-3.

Leekam, S.R. *et al.* (2007) 'Describing the Sensory Abnormalities of Children and Adults with Autism', *Journal of Autism and Developmental Disorders*, 37(5), pp. 894–910. Available at: https://doi.org/10.1007/s10803-006-0218-7.

Lendvai, B. *et al.* (2000) 'Experience-dependent plasticity of dendritic spines in the developing rat barrel cortex in vivo', *Nature*, 404(6780), pp. 876–881. Available at: https://doi.org/10.1038/35009107.

Leontiadis, L.J. *et al.* (2023) 'Increased Inhibition May Contribute to Maintaining Normal Network Function in the Ventral Hippocampus of a Fmr1-Targeted Transgenic Rat

Model of Fragile X Syndrome', *Brain Sciences*, 13(11), p. 1598. Available at: https://doi.org/10.3390/brainsci13111598.

Leyva-Díaz, E. *et al.* (2014) 'FLRT3 Is a Robo1-Interacting Protein that Determines Netrin-1 Attraction in Developing Axons', *Current Biology*, 24(5), pp. 494–508. Available at: https://doi.org/10.1016/j.cub.2014.01.042.

Li, B.-Z. *et al.* (2023) 'Current Best Practices for Analysis of Dendritic Spine Morphology and Number in Neurodevelopmental Disorder Research', *ACS Chemical Neuroscience*, 14(9), pp. 1561–1572. Available at: https://doi.org/10.1021/acschemneuro.3c00062.

Li, C., Bassell, G.J. and Sasaki, Y. (2009) 'Fragile X Mental Retardation Protein is involved in protein synthesis-dependent collapse of growth cones induced by Semaphorin-3A', *Frontiers in Neural Circuits*, 3. Available at: https://doi.org/10.3389/neuro.04.011.2009.

Li, Q. *et al.* (2023) 'Prevalence and trends of developmental disabilities among US children and adolescents aged 3 to 17 years, 2018–2021', *Scientific Reports*, 13(1), p. 17254. Available at: https://doi.org/10.1038/s41598-023-44472-1.

Li, Z. (2001) 'The fragile X mental retardation protein inhibits translation via interacting with mRNA', *Nucleic Acids Research*, 29(11), pp. 2276–2283. Available at: https://doi.org/10.1093/nar/29.11.2276.

Life Technologies (2013) *SuperaseIn RNase Inhibitor: Product Information Sheet.* Available at: https://www.thermofisher.com/order/catalog/product/AM2694.

Lipovsek, M. *et al.* (2021) 'Patch-seq: Past, Present, and Future', *The Journal of Neuroscience*, 41(5), pp. 937–946. Available at: https://doi.org/10.1523/JNEUROSCI.1653-20.2020.

Lipovsek, M., Browne, L. and Grubb, M.S. (2020) 'Protocol for Patch-Seq of Small Interneurons', *STAR Protocols*, 1(3), p. 100146. Available at: https://doi.org/10.1016/J.XPRO.2020.100146.

Liu, Y. *et al.* (2025) 'A molecularly defined mPFC-BLA circuit specifically regulates social novelty preference', *Science Advances*, 11(17). Available at: https://doi.org/10.1126/sciadv.adt9008.

Van der Loos, H. and Woolsey, T.A. (1973) 'Somatosensory Cortex: Structural Alterations following Early Injury to Sense Organs', *Science*, 179(4071), pp. 395–398. Available at: https://doi.org/10.1126/science.179.4071.395.

Louros, S.R. *et al.* (2023) 'Excessive proteostasis contributes to pathology in fragile X syndrome', *Neuron*, 111(4), pp. 508-525.e7. Available at: https://doi.org/10.1016/j.neuron.2022.11.012.

Love, M.I., Huber, W. and Anders, S. (2014) 'Moderated estimation of fold change and dispersion for RNA-seq data with DESeq2', *Genome Biology*, 15(12), p. 550. Available at: https://doi.org/10.1186/s13059-014-0550-8.

Lovelace, J.W. *et al.* (2018) 'Translation-relevant EEG phenotypes in a mouse model of Fragile X Syndrome', *Neurobiology of Disease*, 115, pp. 39–48. Available at: https://doi.org/10.1016/j.nbd.2018.03.012.

Lun, A.T.L. and Marioni, J.C. (2017) 'Overcoming confounding plate effects in differential expression analyses of single-cell RNA-seq data', *Biostatistics*, 18(3), pp. 451–464. Available at: https://doi.org/10.1093/biostatistics/kxw055.

Lundström, S. *et al.* (2012) 'Autism Spectrum Disorders and Autistic like Traits', *Archives of General Psychiatry*, 69(1), p. 46. Available at: https://doi.org/10.1001/archgenpsychiatry.2011.144.

Lundström, S. *et al.* (2015) 'Autism spectrum disorders and coexisting disorders in a nationwide Swedish twin study', *Journal of Child Psychology and Psychiatry*, 56(6), pp. 702–710. Available at: https://doi.org/10.1111/jcpp.12329.

Maravall, M., Stern, E.A. and Svoboda, K. (2004) 'Development of Intrinsic Properties and Excitability of Layer 2/3 Pyramidal Neurons During a Critical Period for Sensory Maps in Rat Barrel Cortex', *Journal of Neurophysiology*, 92(1), pp. 144–156. Available at: https://doi.org/10.1152/jn.00598.2003.

Marfull-Oromí, P. *et al.* (2023) 'The Fragile X Messenger Ribonucleoprotein 1 Participates in Axon Guidance Mediated by the Wnt/Planar Cell Polarity Pathway', *Neuroscience*, 508, pp. 76–86. Available at: https://doi.org/10.1016/j.neuroscience.2022.09.018.

Maurin, T. *et al.* (2018) 'HITS-CLIP in various brain areas reveals new targets and new modalities of RNA binding by fragile X mental retardation protein', *Nucleic Acids Research*, 46(12), pp. 6344–6355. Available at: https://doi.org/10.1093/nar/gky267.

Maurin, T. *et al.* (2019) 'Involvement of Phosphodiesterase 2A Activity in the Pathophysiology of Fragile X Syndrome', *Cerebral Cortex*, 29(8), pp. 3241–3252. Available at: https://doi.org/10.1093/cercor/bhy192.

McCarthy, D.J. *et al.* (2017) 'Scater: pre-processing, quality control, normalization and visualization of single-cell RNA-seq data in R', *Bioinformatics*, 33(8), pp. 1179–1186. Available at: https://doi.org/10.1093/bioinformatics/btw777.

McKinney, W.S. *et al.* (2025) 'Results from a Double-Blind, Randomized, Placebo-Controlled, Single-Dose, Crossover Trial of Lovastatin or Minocycline in Fragile X Syndrome', *Journal of Child and Adolescent Psychopharmacology*, 35(4), pp. 211–221. Available at: https://doi.org/10.1089/cap.2024.0103.

Micai, M. *et al.* (2023) 'Prevalence of co-occurring conditions in children and adults with autism spectrum disorder: A systematic review and meta-analysis', *Neuroscience & Biobehavioral Reviews*, 155, p. 105436. Available at: https://doi.org/10.1016/j.neubiorev.2023.105436.

Michalon, A. *et al.* (2012) 'Chronic Pharmacological mGlu5 Inhibition Corrects Fragile X in Adult Mice', *Neuron*, 74(1), pp. 49–56. Available at: https://doi.org/10.1016/j.neuron.2012.03.009.

Mineur, Y.S., Huynh, L.X. and Crusio, W.E. (2006) 'Social behavior deficits in the Fmr1 mutant mouse', *Behavioural Brain Research*, 168(1), pp. 172–175. Available at: https://doi.org/10.1016/j.bbr.2005.11.004.

Modabbernia, A., Velthorst, E. and Reichenberg, A. (2017) 'Environmental risk factors for autism: an evidence-based review of systematic reviews and meta-analyses', *Molecular Autism*, 8(1), p. 13. Available at: https://doi.org/10.1186/s13229-017-0121-4.

Moissidis, M. *et al.* (2025) 'A postnatal molecular switch drives activity-dependent maturation of parvalbumin interneurons', *Cell*, 188(20), pp. 5555-5575.e26. Available at: https://doi.org/10.1016/j.cell.2025.06.029.

Van der Molen, M.J.W. *et al.* (2012) 'Auditory change detection in fragile X syndrome males: A brain potential study', *Clinical Neurophysiology*, 123(7), pp. 1309–1318. Available at: https://doi.org/10.1016/j.clinph.2011.11.039.

van der Molen, M.J.W., Stam, C.J. and van der Molen, M.W. (2014) 'Resting-State EEG Oscillatory Dynamics in Fragile X Syndrome: Abnormal Functional Connectivity and Brain Network Organization', *PLoS ONE*, 9(2), p. e88451. Available at: https://doi.org/10.1371/journal.pone.0088451.

Momin, A. *et al.* (2008) 'Role of the hyperpolarization-activated current Ih in somatosensory neurons', *The Journal of Physiology*, 586(24), pp. 5911–5929. Available at: https://doi.org/10.1113/jphysiol.2008.163154.

Montminy, M.R. *et al.* (1986) 'Identification of a cyclic-AMP-responsive element within the rat somatostatin gene.', *Proceedings of the National Academy of Sciences*, 83(18), pp. 6682–6686. Available at: https://doi.org/10.1073/pnas.83.18.6682.

Morin-Parent, F. *et al.* (2019) 'Hyperexcitability and impaired intracortical inhibition in patients with fragile-X syndrome', *Translational Psychiatry*, 9(1), p. 312. Available at: https://doi.org/10.1038/s41398-019-0650-z.

Morrison, J.H. *et al.* (1983) 'Immunohistochemical distribution of pro-somatostatin-related peptides in cerebral cortex', *Brain Research*, 262(2), pp. 344–351. Available at: https://doi.org/10.1016/0006-8993(83)91031-4.

Moseley, R.L. *et al.* (2015) 'Whole-brain functional hypoconnectivity as an endophenotype of autism in adolescents', *NeuroImage: Clinical*, 9, pp. 140–152. Available at: https://doi.org/10.1016/j.nicl.2015.07.015.

Muhle, R., Trentacoste, S. V. and Rapin, I. (2004) 'The Genetics of Autism', *Pediatrics*, 113(5), pp. e472–e486. Available at: https://doi.org/10.1542/peds.113.5.e472.

Muñoz-Manchado, A.B. *et al.* (2018) 'Diversity of Interneurons in the Dorsal Striatum Revealed by Single-Cell RNA Sequencing and PatchSeq', *Cell Reports*, 24(8), pp. 2179-2190.e7. Available at: https://doi.org/10.1016/j.celrep.2018.07.053.

Muscas, M., Louros, S.R. and Osterweil, E.K. (2019) 'Lovastatin, not Simvastatin, Corrects Core Phenotypes in the Fragile X Mouse Model', *eneuro*, 6(3), p. ENEURO.0097-19.2019. Available at: https://doi.org/10.1523/ENEURO.0097-19.2019.

Nimchinsky, E.A., Sabatini, B.L. and Svoboda, K. (2002) 'Structure and Function of Dendritic Spines', *Annual Review of Physiology*, 64(1), pp. 313–353. Available at: https://doi.org/10.1146/annurev.physiol.64.081501.160008.

Nomura, T. *et al.* (2017) 'Delayed Maturation of Fast-Spiking Interneurons Is Rectified by Activation of the TrkB Receptor in the Mouse Model of Fragile X Syndrome', *The Journal of Neuroscience*, 37(47), pp. 11298–11310. Available at: https://doi.org/10.1523/JNEUROSCI.2893-16.2017.

Norris, J.E. *et al.* (2024) 'Auditory N1 event-related potential amplitude is predictive of serum concentration of BPN14770 in fragile X syndrome', *Molecular Autism*, 15(1), p. 47. Available at: https://doi.org/10.1186/s13229-024-00626-0.

Ntoulas, G. *et al.* (2024) 'Multi-level profiling of the Fmr1 KO rat unveils altered behavioral traits along with aberrant glutamatergic function', *Translational Psychiatry*, 14(1), p. 104. Available at: https://doi.org/10.1038/s41398-024-02815-0.

Oakes, A. *et al.* (2016) 'Characterising repetitive behaviours in young boys with fragile X syndrome', *Journal of Intellectual Disability Research*, 60(1), pp. 54–67. Available at: https://doi.org/10.1111/jir.12234.

O'Donnell, W.T. and Warren, S.T. (2002) 'A Decade of Molecular Studies of Fragile X Syndrome', *Annual Review of Neuroscience*, 25(1), pp. 315–338. Available at: https://doi.org/10.1146/annurev.neuro.25.112701.142909.

Oh, W.C., Hill, T.C. and Zito, K. (2013) 'Synapse-specific and size-dependent mechanisms of spine structural plasticity accompanying synaptic weakening', *Proceedings of the National Academy of Sciences*, 110(4). Available at: https://doi.org/10.1073/pnas.1214705110.

Oishi, K., Aramaki, M. and Nakajima, K. (2016) 'Mutually repressive interaction between Brn1/2 and Rorb contributes to the establishment of neocortical layer 2/3 and layer

4', *Proceedings of the National Academy of Sciences*, 113(12), pp. 3371–3376. Available at: https://doi.org/10.1073/pnas.1515949113.

O'Keeffe, M. *et al.* (2025) 'Typical development of synaptic and neuronal properties can proceed without microglia in the cortex and thalamus', *Nature Neuroscience*, 28(2), pp. 268–279. Available at: https://doi.org/10.1038/s41593-024-01833-x.

O'Leary, D.D. and Sahara, S. (2008) 'Genetic regulation of arealization of the neocortex', *Current Opinion in Neurobiology*, 18(1), pp. 90–100. Available at: https://doi.org/10.1016/j.conb.2008.05.011.

Olmos-Serrano, J.L. *et al.* (2010) 'Defective GABAergic Neurotransmission and Pharmacological Rescue of Neuronal Hyperexcitability in the Amygdala in a Mouse Model of Fragile X Syndrome', *Journal of Neuroscience*, 30(29), pp. 9929–9938. Available at: https://doi.org/10.1523/JNEUROSCI.1714-10.2010.

Orefice, L.L. *et al.* (2016) 'Peripheral Mechanosensory Neuron Dysfunction Underlies Tactile and Behavioral Deficits in Mouse Models of ASDs', *Cell*, 166(2), pp. 299–313. Available at: https://doi.org/10.1016/j.cell.2016.05.033.

Osterweil, E.K. *et al.* (2010) 'Hypersensitivity to mGluR5 and ERK1/2 Leads to Excessive Protein Synthesis in the Hippocampus of a Mouse Model of Fragile X Syndrome', *The Journal of Neuroscience*, 30(46), pp. 15616–15627. Available at: https://doi.org/10.1523/JNEUROSCI.3888-10.2010.

Pacey, L.K.K. *et al.* (2013) 'Delayed myelination in a mouse model of fragile X syndrome', *Human Molecular Genetics*, 22(19), pp. 3920–3930. Available at: https://doi.org/10.1093/hmg/ddt246.

Pan, F. *et al.* (2010) 'Dendritic spine instability and insensitivity to modulation by sensory experience in a mouse model of fragile X syndrome', *Proceedings of the National Academy of Sciences*, 107(41), pp. 17768–17773. Available at: https://doi.org/10.1073/pnas.1012496107.

Paradis, S. *et al.* (2007) 'An RNAi-Based Approach Identifies Molecules Required for Glutamatergic and GABAergic Synapse Development', *Neuron*, 53(2), pp. 217–232. Available at: https://doi.org/10.1016/j.neuron.2006.12.012.

Pastoll, H. *et al.* (2020) 'Inter- and intra-animal variation in the integrative properties of stellate cells in the medial entorhinal cortex', *eLife*, 9. Available at: https://doi.org/10.7554/eLife.52258.

Patel, Y.C. *et al.* (1994) 'All Five Cloned Human Somatostatin Receptors (hSSTR1-5) Are Functionally Coupled to Adenylyl Cyclase', *Biochemical and Biophysical Research Communications*, 198(2), pp. 605–612. Available at: https://doi.org/10.1006/bbrc.1994.1088.

Pederick, D.T. *et al.* (2021) 'Reciprocal repulsions instruct the precise assembly of parallel hippocampal networks', *Science*, 372(6546), pp. 1068–1073. Available at: https://doi.org/10.1126/science.abg1774.

Pérez-Torres, S. *et al.* (2000) 'Phosphodiesterase type 4 isozymes expression in human brain examined by in situ hybridization histochemistry and [3H]rolipram binding autoradiography', *Journal of Chemical Neuroanatomy*, 20(3–4), pp. 349–374. Available at: https://doi.org/10.1016/S0891-0618(00)00097-1.

Petersen, C.C.H. (2007) 'The Functional Organization of the Barrel Cortex', *Neuron*, 56(2), pp. 339–355. Available at: https://doi.org/10.1016/j.neuron.2007.09.017.

Pieretti, M. *et al.* (1991) 'Absence of expression of the FMR-1 gene in fragile X syndrome', *Cell*, 66(4), pp. 817–822. Available at: https://doi.org/10.1016/0092-8674(91)90125-I.

Pierret, T., Lavallée, P. and Deschênes, M. (2000) 'Parallel Streams for the Relay of Vibrissal Information through Thalamic Barreloids', *The Journal of Neuroscience*, 20(19), pp. 7455–7462. Available at: https://doi.org/10.1523/JNEUROSCI.20-19-07455.2000.

Pilpel, Y. *et al.* (2009) 'Synaptic ionotropic glutamate receptors and plasticity are developmentally altered in the CA1 field of Fmr1 knockout mice', *The Journal of Physiology*, 587(4), pp. 787–804. Available at: https://doi.org/10.1113/jphysiol.2008.160929.

Pohlkamp, T. *et al.* (2014) 'Characterization and Distribution of Reelin-Positive Interneuron Subtypes in the Rat Barrel Cortex', *Cerebral Cortex*, 24(11), pp. 3046–3058. Available at: https://doi.org/10.1093/cercor/bht161.

Pretto, D. *et al.* (2014) 'Clinical and molecular implications of mosaicism in FMR1 full mutations', *Frontiers in Genetics*, 5. Available at: https://doi.org/10.3389/fgene.2014.00318.

Prieto, M. *et al.* (2021) 'Missense mutation of Fmr1 results in impaired AMPAR-mediated plasticity and socio-cognitive deficits in mice', *Nature Communications*, 12(1), p. 1557. Available at: https://doi.org/10.1038/s41467-021-21820-1.

Priya, R. *et al.* (2018) 'Activity Regulates Cell Death within Cortical Interneurons through a Calcineurin-Dependent Mechanism', *Cell Reports*, 22(7), pp. 1695–1709. Available at: https://doi.org/10.1016/j.celrep.2018.01.007.

Purohit, A.A. *et al.* (2012) 'Down Syndrome Cell Adhesion Molecule (DSCAM) Associates with Uncoordinated-5C (UNC5C) in Netrin-1-mediated Growth Cone Collapse', *Journal of Biological Chemistry*, 287(32), pp. 27126–27138. Available at: https://doi.org/10.1074/jbc.M112.340174.

Qian, X. *et al.* (2024) 'Spatial Single-cell Analysis Decodes Cortical Layer and Area Specification', *bioRxiv* [Preprint]. Available at: https://doi.org/10.1101/2024.06.05.597673.

Quartier, A. *et al.* (2017) 'Intragenic FMR1 disease-causing variants: a significant mutational mechanism leading to Fragile-X syndrome', *European Journal of Human Genetics*, 25(4), pp. 423–431. Available at: https://doi.org/10.1038/ejhg.2016.204.

Rais, M. *et al.* (2018) 'Sensory Processing Phenotypes in Fragile X Syndrome', *ASN Neuro*, 10(1). Available at: https://doi.org/10.1177/1759091418801092.

Rema, V. *et al.* (2006) 'Short exposure to an enriched environment accelerates plasticity in the barrel cortex of adult rats', *Neuroscience*, 140(2), pp. 659–672. Available at: https://doi.org/10.1016/j.neuroscience.2006.02.043.

Reyniers, E. *et al.* (1999) 'Postmortem examination of two fragile X brothers with anFMR1 full mutation', *American Journal of Medical Genetics*, 84(3), pp. 245–249. Available at: https://doi.org/10.1002/(SICI)1096-8628(19990528)84:3<245::AID-AJMG16>3.0.CO;2-U.

Rice, F.L. (1985) 'Gradual changes in the structure of the barrels during maturation of the primary somatosensory cortex in the rat', *Journal of Comparative Neurology*, 236(4), pp. 496–503. Available at: https://doi.org/10.1002/cne.902360406.

Richter, J.D. and Zhao, X. (2021) 'The molecular biology of FMRP: new insights into fragile X syndrome', *Nature Reviews Neuroscience*, 22(4), pp. 209–222. Available at: https://doi.org/10.1038/s41583-021-00432-0.

Rogers, S.J., Hepburn, S. and Wehner, E. (2003) 'Parent Reports of Sensory Symptoms in Toddlers with Autism and Those with Other Developmental Disorders', *Journal of Autism and Developmental Disorders*, 33(6), pp. 631–642. Available at: https://doi.org/10.1023/B:JADD.0000006000.38991.a7.

Rosenberg, A.B. *et al.* (2018) 'Single-cell profiling of the developing mouse brain and spinal cord with split-pool barcoding', *Science*, 360(6385), pp. 176–182. Available at: https://doi.org/10.1126/science.aam8999.

Rosenheck, M. *et al.* (2021) 'Effects of chronic inhibition of phosphodiesterase-4D on behavior and regional rates of cerebral protein synthesis in a mouse model of fragile X syndrome', *Neurobiology of Disease*, 159, p. 105485. Available at: https://doi.org/10.1016/j.nbd.2021.105485.

Rosenstein, J.M. *et al.* (2003) 'Neurotrophic Effects of Vascular Endothelial Growth Factor on Organotypic Cortical Explants and Primary Cortical Neurons', *The Journal of Neuroscience*, 23(35), pp. 11036–11044. Available at: https://doi.org/10.1523/JNEUROSCI.23-35-11036.2003.

Routh, B.N. *et al.* (2017) 'Increased transient Na+ conductance and action potential output in layer 2/3 prefrontal cortex neurons of the fmr1−/y mouse', *The Journal of Physiology*, 595(13), pp. 4431–4448. Available at: https://doi.org/10.1113/JP274258.

Routh, B.N., Johnston, D. and Brager, D.H. (2013) 'Loss of Functional A-Type Potassium Channels in the Dendrites of CA1 Pyramidal Neurons from a Mouse Model of Fragile X Syndrome', *The Journal of Neuroscience*, 33(50), pp. 19442–19450. Available at: https://doi.org/10.1523/JNEUROSCI.3256-13.2013.

Rubenstein, J.L.R. and Merzenich, M.M. (2003) 'Model of autism: increased ratio of excitation/inhibition in key neural systems', *Genes, Brain and Behavior*, 2(5), pp. 255–267. Available at: https://doi.org/10.1034/j.1601-183X.2003.00037.x.

Rudelli, R.D. *et al.* (1985) 'Adult fragile X syndrome', *Acta Neuropathologica*, 67(3–4), pp. 289–295. Available at: https://doi.org/10.1007/BF00687814.

Rudy, B. *et al.* (2011) 'Three groups of interneurons account for nearly 100% of neocortical GABAergic neurons', *Developmental Neurobiology*, 71(1), pp. 45–61. Available at: https://doi.org/10.1002/dneu.20853.

Sabaratnam, M. (2000) 'Pathological and neuropathological findings in two males with fragile-X syndrome', *Journal of Intellectual Disability Research*, 44(1), pp. 81–85. Available at: https://doi.org/10.1046/j.1365-2788.2000.00261.x.

Sánchez-Muñoz, I. *et al.* (2010) 'Activity-dependent somatostatin gene expression is regulated by cAMP-dependent protein kinase and Ca2+ -calmodulin kinase pathways', *Journal of Neuroscience Research*, 88(4), pp. 825–836. Available at: https://doi.org/10.1002/jnr.22264.

Sandin, S. *et al.* (2014) 'The Familial Risk of Autism', *JAMA*, 311(17), p. 1770. Available at: https://doi.org/10.1001/jama.2014.4144.

Sassone-Corsi, P. (2012) 'The Cyclic AMP Pathway', *Cold Spring Harbor Perspectives in Biology*, 4(12), pp. a011148–a011148. Available at: https://doi.org/10.1101/cshperspect.a011148.

Scala, F. *et al.* (2019) 'Layer 4 of mouse neocortex differs in cell types and circuit organization between sensory areas', *Nature Communications*, 10(1), p. 4174. Available at: https://doi.org/10.1038/s41467-019-12058-z.

Scala, F. *et al.* (2021) 'Phenotypic variation of transcriptomic cell types in mouse motor cortex', *Nature*, 598(7879), pp. 144–150. Available at: https://doi.org/10.1038/s41586-020-2907-3.

Scarnati, M.S. *et al.* (2020) 'Presynaptic Calcium Channel Open Probability and Changes in Calcium Influx Throughout the Action Potential Determined Using AP-Waveforms', *Frontiers in Synaptic Neuroscience*, 12. Available at: https://doi.org/10.3389/fnsyn.2020.00017.

Schaefer, G.B. and Mendelsohn, N.J. (2008) 'Genetics evaluation for the etiologic diagnosis of autism spectrum disorders', *Genetics in Medicine*, 10(1), pp. 4–12. Available at: https://doi.org/10.1097/GIM.0b013e31815efdd7.

Schaeffer, C. (2001) 'The fragile X mental retardation protein binds specifically to its mRNA via a purine quartet motif', *The EMBO Journal*, 20(17), pp. 4803–4813. Available at: https://doi.org/10.1093/emboj/20.17.4803.

Schieve, L.A. *et al.* (2015) 'Comparison of Perinatal Risk Factors Associated with Autism Spectrum Disorder (ASD), Intellectual Disability (ID), and Co-occurring ASD and ID', *Journal of Autism and Developmental Disorders*, 45(8), pp. 2361–2372. Available at: https://doi.org/10.1007/s10803-015-2402-0.

Schindelin, J. *et al.* (2012) 'Fiji: an open-source platform for biological-image analysis', *Nature Methods*, 9(7), pp. 676–682. Available at: https://doi.org/10.1038/nmeth.2019.

Schlaggar, B.L., Fox, K. and O'Leary, D.M. (1993) 'Postsynaptic control of plasticity in developing somatosensory cortex', *Nature*, 364(6438), pp. 623–626. Available at: https://doi.org/10.1038/364623a0.

Schulz, S. *et al.* (2000) 'Localization of five somatostatin receptors in the rat central nervous system using subtype-specific antibodies', *Journal of Physiology-Paris*, 94(3–4), pp. 259–264. Available at: https://doi.org/10.1016/S0928-4257(00)00212-6.

Schweitzer, P., Madamba, S.G. and Siggins, G.R. (1998) 'Somatostatin Increases a Voltage-Insensitive K + Conductance in Rat CA1 Hippocampal Neurons', *Journal of Neurophysiology*, 79(3), pp. 1230–1238. Available at: https://doi.org/10.1152/jn.1998.79.3.1230.

Selby, L., Zhang, C. and Sun, Q.-Q. (2007) 'Major defects in neocortical GABAergic inhibitory circuits in mice lacking the fragile X mental retardation protein', *Neuroscience Letters*, 412(3), pp. 227–232. Available at: https://doi.org/10.1016/j.neulet.2006.11.062.

Seo, S.S. *et al.* (2022) 'Excess ribosomal protein production unbalances translation in a model of Fragile X Syndrome', *Nature Communications*, 13(1), p. 3236. Available at: https://doi.org/10.1038/s41467-022-30979-0.

Shao, L. *et al.* (1999) 'The role of BK-type Ca 2+ -dependent K + channels in spike broadening during repetitive firing in rat hippocampal pyramidal cells', *The Journal of Physiology*, 521(1), pp. 135–146. Available at: https://doi.org/10.1111/j.1469-7793.1999.00135.x.

Sharma, S. Das *et al.* (2023) 'Astrocytes mediate cell non-autonomous correction of aberrant firing in human FXS neurons', *Cell Reports*, 42(4), p. 112344. Available at: https://doi.org/10.1016/j.celrep.2023.112344.

Shi, D. *et al.* (2019) 'White Matter Alterations in Fmr1 Knockout Mice during Early Postnatal Brain Development', *Developmental Neuroscience*, 41(5–6), pp. 274–289. Available at: https://doi.org/10.1159/000506679.

Shi, Y. *et al.* (2021) 'Mouse and human share conserved transcriptional programs for interneuron development', *Science*, 374(6573). Available at: https://doi.org/10.1126/science.abj6641.

Sholl, D.A. (1953) 'Dendritic organization in the neurons of the visual and motor cortices of the cat.', *Journal of anatomy*, 87(4), pp. 387–406.

Sidorov, M.S., Auerbach, B.D. and Bear, M.F. (2013) 'Fragile X mental retardation protein and synaptic plasticity', *Molecular Brain*, 6(1), p. 15. Available at: https://doi.org/10.1186/1756-6606-6-15.

Siletti, K. *et al.* (2023) 'Transcriptomic diversity of cell types across the adult human brain', *Science*, 382(6667). Available at: https://doi.org/10.1126/science.add7046.

Simões de Oliveira, L. *et al.* (2024) 'Enhanced hippocampal LTP but normal NMDA receptor and AMPA receptor function in a rat model of CDKL5 deficiency disorder', *Molecular Autism*, 15(1), p. 28. Available at: https://doi.org/10.1186/s13229-024-00601-9.

Simon, A. *et al.* (2005) 'Gap-Junctional Coupling between Neurogliaform Cells and Various Interneuron Types in the Neocortex', *The Journal of Neuroscience*, 25(27), pp. 6278–6285. Available at: https://doi.org/10.1523/JNEUROSCI.1431-05.2005.

Southwell, D.G. *et al.* (2012) 'Intrinsically determined cell death of developing cortical interneurons', *Nature*, 491(7422), pp. 109–113. Available at: https://doi.org/10.1038/nature11523.

Spencer, C.M. *et al.* (2005) 'Altered anxiety-related and social behaviors in the *Fmr1* knockout mouse model of fragile X syndrome', *Genes, Brain and Behavior*, 4(7), pp. 420–430. Available at: https://doi.org/10.1111/j.1601-183X.2005.00123.x.

Squair, J.W. *et al.* (2021) 'Confronting false discoveries in single-cell differential expression', *Nature Communications*, 12(1), p. 5692. Available at: https://doi.org/10.1038/s41467-021-25960-2.

Srivastava, A.K. and Schwartz, C.E. (2014) 'Intellectual disability and autism spectrum disorders: Causal genes and molecular mechanisms', *Neuroscience & Biobehavioral Reviews*, 46, pp. 161–174. Available at: https://doi.org/10.1016/j.neubiorev.2014.02.015.

Staiger, J.F. (2004) 'Functional Diversity of Layer IV Spiny Neurons in Rat Somatosensory Cortex: Quantitative Morphology of Electrophysiologically Characterized and Biocytin Labeled Cells', *Cerebral Cortex*, 14(6), pp. 690–701. Available at: https://doi.org/10.1093/cercor/bhh029.

Stefani, G. *et al.* (2004) 'Fragile X Mental Retardation Protein Is Associated with Translating Polyribosomes in Neuronal Cells', *The Journal of Neuroscience*, 24(33), pp. 7272–7276. Available at: https://doi.org/10.1523/JNEUROSCI.2306-04.2004.

Stern, E.A., Maravall, M. and Svoboda, K. (2001) 'Rapid Development and Plasticity of Layer 2/3 Maps in Rat Barrel Cortex In Vivo', *Neuron*, 31(2), pp. 305–315. Available at: https://doi.org/10.1016/S0896-6273(01)00360-9.

Stessman, H.A.F. *et al.* (2017) 'Targeted sequencing identifies 91 neurodevelopmental-disorder risk genes with autism and developmental-disability biases', *Nature Genetics*, 49(4), pp. 515–526. Available at: https://doi.org/10.1038/ng.3792.

Stoppel, D.C. *et al.* (2021) 'mGluR5 Negative Modulators for Fragile X: Treatment Resistance and Persistence', *Frontiers in Psychiatry*, 12. Available at: https://doi.org/10.3389/fpsyt.2021.718953.

Straub, D. *et al.* (2023) 'A sensitive and reproducible qRT-PCR assay detects physiological relevant trace levels of FMR1 mRNA in individuals with Fragile X syndrome', *Scientific Reports*, 13(1), p. 3808. Available at: https://doi.org/10.1038/s41598-023-29786-4.

Sun, J. *et al.* (2024) 'Correcting PCR amplification errors in unique molecular identifiers to generate accurate numbers of sequencing molecules', *Nature Methods*, 21(3), pp. 401–405. Available at: https://doi.org/10.1038/s41592-024-02168-y.

Sutcliffe, J.S. *et al.* (1992) 'DNA methylation represses *FMR-1* transcription in fragile X syndrome', *Human Molecular Genetics*, 1(6), pp. 397–400. Available at: https://doi.org/10.1093/hmg/1.6.397.

Swanson, M.R. *et al.* (2018) 'Development of White Matter Circuitry in Infants With Fragile X Syndrome', *JAMA Psychiatry*, 75(5), p. 505. Available at: https://doi.org/10.1001/jamapsychiatry.2018.0180.

Sztainberg, Y. and Zoghbi, H.Y. (2016) 'Lessons learned from studying syndromic autism spectrum disorders', *Nature Neuroscience*, 19(11), pp. 1408–1417. Available at: https://doi.org/10.1038/nn.4420.

Tamamaki, N. *et al.* (2003) 'Green fluorescent protein expression and colocalization with calretinin, parvalbumin, and somatostatin in the GAD67-GFP knock-in mouse', *Journal of Comparative Neurology*, 467(1), pp. 60–79. Available at: https://doi.org/10.1002/cne.10905.

Tapia-Arancibia, L. and Astier, H. (1989) 'Actions of Excitatory Amino Acids on Somatostatin Release from Cortical Neurons in Primary Cultures', *Journal of Neurochemistry*, 53(4), pp. 1134–1141. Available at: https://doi.org/10.1111/j.1471-4159.1989.tb07406.x.

Thomson, S.R. *et al.* (2017) 'Cell-Type-Specific Translation Profiling Reveals a Novel Strategy for Treating Fragile X Syndrome', *Neuron*, 95(3), pp. 550-563.e5. Available at: https://doi.org/10.1016/j.neuron.2017.07.013.

Thurman, A.J. *et al.* (2020) 'Controlled trial of lovastatin combined with an open-label treatment of a parent-implemented language intervention in youth with fragile X syndrome', *Journal of Neurodevelopmental Disorders*, 12(1), p. 12. Available at: https://doi.org/10.1186/s11689-020-09315-4.

Thurman, A.L. *et al.* (2021) 'Differential gene expression analysis for multi-subject single-cell RNA-sequencing studies with *aggregateBioVar*', *Bioinformatics*, 37(19), pp. 3243–3251. Available at: https://doi.org/10.1093/bioinformatics/btab337.

Tian, Y. *et al.* (2017) 'Loss of FMRP Impaired Hippocampal Long-Term Plasticity and Spatial Learning in Rats', *Frontiers in Molecular Neuroscience*, 10. Available at: https://doi.org/10.3389/fnmol.2017.00269.

Till, S.M. (2010) 'The developmental roles of FMRP', *Biochemical Society Transactions*, 38(2), pp. 507–510. Available at: https://doi.org/10.1042/BST0380507.

Till, S.M. *et al.* (2012) 'Altered maturation of the primary somatosensory cortex in a mouse model of fragile X syndrome', *Human Molecular Genetics*, 21(10), pp. 2143–2156. Available at: https://doi.org/10.1093/hmg/dds030.

Till, S.M. *et al.* (2015) 'Conserved hippocampal cellular pathophysiology but distinct behavioural deficits in a new rat model of FXS', *Human Molecular Genetics*, 24(21), pp. 5977–5984. Available at: https://doi.org/10.1093/hmg/ddv299.

Todd, P.K., Malter, J.S. and Mack, K.J. (2003) 'Whisker stimulation-dependent translation of FMRP in the barrel cortex requires activation of type I metabotropic glutamate receptors', *Molecular Brain Research*, 110(2), pp. 267–278. Available at: https://doi.org/10.1016/S0169-328X(02)00657-5.

Tuchman, R. and Cuccaro, M. (2011) 'Epilepsy and Autism: Neurodevelopmental Perspective', *Current Neurology and Neuroscience Reports*, 11(4), pp. 428–434. Available at: https://doi.org/10.1007/s11910-011-0195-x.

Turner, G. *et al.* (1996) 'Prevalence of fragile X syndrome', *American Journal of Medical Genetics*, 64(1), pp. 196–197. Available at: https://doi.org/10.1002/(SICI)1096-8628(19960712)64:1<196::AID-AJMG35>3.0.CO;2-G.

Uematsu, M. *et al.* (2008) 'Quantitative Chemical Composition of Cortical GABAergic Neurons Revealed in Transgenic Venus-Expressing Rats', *Cerebral Cortex*, 18(2), pp. 315–330. Available at: https://doi.org/10.1093/cercor/bhm056.

Ulrich, D. (2002) 'Dendritic Resonance in Rat Neocortical Pyramidal Cells', *Journal of Neurophysiology*, 87(6), pp. 2753–2759. Available at: https://doi.org/10.1152/jn.2002.87.6.2753.

Ultanir, S.K. *et al.* (2007) 'Regulation of spine morphology and spine density by NMDA receptor signaling in vivo', *Proceedings of the National Academy of Sciences*, 104(49), pp. 19553–19558. Available at: https://doi.org/10.1073/pnas.0704031104.

Utami, K.H. *et al.* (2020) 'Integrative Analysis Identifies Key Molecular Signatures Underlying Neurodevelopmental Deficits in Fragile X Syndrome', *Biological Psychiatry*, 88(6), pp. 500–511. Available at: https://doi.org/10.1016/j.biopsych.2020.05.005.

Valiullina, F. *et al.* (2016) 'Developmental Changes in Electrophysiological Properties and a Transition from Electrical to Chemical Coupling between Excitatory Layer 4 Neurons in the Rat Barrel Cortex', *Frontiers in Neural Circuits*, 10. Available at: https://doi.org/10.3389/fncir.2016.00001.

Valverde, P. (1967) 'Apical dendritic spines of the visual cortex and light deprivation in the mouse', *Experimental Brain Research*, 3(4). Available at: https://doi.org/10.1007/BF00237559.

Verkerk, A.J.M.H. *et al.* (1991) 'Identification of a gene (FMR-1) containing a CGG repeat coincident with a breakpoint cluster region exhibiting length variation in fragile X syndrome', *Cell*, 65(5), pp. 905–914. Available at: https://doi.org/10.1016/0092-8674(91)90397-H.

Villalobos, C. *et al.* (2004) 'SK Ca Channels Mediate the Medium But Not the Slow Calcium-Activated Afterhyperpolarization in Cortical Neurons', *The Journal of Neuroscience*, 24(14), pp. 3537–3542. Available at: https://doi.org/10.1523/JNEUROSCI.0380-04.2004.

Wainger, B.J. *et al.* (2001) 'Molecular mechanism of cAMP modulation of HCN pacemaker channels', *Nature*, 411(6839), pp. 805–810. Available at: https://doi.org/10.1038/35081088.

Wakabayashi, Y. *et al.* (2020) 'Discovery, Radiolabeling, and Evaluation of Subtype-Selective Inhibitors for Positron Emission Tomography Imaging of Brain Phosphodiesterase-4D', *ACS Chemical Neuroscience*, 11(9), pp. 1311–1323. Available at: https://doi.org/10.1021/acschemneuro.0c00077.

Wang, H. and Zhuo, M. (2012) 'Group I Metabotropic Glutamate Receptor-Mediated Gene Transcription and Implications for Synaptic Plasticity and Diseases', *Frontiers in Pharmacology*, 3. Available at: https://doi.org/10.3389/fphar.2012.00189.

Wang, K. *et al.* (2009) 'Common genetic variants on 5p14.1 associate with autism spectrum disorders', *Nature*, 459(7246), pp. 528–533. Available at: https://doi.org/10.1038/nature07999.

Wang, T. *et al.* (2016) 'De novo genic mutations among a Chinese autism spectrum disorder cohort', *Nature Communications*, 7(1), p. 13316. Available at: https://doi.org/10.1038/ncomms13316.

Wang, X. *et al.* (2011) 'Synaptic dysfunction and abnormal behaviors in mice lacking major isoforms of Shank3', *Human Molecular Genetics*, 20(15), pp. 3093–3108. Available at: https://doi.org/10.1093/hmg/ddr212.

Wang, X. *et al.* (2018) 'Postsynaptic FMRP Regulates Synaptogenesis *In Vivo* in the Developing Cochlear Nucleus', *The Journal of Neuroscience*, 38(29), pp. 6445–6460. Available at: https://doi.org/10.1523/JNEUROSCI.0665-18.2018.

Wang, Y. *et al.* (2004) 'Anatomical, physiological and molecular properties of Martinotti cells in the somatosensory cortex of the juvenile rat', *The Journal of Physiology*, 561(1), pp. 65–90. Available at: https://doi.org/10.1113/jphysiol.2004.073353.

Warren, T.G. and Shields, D. (1984) 'Expression of preprosomatostatin in heterologous cells: Biosynthesis, posttranslational processing, and secretion of mature somatostatin', *Cell*, 39(3), pp. 547–555. Available at: https://doi.org/10.1016/0092-8674(84)90461-6.

Weiler, I.J. and Greenough, W.T. (1999) 'Synaptic synthesis of the fragile X protein: Possible involvement in synapse maturation and elimination', *American Journal of Medical Genetics*, 83(4), pp. 248–252. Available at: https://doi.org/10.1002/(SICI)1096-8628(19990402)83:4<248::AID-AJMG3>3.0.CO;2-1.

Weiss, L.A. *et al.* (2009) 'A genome-wide linkage and association scan reveals novel loci for autism', *Nature*, 461(7265), pp. 802–808. Available at: https://doi.org/10.1038/nature08490.

Welker, C. and Woolsey, T.A. (1974) 'Structure of layer IV in the somatosensory neocortex of the rat: Description and comparison with the mouse', *Journal of Comparative Neurology*, 158(4), pp. 437–453. Available at: https://doi.org/10.1002/cne.901580405.

Wen, T.H. *et al.* (2019) 'Developmental Changes in EEG Phenotypes in a Mouse Model of Fragile X Syndrome', *Neuroscience*, 398, pp. 126–143. Available at: https://doi.org/10.1016/j.neuroscience.2018.11.047.

West, J.W. *et al.* (1991) 'A Phosphorylation Site in the Na + Channel Required for Modulation by Protein Kinase C', *Science*, 254(5033), pp. 866–868. Available at: https://doi.org/10.1126/science.1658937.

Wickham, H. *et al.* (2016) 'ggplot2: Create Elegant Data Visualisations Using the Grammar of Graphics', *CRAN: Contributed Packages* [Preprint]. Available at: https://doi.org/10.32614/CRAN.package.ggplot2.

Wilfert, A.B. *et al.* (2017) 'Recurrent de novo mutations in neurodevelopmental disorders: properties and clinical implications', *Genome Medicine*, 9(1), p. 101. Available at: https://doi.org/10.1186/s13073-017-0498-x.

Wilhelmsson, U. *et al.* (2006) 'Redefining the concept of reactive astrocytes as cells that remain within their unique domains upon reaction to injury', *Proceedings of the National Academy of Sciences*, 103(46), pp. 17513–17518. Available at: https://doi.org/10.1073/pnas.0602841103.

Willemsen, R. *et al.* (2002) 'Timing of the absence of FMR1 expression in full mutation chorionic villi', *Human Genetics*, 110(6), pp. 601–605. Available at: https://doi.org/10.1007/s00439-002-0723-5.

Willemsen, R., Levenga, J. and Oostra, B. (2011) 'CGG repeat in the FMR1 gene: size matters', *Clinical Genetics*, 80(3), pp. 214–225. Available at: https://doi.org/10.1111/j.1399-0004.2011.01723.x.

Wisniewski, K.E. *et al.* (1991) 'The fra(X) syndrome: Neurological, electrophysiological, and neuropathological abnormalities', *American Journal of Medical Genetics*, 38(2–3), pp. 476–480. Available at: https://doi.org/10.1002/ajmg.1320380267.

Wong, H. *et al.* (2020) 'Sexually dimorphic patterns in electroencephalography power spectrum and autism-related behaviors in a rat model of fragile X syndrome', *Neurobiology of Disease*, 146, p. 105118. Available at: https://doi.org/10.1016/j.nbd.2020.105118.

Wong, H. *et al.* (2023) 'CNS-dominant human FMRP isoform rescues seizures, fear, and sleep abnormalities in Fmr1-KO mice', *JCI Insight*, 8(11). Available at: https://doi.org/10.1172/jci.insight.169650.

Wright-Talamante, C. *et al.* (1996) 'A controlled study of longitudinal IQ changes in females and males with fragile X syndrome', *American Journal of Medical Genetics*, 64(2), pp. 350–355. Available at: https://doi.org/10.1002/(SICI)1096-8628(19960809)64:2<350::AID-AJMG23>3.0.CO;2-D.

Xu, H. *et al.* (2013) 'Neocortical Somatostatin-Expressing GABAergic Interneurons Disinhibit the Thalamorecipient Layer 4', *Neuron*, 77(1), pp. 155–167. Available at: https://doi.org/10.1016/j.neuron.2012.11.004.

Xu, J. *et al.* (2018) 'Both Hypo-Connectivity and Hyper-Connectivity of the Insular Subregions Associated With Severity in Children With Autism Spectrum Disorders', *Frontiers in Neuroscience*, 12. Available at: https://doi.org/10.3389/fnins.2018.00234.

Xu, X., Roby, K.D. and Callaway, E.M. (2010) 'Immunochemical characterization of inhibitory mouse cortical neurons: Three chemically distinct classes of inhibitory cells', *Journal of Comparative Neurology*, 518(3), pp. 389–404. Available at: https://doi.org/10.1002/cne.22229.

Yan, Q.J. *et al.* (2005) 'Suppression of two major Fragile X Syndrome mouse model phenotypes by the mGluR5 antagonist MPEP', *Neuropharmacology*, 49(7), pp. 1053–1066. Available at: https://doi.org/10.1016/j.neuropharm.2005.06.004.

Yang, Y.-M. and Wang, L.-Y. (2006) 'Amplitude and Kinetics of Action Potential-Evoked Ca2+ Current and Its Efficacy in Triggering Transmitter Release at the Developing Calyx of Held Synapse', *The Journal of Neuroscience*, 26(21), pp. 5698–5708. Available at: https://doi.org/10.1523/JNEUROSCI.4889-05.2006.

Yao, Z. *et al.* (2023) 'A high-resolution transcriptomic and spatial atlas of cell types in the whole mouse brain', *Nature*, 624(7991), pp. 317–332. Available at: https://doi.org/10.1038/s41586-023-06812-z.

Young, M.D. and Behjati, S. (2020) 'SoupX removes ambient RNA contamination from droplet-based single-cell RNA sequencing data', *GigaScience*, 9(12). Available at: https://doi.org/10.1093/gigascience/giaa151.

Yu, G. *et al.* (2012) 'clusterProfiler: an R Package for Comparing Biological Themes Among Gene Clusters', *OMICS: A Journal of Integrative Biology*, 16(5), pp. 284–287. Available at: https://doi.org/10.1089/omi.2011.0118.

Yu, J. *et al.* (2019) 'Recruitment of GABAergic Interneurons in the Barrel Cortex during Active Tactile Behavior', *Neuron*, 104(2), pp. 412-427.e4. Available at: https://doi.org/10.1016/j.neuron.2019.07.027.

Zahra, A. *et al.* (2022) 'Shared Etiology in Autism Spectrum Disorder and Epilepsy with Functional Disability', *Behavioural Neurology*, 2022, pp. 1–13. Available at: https://doi.org/10.1155/2022/5893519.

Zalfa, F. *et al.* (2003) 'The Fragile X Syndrome Protein FMRP Associates with BC1 RNA and Regulates the Translation of Specific mRNAs at Synapses', *Cell*, 112(3), pp. 317–327. Available at: https://doi.org/10.1016/S0092-8674(03)00079-5.

Zalfa, F. *et al.* (2007) 'A new function for the fragile X mental retardation protein in regulation of PSD-95 mRNA stability', *Nature Neuroscience*, 10(5), pp. 578–587. Available at: https://doi.org/10.1038/nn1893.

Zappia, L. and Oshlack, A. (2018) 'Clustering trees: a visualization for evaluating clusterings at multiple resolutions', *GigaScience*, 7(7). Available at: https://doi.org/10.1093/gigascience/giy083.

Zarakoviti, E. *et al.* (2023) 'Factor associated with the occurrence of epilepsy in autism: a systematic review', *Journal of Autism and Developmental Disorders*, 53(10), pp. 3873–3890. Available at: https://doi.org/10.1007/s10803-022-05672-2.

Zeisel, A. *et al.* (2018) 'Molecular Architecture of the Mouse Nervous System', *Cell*, 174(4), pp. 999-1014.e22. Available at: https://doi.org/10.1016/j.cell.2018.06.021.

Zhang, C. *et al.* (2018) 'Memory enhancing effects of BPN14770, an allosteric inhibitor of phosphodiesterase-4D, in wild-type and humanized mice', *Neuropsychopharmacology*, 43(11), pp. 2299–2309. Available at: https://doi.org/10.1038/s41386-018-0178-6.

Zhang, C. and Wong-Riley, M.T.T. (2000) 'Synthesis and degradation of cytochrome oxidase subunit mRNAs in neurons: Differential bigenomic regulation by neuronal activity', *Journal of Neuroscience Research*, 60(3), pp. 338–344. Available at: https://doi.org/10.1002/(SICI)1097-4547(20000501)60:3<338::AID-JNR8>3.0.CO;2-1.

Zhang, F. *et al.* (2018) 'Fragile X mental retardation protein modulates the stability of its m6A-marked messenger RNA targets', *Human Molecular Genetics* [Preprint]. Available at: https://doi.org/10.1093/hmg/ddy292.

Zhang, J. *et al.* (2009) 'Altered Hippocampal Synaptic Plasticity in the *Fmr1* Gene Family Knockout Mouse Models', *Journal of Neurophysiology*, 101(5), pp. 2572–2580. Available at: https://doi.org/10.1152/jn.90558.2008.

Zhang, P. *et al.* (2015) 'Novel RNA- and FMRP-binding protein TRF2-S regulates axonal mRNA transport and presynaptic plasticity', *Nature Communications*, 6(1), p. 8888. Available at: https://doi.org/10.1038/ncomms9888.

Zhang, Y. *et al.* (2014) 'Dendritic channelopathies contribute to neocortical and sensory hyperexcitability in Fmr1−/y mice', *Nature Neuroscience*, 17(12), pp. 1701–1709. Available at: https://doi.org/10.1038/nn.3864.

Zhang, Z. *et al.* (2019) 'SCINA: A Semi-Supervised Subtyping Algorithm of Single Cells and Bulk Samples', *Genes*, 10(7), p. 531. Available at: https://doi.org/10.3390/genes10070531.

Zheng, H.J. V. *et al.* (2021) 'Environmental Enrichment Sharpens Sensory Acuity by Enhancing Information Coding in Barrel Cortex and Premotor Cortex', *eneuro*, 8(3), p. ENEURO.0309-20.2021. Available at: https://doi.org/10.1523/ENEURO.0309-20.2021.

Zhou, L.-T. *et al.* (2017) 'A novel role of fragile X mental retardation protein in pre-mRNA alternative splicing through RNA-binding protein 14', *Neuroscience*, 349, pp. 64–75. Available at: https://doi.org/10.1016/j.neuroscience.2017.02.044.